



**LEAST-SQUARES, CONTINUOUS SENSITIVITY ANALYSIS
FOR NONLINEAR FLUID-STRUCTURE INTERACTION**

DISSERTATION

Douglas P Wickert, Major, USAF

AFIT/DS/ENY/09-S04

**DEPARTMENT OF THE AIR FORCE
AIR UNIVERSITY**

AIR FORCE INSTITUTE OF TECHNOLOGY

Wright-Patterson Air Force Base, Ohio

APPROVED FOR PUBLIC RELEASE; DISTRIBUTION UNLIMITED

The views expressed in this thesis are those of the author and do not reflect the official policy or position of the United States Air Force, Department of Defense, or the U.S. Government.

AFIT/DS/ENY/09-S04

**LEAST-SQUARES, CONTINUOUS SENSITIVITY ANALYSIS
FOR NONLINEAR FLUID-STRUCTURE INTERACTION**

DISSERTATION

Presented to the Faculty

Department of Aeronautics and Astronautics

Graduate School of Engineering and Management

Air Force Institute of Technology

Air University

Air Education and Training Command

in Partial Fulfillment of the Requirements for the

Degree of Doctor of Philosophy

Douglas P Wickert

Major, USAF

20 August 2009

APPROVED FOR PUBLIC RELEASE; DISTRIBUTION UNLIMITED

AFIT/DS/ENY/09-S04

**LEAST-SQUARES, CONTINUOUS SENSITIVITY ANALYSIS
FOR NONLINEAR FLUID-STRUCTURE INTERACTION**

Douglas P Wickert

Major, USAF

Approved:

Dr. Robert A. Canfield (Chairman)

Date

Dr. Donald L. Kunz (Member)

Date

Dr. Aihua W Wood (Member)

Date

Dr. Junuthula N. Reddy (Member)

Date

Accepted:

M. U. THOMAS
Dean, Graduate School of
Engineering and Management

Date

Abstract

A least-squares, continuous sensitivity analysis method is developed for transient aeroelastic gust response problems to support computationally efficient analysis and optimization of aeroelastic design problems. The continuous sensitivity equations are a linear boundary-value problem and render computationally efficient design or shape parameter gradients from a continuous system of partial differential equations. A key distinction between the local and total derivative forms of the sensitivity system is introduced. The continuous sensitivity equations and sensitivity boundary conditions are derived in local derivative form which is shown to be superior for several applications. The analysis and sensitivity problems are both posed in a first-order form which is amenable to a solution using the least-squares finite element method. Several example and validation problems are presented and solved, including elasticity, fluid, and fluid-structure interaction problems. Most have known analytic solutions which are compared to the continuous sensitivity solutions. The continuous sensitivity results for both the local and total material derivatives are presented and compared to analytic gradients and gradients obtained by finite-difference methods. Significant contributions of the research include the first sensitivity analysis of nonlinear transient gust response, a local derivative formulation for shape variation that requires parameterizing only the boundary, and statement of sufficient conditions for using nonlinear "black box" software to solve the sensitivity equations. Promising paths for future investigation are presented and discussed.

Acknowledgements

To misappropriate Tolstoy, *successful dissertations are all alike; every unsuccessful dissertation is unsuccessful in its own way.* By this it is meant that if an effort as long and complex as a dissertation is to be successful, there are a series of vital ingredients that are indispensable. The omission of any one of these can lead only to disaster.

The first of these ingredients is a research advisor with vision, patience, and an ability to encourage the student forward when the course seems bleak and uncertain. Professor Robert Canfield could not have been more perfect in any of these attributes. From the first day in which he pitched his idea of a possible research topic through our increasing understanding of the details of the research, his foresight and intuition have proved prescient. Perhaps even more important, he always seemed to know how to move forward towards our goal when the setbacks and obstacles loomed despairingly.

I am also am grateful for the support, commitment, and encouragement from my committee members: Dr. Donald Kunz, whose course in structural dynamics and aeroelasticity laid the foundation of my understanding; Dr. Aihua Wood, whose functional analysis course allowed me to understand the mathematical theory behind the variational methods; and Dr. J. N. Reddy, whose many textbooks have been a critical part of my education and whose collaboration has been welcomed as the greatest of academic honors.

With absolute certainty, the most critical element behind this, the paramount ingredient that sustained an effort exceeding all previously known limits of time and energy, is the understanding, support, and nurturing love of my family. They granted me the freedom to pursue this dream and their understanding and compassion far exceeded what any reasonable person should expect. If all happy families are truly alike, then I now understand the reason why. Thank-you.

Table of Contents

	Page
Abstract	iv
Acknowledgements	v
Table of Contents	vi
List of Figures	viii
List of Tables	xi
 1 Introduction.....	 14
1.1 Background and Motivation.....	14
1.2 Original and Significant Contributions of Research	16
1.3 Overview of Sensitivity and FSI Analysis Methods	19
1.4 Organization of Dissertation	23
 2 Literature Review	 24
2.1 Continuous Sensitivity Equation (CSE) Methods.....	24
2.2 Fluid-Structure Interaction Analysis.....	28
2.3 Sensitivity Analysis of Fluid-Structure Interaction Problems.....	33
2.3.1 Classic sensitivity methods for FSI problems.....	34
2.3.2 Continuous Sensitivity of FSI Problems.....	35
2.3.3 Adjoint Sensitivity Methods	39
2.4 Least-Squares Finite Element Method	40
2.4.1 LSFEM for Fluids.....	42
2.4.2 LSFEM for Structures.....	43
2.4.3 Summary of the advantages & disadvantages of LSFEM for FSI	48
2.5 Summary	49
 3 Continuous Sensitivity Equation Method	 51
3.1 Continuous Sensitivity Equations	51
3.2 Boundary Conditions for Shape Variation CSE.....	58
3.3 Local and Total Derivatives	63
3.3.1 Local and Total Derivative Example	64
3.3.2 Potential Pitfall from Neglecting Local/Total Derivative Distinction	71
3.3.3 Comparison of local derivative and Pelletier’s mixed derivative FSI forms	73
3.4 Summary of Advantages of Local Derivative CSE	74
 4 Least-Squares Finite Element Method.....	 76
4.1 Variational Least-Squares	76
4.2 p -elements	79
4.2.1 Convergence and Error Rates	80
4.2.2 Serendipity and tensor expansion basis comparison.....	82
4.2.3 Coercivity Implications	84
4.2.4 Need for p -elements in LSFEM.....	86
4.2.5 Advantages of p -elements for CSE.....	88
4.3 Alternate norms in LSFEM.....	89
4.3.1 Bar Example using H^1 Norm	91

4.3.2	Two-dimension implementation of the H^1 norm.	93
4.3.3	Plate with a hole H^1 example.....	95
4.4	Improving Condition Number for LSFEM with Weak Boundary Enforcement.....	97
4.5	LSFEM Fluid Models	104
4.5.1	Linear Potential Flow	105
4.5.2	Compressible Potential Flow.....	106
4.5.3	Transient, Compressible Potential Flow.....	109
4.5.4	Stokes Equations.....	113
4.5.5	Transient, Incompressible Euler	114
4.5.6	Transient, Compressible Euler.....	117
4.6	Structural Elasticity Models.....	118
4.6.1	Plane Stress (u - σ formulation)	119
4.6.2	Steady, Linear Euler-Bernoulli Beam.....	121
4.6.3	Transient, Nonlinear Euler-Bernoulli Beam.....	122
4.6.4	Elastic Mesh Deformation	127
4.7	Transient LSFEM.....	131
4.7.1	Time-space formulation.....	131
4.7.2	Continuous Space, Backward-Difference Time Formulation	133
4.8	Fluid-Structure Interface Relations	140
5	<i>LS-CSE For Elasticity</i>	147
5.1	Timoshenko and Goodier Example.....	147
5.2	Plate with a hole.....	156
5.2.1	Infinite Plate Analytic Solution	158
5.2.2	Shape Optimization of a Biaxially-Loaded Plate with a Hole	166
5.3	Summary	170
6	<i>LS-CSE For Fluids</i>	171
6.1	Sphere in Stokes Flow.....	171
6.2	Airfoil in potential flow	177
7	<i>LS-CSE For Transient FSI.....</i>	183
7.1	Golden Piston.....	184
7.2	Flexible beam in a channel.....	187
7.3	Airfoil on a Sting.....	194
7.3.1	Steady Solution (Linear and Compressible Potential, Linear Structure)	196
7.3.2	Typical Section and Gust Models.....	209
7.3.3	Potential Transient FSI (Nonlinear Structure)	211
7.3.4	Nonlinear, Compressible Transient FSI.....	219
7.4	Summary of LS-CSE for Transient FSI.....	225
8	<i>Practical Considerations for CSE</i>	228
8.1	Multiple Design Variables	229
8.2	CSE for Material or Sizing Parameters.....	235
8.3	Adjoint CSE.....	239
8.4	Nonlinear Analysis and “Black-box” implementation of CSE	241
8.4.1	Newton-Raphson Nonlinear Iteration for CSE	242
8.4.2	Direct Substitution Nonlinear Iteration for CSE.....	253
8.4.3	Summary of Nonlinear Black-Box Solver Strategies for CSE	257

9	<i>Conclusions & Future Work</i>	259
9.1	General Conclusions	260
9.2	Summary of Work.....	261
9.3	Summary of Significant Results and Contributions.....	263
9.4	Avenues for Future Research.....	266
9.4.1	Problem and domain scaling.....	266
9.4.2	Using commercial FSI software to solve the sensitivity system.....	268
9.4.3	Large-scale CSE (multiple design parameters).....	268
9.5	Final Word on CSE for FSI applications	269
	Bibliography	271
	Vita.....	283

List of Figures

	Page
Figure 1.1: Boeing design study (left) and AFRL Sensor-Craft concept (right) configurations.....	15
Figure 1.2: Classification and methods of design sensitivity analysis	21
Figure 2.1: Segregated or iterative fluid-structure interaction solution.....	29
Figure 3.1: First-order finite difference approximation error example.....	53
Figure 3.2: Bar sensitivity example	64
Figure 3.3: Bar sensitivity comparison	68
Figure 3.4: Two options for bar domain parameterization	69
Figure 4.1: Pascal's triangle for serendipity and tensor product expansions (from [70])	83
Figure 4.2: Degree of freedom comparison for Serendipity and Tensor product expansion basis.....	84
Figure 4.3: LSFEM system residual p -convergence as a function of total system degrees of freedom (N).....	88
Figure 4.4: Vertically loaded bar	91
Figure 4.5: Comparison of LSFEM L^2 (left) and H^1 (right) norm solutions ($p = 2$) for a 2-element vertically loaded bar	93
Figure 4.6: L^2 norm solution to Reddy Ex. 13.2.4	94
Figure 4.7: H^1 norm solution to Reddy Ex. 13.2.4	95
Figure 4.8: Comparison of L^2 and H^1 norm boundary data for the plate with a circular hole CSE problem.	97
Figure 4.9: Partitioned domain and boundary value problem.....	100
Figure 4.10: Weak and condensed system condition number as a function of boundary weighting factor	102
Figure 4.11: Plunging sphere compressible flow velocity components solution for 0.25 M ($\alpha_{effective} = 30\text{deg}$, peak shoulder velocity is 0.57 M)	112
Figure 4.12: Comparison of quasi-steady compressible and full potential flow for LSFEM solution to plunging cylinder validation problem; velocity components (<i>left</i>) and pressure coefficient (<i>right</i>).	113
Figure 4.13: LSFEM solution of steady, incompressible Euler flow about a sphere ($p = 8$)	116
Figure 4.14: Comparison of LSFEM solution with theoretical solution (solid lines) for steady, incompressible Euler flow about a sphere	117
Figure 4.15: Beam free-body diagram	123
Figure 4.16: 1D stress and strain reference area and configuration definitions.....	127
Figure 4.17: Plucked bar time-space mesh and boundary conditions.....	132
Figure 4.18: Displacement, stress, and velocity during the first quarter period of a clamped-free bar plucked in the first mode shape (initial position <i>blue</i> to quarter period <i>red</i>).....	133

Figure 4.19: First quarter period of a beam plucked in the first mode shape ($\Delta t = 0.02$, $p = 4$, 5 pts backward difference) (initial position <i>blue</i> to quarter period <i>red</i>)	136
Figure 4.20: Comparison demonstrating effect of number of BD points on numerical stability of quarter period plucked beam solution.....	144
Figure 4.21: Comparison showing rapid deterioration of numerical stability due to too small Δt of quarter period plucked beam solution	145
Figure 4.22: Comparison showing improvement of numerical stability due to increased p on quarter period plucked beam solution	146
Figure 5.1: Timoshenko and Goodier example 3.24.....	149
Figure 5.2: Timoshenko and Goodier example 3.24 boundary conditions.....	150
Figure 5.3: T&G LSFEM solution and residual ($p = 12$).....	152
Figure 5.4: T&G CSE solution and residual ($p = 12$) for sensitivity to beam length....	153
Figure 5.5: T&G analytic local sensitivity to beam length.....	154
Figure 5.6: T&G CSE analytic total sensitivity to beam length	154
Figure 5.7: Comparison of T&G LS-CSE and analytic derivatives for on boundary Γ_3	155
Figure 5.8: Comparison of T&G LS-CSE and analytic derivatives for on Boundary Γ_4	156
Figure 5.9: Plate with an elliptical hole	157
Figure 5.10 LSFEM Solution ($p = 8$) for Displacements (u, v), Stresses ($\sigma_x, \sigma_y, \sigma_{xy}$), and Residual Error Norm of a Quarter Plate with a Circular Hole Subject to Normal- x Stress Value of 10.	159
Figure 5.11 Comparison of LSFEM and Analytic Solution Along the Hole ($p = 8$) ...	160
Figure 5.12 Comparison of analytic and LSFEM-derived sensitivity boundary conditions	163
Figure 5.13 LS-CSE Solution ($p = 8$) and Residual Error Norm for the Sensitivity of Field Variables to Hole Radius, a , for a Quarter Plate with a Circular Hole	164
Figure 5.14 Comparison of Analytic, Finite Difference, and LS-CSE Solutions along the Hole Boundary for Tangential Stress Sensitivity to Hole Radius, a	165
Figure 5.15 Elasticity and Sensitivity Problem p -convergence and Stress-Concentration Convergence for a Uniaxially Loaded Plate with a Circular Hole.....	166
Figure 5.16 Tangential stress optimization convergence to uniform value ($\bar{\sigma}_{\theta\theta} = 1.797$) as a function of eccentric anomaly (E) and Objective function value as a function of semi-minor axis (b)	169
Figure 6.1: Sphere surface boundary parameterization and description.....	172
Figure 6.2: Immersed sphere computational mesh and boundary conditions.....	173
Figure 6.3: Immersed sphere sensitivity boundary conditions	174
Figure 6.4: Sphere immersed in Stokes flow analytic solution	175
Figure 6.5: LSFEM solution for sphere immersed in Stokes Flow	175
Figure 6.6: Sphere immersed in Stokes flow analytic sensitivity	176
Figure 6.7: LS-CSE for sphere immersed in Stokes flow.....	176

Figure 6.8: Velocity component solution for potential flow about NACA 0012 airfoil at 10 deg AOA ($p = 12$)	178
Figure 6.9: NACA 0012 airfoil 238 element computational mesh (full mesh, left; close-up of airfoil, right).....	178
Figure 6.10: Comparison of flow solution at airfoil surface to vortex panel solution ($p = 12$)	179
Figure 6.11: C_p for LSFEM and vortex panel for NACA 0012 airfoil.....	179
Figure 6.12: Potential flow u component velocity sensitivity to angle of attack for NACA 0012 airfoil.	180
Figure 6.13: Potential flow v component velocity sensitivity to angle of attack for NACA 0012 airfoil.	180
Figure 6.14: Steady, compressible flow solution (0.5 M) for the nonlinear potential model (8 nonlinear iterations) and the linear potential solution and vortex panel data corrected for compressibility.....	182
Figure 7.1: Golden Piston problem description	184
Figure 7.2: Beam immersed in a channel flow (X. Wang)	188
Figure 7.3: LSFEM FSI solution ($p = 2$) showing beam deflection	190
Figure 7.4: LSFEM and analytic solution for beam deflection	191
Figure 7.5: LS CSE solution ($p = 12$) showing beam deflection sensitivity	193
Figure 7.6: LS-CSE beam deflection sensitivity and relative error	194
Figure 7.7: Flexible sting mounted airfoil	195
Figure 7.8: Sting length boundary parameterization.....	196
Figure 7.9: Airfoil coordinate system for integrating fluid forces.....	199
Figure 7.10: Steady LS-CSE velocity sensitivity for NACA 0012 airfoil on a sting (10 deg effective angle of attack)	201
Figure 7.11: Steady LS-CSE pressure coefficient sensitivity for NACA 0012 airfoil on a sting (10 deg effective angle of attack)	201
Figure 7.12: Steady LSFEM pressure solution for NACA 0012 airfoil on a sting (tip rotation 10 deg)	202
Figure 7.13: Steady LSFEM pressure solution for NACA 0012 airfoil on a sting.....	203
Figure 7.14: Comparison of steady, linear potential FSI solution with analytic solution	204
Figure 7.15: Steady, linear potential LS-CSE solution with analytic sensitivity.....	205
Figure 7.16: LS-CSE solution ($p = 12$) for pressure sensitivity to angle of incidence. (Sting rotation sensitivity is plotted to scale; sting transverse deflection sensitivity is not to scale).	207
Figure 7.17: Comparison of steady linear potential solution and compressible potential solution ($M = 0.5$) for NACA 0012 airfoil on a sting	208
Figure 7.18: Vertical gust relation	209
Figure 7.19: Comparison of time-sequential linear potential fluid and quasi-steady thin airfoil (TA) typical section solutions for an oscillating airfoil with pitch and plunge	210
Figure 7.20: Nonlinear transient response for beam tip deflection, velocity, rotation, and internal shear to a 1 sec <i>one-minus-cosine</i> gust	215

Figure 7.21: Comparison of finite difference and LS-CSE solution for beam deflection, velocity, rotation, and internal shear sensitivity to the beam length for a 1 sec <i>one-minus-cosine</i> gust	216
Figure 7.22: Beam deflection, rotation, and internal moment sensitivity to the nonlinear gust response at $t = 3$	218
Figure 7.23: Extrapolated and actual beam deflection and rotation to <i>one-minus-cosine gust</i> ($t = 3$ sec) for a 3% and 6% longer sting	219
Figure 7.24: Sequential FSI coupling solution architecture for nonlinear, compressible fluid and nonlinear structure.	220
Figure 7.25: Transient, nonlinear gust response of sting tip to <i>one-minus-cosine</i> gust (peak α_{gust} magnitude of 10 deg) for compressible and incompressible fluid	222
Figure 7.26: Transient, gust CSE of sting tip for <i>one-minus-cosine</i> gust (peak α_{gust} magnitude of 10 deg) based on compressible and incompressible FSI solution.....	223
Figure 7.27: Nonlinear compressible FSI (0.5 M) pressure field and structure deformation to <i>one-minus-cosine gust</i> ($t = 0$ sec top, $t = 3.5$ sec bottom)	224
Figure 7.28: CSE pressure sensitivity to beam length with structure deformation sensitivity depicted ($t = 3.5$ sec). (Sting rotation sensitivity is plotted to scale; sting transverse deflection sensitivity is not to scale).	225
Figure 8.1: Two-section bar sensitivity example	230

List of Tables

	Page
Table 3.1: Summary of CSE operators in first-order form	57
Table 4.1: Comparison of weak and condensed condition number order of magnitude for four example problems.....	103
Table 4.2: Summary of fluid model equations, variables, assumptions, and notes	105
Table 4.3: Boundary condition combinations for the Stokes equations [69].....	114
Table 4.4: Multipoint backward-difference representations	134
Table 4.5: Backward difference discrete time stability and accuracy considerations ...	140
Table 5.1: Boundary Data for Timoshenko and Goodier example 3.24 elasticity and sensitivity problems	151
Table 5.2: Boundary conditions for plate with a circular hole	157
Table 5.3: Plate with a elliptical hole optimization	169
Table 7.1: Beam in channel flow boundary conditions	188
Table 7.2: Immersed Beam Problem Parameters.....	189
Table 7.3: Sting-mounted airfoil FSI problem boundary conditions	198
Table 7.4: Sting-mounted airfoil CSE problem boundary conditions	198
Table 7.5: Airfoil on a Sting Problem Parameters	201
Table 7.6: Steady FSI and CSE solutions for incompressible and compressible flow ...	221

LEAST-SQUARES, CONTINUOUS SENSITIVITY ANALYSIS FOR NONLINEAR FLUID-STRUCTURE INTERACTION

1 Introduction

1.1 Background and Motivation

Due to excessive computational expense, the design and shape optimization of a lightweight, flexible air-vehicle structure susceptible to aeroelastic loads and nonlinear response is currently not practical. This research has endeavored to develop a sensitivity analysis method for nonlinear, transient fluid-structure interaction problems that avoids some of the computational limitations of existing methods and renders a potentially more efficient method for design optimization of future aerospace applications.

Aeroelasticity is a challenging science, dealing with the interaction of two very different domains governed by disparate physics. Nonlinear aspects of both the fluid and structural domains can make accurate calculations of the interaction problematic, not the least due to the substantial computational expenses involved. Since optimization and inverse design methods typically require some measure of the change of an objective function or performance parameter to variations in design parameters, optimization of aeroelastic problems, which are themselves computationally intensive, challenging, and expensive to solve, can be outright formidable. Thus, this subject represents a very prime frontier for basic research and even small contributions for advancing towards a

computationally efficient analysis and sensitivity method for nonlinear fluid-structure interaction (FSI) problems may prove significant and fruitful. Of more than mere academic interest, the inverse design and optimization problem for which sensitivity to shape design parameters is desired is vital for the next-generation of USAF persistent Intelligence, Surveillance, and Reconnaissance (ISR) aerospace platforms. Some of the proposed configurations currently being studied by AFRL/RB, the primary sponsor of this research, are depicted in Figure 1.1. A critical mission requirement is long endurance which dictates large fuel fractions and lightweight structures. The lightweight requirements and large aspect ratio of these configurations contribute to large deformations of the structure and significant geometrically nonlinear effects. Further, the low wing-loading results in significant gust response. Indeed gust response loads have been identified as the critical load condition for joined wing configurations similar to the designs of interest in Figure 1.1 [20, 38, 75, 78, 131, 132].

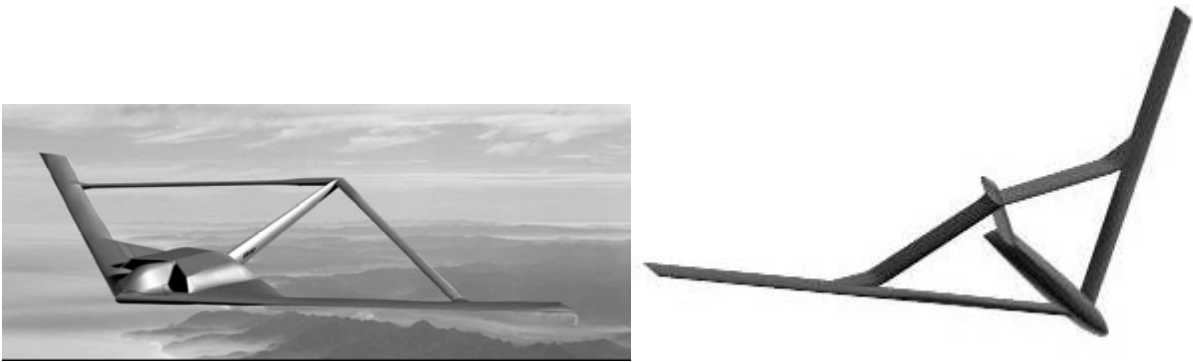


Figure 1.1: Boeing design study (left) and AFRL Sensor-Craft concept (right) configurations

The research goal of this dissertation is motivated by the need for a computationally efficient design optimization method for nonlinear aeroelastic response

of a lightweight, flexible aerospace structure. Thus, this research endeavors to develop a sensitivity analysis framework that might enable computationally efficient methods for design optimization of future aerospace applications. Specifically, the research develops the continuous sensitivity equation (CSE) method for fluid-structure interaction problems. To solve the sensitivity problem, the fluid-structure response problem must be solved first. This includes modeling the transient, nonlinear gust response of a representative fluid-structure problem in which to demonstrate the continuous sensitivity method theory and verify that it provides the desired gust response sensitivity. Shape variation problems are of particular interest because they are more computationally challenging for other sensitivity methods and are typically of interest in early inverse design studies. Thus a focus of the research is to calculate the shape parameter design gradients for any dependent domain variable.

The next section outlines the results of these research efforts and the significant and minor contributions to the subject.

1.2 Original and Significant Contributions of Research

Accurate aeroelastic analysis of the nonlinear gust response of a flexible structure undergoing large deformation is technically challenging and limited by the computational complexity of the transient, nonlinear fluid-structure interaction. Although we have solved the aeroelastic gust analysis problem for only simple examples in the course of this research, this dissertation demonstrates that a least-squares, continuous sensitivity approach is a straightforward method for calculating the shape design sensitivity of the fluid-structure system once the aeroelastic analysis is completed. The approach is

computationally efficient and avoids many of the problematic and computationally expensive steps for sensitivity analysis of other currently employed methods.

This dissertation makes two significant contributions to the state of knowledge for the application of continuous sensitivity methods. Although they are posed in support of the sensitivity analysis of fluid-structure interaction problems, they are more general and more fundamental than the application to FSI. The first of the two major contributions of the present work is the recognition that the sensitivity system is simpler to pose in local derivative form than in total (material) derivative form. For shape sensitivity problems, the local sensitivity form is not unique (itself a significant recognition and contribution), but it may be transformed to the unique total derivative form as needed. The local CSE form as posed in this dissertation makes explicit that only boundary data is needed for shape variation problems. This is in contrast to other local CSE formulations that are written as domain variation problems. These distinctions are explained in detail in Chapter 3.

The second major contribution is the detailed explanation of how to employ the same code for continuous sensitivity analysis as was used to solve the original, parent analysis problem. This may be done in a “black box” manner without access to the source code and is explained in detail in Chapter 8.

Both of these two major contributions should allow a more widespread adoption of the CSE method. First, because the system of equations is simpler to state; second, because special analysis software is unnecessary to solve the sensitivity problem. In the course of the research and method development, other original contributions have also

been made that advance the state of knowledge. Each of the items in the following list of contributions is explained in more detail in the dissertation:

- 1) First sensitivity calculation for a nonlinear FSI, transient gust response (Chapter 7)
- 2) Explicit explanation that local sensitivities for shape variation problems are not unique, but that the material derivative is unique (Chapter 3)
- 3) Simpler sensitivity boundary condition for elasticity problems with traction boundary conditions (Chapter 3, Chapter 5)
- 4) Most detailed application of continuous sensitivity to the solution of an elasticity problem to appear in the literature (Chapter 5)
- 5) Demonstration that transient sensitivity problems need not be solved as a transient problem (Chapter 7)
- 6) Demonstration of a condensation and recovery method for improving the condition number of least-squares finite element weakly enforced boundary data (Chapter 4)
- 7) Observations on an apparent relationship between the minimum recommended polynomial order for the least-squares finite element (LSFEM) solution to elasticity problems and the lowest order stable-mixed element for elasticity (Chapter 4)
- 8) First known documented use of an alternative norm solution for a LSFEM elasticity system and comparison with the traditional L^2 norm (Chapter 4)
- 9) Numerical stability analysis for a LSFEM domain with higher-order backward-difference discrete time formulation method for transient LSFEM (Chapter 4)
- 10) Proof of the equivalence of Newton-Raphson tangent stiffness matrix and CSE system matrix for Galerkin FEM (Chapter 8)

11) Derivation of an improved Newton-Raphson method for LSFEM (Chapter 8)

Furthermore, the FSI analysis in Chapter 7 is the first analysis known in the literature which studies the nonlinear response to a transient gust load. The subsequent sensitivity analysis of the same problem is also the first attempt to study transient gust sensitivity in the literature. The ultimate application and goal of this research is that it will permit a computationally efficient analysis method to calculate nonlinear, aeroelastic design gradients that may someday ultimately be used to design and optimize very flexible aerospace structures.

1.3 Overview of Sensitivity and FSI Analysis Methods

This section provides a brief background and roadmap overview of the sensitivity and fluid-structure interaction analysis methods used in the dissertation. In-depth background, theory, and results are provided in the remainder of the dissertation. This section provides the strategic overview.

Many of the most widely used optimization algorithms are gradient-based in which the design parameter gradients of objective and/or constraint functions with respect to design variables are required. The design parameter gradients are commonly referred to as sensitivities and can be calculated in various ways. Design sensitivity methods can be grouped into numerical approximate methods (*e.g.* finite difference) and analytic/semi-analytic methods, Figure 1.2. Numerical approximate methods calculate parameter derivatives by perturbation finite difference methods [60]. This can be costly if the original numerical solution is itself costly (*e.g.* CFD, FEM). Analytic and semi-analytic methods can be further classified as either discrete or continuous, the difference

depending on the order of the discretization and the differentiation steps [34, 60]. The most common approach is to discretize the system first and then calculate sensitivities by either direct or adjoint methods. For shape sensitivity problems, the boundary and domain of the problem vary with the design parameters and the mesh sensitivity must also be calculated in the discrete approach. This dissertation employs the continuous sensitivity method, in which the design parameter gradients are calculated by solving the continuous sensitivity equations (CSE), typically a system of partial differential equations [23]. The continuous sensitivity method is variously known as variational shape design [60], the continuum sensitivity method [39], and the variational sensitivity method [59]. Since the CSE system is posed as a continuous system, it can efficiently produce shape parameter gradients without calculating the mesh sensitivity (which often amounts to the expensive task of inverting a large mesh Jacobian). Thus, the continuous sensitivity method for gradient calculation can efficiently produce design parameter gradients for shape optimization problems without needing to calculate the problematic mesh sensitivities. The resulting sensitivity equations are always linear, even for nonlinear systems, which is particularly attractive for the nonlinear aeroelastic problems considered here.

Continuous sensitivity methods were first introduced for structural problems [39, 41], but few actual applications to structural problems appeared in the literature. The application of CSE to fluid problems appeared later but was more widely adopted for flow optimization problems and is now more mature with commercial code packages available. Recent work by Pelletier and his students at Ecole Polytechnique de Montreal

have extended CSE methods to unsteady fluid-structure problems, but their primary interest has been in examining the flow sensitivity (see Section 2.3.2). The motivating interest behind this dissertation is in the structural sensitivity and subsequent optimization to an aeroelastic response. This dissertation thus develops a CSE method appropriate for the structural analysis and sensitivity of a nonlinear gust response. To our knowledge, this is the first example in the literature that employs least-squares formulations to solve the CSE system for a coupled fluid-structure system. As will be explained, the choice of least-squares finite elements to solve both the fluid-structure system and the CSE system was based on expected analysis advantages for the fluid-structure problem. Additionally, very few applications of CSE methods to transient problems exist in the literature and none that are based on a transient, compressible fluid formulation.

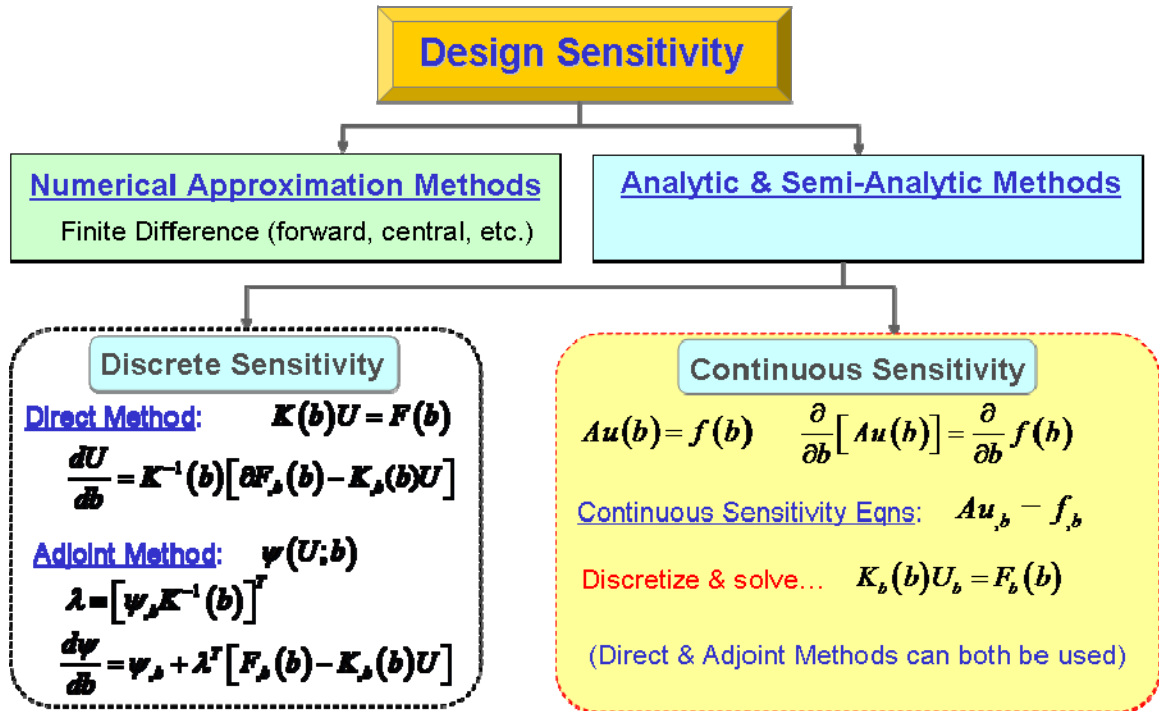


Figure 1.2: Classification and methods of design sensitivity analysis

The least-squares finite element method (LSFEM) is a numerical method for solving differential equations. It is similar to other variational methods in which a solution (function) is sought that minimizes some objective (functional). In LSFEM, the square of the system residual is minimized. LSFEM is capable of numerically solving all types of partial differential equations within a single computational framework without any special numerical treatment. Thus a LSFEM solution strategy for monolithic FSI formulations (suitable for optimization) is promising. LSFEM for time-dependent and nonlinear problems are well-established in the literature, and are applicable to analysis of transient, nonlinear gust response with certain cautions that are explained in Chapter 4.

A LSFEM solution strategy is also a natural choice for CSE. Sensitivity expressions are often desired for both primal and dual variables. Since the LSFEM method commonly uses a first-order form for the governing system of equations, a LSFEM implementation offers equal degrees of accuracy in all the problem variables. Unless specific mixed-elements are designed for the problem, this is not generally true for a Galerkin-formulated finite element model. For example, elasticity systems are typically solved using displacement variables and the stress field is calculated by differentiating the solution. This decreases the continuity of the approximated stress tensor as well as the accuracy of the estimate. This can have a profound effect on the continuous sensitivity equations, since the FEM solution of the original system is used to estimate the boundary conditions for the CSE system.

1.4 Organization of Dissertation

Chapter 2 outlines the history and the current state of known research from the literature in continuous sensitivity analysis methods, least-squares finite element methods, and fluid-structure iteration analysis methods. Chapter 3 derives the theory for the continuous sensitivity analysis methods, including an important distinction between the local and total (material) derivative form of the equations. Chapter 4 explains the theory and implementation of the least-squares finite element method for the various fluid and structural models used in the subsequent fluid-structure interaction analysis. Chapter 5 presents least-squares continuous sensitivity equation (LS-CSE) results for structural systems and Chapter 6 presents sensitivity results for fluid problems. The emphasis in both cases is on comparing CSE method results with analytic derivatives for both local and total derivatives. Thus, these are useful validation examples for the current work and for future efforts. Chapter 7 presents the LS-CSE results for several example FSI problems. Chapter 8 discusses several practical considerations for implementation of CSE and explains how to use the existing analysis code for a parent problem to solve the sensitivity problem. This can be done in a “black box” manner without access to the underlying source code. Finally, Chapter 9 summarizes the work, discusses the overall significance of the research, and recommends several avenues for future study.

2 Literature Review

The purpose of this chapter is to outline the history and research background of the various components of the dissertation. Special emphasis is given to the known limits of the current state of knowledge as established in the published literature. This chapter is divided into four main sections: continuous sensitivity analysis methods (Section 2.1), fluid-structure interaction analysis methods (Section 2.2), sensitivity analysis of fluid-structure systems (Section 2.3), and least-squares finite element methods (Section 2.4).

2.1 Continuous Sensitivity Equation (CSE) Methods

Design optimization methods rapidly evolved as a practical science in the years following WWII. The fruits of optimization in a wide variety of fields are often traced to common roots in the birth of operations research in the RAF bomber command during the war. For example, Schmit's 1960 paper [113], recognized as one of the founding papers in the field of structural optimization, is based on the same linear and nonlinear mathematical programming techniques developed for bomb-to-target allocation problems. Sensitivity methods, which describe how an outcome or performance measure varies in proportion to the variation of some input, are one of the most widely employed methods of analysis for optimization and have a range of meanings (both quantitative and qualitative) that match the range of disciplines in which they have been used [139]. In the present context, we use *sensitivity* to mean the gradient of response functions with respect to a design variable. Response functions are dependent state variables (or functions of the state variables) governed by mechanical or constitutive laws.

As described in Section 1.3 and depicted in Figure 1.2, design sensitivity methods can be grouped into numerical approximate methods or analytic (and semi-analytic) methods. Analytic sensitivity is also a mature subject, particularly as applied to structural systems, as indicated by the presence of many excellent textbooks on the subject [34, 59, 60]. The efficient choice of direct or adjoint methods of sensitivity analysis (based on the number of responses vs. the number of design variables) is also well-established. Sensitivity optimization for fluid problems followed a roughly parallel development, including rapid development of computational techniques for airfoil design in the 1970s [1]. The emphasis in optimization of fluid problems appears to be on parameter and shape optimization techniques, whereas structural optimization during the same period addressed both shape and size optimization problems. Overall, shape sensitivity and optimization methods are more developed and applications are more common for structural problems [9, 10, 39, 59, 92] than they are for fluid problems, but they have not typically employed continuous sensitivity methods for the solution of representative example problems.

The analytic and semi-analytic sensitivity methods can be further classified as either discrete or continuous, the difference depending on the order of the discretization and differentiation steps [34]. The most widely used approach is to discretize the system first and calculate sensitivities by either direct or adjoint methods. This is commonly referred to as “discretize first, then differentiate” in the literature [119]. For shape sensitivity problems, the mesh sensitivity must also be calculated for this approach which can be problematic.

The continuous sensitivity method “differentiates first, then discretizes.” The governing system of equations (for the original parent problem) is differentiated with respect to the design parameters to yield another system of equations for what are now called the sensitivity variables. The sensitivity variables, governed by the continuous sensitivity equations (CSEs), are then discretized and numerically solved. In practice, it is convenient to use the same numerical solution method, *e.g.* CFD or FEM, to solve both the parent and sensitivity problems. This approach avoids having to calculate the problematic mesh Jacobian sensitivity which plagues the discrete shape sensitivity method. The CSE system is always a linear system of equations, even when the original system is nonlinear, which can simplify the computational burden (depending on the numerical method used for solving the CSE system).

Continuous sensitivity methods were developed for solid mechanics in the mid-80s by a series of notable works by Dems and Mroz [40-42] and Dems and Haftka [39]. Huag *et al.*’s 1986 textbook on the subject [60] was also an important contribution. Arora *et al.* proved that the material derivative and control volume approaches for continuous sensitivity are equivalent [9]. The CSE method for CFD (and the operator implementation method of CSE as it is currently recognized) was first introduced by Borggaard and Burns (1994) for the shape optimization of a fluid problem in a NASA contractor report [24], but did not receive widespread attention until the seminal 1997 paper[23]. Since then, the application of CSE methods has been far better documented for fluid problems. This includes the PhD dissertations of two of Prof Burn’s students at Virginia Tech, Stewart [121] in 1998 and Stanley [119] in 1999 as well as a textbook by

Stanley and Stewart [120]. This is also the same period during which Prof Pelletier at École Polytechnique de Montréal began examining the fluid sensitivity of computational fluid problems using continuous sensitivity methods [128]. Most non-fluid applications of CSE in the literature have been limited to 1D scalar problems (*e.g.* heat flow) and 1D beam problems [118, 120].

The dearth in the literature of structural applications of the continuous sensitivity method, despite the method's theoretical origin in the realm of solid mechanics, probably stems from the complicated form for the sensitivity boundary conditions (ref. Section 3.1) and the maturity of other design sensitivity methods for structural optimization. Bhaskaran and Berkooz presented an FEM-based continuous sensitivity solution for a 2D structural elasticity problem that is also considered in Chapter 5 [18], but much of the useful detail and validation of the gradient information of the solution was not included. Earlier, Phelan and Haber [92] presented a FEM solution for the sensitivity of a 2D structural elasticity problem using a domain parameterization method that is similar in nature to the continuous sensitivity method (though it is derived and posed in a more complicated form), but much of the remaining literature presents structural CSE theory without any representative example problems. A 1997 survey of multidisciplinary aerospace design optimization papers [115] listed almost 300 papers with not a single reference to the continuous sensitivity approach for obtaining design gradients. To partially fill the gap in the literature and build a better understanding of the CSE method for 2D elasticity, we undertook the work presented in Chapter 5 (and recently reported [136, 138]).

Due to the relative rarity of continuous sensitivity applications in the literature, it is not surprising that there are no published accounts which employ LSFEM to solve the CSE system. Thus, the research associated with this dissertation is the first effort to study the benefits and disadvantages of employing least-squares methods to solve the sensitivity equations. The least-squares method for fluid-structure interaction, the subject of the next section, is also a recent research endeavor.

2.2 Fluid-Structure Interaction Analysis

Fluid-structure interaction (FSI) problems can be difficult to solve due to the coupling of the disparate fluid and solid physics. Coupling between the fluid and structure domains can generally be classified into three different schemes:

- 1) Segregated fluid-structure (fully decoupled or loosely-coupled systems)
- 2) Coupled fluid-structure, segregated (decoupled) mesh deformation
- 3) Fully-coupled, fluid-structure-mesh deformation (three-field formulation)

The first scheme is also known as iterative FSI coupling and the last two as direct FSI coupling. Until recently, the most common practical approaches for solving fluid-structure interaction problems employ the segregated strategy using different theoretical formulations and numerical methods to solve the fluid and structure problems separately. This segregated solution strategy is illustrated in Figure 2.1. The fluid domain problem is solved using computational fluid dynamics (CFD) and the resultant fluid loads are then applied to the structure. The finite element method (FEM) is then used to calculate the displacement of the structure, a new fluid mesh is formed around the deformed structure, and the cycle is begun anew. The segregated approach can obviously leverage the state

of the art methods and technology in each separate domain. This is also the main approach used in industry and commercial programs, e.g. MSC.Nastran and ZAERO. ADINA FSI, a nonlinear commercial software package for FSI, recommends a segregated (iterative FSI) solution for many example applications since it requires less memory (ADINA FSI is also capable of fully-coupled, nonlinear solutions). Mapping the fluid pressure onto the structure in iterative FSI was first accomplished using spline methods, though more sophisticated methods have been introduced in the literature. The disadvantage of the segregated/iterative approach, however, is the potentially slow convergence and no *a priori* guarantee of convergence [17, 77].

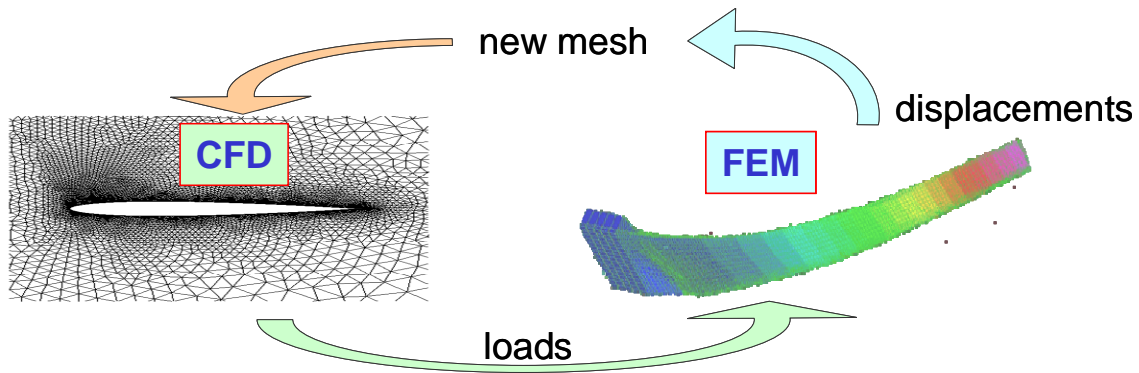


Figure 2.1: Segregated or iterative fluid-structure interaction solution

The desire to overcome the shortcomings of the segregated approach motivated a monolithic formulation of the fluid-structure interaction problem in which the entire system is implicitly solved. Monolithic means cast as a single unit/piece and in this approach the physics of the fluid and the structure domains are cast as a fully-coupled system that can be solved simultaneously rather than in an iterative, segregated scheme.

This approach is also known as direct FSI coupling. The fluid mesh deformation portion of the problem may either be coupled with the fluid and structure physics or solved iteratively between each time step in transient problems. The coupled fluid-structure with decoupled mesh deformation approach has been used in several cases [53, 58, 79]. The location of the interface (the mesh deformation) is calculated separately from the coupled fluid-structure solution and is updated at every iteration. The primary advantage of the coupled fluid-structure approach compared to the segregated strategy is continuity (*i.e.* satisfaction) of the interface boundary conditions between the fluid and structure domains. Even if weakly enforced using a boundary integral method [105], the continuity of the shared interface tractions and velocities along the boundary are considered fully enforced.

In other recent works, a separate fluid-structure interface (a “mortar” in some contexts) has been added to the fluid and structure domains to form a three-field domain problem at the fluid-structure boundary [12, 16, 114, 122, 123]. In another new approach, Bendiksen [17] eliminated the traditional spline mapping between the fluid and structure degrees of freedom and satisfied the interface boundary conditions by matching the shape functions used in the fluid and structure domains. In all cases, a mesh deformation or regeneration is required during iteration. As overall computer performance improves and the expense of approaches employing large memory decreases, the trend in aeroelastic computational methods is towards full coupling of the fluid-structure-mesh systems [12, 13].

Full coupling of the fluid-structure-mesh system is a true monolithic formulation [50, 64, 84, 129]. This approach generally gives the fastest convergence [61], though the memory requirements are substantially greater, since the fluid, structure, and mesh degrees of freedom must be treated and solved simultaneously. Matthies compared the overall numerical performance of monolithic solutions with weakly-coupled partitioned schemes with overall favorable conclusions for the monolithic approach [81]. Rasmussen [102] posed and solved the fully-coupled nonlinear, transient FSI system using LSFEM. Rasmussen's [101] results confirmed the conclusions of Bendiksen [17] that failing to solve the system monolithically can sometimes lead to erroneous solutions for some types of transient FSI problems.

In all of the approaches listed above, the mesh deformation problem can be modeled either discretely or on a continuum basis. The discrete method typically uses a spring system between grid points to move the fluid domain proportionally. Diagonal springs between grid points can control element or control volume distortion and torsional springs can be included to prevent the mesh from folding over itself [52]. Since the mesh is discrete, in most cases there is no need to model the mesh deformation as a continuous problem. One notable relevant exception is the fluid-structure analysis and sensitivity approach developed by Pelletier *et al.* [51], discussed further in Section 2.3.2. Their approach for the mesh deformation domain adapts the continuum pseudo-solid approach introduced by Sackinger [112] for free-boundary fluid problems.

For the purpose of validating the CSE method, FSI problems that appear in the literature with analytic solutions are particularly interesting. Unfortunately, there are few

examples that are directly applicable to the nature of the motivating problem and which are conducive to shape variation and sensitivity analysis. Wang [130] gave one system, a flexible beam immersed in channel flow, which is explored in Section 7.2. A 2D example problem, Section 7.3, is traceable to the joined-wing configuration of interest to the sponsor and was originally posed by Rasmussen [101]. This problem is studied extensively throughout the dissertation.

Since the least-squares finite element method (LSFEM) is a near universal¹ approach for solving problems governed by systems of partial differential equations, it is a natural technique for treating coupled domains governed by different physics. It is this aspect of LSFEM that makes it attractive for FSI analysis. The background for the LSFEM is more fully explored in Section 2.3.3, but at this point, we note that only two applications of LSFEM to fluid-structure interaction problems have been documented [71, 72, 101]. Both researchers reported problems in determining the appropriate boundary and domain weighting factors for the least-squares functional statement of the problem. This is also mentioned in several early (non-FSI) papers covered by the Eason’s survey of least-squares applications [46] and was also encountered in the present effort.

¹ The term is used by Jiang [69] to contrast the LSFEM for solving first-order systems of differential equations with the Rayleigh-Ritz method (applicable only to self-adjoint operators) and the Galerkin weighted residual method (which exhibits problems with non-self-adjoint systems and is subject to the restrictions of the LBB condition for mixed formulations).

The sponsor is primarily and ultimately interested in aeroelastic optimization of a long-endurance aerospace platform, potentially similar to the AFRL Sensor-Craft configuration discussed in Section 1.1. Joined-wing aeroelasticity has received significant recent attention in the literature, much of which emphasized the structural nonlinear aspects of the configuration [37, 75, 78]. A linear aerodynamic model and structural nonlinear FEM model in [38] identified significant compressive forces in the aft wing from the forward wing joint. Similar nonlinear compressive forces are included in the aeroelastic sting model considered in Section 7.3.3. Other research [131, 132] emphasized the importance of modeling both the nonlinear aerodynamics and nonlinear structural coupling of the joined wing configuration for dynamic problems. Most significantly, a prior collaboration between AFRL and AFIT [20] identified gust response as the critical load condition for a flexible, lightweight joined wing configuration. This is the primary motivation for studying the nonlinear gust response sensitivity that is the subject of this dissertation. We first review, in the next section, the methods previous researchers have employed in FSI sensitivity analysis before introducing the least-squares continuous sensitivity method in Chapter 3.

2.3 Sensitivity Analysis of Fluid-Structure Interaction Problems

We divide the review of sensitivity analysis for FSI problems in to those that use classic (numerical approximation and discrete) design sensitivity methods, Section 2.3.1, and those that employ continuous sensitivity methods, Section 2.3.2. Additionally, we review some aerodynamic and aeroelastic sensitivity analysis approaches which employ adjoint formulations in Section 2.3.3.

2.3.1 Classic sensitivity methods for FSI problems

Just as the majority of FSI analysis is based on segregated methods, so has the majority of design sensitivity analysis been accomplished using segmented analysis for the fluid and structure domains. This approach requires a computationally inefficient iteration between the fluid and structure systems [79]. Due to the computational expense, the vast majority of practical applications in aeroelastic sensitivity and optimization have focused on static or steady-state fluid-structure interaction problems [77, 82, 83], or on simple linear structure and linear aerodynamic models [33, 85, 86]. The results described in Section 7.3 and reported in [137] are the first known published results for nonlinear, transient gust response sensitivity. Overall, research in aeroelastic optimization of dynamic problems, including sensitivities of nonlinear flutter to aerodynamic shape design variables, is in the very earliest stages of methods development. Use of continuous sensitivity methods is even more limited and is discussed in more detail in the next section. Not surprisingly, the primary limitation of coupled, dynamic fluid-structure sensitivity analysis of nonlinear fluid and structure models is the formidable computational expense of the analysis: *“The computational resources required for even one dynamic coupled CSM/CFD [Computational Structural Mechanics/Computational Fluid Dynamics] are significant. Establishing stability boundaries and tracking behavior histories, and then calculating sensitivities of those repetitively, cannot yet be carried out efficiently and is not expected to be practical in the near future”* [77].

An early example of segregated FSI sensitivity analysis by Ghatta [57] used the discrete sensitivity method. This work extended an earlier variational formulation [58]

and decomposed the coupled problem into separate fluid and structure domains. The coupled Jacobian between the domains was only approximated in order to avoid a large burden of the computational expense associated with inverting the mesh Jacobian that is required in the discrete sensitivity method.

To our knowledge, Lund's 2001 paper [79] is the first and most widely-cited design sensitivity analysis applied to non-segregated FSI. Lund employed a strongly-coupled fluid and structure domain to shape optimize (minimize drag) a flexible structure undergoing large deformation. Lund used incompressible Navier-Stokes to govern the fluid domain and formulated a solution using the weak-Galerkin approach for both the fluid and structure. Mesh deformation was not included in the problem formulation. To account for the large deformations, a new mesh computation algorithm was used, necessitating an iterative solution towards the full sensitivity solution. This is reportedly only a minor-penalty, since an iterative Newton's method was used to solve the nonlinear system.

2.3.2 Continuous Sensitivity of FSI Problems

We are aware of only two applications of CSE analysis for FSI problems. In the first, Newsome [89] used the sensitivity to geometry changes as an input into a structural analysis code. Following the development of Borggaard and Burns [23], Newsome employed 2D compressible Euler equations for the CSE fluid domain. The static aeroelastic structural sensitivity was bootstrapped by using the fluid sensitivity solution in place of linear, panel-method aerodynamics to calculate sensitivity results. This was valid, if limited, since, as a linear system, the structural governing equations and

sensitivity equations will be identical. This characteristic of sensitivity of linear systems is further explained in Section 3.1.

The second application of CSE appeared in a series of conference papers and journal articles by Pelletier and his students at Ecole Polytechnique de Montreal. Following the development of a CSE method for the calculation of the flow sensitivity of the steady, incompressible Navier-Stokes equations [45, 80], Etienne applied the method to a channel flow problem with flexible vertical beams which interacted with the flow [49]. This represented the first true application of the CSE method to a fluid-structure interaction problem. This was further extended to unsteady (though still incompressible) Navier-Stokes fluid problems in [47, 48]. Though each of these formulations allowed for large deformations of the structure, the primary emphasis was on the fluid flow sensitivity solution. This is further reflected in the subsequent research which introduced turbulence models into the sensitivity equations [31, 32].

All of the applications of Pelletier *et al.* were formulated using an elasticity-derived pseudo-solid mechanics (first introduced by Sackinger [112] for free and moving boundary fluid dynamics problems) to solve the fluid mesh deformation problem. Though all of the work clearly recognized the distinction between the local and material derivatives (a distinction that is made more explicit in Chapter 3), the fluid sensitivity equations were expressed in Eulerian form and the structure sensitivity equations were expressed in Lagrangian form. The total Lagrangian description of structure is referenced to the unperturbed configuration (*i.e.*, the original shape in a shape variation problem), and the fluid equations are referenced to the deformed configuration. This

results in mixed-form FSI interface conditions. The pseudo-solid is used to facilitate the expression of the interface conditions in deformed geometry for the fluid and undeformed geometry for the structure, but the explicit inclusion of the pseudo-solid results in a calculation of the mesh sensitivity along with the fluid and structure sensitivity. The calculation includes a term very similar to the inversion of the mesh Jacobian. One of the primary motivations of the CSE method was avoid the computationally expensive mesh sensitivity problem. Thus the Pelletier CSE method for FSI expressed in mixed-form interface conditions included undesirable the mesh sensitivity calculations. The CSE method for FSI developed in Chapters 3 and 7 is formulated in local derivate terms and avoids the necessity of calculating the mesh sensitivity.

As a result of their focus on the flow sensitivity for FSI problems, Pelletier *et al.* did not consider the structural shape variation problem which is the primary interest of the present effort. They claim, not without reason, that they could handle shape variation FSI problems since, due to the manner in which they posed their boundary conditions, all sensitivity problems behave like a classical shape parameter problems. That is, changing fluid inflow boundary conditions would affect the geometry of the fluid-structure interface and hence the solution to the sensitivity problem. Nevertheless, there are certain subtleties to shape variation problems that are best exposed by pure shape parameter formulation. This will be particularly important for structural design optimization which is again one of the primary motivating aspects of our research.

Although developed for an airfoil design optimization problem and not a FSI application, Cori and Pelletier [36] introduced a local derivative boundary condition

formulation for fluid derivatives in CSE that motivates the approach developed in Chapter 3 and is used throughout the present work. This boundary condition formulation can be derived from the total derivative equation and proves particularly simplifying for structural elasticity applications. As will be shown, when the system is posed in local derivative form, the sensitivity equations for FSI problems are often simplified significantly.

The impressive work and contributions of Pelletier and his students over the last decade have significantly extended the application of CSE methods to FSI problems. There are, however, several important distinctions between the present effort and that of Pelletier's, described above, which are now summarized. The continuous sensitivity equations derived in the remainder of this work are completely local formulations and do not require the expensive mesh sensitivity calculations that are necessary in the mixed formulations of Pelletier *et al.* Additionally, the local derivative CSE form is often simpler to implement. Another distinct difference stems from the boundary solution approximation that Pelletier *et al.* employed for fluid domain, identified as one of the primary sources of sensitivity error in [45]. We employ a first-order form (inherent to the LSFEM implementation) that does not require post-processing approximation of the FSI solution to generate the sensitivity boundary conditions. Additionally, for transient CSE applications, such as the gust response sensitivity analysis considered in Chapter 7, our method allows a time slice solution of the transient CSEs without requiring a solution to the full unsteady sensitivity equations. It is unclear if the unsteady fluid sensitivity problems studied in [47, 48] were able to use this computational shortcut to the

sensitivity solution. Finally, in contrast to Pelletier's interest in flow sensitivity in FSI applications, our primary interest in the aeroelastic analysis is the structural design sensitivity and shape parameter gradients in particular.

2.3.3 Adjoint Sensitivity Methods

The adjoint equation method was probably first used for optimization in the field of optimal control theory [28] before being adopted for structural optimization [60] and aerodynamic optimization [65]. Since adjoint methods are computationally attractive for large scale problems when the number of design variables exceeds the number of constraints and objective functions, we consider an adjoint CSE method in Chapter 8, but this is not the main scope of the current research. We briefly review some of the pertinent adjoint sensitivity literature for aeroelastic applications which are interesting comparisons to the method derived in Section 8.3.

Jameson *et al.* have developed continuous adjoint methods for unsteady aerodynamic problems [68, 87]. The ideas are based on earlier adjoint methods motivated by optimal control theory approaches to the constrained optimization problem [66]. This adjoint sensitivity approach was also applied to aerodynamic shape optimization problems [67, 109, 110]. Other researchers have also employed adjoint methods in aerodynamic applications to avoid the mesh sensitivity problem [90]. Another interesting sensitivity approach based on a Newton-linearization of the full-potential equations was presented in [117].

2.4 Least-Squares Finite Element Method

Least-squares methods for solving systems of partial differential equations are well established. A least-squares fit was first famously used by Gauss in 1801 to predict the orbit of the newly-discovered Ceres [15]. Two centuries later, a 1976 survey paper [46] listed more than 240 references and papers detailing application of least-squares techniques for partial differential equations. Despite a rich and successful history of applications, the LSFEM has been employed far less frequently than Ritz and Galerkin-based formulations which are almost universal in all commercial finite element programs. The main reason is that differentiability requirements on the finite element shape functions are less in these weak integral forms (which permits C^0 , or at most C^1 , elements) while maintaining symmetric system matrices [105]. The last decade has seen a resurgence of interest in least-squares finite element methods; [22, 69, 72, 93, 94, 98, 100, 101, 105] are just a few examples.

The recent renaissance of interest may be due in part to the more widespread adoption of higher-order p -elements and the realization that C^0 -elements are permitted in the LSFEM if the governing systems are reduced to first-order form. This is possible for both fluid and elasticity domains. This reflects the LSFEM practicality principle of Bochev and Gunzburger [22]: to be practical (that is, implemented with C^0 -elements and a convenient, appropriate norm), a least-squares system should be decomposed and transformed into a first-order system. This often requires the introduction of auxiliary variables. Some authors used first-order system least-squares (FOSLS) [29, 30, 73] to refer to these formulations. Bochev and Gunzburger [22] derived or reported from the

literature a variety of first-order least squares forms which they showed to be variously coercive in the appropriate function spaces.

The cost of a first-order (mixed) LSFEM formulation is an increase in the number of unknowns and hence the degrees of freedom that must be solved. The additional unknowns are typically variables of interest, however (e.g. stress in elasticity or vorticity in fluids). Thus, the LSFEM solution typically improves the accuracy of the desired unknown variables over primal variable Ritz/Galerkin finite element methods in which the non-primal variables are obtained from post-processing [107]. Furthermore, the LSFEM exhibits stable solutions for non-self-adjoint systems which are famously problematic for conventional weak Galerkin approaches [69]. Examples of these systems include diffusion problems and other purely first-order systems. The problem with the Galerkin formulation in these cases (which include mixed-element methods) is that, when a functional exists, the variational form leads to a saddle-point problem for which it is difficult to establish stability criteria for the solution. This is the well-known inf-sup or Ladyzhenskaya-Babuška-Brezzi (LBB) condition [27]. More often, the Galerkin weighted residual method has no known functional for which the variation is an extrema. LSFEM avoids the problem of satisfying the LBB condition for mixed elements since the least-squares functional is convex. The LBB condition becomes increasingly difficult to satisfy with increasing p -values [4]. A final advantage of the LSFEM is that the formulation yields symmetric and positive-definite matrices for which well-conditioned computational processes are readily available.

Least-squares methods also provide a ready posterior estimate of the system residual and hence a built-in measure of the accuracy of the numerical solution. If the LSFEM formulation system is coercive (see Section 4.2.3), then the convergence rate has been shown to be optimal [69]. By optimal it is meant that the error is bounded in the same manner (order) as the interpolation of the exact solution would be. If the system is further elliptic, then an improved, optimal convergence rate is guaranteed [69]. See Section 4.2.1 for further details.

The various proofs of the existence and uniqueness of LSFEM solutions are based on the bounded-inverse theorem and associated mathematics of linear operator theory [69, 88]. The LSFEM for time-dependent and nonlinear problems is also well-established in the literature [69]. Theoretical aspects of the LSFEM are further detailed in Chapter 4.

2.4.1 LSFEM for Fluids

Least-squares finite elements have been formulated for CFD applications with very good results. Jiang's textbook on the LSFEM [69] is focused primarily on fluid applications and covers a wide variety of different models and formulations: inviscid irrotational flow; incompressible viscous, rotational flow; compressible flow, subsonic to supersonic; convective transport flow; and fully-coupled interaction between two fluid flow domains. Jiang demonstrates that the LSFEM avoids the need to employ upwinding or other artificial viscosity techniques to achieve physical solutions. Additionally, he shows that the LSFEM does not need many of the other numerical "tweaks" needed for

conventional CFD methods, *e.g.* operator splitting, artificial compressibility or viscosity for stabilization, preconditioning, and staggered grids.

Pontaza and Reddy have published a series of important papers that introduce spectral methods from LSFEM fluid applications [95, 96, 98, 99]. The importance of their work involves establishing improved results for higher-order p -element implementations, something that Jiang did not consider in his textbook. Higher-order LSFEMs for fluid applications are now well-established and well-documented. The LSFEM models for fluid flow are presented in Section 4.5

2.4.2 LSFEM for Structures

As noted above, to be practical, the LSFEM should be based on a first-order decomposition of the governing equations. This leads to mixed elements, which have proven problematic for traditional FEM formulations without specially designed elements. This is particularly true for elasticity problems due to the symmetry requirements of the stress tensor and its gradient [3]. Indeed, it took researchers more than four decades (beginning in the 1960s until 2003) to develop a stable mixed element for elasticity based on polynomial shapes functions. Theoretically, LSFEM implementations avoid the saddlepoint stability problems of other weighted-residual methods. Nevertheless, though stable, mixed-LSFEM solutions for elasticity problems can be plagued by slow convergence, perhaps due to the underlying characteristics of the physics (*e.g.*, symmetry of the stress tensor). Thus, the lessons and approaches used for stabilizing mixed elements are relevant to LSFEM. We review these methods in the next section and then survey the LSFEM applications to elasticity available in the literature.

2.4.2.1. Mixed Elements For Elasticity

The earliest stable mixed element, the Raviart-Thomas element [55], was introduced as a mixed (displacement-displacement gradient) triangular element for second-order elliptic (Poisson-type) problems. Since the second-order, two-dimensional (elliptic) elasticity equations are analogous to the second-order elliptic Poisson problem, it is natural to expect that the Raviart-Thomas mixed element introduced would also apply to plane elasticity. However, the symmetry of the stress tensor and the gradient of the stress tensor changes the structure of the problem significantly.

One approach for a mixed least-squares element introduced by Cai and Starke [30, 73] enforces the stress tensor symmetry weakly by including the equality of the off diagonal terms in the system residual. Another method by the same researchers [29], based on a perturbed-form of the Stokes equations, is augmented by pressure and displacement gradient variables. This div-curl decomposition of the elasticity equations is essentially a first-order form with displacement as the primal variable. Components of the stress tensor are derived from the displacement fluxes and are not directly available as system variables.

A true mixed-element approach for LSFEM was introduced by Bramble [25] which builds upon the use of the -1 (inverse) norm for the elasticity residual developed in [26]. Although not widely cited, the -1 norm is also used in the stress-displacement and stress-pressure-displacement first-order LSFEM formulations of Yang [140, 141].

$$\|\phi\|_{-1} = \sup_{0 \neq \psi \in H^1(\psi)} \frac{(\phi, \psi)}{\|\psi\|_1} \quad (2.1)$$

The -1 norm allows second-order derivatives in the residual while still using C^0 shape functions, however the continuity of stress components across elements is forfeit. The element does have the advantage for elasticity boundary value problems that the implemented variables are displacement and stress which are the primary variables of interest for our coupled FSI approach.

The first stable, mixed stress-displacement element for plane elasticity was created by Arnold and Winther in 2003 [7, 8]. It is a fairly complicated triangular element. The lowest order element is composed of piecewise cubic functions for the stress tensor (minimum of 24 degrees of freedom) and piecewise linear functions for the displacement field (6 degrees of freedom). In 2005, Arnold and Awanou [5], constructed the first stable, quadrilateral mixed element which has an even more complicated structure. The lowest order element uses up to fifth-order polynomials for the stress tensor (45 degrees of freedom) and piecewise quadratic polynomials for the displacement field (12 degrees of freedom). The stress tensor function space is $H(\text{div}, \Omega, \mathbb{S})$, a Sobolev-type space (the divergence operator replaces the usual total derivative) defined on a domain, Ω , consisting of symmetric matrices. The displacement vector field function space is $L^2(\Omega, \mathbf{R}^2)$ where L^2 denotes the Lebesgue space of square-integrable functions defined on Ω . Both mixed elements, the Arnold-Winther and Arnold-Awanou, were motivated by the operator relationships implied by elasticity differential complexes [3, 6].

Although LSFEMs are theoretically not constrained by the stability problems associated with mixed elements, our experience is that LSFEM mixed stress-displacement elements for elasticity can still be beset by problems of slow convergence. Much of this probably stems from the non-coercivity of the implemented forms. Some preliminary observations may indicate a correspondence between the minimum polynomial order of the Arnold stable mixed element and the p -order element used in a mixed stress-displacement LSFEM solution. This is further explored in Section 4.2.4.

2.4.2.2. LSFEM for Elasticity

The published variational formulations of LSFEM for elasticity problems can be classified in three general groups. They are listed here with the associated dependent state variables in parentheses:

- 1) Perturbed Stokes system: velocity-pressure-vorticity (displacement flux, displacement) plus curl-free constraint
- 2) Displacement/displacement gradient (strain)
- 3) Displacement/stress

Both of the latter two methods above require special treatment of the symmetry of the strain or stress tensor. One option discussed in Section 2.4.2.1 enforces the symmetry weakly and carries as additional variables for each of the off-diagonal (theoretically equal) components of the symmetric tensor. This is done at the expense of additional degrees of freedom. Another option is to only carry one each of the off-diagonal components of the stress tensor. This leads to an odd number of variables which destroys the ellipticity of the elasticity system, however, it represents the minimum number of

degrees of freedom required to formulate a mixed-element approximation. Our results for several elasticity examples (some included in Chapter 5) indicate that, although the system is no longer elliptic for these formulations, the convergence rate does not suffer when compared to strictly elliptic formulations with an equivalent number of degrees of freedom. This conclusion is also supported by results given in [101]. See Section 4.2.1 for further discussion of ellipticity and convergence rates.

Pontaza and Reddy published a series of important papers for a range of elasticity applications from the bending of thin and thick plates to shear-deformable shells [93, 94, 97]. Much of their work underscored the importance and value of higher-order p -elements. Pontaza and Reddy demonstrated that the LSFEM yields exponential rates of convergence without use of reduced-order integration techniques and with moderate p -order refinement. Indeed, some preliminary observations stemming from our work have precipitated a conjecture that a minimum moderate p -value may be required for LSFEM solutions of elasticity problems. Arnold [4] also noted that it is usually easier to obtain stability of mixed elements with higher-order elements. Arnold pointed out that many of the “natural” mixed formulations that were attempted over the years “usually” turned out to be unstable and produced poor results (in some cases, converging to the wrong solution). The potential necessity for a minimum polynomial order for elasticity problems is further explored in Section 4.2.4.

Most applications of LSFEM in the literature have dealt with linear elastic problems. The results given in Chapter 7 as well as examples from Rasmussen’s dissertation [101] are the first known extensions of the LSFEM to include geometric

nonlinearity. It is noted in Chapter 8 that Newton-Raphson methods for nonlinear LSFEM requires a different formulation from that used for traditional Galerkin methods. There are some practical limitations to using Newton-Raphson for nonlinear LSFEM and the associated linear sensitivity problem. This is also discussed in Chapter 8.

2.4.3 Summary of the advantages & disadvantages of LSFEM for FSI

The original reason for selecting the LSFEM as the computational method for fluid-structure interaction problems is that, in contrast to conventional weak-Galerkin methods, it is a mixed-element formulation that allows equal approximation accuracy and continuity for all variables. This is particularly convenient for mixed boundary value problems inherent to FSI systems, since it gives direct access to the degrees of freedom for the kinematic and equilibrium conditions at the fluid-structure interface. Equal approximation of all formulation variables is also an advantage, since the LSFEM solution is used to determine the CSE boundary conditions. Another initially attractive aspect of LSFEM is that it is a universal, variationally consistent method that yields symmetric, positive-definite matrices, even for non-self adjoint systems, for which robust numerical solution methods are available (*e.g.* preconditioned conjugate gradient). The LSFEM gives optimal rates of convergence and has a built-in posterior error estimate (the system residual). Because of its universal nature, it is also straightforward to formulate multiple-domain, fully-coupled systems governed by disparate physics.

The disadvantages of the LSFEM are relatively slight for single domain problems. For structures, some results indicate that LSFEM solutions are less efficient on a total degree of freedom comparison to weak-Galerkin FEM [103]. For fluids, LSFEM models

have been well-documented in the literature, but are far-less widely employed than finite difference and finite volume CFD approaches. Additionally, mass conservation is not guaranteed (unless it is explicitly included in the residual formulation). The implication of this is still an open research question.

The disadvantages of the LSFEM approach for multiple-domain (*e.g.* fluid-structure) problems are more significant. This primarily stems from the sensitivity to the domain and boundary weighting factors. Eason's 1976 survey paper [46] lists a dozen early attempts for different weighting strategies for problems involving multiple boundary conditions, mixed methods, and systems of differential equations. Rasmussen [101] explored many weighting strategies specific to least-squares fluid-structure problems and concluded that most of the strategies were either impractical or did not work. The few strategies that did work required multiple iterations and an outer-loop to balance the domain residual error between the fluid, structure, and boundary functionals. Rasmussen also concluded that equation-level weighting may also be required to achieve satisfactory results. Kayser-Herold experienced similar problems in his solution of FSI problems via LSFEM [71].

2.5 Summary

This chapter documented the known limits of the published literature for three main topics: continuous sensitivity analysis methods, fluid-structure interaction analysis methods, and least-squares finite element methods. The LSFEM is very well documented, though its use to solve FSI problems is limited to two recent works [71] and [101]. Continuous sensitivity methods were originally introduced for solid mechanics,

but very few practical applications are known ([92, 138] excepted). The vast majority of published work on CSE applications has been done for fluids problems. We are also aware of no work that uses least-squares to solve the CSEs. Continuous sensitivity analysis of FSI problems is also fairly limited, however ongoing research by Pelletier *et al.* has developed good results using Galerkin methods and the incompressible Navier-Stokes equations, though the primary focus of their work is on the fluid sensitivity solution. The continuous sensitivity equation method is theoretically developed in the next chapter.

3 Continuous Sensitivity Equation Method

The continuous sensitivity equation (CSE) method for obtaining design parameter gradients is derived in Section 3.1. Although CSE can be applied to material and sizing type parameter sensitivity problems, the more difficult (from a conventional design sensitivity approach) and interesting applications are to shape variation problems. Thus, this is the focus of the present effort and the determination of the CSE boundary conditions is described in Section 0. Section 3.3 makes an important distinction between local and total derivative types and demonstrates the distinction with a useful example problem. Section 3.3.2 presents an argument that the local CSE form is superior to other forms of the CSE method, particularly for FSI problems. This is made more explicit in Section 3.3.3 which compares the local derivative form adopted in the present work with Pelletier's mixed derivative form. Section 3.3.3 summarizes the CSE approach and the advantages of the local derivative form.

3.1 Continuous Sensitivity Equations

Consider the following general, nonlinear boundary value system defined in a domain Ω with a boundary Γ for which we seek a solution \mathbf{u} of the equations

$$\mathbf{A}(\mathbf{u})\mathbf{u} = \mathbf{f} \text{ in } \Omega \quad (3.1)$$

$$\mathbf{B}(\mathbf{u})\mathbf{u} = \mathbf{g} \text{ on } \Gamma \quad (3.2)$$

where $\mathbf{A}(\mathbf{u})$ is a first-order, time-space differential operator given by

$$\mathbf{A} = \mathbf{A}_t \frac{\partial}{\partial t} + \sum_{i=1}^{\dim} \mathbf{A}_i \frac{\partial}{\partial x_i} + \mathbf{A}_0 \quad (3.3)$$

The system is nonlinear if the operator \mathbf{A} is a function of the solution \mathbf{u} , or $\mathbf{B}(\mathbf{u})$, the boundary operator

$$\mathbf{B} = \mathbf{B}_t \frac{\partial}{\partial t} + \sum_{i=1}^{\text{dim}-1} \mathbf{B}_i \frac{\partial}{\partial \xi_i} + \mathbf{B}_0 \quad (3.4)$$

is a function of \mathbf{u} . The boundary operator (3.4) specifies the boundary condition (solution) for \mathbf{u} on Γ . In (3.4), ξ_i denotes the coordinates that parameterize the boundary which are naturally at least one dimension less than the domain dimension.

The sensitivity of the solution \mathbf{u} to a design parameter, b , is $\frac{\partial \mathbf{u}}{\partial b}$. For example, the first forward difference for approximating the design sensitivity is

$$\frac{\partial \mathbf{u}}{\partial b} \approx \Delta_b(\mathbf{u}) = \frac{\mathbf{u}(b + \delta b) - \mathbf{u}(b)}{\delta b} \quad (3.5)$$

Besides the computational expense involved in solving the system twice, a drawback of the finite difference method is the challenge of determining the optimum step size, δb . Large steps are dominated by truncation error (which can be significant if the system is nonlinear) and small steps are dominated by numerical round-off error, Figure 3.1. Another shortcoming of the finite difference approach when b represents a shape parameter is that the finite difference calculation approximates the material (or total) derivative and not the desired local derivative, $\frac{\partial \mathbf{u}}{\partial b}$. This is further discussed in Section 3.3.

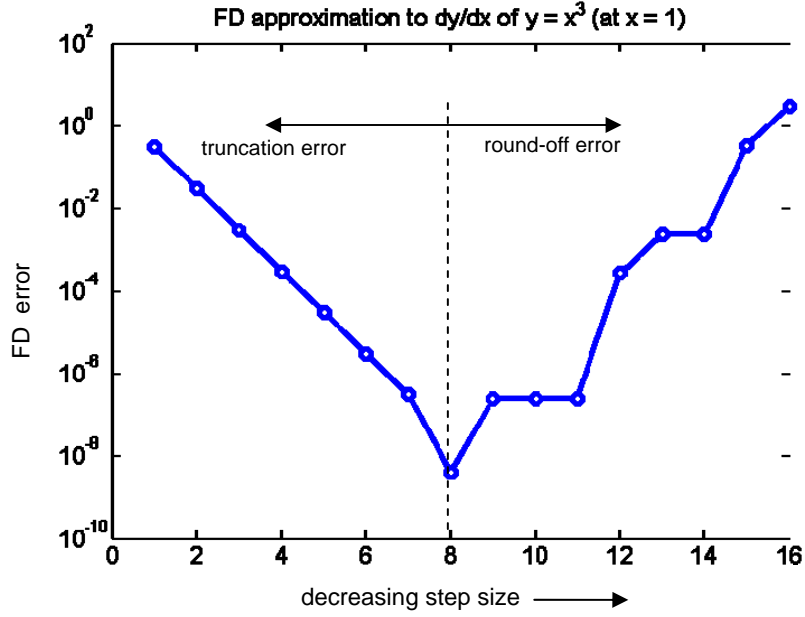


Figure 3.1: First-order finite difference approximation error example

The continuous sensitivity method avoids the numerical shortcomings of finite difference methods by differentiating the field equations (3.1-3.2) to yield a governing continuous system of equations for the desired sensitivity variables. So differentiating (3.1) with respect to a design parameter, b , yields

$$\frac{\partial}{\partial b} \left[\mathbf{A}_0(\mathbf{u}; b) \mathbf{u} + \mathbf{A}_i(\mathbf{u}; b) \mathbf{u}_{,i} + \mathbf{A}_t(\mathbf{u}; b) \mathbf{u}_{,t} \right] = \frac{\partial}{\partial b} \left[\mathbf{f}(\mathbf{x}; b) \right] \quad (3.6)$$

where the subscripted comma notation denotes partial differentiation. Equation (3.6) in component form (with Einstein summation notation implied) is

$$\frac{\partial}{\partial b} \left[a_{ij}^{(0)}(\mathbf{u}; b) u_j + a_{ij}^{(k)}(\mathbf{u}; b) u_{j,k} + a_{ij}^{(t)}(\mathbf{u}; b) u_{j,t} \right] = \frac{\partial}{\partial b} \left[f_i(\mathbf{x}; b) \right] \quad (3.7)$$

where the parenthetical superscript is used to denote the operator. Thus, k is an index ranging from one up to the domain dimension, n_{domain} . Equation (3.7) expands as

$$\begin{aligned} & \left[\frac{\partial a_{ij}^{(0)}}{\partial b} u_j + \frac{\partial a_{ij}^{(0)}}{\partial u_m} \frac{\partial u_m}{\partial b} u_j + a_{ij}^{(0)} \frac{\partial u_j}{\partial b} \right] + \left[\frac{\partial a_{ij}^{(k)}}{\partial b} u_{j,k} + \frac{\partial a_{ij}^{(k)}}{\partial u_m} \frac{\partial u_m}{\partial b} u_{j,k} + a_{ij}^{(k)} \frac{\partial u_{j,k}}{\partial b} \right] + \dots \\ & \frac{\partial a_{ij}^{(t)}}{\partial b} u_{j,t} + \frac{\partial a_{ij}^{(t)}}{\partial u_m} \frac{\partial u_m}{\partial b} u_{j,t} + a_{ij}^{(t)} \frac{\partial u_{j,t}}{\partial b} = \frac{\partial}{\partial b} f_i(\mathbf{x}; b) \end{aligned} \quad (3.8)$$

Since the spatial-temporal derivatives are independent operations from the sensitivity derivative, the order of differentiation may be reversed. Note that this commutation of differentiation is not possible if the sensitivity derivative in (3.6) is not a local derivative [59]. The $\frac{\partial u_m}{\partial b}$ terms are referred to as the sensitivity variables; they represent how the solution changes with respect to a design parameter. Collecting the sensitivity variables in (3.8) then yields the continuous sensitivity system

$$\begin{aligned} & \left[a_{im}^{(0)} + \frac{\partial a_{ij}^{(0)}}{\partial u_m} u_j + \frac{\partial a_{ij}^{(k)}}{\partial u_m} u_{j,k} + \frac{\partial a_{ij}^{(t)}}{\partial u_m} u_{j,t} \right] \frac{\partial u_m}{b} + \left[a_{im}^{(k)} \right] \frac{\partial u_{m,k}}{\partial b} + \left[a_{im}^{(t)} \right] \frac{\partial u_{m,t}}{\partial b} = \\ & \frac{\partial}{\partial b} f_i(\mathbf{x}; b) - \left[u_j \frac{\partial a_{ij}^{(0)}}{\partial b} + u_{j,k} \frac{\partial a_{ij}^{(k)}}{\partial b} + u_{j,t} \frac{\partial a_{ij}^{(t)}}{\partial b} \right] \end{aligned} \quad (3.9)$$

Notice that (3.9) is in the same form as (3.1) with (3.3) operating on the sensitivity variable \mathbf{u}_b instead of the original field variable \mathbf{u} . That is

$$\left[{}^b\mathbf{A}_0 \right] \mathbf{u}_b + \left[\mathbf{A}_i \right] (\mathbf{u}_b)_i + \left[\mathbf{A}_t \right] (\mathbf{u}_b)_t = \mathbf{f}_b(\mathbf{x}; b) - \left[\mathbf{A}_{0,b} \mathbf{u} + \mathbf{A}_{i,b} \mathbf{u}_i + \mathbf{A}_{t,b} \mathbf{u}_t \right] \quad (3.10)$$

The first bracketed matrix term in (3.10) is identified as the ${}^b\mathbf{A}_0$ sensitivity matrix, which is defined in component form by

$${}^b a_{ij}^{(0)} = a_{ij}^{(0)} + \frac{\partial a_{il}^{(0)}}{\partial u_j} u_l + \frac{\partial a_{il}^{(k)}}{\partial u_j} u_{l,k} + \frac{\partial a_{il}^{(t)}}{\partial u_j} u_{l,t} \quad (3.11)$$

This may also be expressed in matrix form as

$$\begin{aligned}
{}^b\mathbf{A}_0 = & \mathbf{A}_0 + \mathbf{A}_{0,u_1} [\{\mathbf{u}\}\{0\}...\{0\}] + \mathbf{A}_{0,u_2} [\{0\}\{\mathbf{u}\}...\{0\}] + \mathbf{A}_{0,u_n} [\{0\}...\{0\}\{\mathbf{u}\}] + ... \\
& + \mathbf{A}_{1,u_1} [\{\mathbf{u}_{,x_1}\}\{0\}...\{0\}] + \mathbf{A}_{1,u_2} [\{0\}\{\mathbf{u}_{,x_1}\}...\{0\}] + \mathbf{A}_{1,u_n} [\{0\}...\{0\}\{\mathbf{u}_{,x_1}\}] + ... \\
& + \mathbf{A}_{n,u_1} [\{\mathbf{u}_{,x_n}\}\{0\}...\{0\}] + \mathbf{A}_{n,u_2} [\{0\}\{\mathbf{u}_{,x_n}\}...\{0\}] + \mathbf{A}_{n,u_n} [\{0\}...\{0\}\{\mathbf{u}_{,x_n}\}] + ... \\
& + \mathbf{A}_{t,u_1} [\{\mathbf{u}_{,t}\}\{0\}...\{0\}] + \mathbf{A}_{t,u_2} [\{0\}\{\mathbf{u}_{,t}\}...\{0\}] + \mathbf{A}_{t,u_n} [\{0\}...\{0\}\{\mathbf{u}_{,t}\}]
\end{aligned} \tag{3.12}$$

This may be written more compactly as

$${}^b\mathbf{A}_0 = \mathbf{A}_0 + \frac{\partial \mathbf{A}_0}{\partial u_i} [u_i \delta_{ji}] + \frac{\partial \mathbf{A}_k}{\partial u_i} [u_{i,k} \delta_{ji}] + \frac{\partial \mathbf{A}_t}{\partial u_i} [u_{i,t} \delta_{ji}] \tag{3.13}$$

Finally, the CSE system associated with (3.1) may be written in compact form as

$$\left(\frac{\partial \mathbf{A}}{\partial \mathbf{u}} \mathbf{u}_\delta + \mathbf{A} \right) {}^b\mathbf{u} = {}^b\mathbf{f} - \frac{\partial \mathbf{A}}{\partial b} \mathbf{u} \tag{3.14}$$

where $\frac{\partial \mathbf{A}}{\partial \mathbf{u}} \mathbf{u}_\delta \equiv \frac{\partial \mathbf{A}}{\partial u_i} [u_i \delta_{ji}]$.

In (3.14) we introduce a superscript prefix notation, ${}^b\mathbf{u}$, to denote the sensitivity variable that is determined by solving the CSEs. In the examples below when an analytic solution is available, the ${}^b\mathbf{u}$ solution will be treated as distinct from an analytic sensitivity, denoted by $\mathbf{u}_{,b}$. The analytic solution notation will be used to represent the sensitivity determined by taking the derivative of an analytic solution \mathbf{u} to equations (3.1-3.2). We also introduce notation for the finite difference operator, $\Delta_b(\mathbf{u})$, given by (3.5), and the material derivative operator, $D_b(\mathbf{u})$, defined in the next section.

Note that the gradient operators, the \mathbf{A}_i 's in (3.3), are unchanged for the CSE system, (3.10). Further, for linear systems, the sensitivity matrix ${}^b\mathbf{A}_0 = \mathbf{A}_0$. Equation

(3.9) includes both the explicit dependence of the system solution on b (e.g. as with sizing or shape sensitivity), as well as the implicit, nonlinear dependence of the system solution on b (e.g. as in shape optimization). Additionally, in shape sensitivity problems, where b represents a boundary shape parameter, the system operators typically have no explicit dependence on b and the brackets terms on the right-hand side of (3.10), e.g. $\mathbf{A}_{i,b}$, vanish. Thus, for linear, shape variation problems, the component CSE operators are identical to the original system operators.

Note also that the continuous sensitivity system (3.10) is always linear in the sensitivity variable, $\mathbf{u}_{,b}$, even when the original system is nonlinear. The conclusion that only the ${}^b\mathbf{A}_0$ operator changes for a nonlinear system is due to the assumption that system (3.1-3.2) only being nonlinear in \mathbf{u} . If the nonlinearity appeared explicitly in a derivative of \mathbf{u} , $\mathbf{u}_{,x}$ for example, then

$$\left[\mathbf{A}(\mathbf{u}_{,x})\right](\cdot) = \sum_{i=1}^{\dim} \mathbf{A}_i(\mathbf{u}_{,x}) \frac{\partial}{\partial x_i} + \mathbf{A}_0(\mathbf{u}_{,x}) \quad (3.15)$$

and only the ${}^b\mathbf{A}_1$ component operator of the CSE system would differ from the component operators of the original system. The general conclusion is that the CSE system will differ from the parent system in whichever operator component represents the nonlinearity. Note that when the parent system is written in first-order form, the nonlinear problem can always be factored so that the nonlinearities appear explicitly in \mathbf{u} . Table 3.1 summarizes the form of the CSE operators in terms of the original system operators from (3.1) for both linear and nonlinear systems, as well as shape variation

problems (with no explicit dependence on the design parameter) and non-shape variation problems with explicit dependence on the design parameter.

Table 3.1: Summary of CSE operators in first-order form

Problem Type	${}^b\mathbf{A}_0$	${}^b\mathbf{A}_k \quad k=1,\dots,n_{dom},t$	${}^b\mathbf{f}$
Linear, shape	\mathbf{A}_0	\mathbf{A}_k	0
Linear, explicit b (size, material)	\mathbf{A}_0	\mathbf{A}_k	$\mathbf{f}_{,b}(\mathbf{x};b) - [\mathbf{A}_{0,b}\mathbf{u} + \mathbf{A}_{k,b}\mathbf{u}_{,k}]$
Nonlinear, shape	${}^b\mathbf{A}_0$	\mathbf{A}_k	0
Nonlinear, explicit b (size, material)	${}^b\mathbf{A}_0$	\mathbf{A}_k	$\mathbf{f}_{,b}(\mathbf{x};b) - [\mathbf{A}_{0,b}\mathbf{u} + \mathbf{A}_{k,b}\mathbf{u}_{,k}]$

We now illustrate the formulation of the CSE system (3.10) with a nonlinear example. Consider the 1D, nonlinear system with an explicit dependence on b (this is not necessarily a physical example, but it demonstrates all aspects of the formulation of the CSE system)

$$\begin{aligned} bu + u^2v &= f_1 \\ uv + 2v + uv_{,x} &= f_2 \end{aligned} \tag{3.16}$$

which has the matrix operator form, $\mathbf{A}_0\mathbf{u} + \mathbf{A}_1\mathbf{u}_{,x} = \mathbf{f}$, of

$$\begin{bmatrix} b & u^2 \\ v & 2 \end{bmatrix} \begin{Bmatrix} u \\ v \end{Bmatrix} + \begin{bmatrix} 0 & 0 \\ 0 & u \end{bmatrix} \begin{Bmatrix} u \\ v \end{Bmatrix}_{,x} = \begin{Bmatrix} f_1 \\ f_2 \end{Bmatrix} \tag{3.17}$$

Using (3.12), the CSE ${}^b\mathbf{A}_0$ operator is

$$\begin{aligned} {}^b\mathbf{A}_0 &= \begin{bmatrix} b & u^2 \\ v & 2 \end{bmatrix} + \begin{bmatrix} 0 & 2u \\ 0 & 0 \end{bmatrix} \begin{bmatrix} \begin{Bmatrix} u \\ v \end{Bmatrix} \begin{Bmatrix} 0 \\ 0 \end{Bmatrix} \end{bmatrix} + \begin{bmatrix} 0 & 0 \\ 1 & 0 \end{bmatrix} \begin{bmatrix} \begin{Bmatrix} 0 \\ 0 \end{Bmatrix} \begin{Bmatrix} u \\ v \end{Bmatrix} \end{bmatrix} + \dots \\ &\quad \begin{bmatrix} 0 & 0 \\ 0 & 1 \end{bmatrix} \begin{bmatrix} \begin{Bmatrix} u_{,x} \\ v_{,x} \end{Bmatrix} \begin{Bmatrix} 0 \\ 0 \end{Bmatrix} \end{bmatrix} + \begin{bmatrix} 0 & 0 \\ 0 & 0 \end{bmatrix} \begin{bmatrix} \begin{Bmatrix} 0 \\ 0 \end{Bmatrix} \begin{Bmatrix} u_{,x} \\ v_{,x} \end{Bmatrix} \end{bmatrix} \end{aligned} \tag{3.18}$$

or

$${}^b\mathbf{A}_0 = \begin{bmatrix} b & u^2 \\ v & 2 \end{bmatrix} + \begin{bmatrix} 2uv & 0 \\ 0 & 0 \end{bmatrix} + \begin{bmatrix} 0 & 0 \\ 0 & u \end{bmatrix} + \begin{bmatrix} 0 & 0 \\ v_{,x} & 0 \end{bmatrix} \quad (3.19)$$

The \mathbf{A}_1 for the CSE system is the same as in (3.17). The total CSE system is thus

$$\begin{bmatrix} b + 2uv & u^2 \\ v + v_{,x} & 2 + u \end{bmatrix} \begin{Bmatrix} {}^b u \\ {}^b v \end{Bmatrix} + \begin{bmatrix} 0 & 0 \\ 0 & u \end{bmatrix} \begin{Bmatrix} {}^b u \\ {}^b v \end{Bmatrix}_{,x} = \begin{Bmatrix} f_{1,b} \\ f_{2,b} \end{Bmatrix} - \begin{Bmatrix} u \\ 0 \end{Bmatrix} \quad (3.20)$$

which is the same result obtained by differentiating (3.16) with respect to b and rearranging terms

$$\begin{aligned} bu_{,b} + 2uvu_{,b} + u^2v_{,b} &= f_{1,b} - u \\ u_{,b}v + uv_{,b} + 2v_{,b} + u_{,b}v_{,x} + uv_{,bx} &= f_{2,b} \end{aligned} \quad (3.21)$$

or in matrix form

$$\begin{bmatrix} b + 2uv & u^2 \\ v + v_{,x} & u + 2 \end{bmatrix} \begin{Bmatrix} {}^b u \\ {}^b v \end{Bmatrix} + \begin{bmatrix} 0 & 0 \\ 0 & u \end{bmatrix} \begin{Bmatrix} {}^b u \\ {}^b v \end{Bmatrix}_{,x} = \begin{Bmatrix} f_{1,b} \\ f_{2,b} \end{Bmatrix} - \begin{Bmatrix} u \\ 0 \end{Bmatrix} \quad (3.22)$$

To summarize, the CSE system is defined by differentiating the continuous system (3.1) with respect to the design parameter of interest. The result is a system of differential equations, (3.14), which may be solved, with the appropriate boundary data, to yield the desired parameter sensitivity solution. The CSE boundary conditions are considered next.

3.2 Boundary Conditions for Shape Variation CSE

The boundary conditions of the sensitivity equation specify how the sensitivity variables behave on the boundary of the domain. Thus, the sensitivity of the boundary operator system may be written as a first-order CSE system analogous to (3.14)

$$\left[\mathbf{B}_0 + \frac{\partial \mathbf{B}_0}{\partial u_i} [\{u_i\} \delta_{ji}] + \frac{\partial \mathbf{B}_\xi}{\partial u_i} [\{u_{i,\xi}\} \delta_{ji}] \right]^b \mathbf{u} + \mathbf{B}_\xi^b \mathbf{u}_{,\xi} = \mathbf{g}_{,b}(\mathbf{x}; b) - [\mathbf{B}_{0,b} \mathbf{u} + \mathbf{B}_{\xi,b} \mathbf{u}_{,\xi}] \quad \text{on } \Gamma(b) \quad (3.23)$$

where ξ denotes coordinates that parameterize the boundary (which has dimension of at least one less than the domain). The continuous sensitivity domain equations, (3.9), is simply another system of differential equations, which, given with the appropriate boundary data, (3.23), represents a well-posed boundary value problem that may be solved by a wide variety of numerical approaches. It is convenient in many cases to use the same numerical method and framework to solve the sensitivity system as was used to solve the original system.

For shape variation problems, the boundary Γ is a function of the design parameter b and the evaluation of (3.23) must account for the total variation of a material point on the boundary. For a scalar, u , the Eulerian and material points are related through the total (material) derivative

$$D_b(u) \equiv \frac{Du}{Db} \Big|_{\mathbf{x}} = \frac{\partial u}{\partial b} \Big|_{\mathbf{x}} + \nabla u \cdot \frac{\partial \mathbf{X}_\Omega}{\partial b} \Big|_{\mathbf{x}} \quad (3.24)$$

where $D_b(\cdot)$ is the material derivative operator with respect to the parameter b , \mathbf{X} denotes a material coordinate and \mathbf{x} denotes a spatial coordinate (Eulerian description). Thus the total derivative of u with respect to b at a material point \mathbf{X} consists of the local derivative of u with respect to parameter b and the convective transport term which accounts for how the material point \mathbf{X} moves as the design parameter b varies. For the vector quantity \mathbf{u} , the local derivative, gradient operation, and dot product in (3.24) are carried out

component-wise. Solving (3.24) for the local derivative gives the desired sensitivity boundary condition for the CSE system

$$^b\mathbf{u}|_{\Gamma} \equiv \frac{\partial \mathbf{u}}{\partial b} \Big|_{\mathbf{x}=\Gamma} = \frac{D\mathbf{u}}{Db} \Big|_{\Gamma} - \nabla \mathbf{u} \cdot \frac{\partial \mathbf{X}_{\Gamma(b)}}{\partial b} \quad (3.25)$$

where in 2D

$$\mathbf{X}_{\Gamma(b)} = \{(x, y) \in \Gamma(b)\} \quad (3.26)$$

are the coordinates (ordered pairs in \mathbf{R}^2) that define the boundary as a function of b . The first term on the right side of (3.25) accounts for how the boundary conditions for the problem change with respect to the design parameter. This term is often zero; that is, the nature of the boundary condition often does not change as the shape changes. For example, the boundary conditions for the fixed end of a cantilevered beam are zero displacement and rotation at the root. A shape variation parameter can move the location of the root in an Eulerian reference frame, but the material point at the root will still be fixed and the displacement and rotation boundary conditions are still those of a cantilevered beam. Some examples are considered in Chapters 5 and 6 where the first term on the right-hand side of (3.25) does not vanish, but these tend to be the exception to most applications.

The transport term in (3.25) (the second term on the right-hand side) is the dot product of the derivative of the set of spatial coordinates that define the boundary with the gradient of the solution to (3.1)-(3.2). Again, in the case of vector quantities, the gradient operation is carried out row-wise.

Contrast (3.25) with the classic continuum stress sensitivity expression derived by Dems and Haftka [39]

$${}^b\sigma_{ij}n_j = \frac{DT_i}{Db} - \sigma_{ij,k}n_j \frac{\partial\phi_k}{\partial b} - \sigma_{ij}(n_jn_l - \delta_{jl})n_k \left[\frac{\partial\phi_k}{\partial b} \right]_{,l} \quad (3.27)$$

where T_i are the components of the surface traction vector, n_i are the components of the unit normal vector, δ is the Kronecker delta function, and ϕ is the transformation field that maps material coordinates of the domain as a function of the design parameter. Equation (3.27) is valid on the boundary and throughout the domain. We now show that (3.27) is equivalent to (3.25) when the latter is expressed in coordinates normal and tangential to the boundary surface. First, take the stress vector [108]

$$\begin{Bmatrix} \sigma_n \\ \sigma_\tau \end{Bmatrix} = \begin{bmatrix} \sigma \end{bmatrix}^T \cdot \{\hat{\mathbf{n}}\} = \mathbf{T}^{(\hat{\mathbf{n}})} = \begin{Bmatrix} T_n \\ T_s \end{Bmatrix} \quad (3.28)$$

where σ_n and σ_τ are the normal and shear components of the stress vector. At any point in the normal-tangential coordinate reference frame on the boundary, we have $n_1 = 1$ and $n_2 = 0$. For the normal stress component, $\sigma_n = \sigma_{11}n_1$, and $(n_1n_l - \delta_{1l}) = 0$ so that the final term in (3.27) vanishes, when it is also expressed in the normal-tangential coordinate reference frame. Similarly, for the tangential shear stress component, $\sigma_\tau = \sigma_{21}n_1$ and $(n_1n_l - \delta_{1l}) = 0$ so that the final term in (3.27) again vanishes. Thus expanding (3.27) in 2D and evaluating the expression in a normal-tangential coordinate system yields

$$\begin{Bmatrix} {}^b\sigma_n \\ {}^b\sigma_\tau \end{Bmatrix} = \begin{Bmatrix} {}^b\sigma_{11} \\ {}^b\sigma_{21} \end{Bmatrix} = \frac{D}{Db} \begin{Bmatrix} T_1 \\ T_2 \end{Bmatrix} - \left\{ \sigma_{11,1}n_1 \cdot \phi_{1,b} + \sigma_{11,2}n_1 \cdot \phi_{2,b} \right\}_{\Gamma(b)} = \frac{D\mathbf{T}^{(\hat{\mathbf{n}})}}{Db} - \nabla \begin{Bmatrix} \sigma_n \\ \sigma_\tau \end{Bmatrix} \cdot \mathbf{X}_{,b} \quad (3.29)$$

Note that ϕ evaluated on the boundary yields the coordinates of points on the boundary. The advantage of using (3.25) over (3.27) is that (3.25) only requires a description of how the boundary varies with respect to the shape parameter. In (3.27), the shape variation of the entire domain must be defined through the transformation field. In both cases, the choice of boundary parameterization, $\mathbf{X}_{\Gamma(b)}$, or the transformation function, ϕ , is analogous and not necessarily unique; however some choices can simplify the problem description and solution. This is demonstrated in an example below.

To reiterate, the continuous sensitivity system is a linear boundary value problem derived by taking the derivatives of the original field equations, (3.1-3.2). The set of sensitivity boundary condition data are of the same form as for the original problem. However, if the design parameter is a shape parameter that alters the Eulerian points of the boundary, the set of boundary conditions from the parent problem on the boundary that moves must be expressed in the form of (3.25). The continuous sensitivity equations may be derived in either total or local derivative form. When expressed in local form as derived above, (3.8) and (3.23), only the boundary parameterization need be described. In total derivative form, the parameterization or transformation function for the entire domain is necessary which is equivalent to having to solve the mesh Jacobian.

The simplicity of the local CSE form is not always used to greatest potential. This was true of (3.27), which though general, could be significantly simplified through a wise choice of boundary degrees of freedom and boundary parameterization. This also arises in the sensitivity boundary condition for an FSI example from [49] which uses the mixed reference configuration form described in Section 2.3.2

$$\left[\sigma'_l \cdot n_0^s + \sigma_l \cdot s_{n_0^s} \right] \delta \Gamma_0 + \left\{ \left[\left(\sigma'_f + \nabla \sigma_f \cdot s_\chi \right) + \sigma_f \cdot \left(\mathbf{J} \mathbf{F}_{ps}^{-T} \right)' \cdot J^{-1} \mathbf{F}_{ps}^T \right] + \sigma_f \cdot \mathbf{F}_{ps}^{-T} \cdot s_{n_0^s} \cdot \mathbf{F}_{ps}^T \cdot n_0^s \right\} \cdot n_1^s \delta \Gamma_1 = 0 \quad (3.30)$$

Not all the terms in (3.30) need be defined to realize the complexity of the FSI interface condition when written in mixed form. \mathbf{F}_{ps} is the deformation gradient tensor of the continuous fluid mesh and J is its Jacobian. These terms are equivalent to the transformation field of [39]. The inverse operation of the mesh mapping is clearly evident in (3.30). The mesh sensitivity gradient terms could probably be eliminated from (3.30) by using the corresponding structure deformation on the interface boundary (which is enforced to be equal to the mesh deformation at the boundary) instead of the pseudo-solid. The domain Jacobian and its inverse also appear in the continuous sensitivity domain parameterization methods [59]. Posing the CSE system in local derivative form (with local derivative boundary data) avoids the numerical complexity and expense of the mesh and domain Jacobian calculations. Next we discuss how to relate the local and total derivative sensitivity forms.

3.3 Local and Total Derivatives

The local derivative is the derivative at an Eulerian point (a particular point in space in an Eulerian reference frame). In a Lagrangian description, the total derivative (also called the material derivative) of a field variable consists of both the local derivative and the change that is due to transporting a material point through Eulerian space. For some applications, notably fluid optimization problems, the sensitivity at an Eulerian point is appropriate. For structural optimization and FSI sensitivity, however, the sensitivity at a material point is generally desired. It is possible to pose the shape

variation CSE system in terms of the total derivative; however, as demonstrated above, it is usually more convenient to solve for the local sensitivity. The total sensitivity for the shape variation problem may then be recovered from the local sensitivity solution by application of (3.24). Although the conversion to the material derivative requires the transformation function for the entire domain, it is not required for the solution of the CSE problem in local form. Additionally, the conversion to the material derivative does not require a solution to the inverse mapping function, or equivalently, an inversion of the mesh Jacobian. Furthermore, if the sensitivity is only required on the boundary, then the boundary parameterization, (3.26), alone is sufficient to calculate the desired material sensitivity. A domain transformation function need not be defined.

3.3.1 Local and Total Derivative Example

Consider, as an example, the equations governing the stress and displacement for the 1D elastic structure (bar) depicted in Figure 3.2

$$(A\sigma_x)_{,x} + f_x = 0 \quad (3.31)$$

$$Eu_{,x} - \sigma_x = 0 \quad (3.32)$$

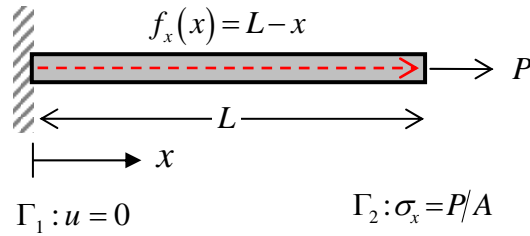


Figure 3.2: Bar sensitivity example

where u is the axial displacement, σ_x is the axial stress, A is the cross-sectional area of the bar, f_x is the applied body force, and E is Young's modulus. Equations (3.31) and (3.32) may be directly integrated to yield the stress and displacement solutions, which, for no tip load, $P=0$, and constant cross-sectional area yields

$$\sigma_x(x;L) = \frac{x^2}{2A} - \frac{Lx}{A} + \frac{L^2}{2A} \quad (3.33)$$

$$u(x;L) = \frac{x^3}{6EA} - \frac{Lx^2}{2AE} + \frac{L^2x}{2AE} \quad (3.34)$$

These are functions of the shape parameter, L , the length of the bar. The analytic (local) sensitivities of displacement and stress to bar length are then

$$\sigma_{x,L}(x) = \frac{L}{A} - \frac{x}{A} \quad (3.35)$$

$$u_{,L}(x) = \frac{Lx}{AE} - \frac{x^2}{2AE} \quad (3.36)$$

which are plotted in Figure 3.3. This can also be calculated by solving the corresponding CSE to (3.31) and (3.32)

$${}^L\sigma_{x,x} + \frac{1}{A} {}^L f_x = 0 \quad (3.37)$$

$${}^L u_{,x} - \frac{1}{E} {}^L \sigma_x = 0 \quad (3.38)$$

where ${}^L f_x = 1$. The sensitivity boundary conditions are determined from (3.25).

Parameterize the boundaries with respect to beam length as

$$\mathbf{X}_{\Gamma_1} = \{0\} \quad , \quad \mathbf{X}_{\Gamma_2} = \{L\} \quad (3.39)$$

The bar remains fixed at the base regardless of the bar length, so the total derivative of displacement at the origin is zero. Additionally, based on the parameterization of (3.39), the material point at the base of the bar does not move with changes in bar length, that is

$\mathbf{X}_{\Gamma_1, L} = 0$. Thus, the convection term in (3.25) is zero at the origin. Since the load at the tip of the bar vanishes at L , the gradient of the axial stress is zero and the total derivative at the tip is also zero. The sensitivity boundary conditions are then

$${}^L u = 0 \quad \text{at } x = 0 \quad (3.40)$$

$${}^L \sigma_x = 0 \quad \text{at } x = L \quad (3.41)$$

Integrating (3.37) and (3.38) with the boundary data (3.40) and (3.41) yields the solution to the sensitivity variables

$${}^L \sigma_x(x) = \frac{L}{A} - \frac{x}{A} \quad (3.42)$$

$${}^L u(x) = \frac{Lx}{AE} - \frac{x^2}{2AE} \quad (3.43)$$

which matches exactly the result, (3.35) and (3.36), obtained from differentiating the analytic solution. The total sensitivity and finite difference sensitivity are also plotted in Figure 3.3. Finite difference results are by nature approximations to total derivatives. For optimization with respect to a cost function in terms of material points, the total derivative is often desired. To convert the local sensitivity, (3.42) and (3.43), into a total derivative, we must define a domain transformation function that is compatible with the boundary data (3.40) and (3.41). An obvious choice defines the material points of the domain by

$$\mathbf{X}_\Omega(x) = \{\xi L \mid \xi = x/L; \xi \in [0, 1]\} \quad (3.44)$$

This expression is equivalent to the domain transformation field used in the continuum approach of Dems and Haftka [39]. The local sensitivities, (3.42) and (3.43), are now converted to total sensitivities by adding the convection term to the local sensitivity. Thus the total sensitivity for displacement is given by

$$D_L(u) = u_{,L} + \nabla u \cdot \mathbf{X}_{\Omega,L} = u_{,L} + xu_{,x} \quad (3.45)$$

or, substituting (3.43) into (3.45) for the first term and differentiating (3.34) and inserting the result in the second term

$$D_L u(x) = \frac{Lx}{AE} - \frac{x^2}{2AE} + \left(\frac{x^2}{2EA} - \frac{Lx}{AE} + \frac{L^2}{2EA} \right) x \quad (3.46)$$

Similarly, the total stress sensitivity is

$$D_L \sigma(x) = \frac{L}{A} - \frac{x}{A} + \left(\frac{x}{A} - \frac{L}{A} \right) x \quad (3.47)$$

The total derivatives for stress and displacement are also plotted in Figure 3.3 and match the finite difference results. The convection term used to convert the local sensitivity to total sensitivity is also plotted in Figure 3.3.

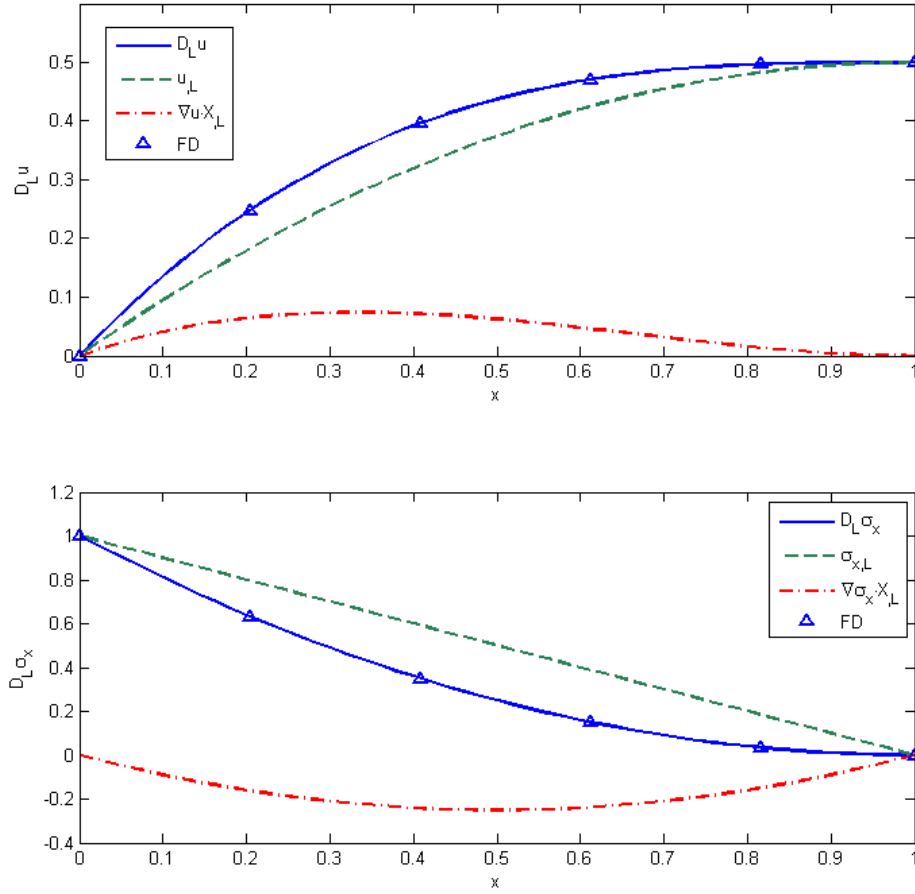


Figure 3.3: Bar sensitivity comparison

In this example, the sensitivity equations could be directly integrated to give an analytic solution to the CSE system. For more complex geometries and systems, a numerical solution, *e.g.* finite elements, is necessary to specify the boundary conditions for the sensitivity equations, but the initial steps are the same. It is usually possible to parameterize the domain in such a way that the material derivative vanishes on a boundary so that the sensitivity boundary conditions are determined solely by the convection term in (3.25). The solution to the original system is used to generate the first term in the convective part of the sensitivity boundary conditions (3.25). Also note that

the parameterization of the boundary used in the second term of the convective part of (3.25) is not unique. In this example, the domain was parameterized by (3.44) so that material points at the tip of the bar moved to the right in Eulerian space as the beam length increases. The domain definition could have also been parameterized so that material points at the base of the bar moved to the left in Eulerian space, while the tip of the bar remains fixed in space. Figure 3.4 compares these two domain parameterization options. In the second, (3.44) becomes

$$\mathbf{X}_\Omega(x) = \{1 - L + \xi L \mid \xi = x/L; \xi \in [0,1]\} \quad (3.48)$$

in which case

$$\mathbf{X}_{\Omega,L}(x) = \{\xi - 1 \mid \xi = x/L; \xi \in [0,1]\} \quad (3.49)$$

With this domain parameterization, the sensitivity boundary conditions are now

$${}^L u = -\nabla u(0) \cdot \mathbf{X}_{\Omega,L}(0) = \frac{L^2}{2EA} \quad \text{at } x = 0 \quad (3.50)$$

$${}^L \sigma_x = -\nabla \sigma(L) \cdot \mathbf{X}_{\Omega,L}(L) = 0 \quad \text{at } x = L \quad (3.51)$$

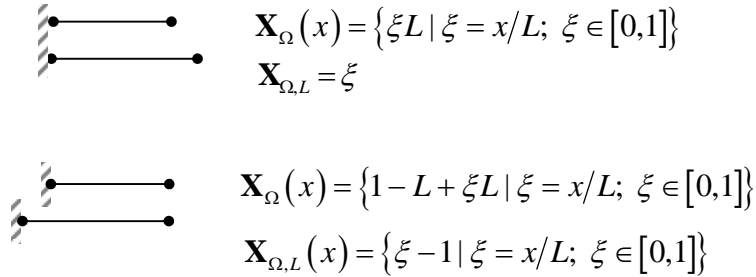


Figure 3.4: Two options for bar domain parameterization

Integrating (3.37) and (3.38) with this boundary data (and with ${}^L f_x = 0$ since $f_x = 1 - x$ for this parameterization), yields

$${}^L u(x) = \frac{L^2}{2EA} \quad (3.52)$$

$${}^L \sigma_x(x) = 0 \quad (3.53)$$

for the local sensitivities which are different results than obtained in (3.42) and (3.43) due to the difference in parameterization. This highlights that the local derivative depends upon the domain parameterization. However, the total derivatives of this parameterization

$$D_L u(x) = \frac{L^2}{2EA} + \left(\frac{x^2}{2EA} - \frac{Lx}{AE} + \frac{L^2}{2EA} \right) (x-1) \quad (3.54)$$

$$D_L \sigma(x) = 0 + \left(\frac{x}{A} - \frac{L}{A} \right) (x-1) \quad (3.55)$$

do match the total derivative results obtained in (3.46) and (3.47). Careful comparison of (3.46) with (3.54) and (3.47) with (3.55) reveals that aside from the local sensitivity solution, only the domain parameterization component of the convective term is different. As implied by the free choice of the transformation field in (3.27), local sensitivities (which are functions of spatial coordinates) are not unique and depend on the choice of domain or boundary parameterization. However, the total derivatives, which are given at material coordinates, are unique. The CSE problem is generally simpler to pose and solve in terms of local sensitivities. Equation (3.45) then gives a straightforward means to convert the local sensitivities from the CSE solution to total sensitivities for optimization.

3.3.2 Potential Pitfall from Neglecting Local/Total Derivative Distinction

This distinction between local sensitivity values and material point sensitivity values is at times overlooked in the literature and can contribute significant error to sensitivity solutions if they are mixed within a single computational approach. For example in [11, 59], the researchers note that

For beam and plate structures the derivative of the displacement field with respect to geometric variables is usually not a legitimate displacement field (for example, it may grossly violate the Kirchhoff assumption). The FEM approximation to this illegitimate field is a valid, though highly unusual, displacement field, which requires large self-canceling components in the pseudo-load. As the FEM mesh is refined, the pseudo load required to generate du/dx acquires ever larger self-canceling components. Thus the errors in the pseudo load due to the FD derivative of the stiffness matrix can be greatly magnified.

This is in reference to an error observed for shape variation problems when using the semi-analytic sensitivity method. The semi-analytic method is a sensitivity approach based on moving the discrete stiffness sensitivity term to the right-hand side to form a pseudo-load

$$\mathbf{K}\mathbf{u}_{,b} = \mathbf{f}_{,b} - \mathbf{K}_{,b}\mathbf{u} \quad (3.56)$$

where the $\mathbf{K}_{,b}$ sensitivity is approximated by finite difference (which is a material derivative)

$$\frac{\partial \mathbf{K}}{\partial b} \approx \frac{\mathbf{K}(b + \delta b) - \mathbf{K}(b)}{\delta b} \quad (3.57)$$

In [11], the semi-analytic method produces grossly erroneous sensitivity results for a shape variation problem which get increasingly worse as the mesh is refined. The researchers’ “prove” that this is attributable to the sensitivity field not being a legitimate displacement field. However, this is only true for the total derivative field, a distinction

that is not made in [11, 59]. The proof starts with the equation for the bending and rotation of a beam:

$$w = \frac{M}{2EI} x^2 = \frac{M}{2EI} \xi^2 L^2 \quad (3.58)$$

$$\theta = \frac{dw}{dx} = \frac{M}{EI} x = \frac{M}{EI} \xi L \quad (3.59)$$

which is written in both Eulerian, x , coordinates and Material, ξ , coordinates. They then show

$$\frac{dw}{dL} = \frac{M}{EI} x = \frac{M}{EI} \xi^2 L \neq \frac{d}{dx} \left(\frac{d\theta}{dL} \right) = \frac{M}{EI} \frac{x}{L} \quad (3.60)$$

so that

$$\frac{dw}{dL} = \frac{2w}{L} \quad (3.61)$$

but

$$\frac{d\theta}{dL} = \frac{\theta}{L} \quad (3.62)$$

They thus conclude that the beam sensitivity field variables are not the solution to a beam field problem. Equation (3.60) is actually a total derivative. Although expressed and used as a local derivative, as soon as the substitution $\xi = x/L$ is made it becomes a material derivative. What the researcher's have proven is that (in our notation)

$$D_L \theta \neq \frac{d}{dx} D_L w \quad (3.63)$$

Following the same argument as the proof, but with a proper distinction between the local and total derivative form, one has

$$D_L w = w_{,L} + \nabla w \cdot \mathbf{X}_{,L} = 0 + \frac{Mx}{EI} \frac{x}{L} = \frac{2w}{L} \quad (3.64)$$

and

$$D_L \theta = \theta_{,L} + \nabla \theta \cdot \mathbf{X}_{,L} = 0 + \frac{M}{EI} \frac{x}{L} = \frac{\theta}{L} \quad (3.65)$$

So that

$${}^L \theta = \frac{d}{dx} {}^L w \quad (3.66)$$

Thus, although the total derivative is not a “legitimate” beam displacement field, the local derivative is. In fact, if it were not, the continuous sensitivity equation method would not work. The failure to make a distinction between local and material derivative for shape variation problems is not uncommon. Nowhere in the literature is the distinction made as explicit as it has been made in this section.

3.3.3 Comparison of local derivative and Pelletier’s mixed derivative FSI forms

We introduce the fluid-structure interface relations, theoretically developed in the next chapter, in order to compare the local derivative form adopted in the present work with Pelletier’s more complicated mixed derivative form. The FSI interface boundary conditions in both approaches are the same and are based on 1) continuity of displacement and velocity of the boundary, and 2) force equilibrium between the fluid stress and structure stress tensors at the interface.

Pelletier *et al.* adopt a pseudo-solid mesh deformation scheme for the fluid domain that permits an Eulerian fluid description and Lagrangian structure description. The structure displacement deforms the pseudo-solid which satisfies condition 1) above, but there is no requirement to balance the surface tractions between the structure and pseudo-solid. The difficulty for sensitivity analysis arises when the interface conditions are differentiated. The mixed derivative form (the Lagrangian structure is referenced to

the unperturbed configuration) necessitates an inversion of the pseudo-solid deformation gradient tensor [49] which is equivalent to inverting the mesh Jacobian. The final form for the sensitivity interface based on condition 2) is (3.30). Contrast this with **Error! Reference source not found.** which avoids the mesh Jacobian calculations because the structure derivatives are expressed in local form. This essentially describes an Eulerian/Eulerian description of the fluid-structure interface. Since the material derivative is generally desired for the structure, the local sensitivity solution must be converted to total derivative form using (3.24).

3.4 Summary of Advantages of Local Derivative CSE

The continuous sensitivity equation method, a useful approach for calculating design sensitivities, is particularly attractive for shape variation problems since it avoids the expense of mesh sensitivity calculations of discrete sensitivity methods. However, the CSEs can be posed in total derivative, local derivative, or mixed derivative form and the choice can negate some of the computational advantages of the CSE method. Local sensitivities for shape variation problems are functions of the choice of boundary parameterization, which is not unique. The advantage of writing the CSE system in local derivative form is that only the boundary parameterization need be described. Furthermore, the CSE problem is generally simpler to pose in terms of local sensitivities than it is in total or mixed form (which necessarily must account for the transpiration of material coordinates in shape sensitivity problems). A comparison of (3.30) and **Error! Reference source not found.**, which represent the same FSI interface condition in different forms, makes this point readily

obvious. Since structural optimization for FSI will generally be carried out with respect to material coordinates, the local CSE solution will have to be transformed to total derivative form, but the computation required to do so on a boundary does not require the definition of the domain transformation field. If domain sensitivity is desired, the local CSE solution can still be transformed to total form, if a domain mapping is defined that is compatible with the boundary parameterization. The computational expense should still be less for this approach than for posing the CSEs in total form, since the total derivative form requires either the inversion of a domain transformation function, mesh Jacobian, or domain Jacobian.

Another advantage of posing and solving the CSEs in local form is that the same numerical solution method can be used for both the analysis and sensitivity problems. For example, a the local CSE form for a linear system can use the same solver with just different boundary conditions since the equations (when written in local derivative form) are identical. Even nonlinear “black box” solvers can used for both system, under certain conditions explained in Chapter 8, even though the equations are different. A total or mixed derivative form does not preclude this, but the more complicated form of the equations can make implementation more complicated than it is for the local CSE form. This is further explored in Chapter 8. We first describe the theory of the least-squares finite element method in the next chapter before solving example problems in subsequent chapters.

4 Least-Squares Finite Element Method

Section 2.4.3 outlined the motivation for using the least-squares finite element method for fluid-structure interaction problems. This chapter describes the theory of LSFEM (Section 4.1). Section 4.2 then describes the higher-order p -elements employed in the LSFEM solver coded in MATLAB[®] that is used to solve the example problems in subsequent chapters. One of the attractive possibilities of LSFEM are alternate norm formulations which are studied in Section 4.3. An original method for improving matrix condition number of LSFEM models is demonstrated in Section 4.4. Then the specific LSFEM formulations for five fluid models (Section 4.5), four elasticity models (Section 4.6), and the transient LSFEM formulations (Section 4.7) are presented. Finally, the fluid-structure boundary interface relations are described in Section 4.8.

This chapter contains a large amount of information that is not necessarily needed or used for the sensitivity solutions in the subsequent chapters. For example, six different LSFEM fluid models are derived in Section 4.5, although only three are used in the FSI examples presented in Chapter 7. The main intent of much of this chapter is to document the theory and models that were developed, though not always used, for the benefit of future researchers.

4.1 Variational Least-Squares

A LSFEM model minimizes the norm of the residual (or error) of the governing differential equations for the boundary value problem

$$\mathbf{A}\mathbf{u} = \mathbf{f} \text{ in } \Omega \tag{3.1}$$

$$\mathbf{B}\mathbf{u} = \mathbf{g} \text{ on } \Gamma \tag{3.2}$$

where the operator notation of (3.1)-(3.2) was described in Section 3.1. The linear form of the boundary value system is given here and in the derivations that follow, but LSFEM works for both linear and nonlinear systems. The weighted sum of the squares of the system residuals defines the least-squares functional

$$J(\mathbf{u}; \mathbf{f}, \mathbf{g}) = \|\mathbf{A}\mathbf{u} - \mathbf{f}\|_{\Omega}^2 + \alpha_{\Gamma} \|\mathbf{B}\mathbf{u} - \mathbf{g}\|_{\Gamma}^2 \quad (4.1)$$

where α_{Γ} is a relative weighting parameter for the residual of error in the boundary condition and the residual of the governing differential equation (both expressed in terms of the L^2 norm). Equation (4.1) represents a weak enforcement (i.e., integral sense) of the boundary conditions. The boundary conditions could alternatively be imposed directly on the boundary degrees of freedom which is referred to as strong enforcement of the boundary conditions. A necessary condition for \mathbf{u} to minimize (4.1) is that the first variation of (4.1) vanishes at \mathbf{u} [56]. This yields an equivalent bilinear-linear inner product form [105] for the boundary value system (3.1)-(3.2).

$$B(\mathbf{u}, \mathbf{v}) = l(\mathbf{f}, \mathbf{v}) \quad \forall \mathbf{v} \in \mathbf{V} \quad (4.2)$$

where the bilinear-linear inner product form for the domain is

$$\begin{aligned} B_{\Omega}(\mathbf{u}, \mathbf{v}) &\equiv (\mathbf{A}\mathbf{u}, \mathbf{A}\mathbf{v}) \\ l_{\Omega}(\mathbf{f}, \mathbf{v}) &\equiv (\mathbf{f}, \mathbf{A}\mathbf{v}) \end{aligned} \quad (4.3)$$

and the bilinear-linear inner product form for the boundary is

$$\begin{aligned} B_{\Gamma}(\mathbf{u}, \mathbf{v}) &\equiv (\mathbf{B}\mathbf{u}, \mathbf{B}\mathbf{v}) \\ l_{\Gamma}(\mathbf{g}, \mathbf{v}) &\equiv (\mathbf{g}, \mathbf{B}\mathbf{v}) \end{aligned} \quad (4.4)$$

The finite element method is based on partitioning the domain into finite elements and approximating the solution in an element by

$$\mathbf{u}^e \approx \mathbf{u}_h^e = \sum_{j=1}^{n_{dof}} c_j \psi_j \quad (4.5)$$

where c_j are the coefficients (to be determined by the solution) of the prescribed element shape functions ψ_j . Substituting (4.5) into (4.3) and (4.4) yields n_{dof} algebraic equations

$$\left[\mathbf{K}^e + \alpha_\Gamma \mathbf{K}_\Gamma^e \right] \mathbf{u} = \mathbf{F}^e + \alpha_\Gamma \mathbf{G}^e \quad (4.6)$$

The LSFEM element stiffness matrices and equivalent force vectors are then defined by

$$\mathbf{K}^e = \int_{\Omega^e} \left(\mathbf{A} \psi_1, \dots, \mathbf{A} \psi_{n_{dof}^e} \right)^T \left(\mathbf{A} \psi_1, \dots, \mathbf{A} \psi_{n_{dof}^e} \right) d\Omega \quad (4.7)$$

$$\mathbf{F}^e = \int_{\Omega^e} \left(\mathbf{A} \psi_1, \dots, \mathbf{A} \psi_{n_{dof}^e} \right)^T \mathbf{f} d\Omega \quad (4.8)$$

$$\mathbf{K}_\Gamma^e = \int_{\Gamma^e} \left(\mathbf{B} \psi_1, \dots, \mathbf{B} \psi_{n_{dof}^e} \right)^T \left(\mathbf{B} \psi_1, \dots, \mathbf{B} \psi_{n_{dof}^e} \right) d\Gamma \quad (4.9)$$

$$\mathbf{G}^e = \int_{\Gamma^e} \left(\mathbf{B} \psi_1, \dots, \mathbf{B} \psi_{n_{dof}^e} \right)^T \mathbf{g} d\Gamma \quad (4.10)$$

The element stiffness and load vectors are assembled into a global system of equations, which has the form

$$\left[\mathbf{K} + \alpha_\Gamma \mathbf{K}_\Gamma \right] \mathbf{u} = \mathbf{F} + \alpha_\Gamma \mathbf{G} \quad (4.11)$$

Note the difference of the LSFEM form of the stiffness matrix, (4.7), and load vector, (4.8), from the classic Galerkin definition

$$\mathbf{K}_{Galerkin}^e = \int_{\Omega^e} \left(\mathbf{I}_{\dim(\mathbf{A})} \psi_1, \dots, \mathbf{I}_{\dim(\mathbf{A})} \psi_{n_{dof}^e} \right)^T \left(\mathbf{A} \psi_1, \dots, \mathbf{A} \psi_{n_{dof}^e} \right) d\Omega \quad (4.12)$$

$$\mathbf{F}_{Galerkin}^e = \int_{\Omega^e} \left(\mathbf{I}_{\dim(\mathbf{A})} \psi_1, \dots, \mathbf{I}_{\dim(\mathbf{A})} \psi_{n_{dof}^e} \right)^T \mathbf{f} d\Omega \quad (4.13)$$

4.2 p -elements

The finite element method approximates the solution within an element by determining the coefficients of a shape function. Often, the shape function coefficients (degrees of freedom) are represented by element nodal values and the shape functions are affine blending functions of spatial coordinates. In the p -element method, championed by Szabo [124], the shape functions are based on higher-order polynomial approximations of the solution in an element. Thus, we approximate the solution \mathbf{u} by

$$\mathbf{u}^e \approx \mathbf{u}_h^e = \left[\psi_j \dots \psi_{n_{dof}^e} \right] \left\{ u_1 \dots u_{n_{nodes}} \quad a_1 \dots a_{n_a} \quad b_1 \dots b_{n_b} \right\}^T \quad (4.14)$$

where ψ_j are higher-order hierarchal shape functions [116]. For the p -element solutions presented below, we employ Szabo's quadrilateral shape function expansion basis [124], a serendipity expansion built of kernel functions constructed from Legendre polynomials. The element degrees of freedom, $n_{dof}^e = n_{nodes} + n_a + n_b$, consist of the element nodal values, $u_1 \dots u_{n_{nodes}}$, the edge coefficients, $a_1 \dots a_{n_a}$, and the interior (bubble) mode coefficients, $b_1 \dots b_{n_b}$.

Another p -element is the tensor product expansion used by Karniadakis [70]. A comparison of the serendipity and tensor product expansions is made in Section 4.2.2. First, however, the convergence and error rate theorem is presented which motivates the

use of higher-order polynomials for finite element approximations (Section 4.2.1). Implications of coercivity of the LSFEM formulations (Section 4.2.3) and the need for p -elements for LSFEM is also discussed (Section 4.2.4). Finally, the merits of higher-order p -elements for CSE are listed (Section 4.2.5).

4.2.1 Convergence and Error Rates

The convergence order of a finite element space is a measure of the rate of reduction in approximation error and is usually expressed as a function of the total number degrees of freedom, N , and the element mesh size, h . For higher-order finite element spaces in which polynomial order, p , refinement is also possible, it is common to examine p -refinement convergence rates as well.

The interpolant operator, Π_h , interpolates the solution, u , on a mesh characterized by h . The interpolation error is then

$$E_{\Pi_h} \equiv \|u - \Pi_h u\| \quad (4.15)$$

This is distinct from the FEM solution error

$$e_h \equiv \|u - u_h\| \quad (4.16)$$

Convergence and stability proofs are usually written with regard to the solution error. In most practical applications, the exact solution is not known and the system residual is used instead.

The following theorem on convergence rate is due to Szabo [124] (see also Bathe [14]). If Q_p is the space of piecewise continuous polynomial functions (order $\leq p$ in

each coordinate direction) defined on quadrilateral triangulations of a closed domain, $\overline{\Omega}$, then given a $u \in H^{p+1}(\Omega)$ there exists a finite element solution, $u_h \in Q_p$, such that

$$\|u - u_h\|_r \leq Ch^{p+1-r} \|u\|_{k+1} \quad (4.17)$$

where $r=0,1$ and C is a constant that does not depend on the mesh. An implicit assumption in (4.17) is that the mesh is optimally graded, that is, that the error is uniformly distributed across the mesh.

Jiang [69] proves an equivalent form of (4.17) for LSFEM in terms of the semi-norm, $|u|_p^2 \equiv \int_{\Omega} \left| \frac{\partial^p}{\partial x^p} u \right|^2 dx$. Given a sufficiently smooth u , then

$$\|u - u_h\|_{L^2} \leq Ch^p |u|_{k+1} \quad (4.18)$$

For strictly elliptic systems, the convergence rate is improved:

$$\|u - u_h\|_{L^2} \leq Ch^{p+1} |u|_{p+1} \quad (4.19)$$

Equations (4.17) thru (4.19) show that convergence rates are improved faster with p -refinement than with h -refinement. This is the basis of the spectral method in FEM. The general rule of thumb is that the mesh should first be refined (in h) to capture sharp gradients (this deals with the optimally graded mesh assumption) and then refined in p to achieve the best improvement in convergence rate.

It should not be surprising that convergence rates for LSFEM solutions are substantially improved by using p -elements. What is somewhat surprising is that several examples of LSFEM applications show poor accuracy at $p = 1$ and 2 (which are or analogous order to the classic Galerkin bilinear QUAD 4 and biquadratic QUAD 8 or QUAD 9 elements [35]). Indeed, a conjecture based on preliminary observations that we

have been unable to prove, may indicate that a minimum of a fifth-order polynomial should be used for the first-order least-squares elasticity applications. The relevant observations are noted in Section 4.2.4.

It is appropriate to note at this point a conclusion made by Jiang (see [69] Section 6.6) that in conventional LSFEM method, the rate of convergence for dual variables (fluxes) is lower than optimal, since the reduction of second-order elliptic problems to the first-order grad-div system destroys full H^1 ellipticity. This conclusion is made on the basis of theoretical and numerical studies. In his work, Jiang did not consider higher-order p -elements. It is unclear if the conclusion regarding sub-optimal convergence due to destroyed ellipticity holds when the higher-order p -values are used for first-order LSFEM formulations. In the range of fluid and elasticity examples solved in the present work using higher-order p -element LSFEM, no instances of decreased convergence for dual variables was observed.

4.2.2 Serendipity and tensor expansion basis comparison

Szabo's serendipity p -element expansion basis [124] is an incomplete polynomial basis. However, comparisons with a complete polynomial basis set (*i.e.* the tensor product expansion of [70]) in [101] indicate that the reduction in convergence character is slight. That is, that the serendipity expansion still provides the expected convergence rate (for an optimal interpolation based on a complete polynomial) despite being an incomplete polynomial. The only difference between the expansions is the inclusion of more interior modes for the tensor product which completes the polynomial basis, Figure 4.1. The serendipity expansion was implemented for the LSFEM solutions presented in

this dissertation, since it effectively achieves higher polynomial order convergence but at a reduced number of required degrees of freedom, Figure 4.2

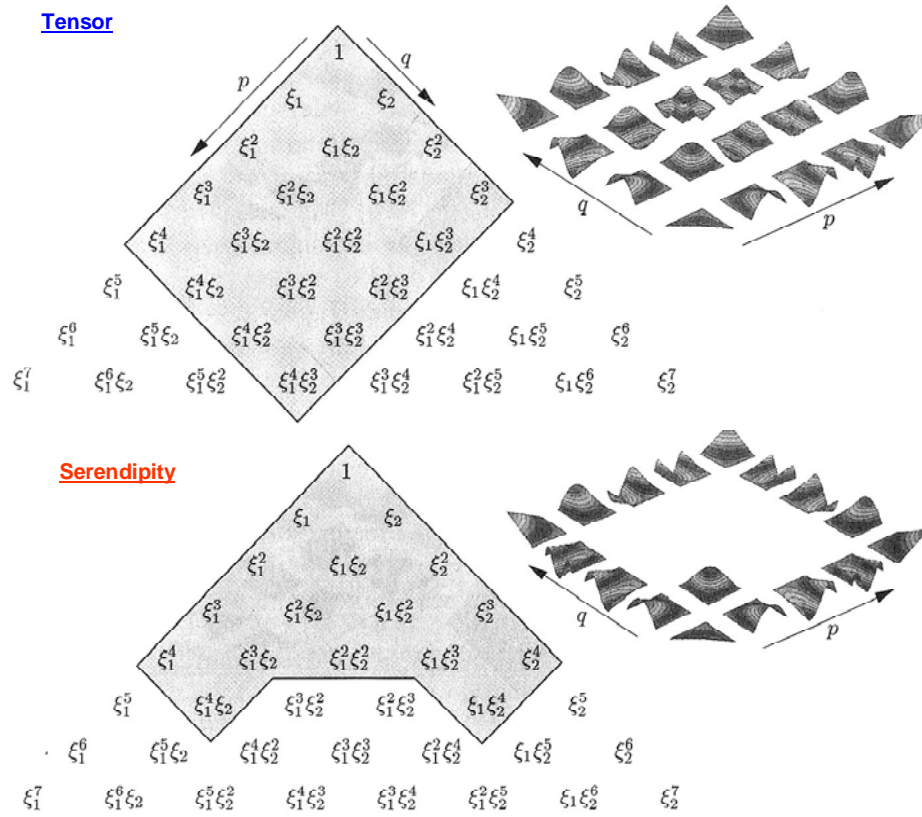


Figure 4.1: Pascal's triangle for serendipity and tensor product expansions (from [70])

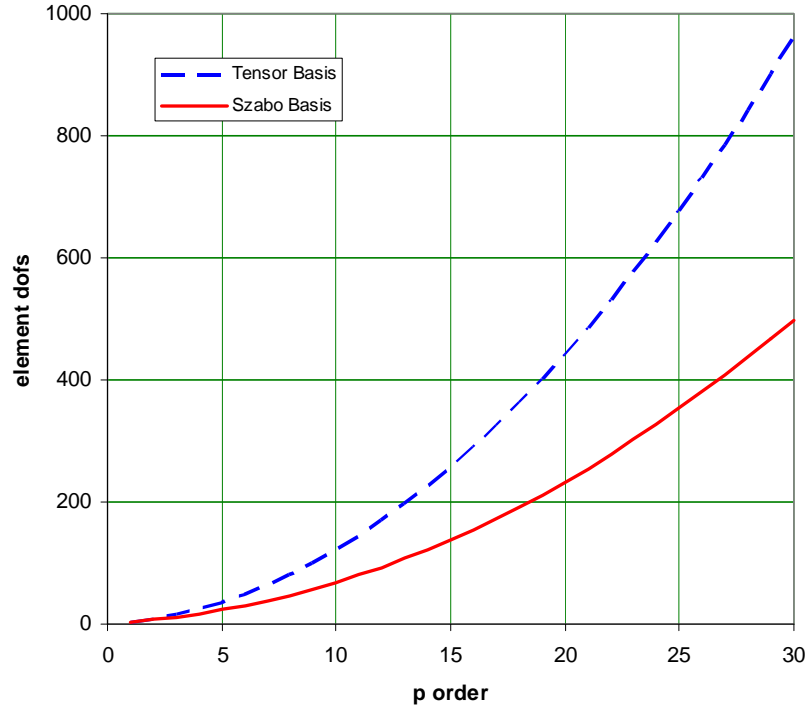


Figure 4.2: Degree of freedom comparison for Serendipity and Tensor product expansion basis.

4.2.3 Coercivity Implications

If a LSFEM formulation is coercive, then the assumptions underlying the convergence and error rate theorems are satisfied and the conclusions are mathematically applicable to the LSFEM solution. A coercive bilinear form is equivalent to an inner product in the underlying function space [22]. The implication of a coercive formulation is that the existence and uniqueness of (variational, weak) solutions can be established using Lax-Milgram variation of the Riesz representation theorem from functional analysis ([88], p. 345):

Let H be a Hilbert space and let l be a bounded linear functional on H . Then there is one and only one vector $y \in H$ such that

$$l(x) = (x, y) \quad \text{for all } x \in H \quad (4.20)$$

The vector y is called the representation of l . (Note that y and l are different objects, l is a linear functional on H and y is a point in H .)

The Lax-Milgram theorem ([88], p. 346) is

Let $B(u, v)$ be a *sesquilinear* functional on a Hilbert space H and assume that there are positive constants a and b such that

$$\begin{aligned} |B(u, v)| &\leq a \|u\| \|v\| \\ b \|u\|^2 &\leq |B(u, u)| \end{aligned} \quad (4.21)$$

for all u, v in H . Let l be any bounded linear functional on H . Then there exist unique points u_o and v_o in H such that

$$l(x) = B(x, v_o) = \overline{B(u_o, x)} \quad \text{for all } x \text{ in } H \quad (4.22)$$

where the over-bar is used to denote the complex conjugate. A *sesquilinear* form is linear in one argument and *anti-linear* or *conjugate linear* in the other argument. A function is *conjugate linear* if $f(ax + by) = \bar{a}f(x) + \bar{b}f(y)$.

A first-order formulation is *fully H^1 -coercive* if it is well-posed in $L^2 \times H^1$ where the data comes from L^2 and the solution comes from H^1 [22]. Bochev & Gunzburger offer *fully-coercive* first-order least squares formulations for plane elasticity problems, but they are velocity-pressure-vorticity formulations and not the mixed displacement-stress formulations presented below in Section 4.6.1. The primary implication of using a non-coercive least-squares formulation is that the assumptions for the theorems on convergence are not met. All problems worked with the non-coercive forms derived below have converged to the analytic solution (when available) and have done so at rates which are approximately equivalent to that predicted by the theorems.

4.2.4 Need for p -elements in LSFEM

Although LSFEMs are theoretically not constrained by the stability problems associated with mixed-elements, our experience is that LSFEM mixed stress-displacement elements for elasticity can still be beset by problems of slow convergence at low p -values. Much of this probably stems from the destroyed ellipticity and non-coercivity of the implemented forms. However, some interesting observations for 2D plane elasticity problems hints at a possible correspondence between a minimum element p -order for decent convergence properties and the polynomial order of the lowest order Arnold-Awanou mixed stress-displacement element.

As described in Section 2.4.2.1, the Arnold-Awanou mixed stress-displacement element [5] is the first stable, quadrilateral mixed finite element for elasticity. The lowest order Arnold-Awanou element is built on a displacement field of second-order polynomials and a stress tensor which is a subspace of 2×2 symmetric tensors consisting of fifth-order polynomials.

A p -convergence analysis of three example elasticity problems solved using the stress-displacement LSFEM formulation developed in Section 4.6.1 demonstrates a distinct improvement in convergence rate when fifth-order (serendipity) p -elements are used. Consider, for example, the distinct knee in the curve in Figure 4.3 for the Timoshenko and Goodier example problem presented in Section 5.1. Below $p = 5$, the slope of the curve is approximately -1 . At $p > 5$, the slope is approximately -9 , almost an order of magnitude steeper. Although not as distinct for the other two elasticity problems plotted in Figure 4.3 (the plate with a hole from Section 5.2 and the elastic CSE

version of the Timoshenko and Goodier example), the $p = 5$ threshold still represents an approximate border between the shallow convergence character of low p -values and the significantly steeper convergence rates of higher p -values. For comparison, a non-elasticity posed problem (Reddy example 13.2.4 [105]) based on a Dirichlet version of the Poisson equation is also plotted. The relatively straight character of the convergence rate implies that the “knee-in-the-curve” is not a particular artifact of Szabo’s serendipity p -element expansion basis.

The pertinent observation is that fifth-order corresponds to the minimum polynomial order for the stress tensor that Arnold proves is required to ensure a stable mixed rectangular element [5]. This suggests that mixed stress-displacement finite elements may require a minimum of a fifth-order polynomial expansion to guarantee good convergence properties. Further investigation is necessary to determine if the observations of convergence rates and the conjectured minimum polynomial order are generalizable beyond the example problems considered thus far.

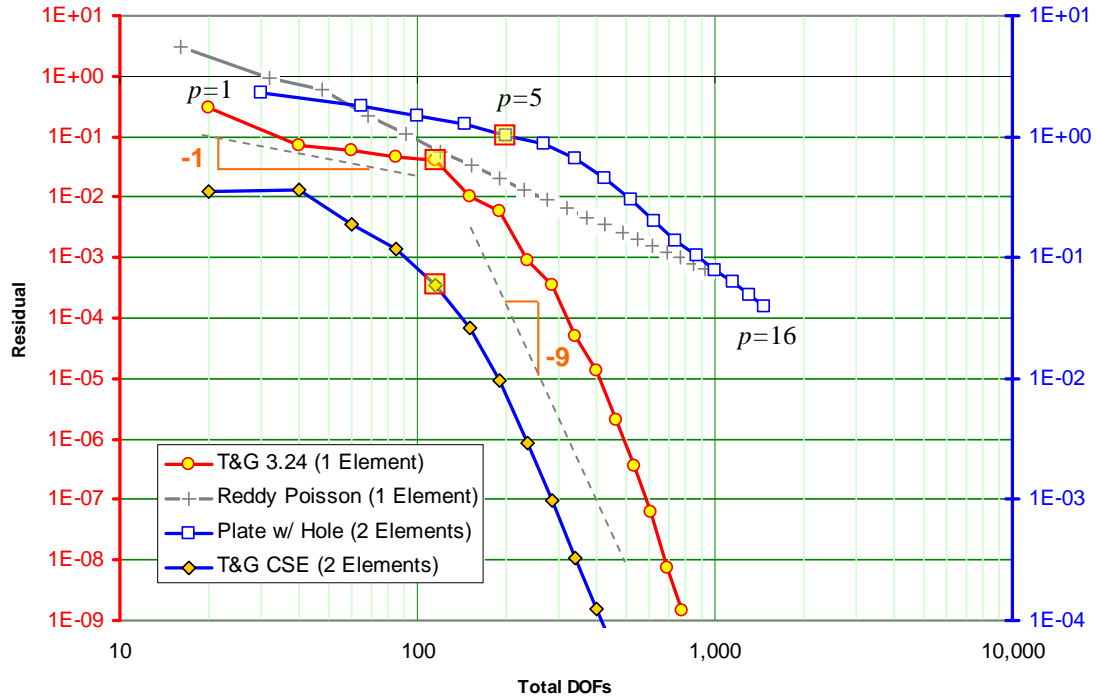


Figure 4.3: LSFEM system residual p -convergence as a function of total system degrees of freedom (N)

4.2.5 Advantages of p -elements for CSE

In the examples considered in Chapter 5-7, we note that a higher-order p -value is required to achieve an equivalent order residual for the CSE system compared to the original system. Sensitivity gradients in the vicinity of a boundary controlled by a shape parameter are typically steeper than gradients of the original system. This result matches the conclusions made by previous researchers that a more refined mesh may be required for the CSE system [120]. Even with the automatic adaptive meshing procedures available and employed by some researchers, it is far more convenient to use the same computational mesh for both the original system and the sensitivity system. This is a

distinct advantage of higher-order FEM since p -refinement allows a straightforward means to achieve a refined solution without needing to create a spatially-refined mesh.

4.3 Alternate norms in LSFEM

An advantage of LSFEM is a flexibility in the choice of norms used to express the variational statement of a problem, (4.1). Typically, the L^2 norm is used, but other norms may be convenient or more useful for some applications. Consider, as an example, evaluating the functional expressed in terms of the H^1 norm in lieu of the L^2 norm as a means of penalizing non-smooth gradients of a solution. Section 4.3.3 provides an example of an application where the H^1 norm is used to smooth a spurious boundary solution resulting in an improved sensitivity solution.

For a single variable in two dimensions, the H^1 norm is

$$\|u\|_{H^1} = \left[\int_{\Omega} \left[|u|^2 + |u_{,x}|^2 + |u_{,y}|^2 \right] d\Omega \right]^{1/2} \quad (4.23)$$

We restate the equivalent L^2 norm for comparison with (4.23)

$$\|u\|_{L^2} = \left[\int_{\Omega} |u|^2 d\Omega \right]^{1/2} \quad (4.24)$$

The bilinear/linear form (4.3) evaluated in the H^1 norm under the same finite element approximation (4.14) yields the element stiffness matrix and load vector

$$\mathbf{K}^e = \int_{\Omega^e} \left[\left(\mathbf{A}\psi_1, \dots, \mathbf{A}\psi_{n_{dof}^e} \right)^T \left(\mathbf{A}\psi_1, \dots, \mathbf{A}\psi_{n_{dof}^e} \right) + \dots \right. \\ \left. \left(\mathbf{A}\psi_{1,x}, \dots, \mathbf{A}\psi_{n_{dof}^e,x} \right)^T \left(\mathbf{A}\psi_{1,x}, \dots, \mathbf{A}\psi_{n_{dof}^e,x} \right) + \left(\mathbf{A}\psi_{1,y}, \dots, \mathbf{A}\psi_{n_{dof}^e,y} \right)^T \left(\mathbf{A}\psi_{1,y}, \dots, \mathbf{A}\psi_{n_{dof}^e,y} \right) \right] d\Omega \quad (4.25)$$

$$\mathbf{F}^e = \int_{\Omega^e} \left[\left(\mathbf{A}\psi_1, \dots, \mathbf{A}\psi_{n_{dof}^e} \right)^T \mathbf{f} + \left(\mathbf{A}\psi_{1,x}, \dots, \mathbf{A}\psi_{n_{dof}^e,x} \right)^T \mathbf{f}_{,x} + \left(\mathbf{A}\psi_{1,y}, \dots, \mathbf{A}\psi_{n_{dof}^e,y} \right)^T \mathbf{f}_{,y} \right] d\Omega \quad (4.26)$$

which should be compared to (4.7)-(4.8) based on the L^2 norm. Note that the practical evaluation of (4.25)-(4.26) becomes more complex due to the presence of the shape function derivatives in the definition of the element matrices. Since the first-order form differential operator \mathbf{A} may contain non-zero first derivatives in each of the coordinate dimensions, second derivatives of each of the shape functions is required. Furthermore, when numerical quadrature is used to evaluate (4.25)-(4.26), the higher-order derivatives of the mapping (Jacobian) to the natural coordinate system for the standard element must be included. Thus, since

$$\begin{aligned}\mathbf{A}\psi_{,x} &= A_0\psi_{,x} + A_1\psi_{,xx} + A_2\psi_{,xy} \\ \mathbf{A}\psi_{,y} &= A_0\psi_{,y} + A_1\psi_{,yx} + A_2\psi_{,yy}\end{aligned}\tag{4.27}$$

and

$$\begin{Bmatrix} \psi_{,x} \\ \psi_{,y} \end{Bmatrix} = J^{-1} \begin{Bmatrix} \psi_{,\xi} \\ \psi_{,\eta} \end{Bmatrix}\tag{4.28}$$

where the Jacobian, J , is defined as

$$J = \begin{bmatrix} \frac{\partial x}{\partial \xi} & \frac{\partial x}{\partial \eta} \\ \frac{\partial y}{\partial \xi} & \frac{\partial y}{\partial \eta} \end{bmatrix}\tag{4.29}$$

Thus, the higher-order derivatives in (4.27) given by the evaluation of the shape functions in their natural coordinates are

$$\begin{aligned}\begin{Bmatrix} \psi_{,x} \\ \psi_{,y} \end{Bmatrix}_{,x} &= J^{-1} \left[\frac{\partial \xi}{\partial x} \frac{\partial}{\partial \xi} \begin{Bmatrix} \psi_{,\xi} \\ \psi_{,\eta} \end{Bmatrix} + \frac{\partial \eta}{\partial x} \frac{\partial}{\partial \eta} \begin{Bmatrix} \psi_{,\xi} \\ \psi_{,\eta} \end{Bmatrix} \right] \\ \begin{Bmatrix} \psi_{,x} \\ \psi_{,y} \end{Bmatrix}_{,y} &= J^{-1} \left[\frac{\partial \xi}{\partial y} \frac{\partial}{\partial \xi} \begin{Bmatrix} \psi_{,\xi} \\ \psi_{,\eta} \end{Bmatrix} + \frac{\partial \eta}{\partial y} \frac{\partial}{\partial \eta} \begin{Bmatrix} \psi_{,\xi} \\ \psi_{,\eta} \end{Bmatrix} \right]\end{aligned}\tag{4.30}$$

or

$$\begin{aligned}
\begin{Bmatrix} \psi_{,x} \\ \psi_{,y} \end{Bmatrix}_{,x} &= J^{-1} \left[\begin{bmatrix} J^{-1} \end{bmatrix}_{11} \begin{Bmatrix} \psi_{,\xi\xi} \\ \psi_{,\eta\xi} \end{Bmatrix} + \begin{bmatrix} J^{-1} \end{bmatrix}_{12} \begin{Bmatrix} \psi_{,\xi\eta} \\ \psi_{,\eta\eta} \end{Bmatrix} \right] \\
\begin{Bmatrix} \psi_{,x} \\ \psi_{,y} \end{Bmatrix}_{,y} &= J^{-1} \left[\begin{bmatrix} J^{-1} \end{bmatrix}_{21} \begin{Bmatrix} \psi_{,\xi\xi} \\ \psi_{,\eta\xi} \end{Bmatrix} + \begin{bmatrix} J^{-1} \end{bmatrix}_{22} \begin{Bmatrix} \psi_{,\xi\eta} \\ \psi_{,\eta\eta} \end{Bmatrix} \right]
\end{aligned} \tag{4.31}$$

4.3.1 Bar Example using H^I Norm

Consider the LSFEM solution to a vertical bar of length L (with a cross-section of A and modulus E) supporting a distributed load $f(x) = rx^4$ and a top load of P , Figure 4.4. The analytic solution for displacement and stress and their gradients for the given load is

$$u(x) = \frac{PL_s}{EA} + \frac{rL_s^6}{30EA} - \frac{Px}{EA} - \frac{rx^6}{30EA} \tag{4.32}$$

$$u_{,x}(x) = -\frac{P}{EA} - \frac{rx^5}{5EA} \tag{4.33}$$

$$\sigma_x(x) = -\frac{P}{A} - \frac{r}{5A}x^5 \tag{4.34}$$

$$\sigma_{x,x}(x) = -\frac{rx^4}{A} \tag{4.35}$$

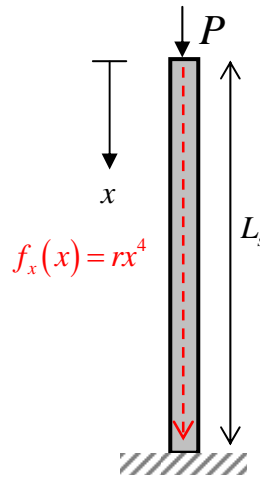


Figure 4.4: Vertically loaded bar

The LSFEM solution for a two-element unit bar ($r = A = E = 1$) solved using both the L^2 and H^1 norms is given in Figure 4.5. The analytic solution is also plotted as a dashed line. A $p = 2$ element was used to avoid exact matching of the analytic solution. The H^1 norm solution has about a 2% higher least squares (L^2) residual than the L^2 norm solution. This is expected. However, the solution for stress is approximately 2% better for the H^1 norm compared to the L^2 norm (and the solution for displacement is approximately 2% worse). The stress degree of freedom is a gradient of the displacement and the higher penalty on gradients in the H^1 norm shifts some of the error from displacement to stress. Note the discontinuities between the elements in the derivatives of both displacement and stress since C^0 elements are employed for both the L^2 and H^1 norms. In other words, although the H^1 norm penalizes gradients within an element (at the cost of a higher overall residual), it does nothing to penalize discontinuities in gradients between elements that exist in the absence of C^1 elements. Nevertheless, there are some potential applications in which the H^1 norm may be desired. One example is given in Section 4.3.3.

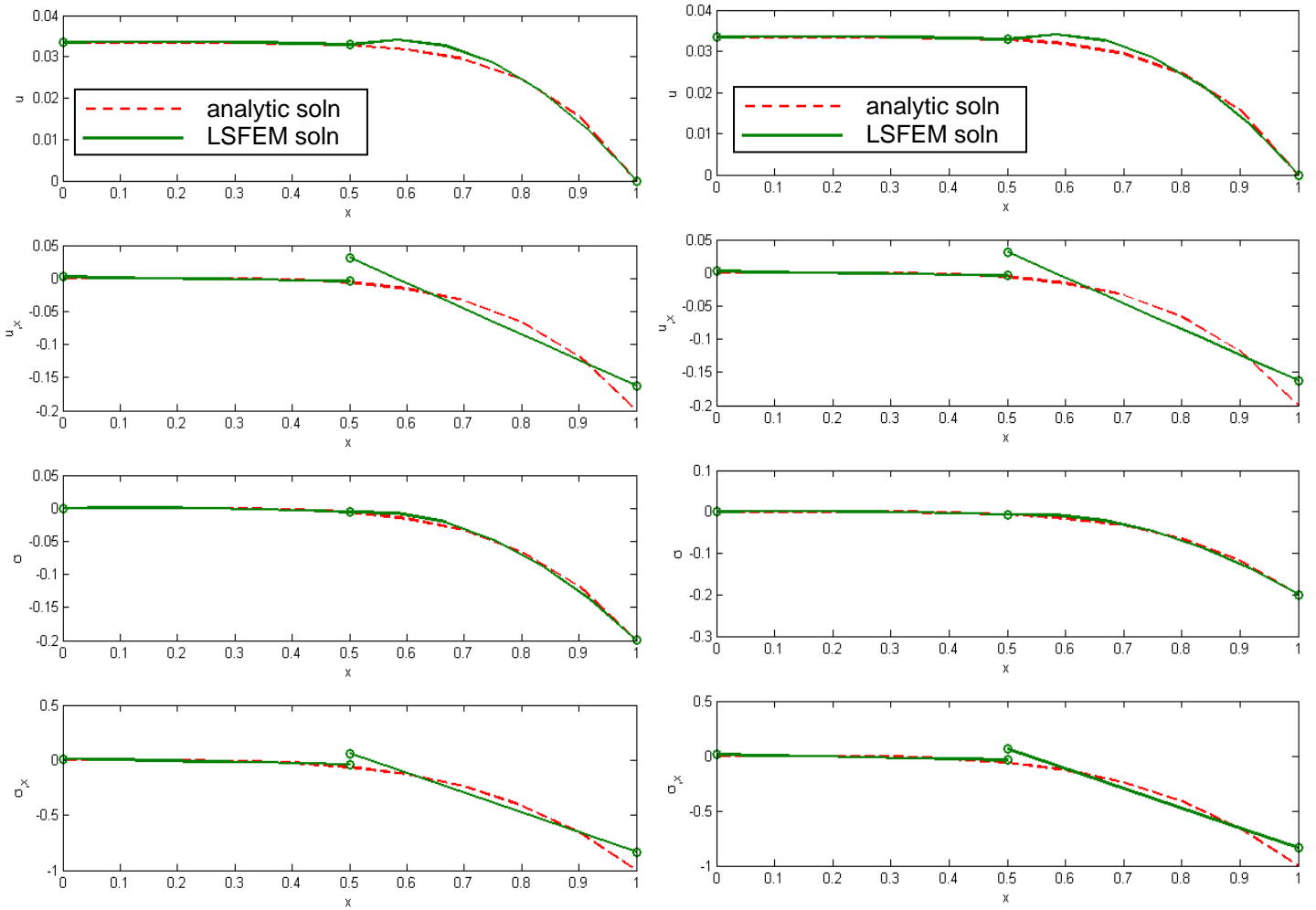


Figure 4.5: Comparison of LSFEM L^2 (left) and H^1 (right) norm solutions ($p = 2$) for a 2-element vertically loaded bar

4.3.2 Two-dimension implementation of the H^1 norm.

The L^2 and H^1 norm LSFEM solutions are now compared for a two-dimensional Poisson equation problem with Dirichlet-type boundary conditions. The problem is Example 14.2.3 from Reddy [105]. The LSFEM solutions for L^2 and H^1 norms for a 4-element mesh ($p = 8$) are given in Figure 4.6 and Figure 4.7 respectively. The first order formulation for this problems contains three derivatives, $u_{,x}, u_{,y}, u_{,xy}$, of the primary variable, u , and the total L^2 residual for the H^1 solution is almost double that of the L^2

solution. The absolute error for the $u_{,xy}$ term is improved by approximately 10% in the H^1 solution. It is permissible to weight each of the terms in the norm of the H^1 variational statement separately depending on their relative importance and desired penalty for a given problem.

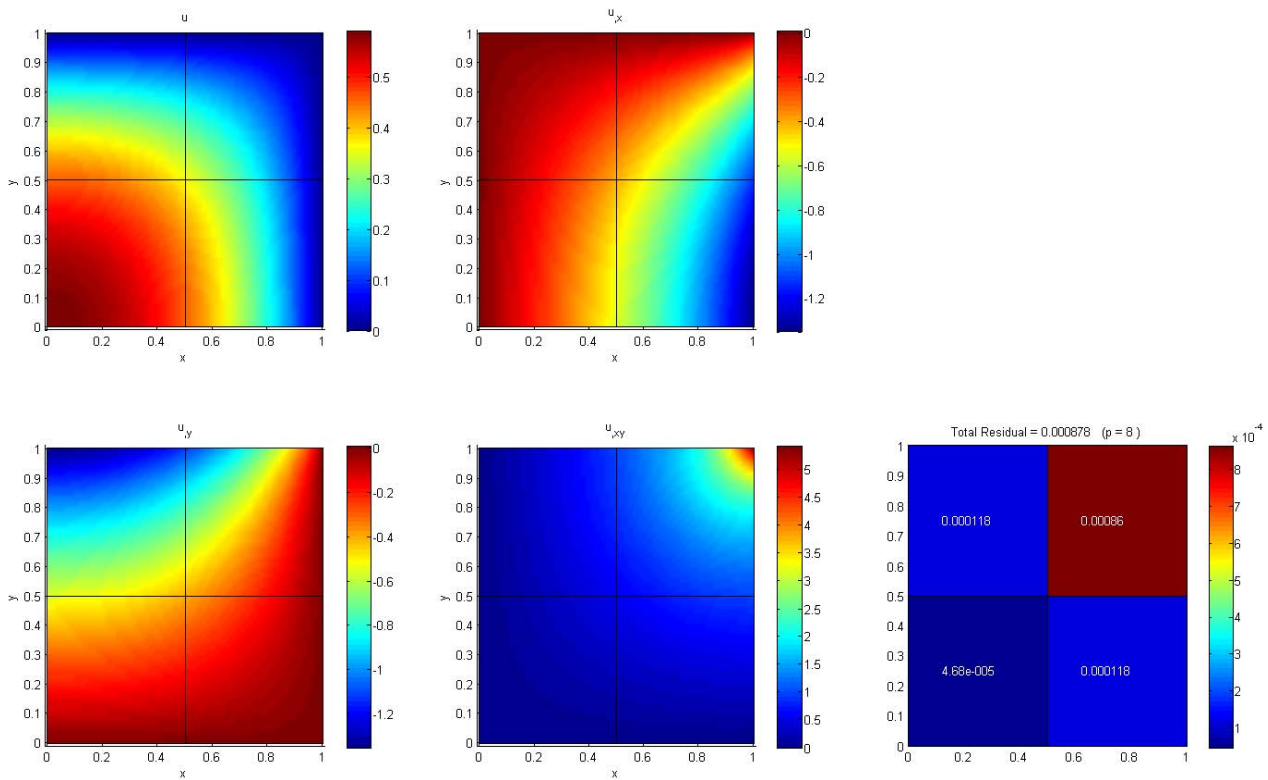


Figure 4.6: L^2 norm solution to Reddy Ex. 13.2.4

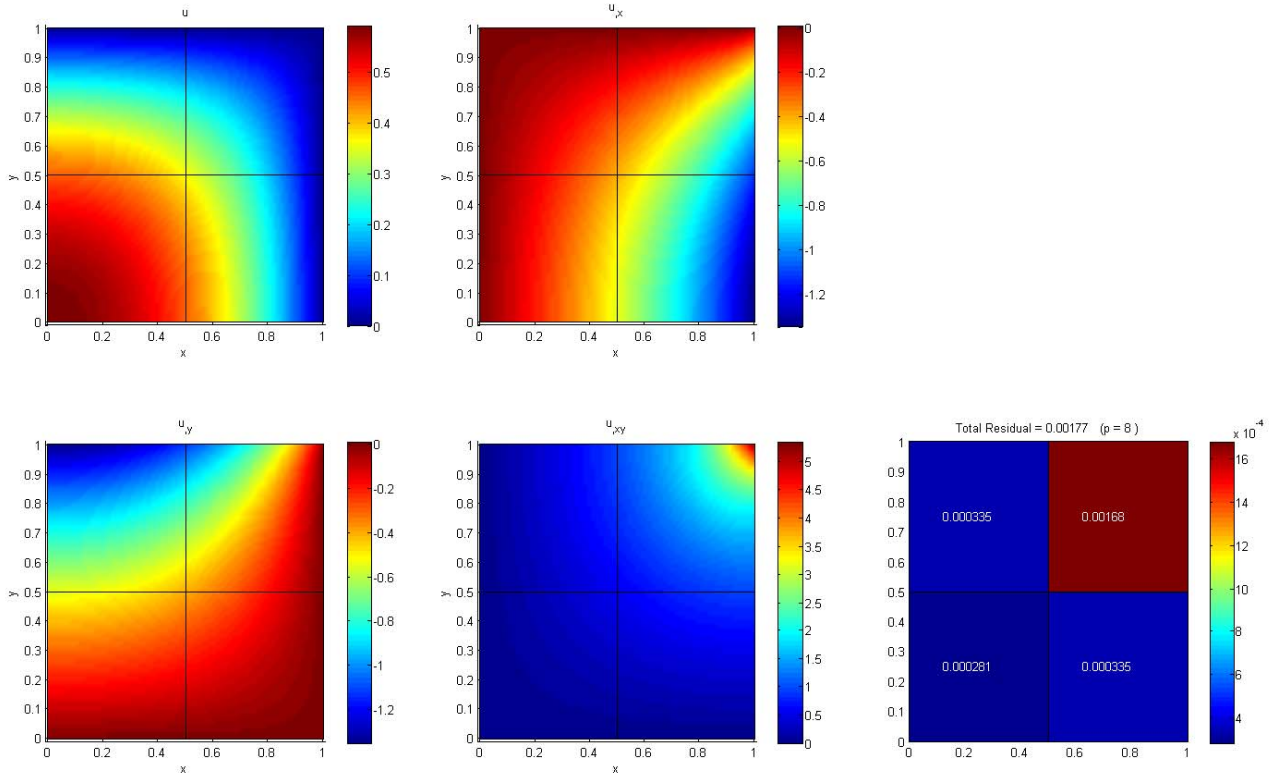


Figure 4.7: H^1 norm solution to Reddy Ex. 13.2.4

4.3.3 Plate with a hole H^1 example

As mentioned above, each term in the H^1 norm may be weighted separately. It is also permissible to only use the H^1 norm in elements where an improved solution for the gradients is desired, *e.g.* in boundary elements where the gradient of the solution will be used to generate the boundary data for the CSE problem. In an example problem considered later (Section 5.2), the CSE boundary data for a system in polar coordinates are generated by taking derivatives of a system posed in Cartesian degrees of freedom. A $p = 8$ LSFEM solution yields a fairly good estimate of the sensitivity boundary conditions. However, for the shape function expansion basis employed, p -values > 8 start

to produce the spurious results in Figure 4.8. This stems from the discontinuity in the shape function derivatives between the elements along the hole. The unstressed boundary condition for the hole in the original LSFEM problem is enforced weakly, and at larger p -values, the additional edge coefficients in the boundary integral have the equivalent effect in over-determining the solution along the hole. Although this does not affect the LSFEM solution, the discontinuity of derivatives of the LSFEM solution increases. Since these derivatives are used to formulate the LS-CSE boundary conditions, this results in the spurious nature of the boundary conditions for higher p -values in Figure 4.8. Evaluating the least-squares functional along the hole in terms of the H^1 norm in lieu of the L^2 norm penalizes non-smooth gradients and improves the approximation of the gradient of the LSFEM solution and hence the CSE boundary conditions. The H^1 norm cannot completely remove the spurious behavior without reducing the accuracy of the original LSFEM solution, but this option may work better for other applications. The flexibility in norm choice is an advantage of the LSFEM as implemented.

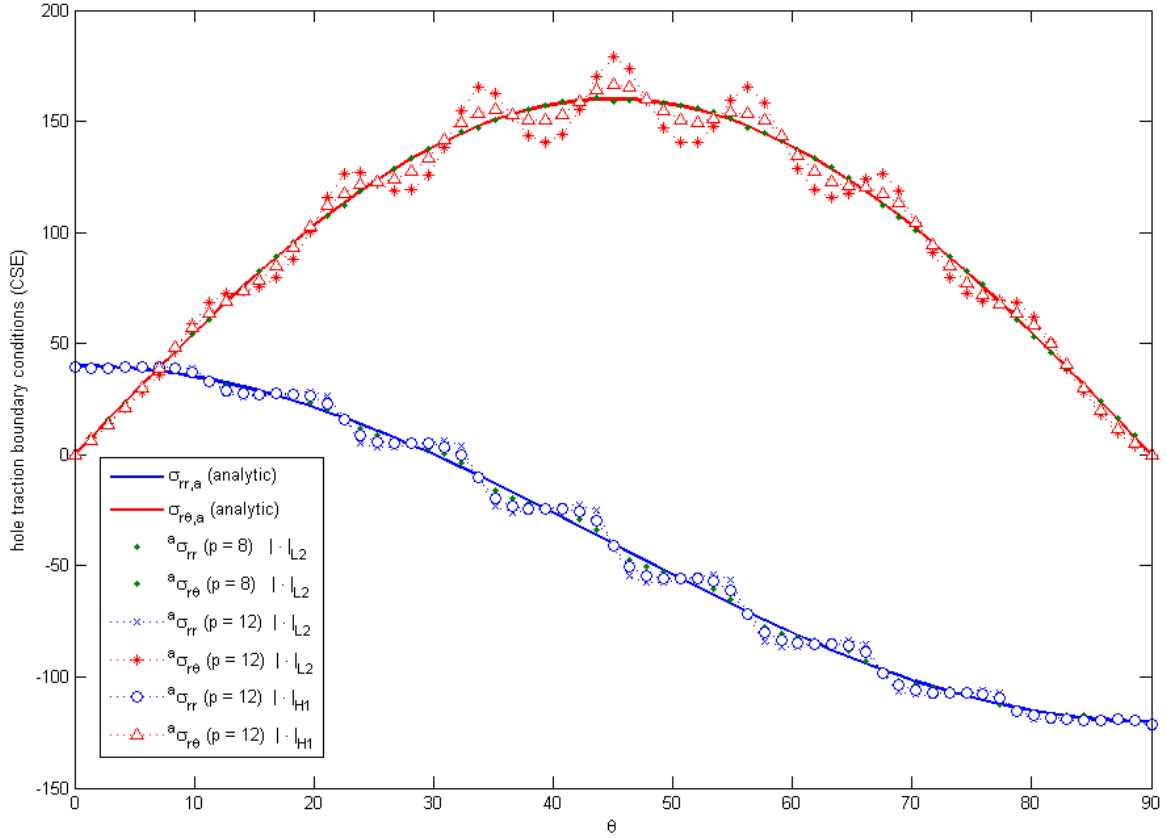


Figure 4.8: Comparison of L^2 and H^1 norm boundary data for the plate with a circular hole CSE problem.

4.4 Improving Condition Number for LSFEM with Weak Boundary Enforcement

Weak enforcement of boundary conditions, that is satisfaction of boundary conditions in an integral sense, *e.g.* (4.1), arises naturally in many weighted residual methods for boundary value problems. Boundary conditions that are specified in terms of functions of primary variables can often only be enforced in a weak sense if expensive iterative solutions are to be avoided. For example, the boundary conditions for the airflow about an airfoil are specified in terms of the surface normal and tangential velocity components, not in the domain coordinate velocity components. Similar

problems arise with stress boundary conditions for elasticity problems. Although weak boundary residuals are simple to state, they can sometimes lead to numerical difficulties in LSFEM due to ill-conditioned matrices. (Determination of proper boundary integral weighting relative to that domain can also be problematic in LSFEM, but this is not necessarily a physical problem.) This section summarizes an original method for improving matrix condition number of weakly-enforced least-squares finite element solutions based on condensation of the weak boundary variables [134]. In addition to improving the numerical stability of the problem, the approach also improves the numerical efficiency of the solution as it reduces the number of variables that must be solved. Results for several examples from elasticity and fluid problems are presented and compared.

For a weighted residual approach in which w denotes a test function, compare the weak enforcement of boundary conditions

$$\int_{\Omega} w(Au - f) d\Omega + \alpha \int_{\Gamma} w(Bu - g) d\Gamma = 0 \quad (4.36)$$

with a strong enforcement form in which the boundary conditions are solved first by

$$\int_{\Gamma} w(Bu - g) d\Gamma = 0 \quad (4.37)$$

which leads to a FEM solution for the boundary degrees of freedom

$$u_{\Gamma} = K_{\Gamma}^{-1} G \quad (4.38)$$

Partitioning all the system degrees of freedom into domain degrees of freedom and boundary degrees of freedom yields

$$\begin{bmatrix} K_{\Omega\Omega} & K_{\Omega\Gamma} \\ K_{\Gamma\Omega} & K_{\Gamma\Gamma} \end{bmatrix} \begin{Bmatrix} u_{\Omega} \\ u_{\Gamma} \end{Bmatrix} = \begin{Bmatrix} F_{\Omega} \\ F_{\Gamma} \end{Bmatrix} \quad (4.39)$$

where u_Ω is really the set of degrees of freedom belonging to $\Omega - \Gamma$. The solution to the non-boundary unknowns u_Ω in terms of the partitioned stiffness matrix and load vector is then

$$u_\Omega = K_{\Omega\Omega}^{-1} [F_\Omega - K_{\Omega\Gamma} u_\Gamma] \quad (4.40)$$

where u_Γ is given by (4.38). By contrast, the finite element solution of the weakly imposed boundary integral in (4.36) leads to a simultaneous solution of both the boundary and non-boundary unknowns.

$$\mathbf{u} = [\mathbf{K} + \alpha \mathbf{K}_\Gamma]^{-1} [\mathbf{F} + \alpha \mathbf{G}] \quad (4.41)$$

The condition number is a measure of amenability to digital computation. A low condition number, on the order of 1, is a “well-conditioned” system and a large condition number is “ill-conditioned”. The conditioning number of a matrix \mathbf{A} is

$$\kappa(\mathbf{A}) = \|\mathbf{A}^{-1}\| \cdot \|\mathbf{A}\| \quad (4.42)$$

Under the L^2 norm, the condition number is

$$\kappa(\mathbf{A}) = \frac{\sigma_{\max}(\mathbf{A})}{\sigma_{\min}(\mathbf{A})} \quad (4.43)$$

where $\sigma(\cdot)$ represents the singular value of \mathbf{A} . Further if \mathbf{A} is normal ($\mathbf{A}^T \mathbf{A} = \mathbf{A} \mathbf{A}^T$)

then

$$\kappa(\mathbf{A}) = \frac{\lambda_{\max}(\mathbf{A})}{\lambda_{\min}(\mathbf{A})} \quad (4.44)$$

where λ is an eigenvalue of \mathbf{A} . It is the large condition number of the $[\mathbf{K} + \alpha \mathbf{K}_\Gamma]$ matrix that must be “inverted” that presents the potential numerical difficulty for weakly enforced boundary conditions. Let us partition the system into domain unknowns,

constrained boundary conditions (strongly enforced), and weakly enforced (integral) boundary degrees of freedom as shown in Figure 4.9.

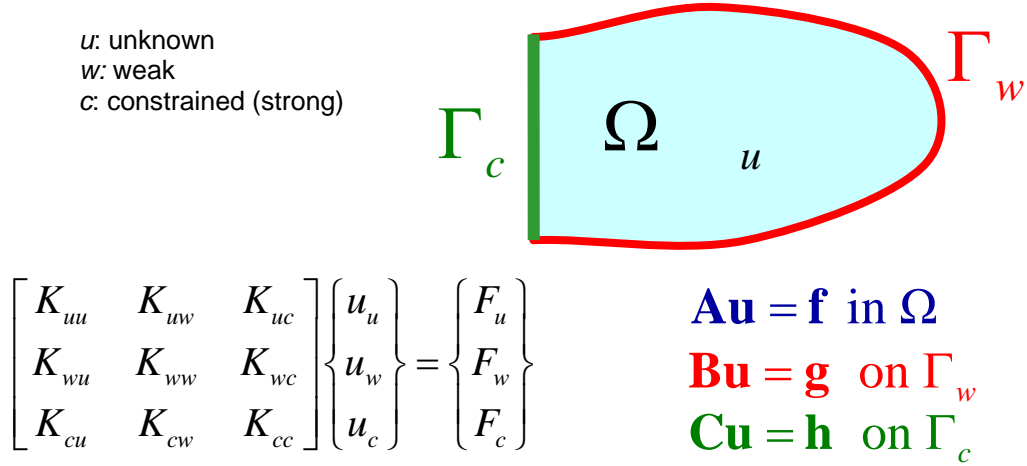


Figure 4.9: Partitioned domain and boundary value problem

The strategy to improve the condition number of the system is to condense the weak degrees of freedom (after solving for constrained boundary values) and solve for the domain unknowns as if all boundary degrees of freedom are constrained. Thus, solving the partitioned system in Figure 4.9 for the weak boundary unknowns yields

$$K_{wu}u_u + K_{ww}u_w + K_{wc}u_c = F_w \quad \Rightarrow \quad u_w = K_{ww}^{-1} [F_w - K_{wc}u_c - K_{wu}u_u] \quad (4.45)$$

which is substituted into

$$K_{uu}u_u + K_{uw}u_w + K_{uc}u_c = F_u \quad (4.46)$$

which yields the domain unknowns

$$u_u = [K_{uu} - K_{uw}K_{ww}^{-1}K_{wu}]^{-1} [F_u - K_{uw}K_{ww}^{-1}F_w + [K_{uw}K_{ww}^{-1}K_{wc} - K_{uc}]u_c] \quad (4.47)$$

The weak boundary unknowns are then recovered by

$$u_w = K_{ww}^{-1} [F_w - K_{wc}u_c - K_{wu}u_u] \quad (4.48)$$

Consider as an example, the rank deficient system of equations

$$\begin{aligned}
x_1 &= x_2 \\
x_2 &= x_3 \\
2x_2 &= x_1 + x_3
\end{aligned} \tag{4.49}$$

which can be represented in matrix form by

$$\begin{bmatrix} 1 & -1 & 0 \\ -1 & 2 & -1 \\ 0 & -1 & 1 \end{bmatrix} \begin{Bmatrix} x_1 \\ x_2 \\ x_3 \end{Bmatrix} = \begin{Bmatrix} 0 \\ 0 \\ 0 \end{Bmatrix} \tag{4.50}$$

The eigenvalues of the (rank 2) matrix are 3, 1, and 0, and the condition number approaches infinity. This is typical of an unconstrained structural system. Adding the constraint (“boundary value”)

$$x_2 + x_3 = 2 \tag{4.51}$$

permits a unique solution $x_1 = x_2 = x_3 = 1$. Solving the constrained system weakly with boundary weighting factor α yields the system

$$\begin{bmatrix} 1 & -1 & 0 \\ -1 & 2+\alpha & -1+\alpha \\ 0 & -1+\alpha & 1+\alpha \end{bmatrix} \begin{Bmatrix} x_1 \\ x_2 \\ x_3 \end{Bmatrix} = \begin{Bmatrix} 0 \\ 2\alpha \\ 2\alpha \end{Bmatrix} \tag{4.52}$$

For equal boundary and domain integral weighting ($\alpha = 1$), the system matrix (now full rank) has eigenvalues of 3.4, 2, 0.58 and a minimum condition number of 5.83 (for $\alpha \neq 1$). Figure 4.10 shows the dependence of the system condition number on the weighting factor. The condensed form of (4.52) in which the weakly enforced boundary conditions for x_2 and x_3 are condensed yields

$$x_1 = \left[1 - \begin{bmatrix} -1 & 0 \end{bmatrix} \begin{bmatrix} 3 & 0 \\ 0 & 2 \end{bmatrix}^{-1} \begin{bmatrix} -1 \\ 0 \end{bmatrix} \right]^{-1} \left[0 - \begin{bmatrix} -1 & 0 \end{bmatrix} \begin{bmatrix} 3 & 0 \\ 0 & 2 \end{bmatrix}^{-1} \begin{bmatrix} 2 \\ 2 \end{bmatrix} \right] = 1 \tag{4.53}$$

and the recovery of x_2 and x_3 yields

$$\begin{Bmatrix} x_2 \\ x_3 \end{Bmatrix} = \begin{bmatrix} 3 & 0 \\ 0 & 2 \end{bmatrix}^{-1} \left[\begin{bmatrix} 2 \\ 2 \end{bmatrix} - \begin{bmatrix} -1 \\ 0 \end{bmatrix} \{1\} \right] = \begin{Bmatrix} 1 \\ 1 \end{Bmatrix} \quad (4.54)$$

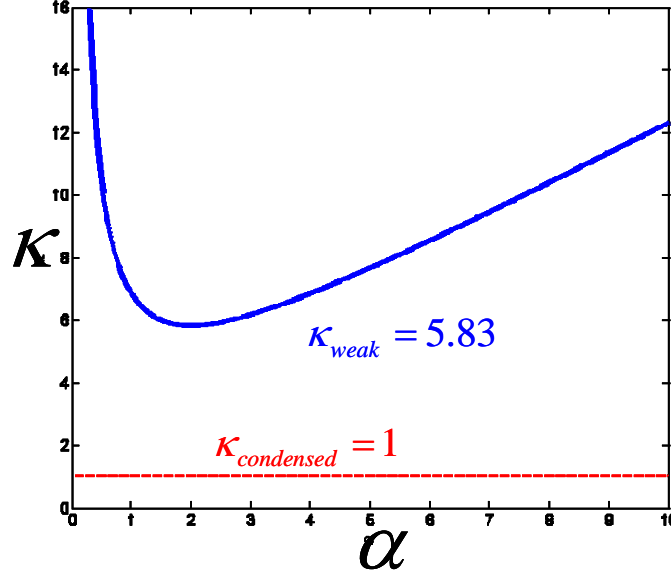


Figure 4.10: Weak and condensed system condition number as a function of boundary weighting factor

Although an improvement in condition number is readily apparent in this simple example, the results for more complex problems are mixed. Furthermore, the condition number of the recovery stiffness matrix should also be considered, since it must be inverted to solve for the weakly-enforced boundary unknowns. In the example above, the recovery matrix condition number is 1.5. Table 4.1 compares the order of magnitude of the condition number of the direct weak system solution, the condensed weak solution, and the recovery matrix for the condensed degrees of freedom for four different example problems. The first two examples are a classic elasticity problem due to Timoshenko and Goodier which is further studied in Section 5.1 with different domain representations and different boundary conditions. In each case, the condition number for both the direct solution of the weak system and the condensed system was on the order of 10^9 to 10^{10} .

Thus no improvement in conditioning is achieved through condensation. The third example is the axially-loaded plate with a circular hole that is studied in Section 5.2. In this case, an improvement of two to three orders of magnitude was achieved by the condensation and recovery approach of the weak boundary conditions. A similar three order of magnitude improvement was realized in a linear potential fluid flow solution about a NACA 0012 airfoil (Section 6.2). Note that these results are based on LSFEM solutions. We also note that increasing the polynomial order of the p -elements in any given problem tended to increase the condition number (this is not apparent in Table 4.1 which only presents result for a single p -value for each problem). It is unknown if other weakly enforced, weighted residual methods would realize similar improvements in condition number through condensation and recovery. This is a potential topic for further research.

Table 4.1: Comparison of weak and condensed condition number order of magnitude for four example problems

$\log(\kappa[\cdot])$	Direct $\kappa(\mathbf{K} + \alpha\mathbf{K}_\Gamma)$	Condensed $\kappa(K_{uu} - K_{uw}K_{ww}^{-1}K_{wu})$	Recovery $\kappa(K_{ww})$
T&G (16 elements, $p = 8$)	10.1	10.1	3.6
T&G (1/4 plate) (16 elements, $p = 8$)	9	9	2.9
Plate w/ a hole (64 elements, $p = 5$)	9.2	6.3	7
NACA 0012 (238 elements, $p = 4$)	5	2	2

In summary, although weak (integral) boundary conditions are simple to state and implement in an LSFEM architecture, they can lead to numerical difficulties due to poorly-conditioned system matrices. Furthermore weak enforcement of boundary

conditions is unavoidable in the fluid-structure interaction problems of current interest. We noted that the condition number was a function of the boundary residual weighting term and that higher-order p -elements result in higher condition numbers. Nevertheless, the condensation of weak boundary degrees of freedom can improve numerical stability when several primary variables are combined in a boundary functional. No change in condition number was observed for “single variable” type boundary conditions. The recovery of weak degrees of freedom is relatively straightforward.

4.5 LSFEM Fluid Models

This section describes five various steady and unsteady LSFEM fluid models that have been implemented and used in subsequent analysis: linear potential flow (4.5.1); compressible potential flow (4.5.2); transient, compressible potential flow (4.5.3); Stokes flow (0); transient, incompressible Euler (4.5.5); and transient, compressible Euler models (4.5.6). All of the fluid models are based on the mass equation

$$\frac{D\rho}{Dt} + \rho \nabla \cdot \mathbf{u} = 0 \quad (4.55)$$

and the momentum equation

$$\rho \frac{D\mathbf{u}}{Dt} = \mathbf{f} + \nabla : \boldsymbol{\sigma}^f \quad (4.56)$$

though they vary in their underlying assumptions. Table 4.2 summarizes the various fluid models, the unknown variables, the underlying assumptions, as well as notes on the properties of the model.

Table 4.2: Summary of fluid model equations, variables, assumptions, and notes

Stokes	Euler		Potential	
	Incompressible	Compressible	Incompressible	Compressible
$\nabla \cdot \mathbf{u} = 0$ $-\mu \nabla^2 \mathbf{u} + \nabla p = \mathbf{f}$	$\nabla \cdot \mathbf{u} = 0$ $\mathbf{u}_t + (\mathbf{u} \cdot \nabla) \mathbf{u} + \nabla p = \mathbf{f}$	$\frac{D\rho}{Dt} + \rho \nabla \cdot \mathbf{u} = 0$ $\mathbf{u}_t + (\mathbf{u} \cdot \nabla) \mathbf{u} + \nabla p = \mathbf{f}$	$\nabla \cdot \mathbf{u} = 0$ $\nabla \times \mathbf{u} = 0$	$\nabla \cdot (\rho \mathbf{u}) = 0$ $\nabla \times \mathbf{u} = 0$
linear steady viscid (creeping flow Re << 1)	nonlinear steady/unsteady inviscid incompressible rotational	nonlinear steady/unsteady inviscid compressible rotational	linear steady inviscid incompressible irrotational	unsteady (FPE) inviscid compressible irrotational
(u, v, p, ω)	(u, v, p, ω)	(u, v, p, ρ)	(u, v)	(u, v, ϕ)
Section 4.5.4	Section 4.5.5	Section 4.5.6	Section 4.5.1	Section 4.5.2 Section 4.5.3

The motivating design problem (the aeroelastic optimization of a long-endurance aerospace platform, Section 1.1) is primarily interested in moderate Mach numbers (approximately 0.3 to 0.7 M). It is assumed that the contribution of viscous effects is negligible compared to the aerodynamic loads encountered in a gust, and thus, that the more physically accurate Navier-Stokes equations which include viscosity are not worth the computational expense and complexity for the current application.

4.5.1 Linear Potential Flow

Linear potential (LP) flow can be modeled by assuming an incompressible and inviscid fluid. Under these assumptions, the mass equation becomes the continuity equation

$$\nabla \cdot \mathbf{u} = 0 \quad \text{in } \Omega^f \quad (4.57)$$

where \mathbf{u} is the fluid velocity vector. The momentum equation may be written

$$\frac{\partial \mathbf{u}}{\partial t} + (\mathbf{u} \cdot \nabla) \mathbf{u} + \nabla p = \mathbf{f} \quad \text{in } \Omega^f \quad (4.58)$$

where p is pressure, and \mathbf{f} is the body force. Under steady conditions with no body forces, the momentum equation reduces to Bernoulli's equation

$$p = p_0 + \frac{1}{2} \rho \mathbf{u} \cdot \mathbf{u} \quad \text{in } \Omega^f \quad (4.59)$$

For irrotational flow, the vorticity, $\boldsymbol{\omega} \equiv \nabla \times \mathbf{u}$, is zero. Thus

$$\nabla \times \mathbf{u} = 0 \quad \text{in } \Omega^f \quad (4.60)$$

In 2D, (4.57) and (4.60) become

$$u_{,x} + v_{,y} = 0 \quad (4.61)$$

and

$$-u_{,y} + v_{,x} = 0 \quad (4.62)$$

which are also the governing equations for a potential flow field governed by Laplace's equation. For $\mathbf{u} = \{u \quad v\}^T$ the matrix operator form is

$$A_0 = \begin{bmatrix} 0 & 0 \\ 0 & 0 \end{bmatrix}, \quad A_1 = \begin{bmatrix} 1 & 0 \\ 0 & 1 \end{bmatrix}, \quad A_2 = \begin{bmatrix} 0 & 1 \\ -1 & 0 \end{bmatrix}, \quad \mathbf{f} = \begin{bmatrix} 0 \\ 0 \end{bmatrix} \quad (4.63)$$

Note that pressure is determined using the fluid velocity solution along with (4.59). The boundary conditions for a surface immersed in potential flow are the no penetration boundary condition

$$\mathbf{u} \cdot \hat{\mathbf{n}} = 0 \quad (4.64)$$

where $\hat{\mathbf{n}}$ is the surface unit normal vector. This is equivalent in 2D to

$$u \cos \theta_n + v \sin \theta_n = 0 \quad (4.65)$$

where θ_n is the surface normal vector angle.

4.5.2 Quasi-Steady Compressible Potential Flow

Quasi-steady compressible potential flow (QSCP) is derived from the transient full potential equation (next section) by assuming negligible effect for the unsteady

terms. Starting from the inviscid form of the momentum equation (4.56) with no body forces is

$$\frac{\partial \mathbf{u}}{\partial t} + (\mathbf{u} \cdot \nabla) \mathbf{u} + \frac{1}{\rho} \nabla p = 0 \quad (4.66)$$

Thompson [126] derives a transient, compressible velocity potential for an inviscid, irrotational fluid from (4.66)

$$\frac{\partial^2 \phi}{\partial t^2} + \frac{\partial}{\partial t} (\nabla \phi)^2 + \frac{1}{2} \nabla \phi \cdot \nabla (\nabla \phi)^2 - a^2 \nabla^2 \phi = 0 \quad (4.67)$$

where a is the speed of sound. As expected, the fluid velocity vector \mathbf{u} is determined by the gradient of the velocity potential

$$\mathbf{u} = \nabla \phi \quad (4.68)$$

Expanding (4.67) for 2D and recognizing that the irrotational condition requires that

$$\nabla \times \mathbf{u} = 0 \Rightarrow -u_{,y} + v_{,x} = 0 \Rightarrow \phi_{,xy} = 0 \quad (4.69)$$

yields

$$\phi_{,tt} + 2\phi_{,x}\phi_{,xt} + 2\phi_{,y}\phi_{,yt} + \phi_{,x}^2\phi_{,xx} + \phi_{,y}^2\phi_{,yy} - a^2\phi_{,xx} - a^2\phi_{,yy} = 0 \quad (4.70)$$

which in the case of the quasi-steady assumption becomes

$$(u^2 - a^2)u_{,x} + (v^2 - a^2)v_{,y} = 0 \quad (4.71)$$

The matrix operator form for the steady, compressible potential system with $\mathbf{u} = \{u, v\}^T$

is then

$$A_0 = \begin{bmatrix} 0 & 0 \\ 0 & 0 \end{bmatrix}, \quad A_1 = \begin{bmatrix} 0 & 1 \\ u^2 - a^2 & 0 \end{bmatrix}, \quad A_2 = \begin{bmatrix} -1 & 0 \\ 0 & v^2 - a^2 \end{bmatrix}, \quad \mathbf{f} = \begin{bmatrix} 0 \\ 0 \end{bmatrix} \quad (4.72)$$

where the first equation is the curl-free constraint (4.69) and the second is steady portion of the compressible potential equation. System (4.72) is nonlinear due to the presence of the u and v terms.

As shown in Section 6.2, the pressure distribution on an airfoil obtained from the nonlinear (4.72) can also be obtained by solving the incompressible, linear potential flow problem and applying the Prandtl-Glauert compressibility correction

$$C_p = \frac{C_{p0}}{\sqrt{1-M_\infty^2}} \quad (4.73)$$

There are more complicated compressibility corrections, *e.g.* the Karman-Tsien correction

$$C_p = \frac{C_{p0}}{\sqrt{1-M_\infty^2} + \left[M_\infty^2 \left(1 + \sqrt{1-M_\infty^2} \right)^{-1} \right] \frac{C_{p0}}{2}} \quad (4.74)$$

and the Laitone correction

$$C_p = \frac{C_{p0}}{\sqrt{1-M_\infty^2} + \left[M_\infty^2 \frac{\left(1 + \frac{\gamma-1}{2} M_\infty^2 \right)}{2\sqrt{1-M_\infty^2}} \right] C_{p0}} \quad (4.75)$$

which produce better correlations with experimental data in transonic regions, but the Prandtl-Glauert correction is probably sufficient for the applications of current interest. A comparison of compressible potential and linear potential corrected for compressibility is given in Chapter 6.

It is worth noting that under the assumption of incompressibility, $a \rightarrow \infty$, and the transient, compressible potential equation (4.67) reduces to Laplace's equation

$$\nabla^2 \phi = 0 \quad (4.76)$$

which can be solved by the formulation in Section 4.5.1. Thus, a mathematically-motivated strategy for solving the transient, compressible potential flow problem is to solve the steady linear potential problem and apply one of the compressibility corrections

(4.73)-(4.75) for the desired Mach number. For transient FSI problems where a structure surface may have a velocity, the surface boundary condition for the flow is

$$\mathbf{u} = \mathbf{v}^s \quad (4.77)$$

where \mathbf{v}^s is the surface velocity vector; reference (4.174).

4.5.3 Transient, Compressible Potential Flow

Both the linear potential and quasi-steady compressible potential formulations only required the velocity components as problem variables. Due to the presence of the temporal derivatives of the velocity potential in (4.70), a transient, compressible formulation also requires the potential function as a variable. Thus, the equations for a transient, full potential equation (FPE) with compressibility flow formulation are

$$u = \phi_{,x} \quad (4.78)$$

$$v = \phi_{,y} \quad (4.79)$$

$$\begin{aligned} \frac{1}{(\Delta t)^2} \phi_k^n + \frac{2u_{k-1}^n}{\Delta t} u_k^n + \frac{2v_{k-1}^n}{\Delta t} v_k^n + \left((u_{k-1}^n)^2 - a^2 \right) u_{,x}^n + \left((v_{k-1}^n)^2 - a^2 \right) v_{,y}^n = \\ \frac{2}{(\Delta t)^2} \phi^{n-1} - \frac{1}{(\Delta t)^2} \phi^{n-2} + \frac{2u^{n-1}}{\Delta t} u^{n-1} + \frac{2v^{n-1}}{\Delta t} v^{n-1} \end{aligned} \quad (4.80)$$

where the velocity time derivatives have been discretized using a first-order, backward difference Euler scheme, and the second temporal derivative of ϕ is approximated by

$$\phi_{,tt}^n \approx (\Delta t)^{-2} (\phi^n - 2\phi^{n-1} + \phi^{n-2}) \quad (4.81)$$

where the superscripts denote the solution at prior time intervals. Equation (4.80) is based on a direct substitution linearization. It is also possible to apply a Newton linearization to (4.70) which yields

$$\begin{aligned}
& \frac{1}{(\Delta t)^2} \phi_k^n + 2 \frac{1}{\Delta t} [2u_{k-1}^n - u_k^{n-1}] u_k^n + 2 \frac{1}{\Delta t} [2v_{k-1}^n - v_k^{n-1}] v_k^n + [2u_{k-1}^n [u_{,x}^n]_{k-1}] u_k^n + \dots \\
& \left[(u_{k-1}^n)^2 - a^2 \right] [u_{,x}^n]_k + [2v_{k-1}^n [v_{,y}^n]_{k-1}] v_k^n + \left[(v_{k-1}^n)^2 - a^2 \right] [v_{,y}^n]_k = \\
& \frac{1}{(\Delta t)^2} (2\phi_k^{n-1} - \phi_k^{n-2}) + 2 \frac{1}{\Delta t} (u_{k-1}^n)^2 + 2 \frac{1}{\Delta t} (v_{k-1}^n)^2 + 2 (u_{k-1}^n)^2 [u_{,x}^n]_{k-1} + 2 (v_{k-1}^n)^2 [v_{,y}^n]_{k-1}
\end{aligned} \tag{4.82}$$

A Newton linearization generally converges faster but has a smaller region of convergence than the direct substitution linearization. In the airfoil examples considered in Chapter 6, the direct substitution yields better results in the vicinity of the leading edge than the Newton linearized form.

In addition to (4.78)-(4.80) {or (4.82)}, the irrotational assumption must be enforced. This is done with the additional, curl-free constraint equation (4.69). This leads to an over-constrained, three-variable formulation for the full potential equations, which in matrix-operator form, is

$$\begin{aligned}
A_0^f &= \begin{bmatrix} 0 & \alpha_\phi & 0 \\ 0 & 0 & \alpha_\phi \\ 0 & 0 & 0 \\ (\Delta t)^{-2} & \frac{2}{\Delta t} u_{k-1} & \frac{2}{\Delta t} v_{k-1} \end{bmatrix}, \quad A_1^f = \begin{bmatrix} -\alpha_\phi & 0 & 0 \\ 0 & 0 & 0 \\ 0 & 0 & 1 \\ 0 & u_{k-1}^2 - a^2 & 0 \end{bmatrix}, \\
A_2^f &= \begin{bmatrix} 0 & 0 & 0 \\ -\alpha_\phi & 0 & 0 \\ 0 & -1 & 0 \\ 0 & 0 & v_{k-1}^2 - a^2 \end{bmatrix}, \quad \mathbf{f}^f = \begin{bmatrix} 0 \\ 0 \\ 0 \\ \frac{1}{(\Delta t)^2} (2\phi^{n-1} - \phi^{n-2}) + \frac{2}{\Delta t} (u^{n-1})^2 + \frac{2}{\Delta t} (v^{n-1})^2 \end{bmatrix}
\end{aligned} \tag{4.83}$$

for the vector $\mathbf{u} = \{\phi \ u \ v\}^T$. Note the presence of the equation-level weighting factor, α_ϕ in (4.83). This weighting factor ($\alpha_\phi \approx 10^{-4}$) is necessary to produce good LSFEM results for this system. Equation (4.83) is based on the direct linearization. The equivalent expression based on a Newton linearization is

$$\begin{aligned}
\mathbf{A}_0 &= \begin{bmatrix} 0 & \alpha_\phi & 0 \\ 0 & 0 & \alpha_\phi \\ 0 & 0 & 0 \\ \frac{1}{(\Delta t)^2} & 2\frac{1}{\Delta t}[2u_{k-1}^n - u_k^{n-1}] + 2u_{k-1}^n[u_{,x}^n]_{k-1} & 2\frac{1}{\Delta t}[2v_{k-1}^n - v_k^{n-1}] + 2v_{k-1}^n[v_{,y}^n]_{k-1} \end{bmatrix} \\
\mathbf{A}_1 &= \begin{bmatrix} -\alpha_\phi & 0 & 0 \\ 0 & 0 & 0 \\ 0 & 0 & 1 \\ 0 & (u_{k-1}^n)^2 - a^2 & 0 \end{bmatrix} \quad \mathbf{A}_2 = \begin{bmatrix} 0 & 0 & 0 \\ -\alpha_\phi & 0 & 0 \\ 0 & -1 & 0 \\ 0 & 0 & (v_{k-1}^n)^2 - a^2 \end{bmatrix} \\
\mathbf{f} &= \begin{bmatrix} 0 \\ 0 \\ 0 \\ \frac{1}{(\Delta t)^2}(2\phi_k^{n-1} - \phi_k^{n-2}) + 2\frac{1}{\Delta t}[(u_{k-1}^n)^2 + (v_{k-1}^n)^2] + 2(u_{k-1}^n)^2[u_{,x}^n]_{k-1} + 2(v_{k-1}^n)^2[v_{,y}^n]_{k-1} \end{bmatrix}
\end{aligned} \tag{4.84}$$

Equations (4.83) and (4.84) are the transient full potential equations. In practice, the unsteady terms in both (4.83) and (4.84) are negligible for the vertical movement of immersed objects at even moderate speeds. For example, for the plunging sphere in Figure 4.11 in which the sphere is moving vertically at one-half the free stream velocity, the unsteady terms in the direct substitution form of the transient FPE, (4.83), are more than two orders of magnitude smaller than the other terms in the differential operator. This is not entirely surprising since the usual application of unsteady aerodynamics is to problems exhibiting high frequency or instantaneous starting or stopping of flow conditions. The discrete gust models explored in the FSI examples in Chapter 7 are at relative gust velocities less than the one-half free-stream plunge velocity in Figure 4.11. Thus, the unsteady terms of the transient FPE may be neglected and the fluid problem can be solved as a quasi-steady problem using the QSCP formulation from Section 4.5.2. Figure 4.12 compares the velocity components and pressure coefficient for the transient

FPE and QSCP flow solutions for the plunging sphere. Since the QSCP formulation does not have to calculate the potential function, ϕ , the computational expense of the transient flow solution can be reduced by one-third by using the QSCP formulation in lieu of the FPE formulation. Additional transient, compressible FSI results are presented in Chapter 7.

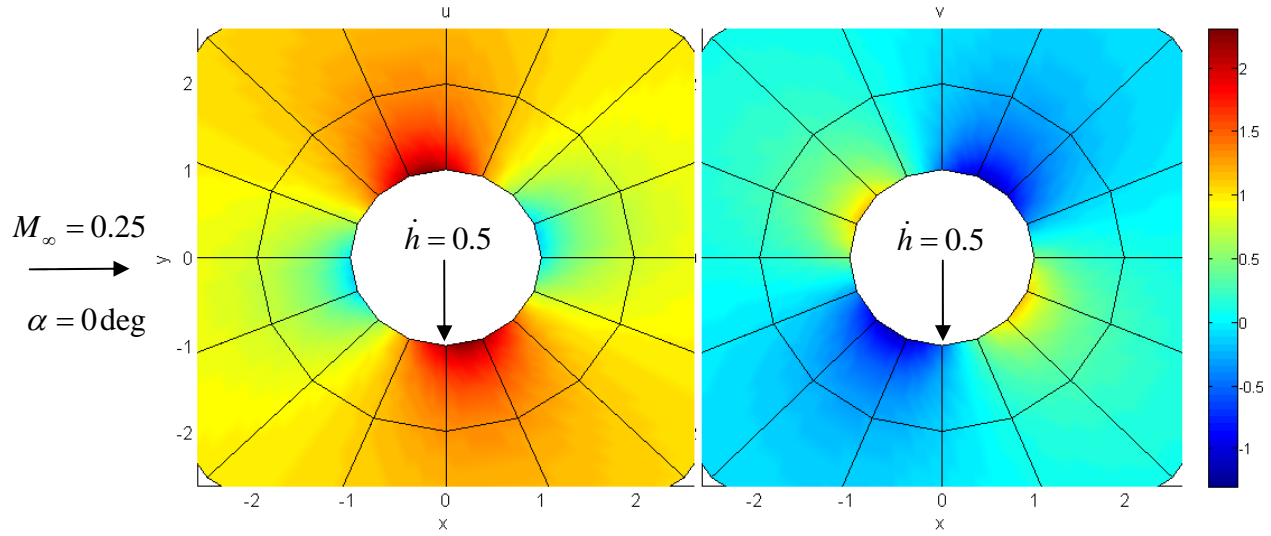


Figure 4.11: Plunging sphere compressible flow velocity components solution for 0.25 M ($\alpha_{effective} = 30deg$, peak shoulder velocity is 0.57 M)

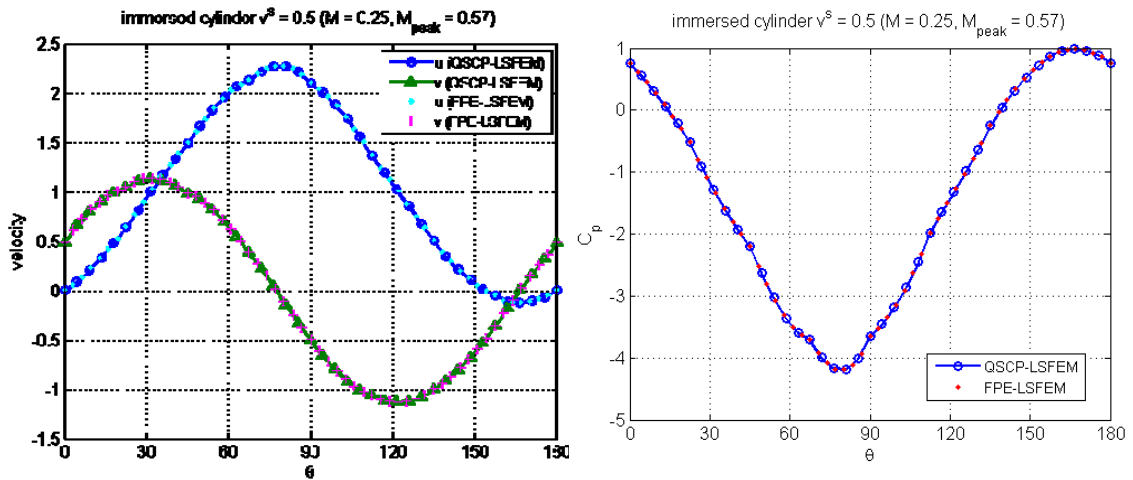


Figure 4.12: Comparison of quasi-steady compressible and full potential flow for LSFEM solution to plunging cylinder validation problem; velocity components (*left*) and pressure coefficient (*right*).

4.5.4 Stokes Equations

Though the Stokes equations are physically valid only for very low Reynolds numbers (high viscosity/low velocity—“creeping flow”), they are sometimes used for initializing the flow for more complicated models (which improves initial convergence). The Stokes equations are a set of linear equations which permitted straightforward solutions for developing and validating FSI and CSE methods without the complexity of nonlinear terms which would contribute little further understanding.

In creeping flow, originally developed by Stokes c. 1851, the fluid inertial forces are considered negligible relative to the viscous forces ($Re \ll 1$). Thus there are no acceleration terms in the momentum equation and it is valid to consider only steady-state conditions. The Stokes equations in basic form are [133]

$$\begin{aligned} -\mu \nabla^2 \mathbf{u} + \nabla p &= \mathbf{f} & \text{in } \Omega \\ \nabla \mathbf{u} &= 0 & \text{in } \Omega \end{aligned} \quad (4.85)$$

where μ is viscosity, \mathbf{u} is the fluid velocity vector, p is pressure, and \mathbf{f} are the body forces.

To implement (4.85) using LSFEM, it is convenient to introduce vorticity, $\boldsymbol{\omega} \equiv \nabla \times \mathbf{u}$, and express (4.85) as a div-curl system [69]

$$\begin{aligned} \nabla p + \mu \nabla \times \boldsymbol{\omega} &= \mathbf{f} & \text{in } \Omega \\ \nabla \cdot \boldsymbol{\omega} &= 0 & \text{in } \Omega \\ \boldsymbol{\omega} - \nabla \times \mathbf{u} &= \mathbf{0} & \text{in } \Omega \\ \nabla \cdot \mathbf{u} &= 0 & \text{in } \Omega \end{aligned} \quad (4.86)$$

which is now a first-order system and practical for LSFEM. In two dimensions vorticity is a scalar, $\omega \equiv u_{,y} + v_{,x}$, and (4.86) in component form is

$$\begin{aligned}
p_{,x} + \mu\omega_{,y} &= f_x & \text{in } \Omega \\
p_{,y} - \mu\omega_{,x} &= f_y & \text{in } \Omega \\
u_{,x} + v_{,y} &= 0 & \text{in } \Omega \\
\omega + u_{,y} - v_{,x} &= 0 & \text{in } \Omega
\end{aligned} \tag{4.87}$$

which in matrix-operator form with $\mathbf{u} = \{u \ v \ p \ \omega\}^T$ is

$$A_0 \mathbf{u} + A_1 \mathbf{u}_{,x} + A_2 \mathbf{u}_{,y} = \mathbf{f} \tag{4.88}$$

where

$$A_0 = \begin{bmatrix} 0 & 0 & 0 & 0 \\ 0 & 0 & 0 & 0 \\ 0 & 0 & 0 & 0 \\ 0 & 0 & 0 & 1 \end{bmatrix} \quad A_1 = \begin{bmatrix} 1 & 0 & 0 & 0 \\ 0 & 0 & 1 & 0 \\ 0 & 0 & 0 & -\mu \\ 0 & -1 & 0 & 0 \end{bmatrix} \quad A_2 = \begin{bmatrix} 0 & 1 & 0 & 0 \\ 0 & 0 & 0 & \mu \\ 0 & 0 & 1 & 0 \\ 1 & 0 & 0 & 0 \end{bmatrix} \quad \mathbf{f} = \begin{bmatrix} 0 \\ f_x \\ f_y \\ 0 \end{bmatrix} \tag{4.89}$$

The appropriate boundary condition combinations for (4.86) are either 1) p and $\mathbf{n} \cdot \boldsymbol{\omega}$ or 2) $\mathbf{n} \times \boldsymbol{\omega}$ (see [69] 8.2.2). For two dimensions, these two sets of boundary conditions reduce to the combinations given in Table 4.3.

Table 4.3: Boundary condition combinations for the Stokes equations [69]

Description	Boundary Condition
Inlet	$\mathbf{n} \cdot \mathbf{u}$ and ω
Inlet	$\mathbf{n} \cdot \mathbf{u}$ and p
Outlet	$\mathbf{n} \times \mathbf{u}$ and p
Uniform outflow	$\mathbf{n} \times \mathbf{u}$ and ω
Wall	$\mathbf{n} \times \mathbf{u}$ and $\mathbf{n} \cdot \mathbf{u}$
Outlet (portion of Γ only)	p and ω

4.5.5 Transient, Incompressible Euler

Jiang [69] derives a transient, incompressible fluid formulation from the momentum and continuity equations. The 2D first-order equations are from the incompressibility relation

$$\nabla \cdot \mathbf{u} = 0 \quad (4.90)$$

the momentum equation

$$\mathbf{u}_{,t} + (\mathbf{u} \cdot \nabla) \mathbf{u} + \nabla p = \mathbf{f} \quad (4.91)$$

the 2D definition of vorticity

$$\omega \equiv -u_{,y} + v_{,x} \quad (4.92)$$

and a vorticity transport term that allows for transient treatment of rotating flow

$$\omega_{,t} + \mathbf{u} \cdot \nabla \omega = 0 \quad (4.93)$$

Jiang's technique is to discretize first in time using backward Euler finite-difference and use direct substitution for nonlinear terms. Under this, (4.90)-(4.93) become

$$\begin{aligned} u_{,x}^{n+1} + v_{,y}^{n+1} &= 0 \\ \frac{1}{\Delta t} u^{n+1} - \frac{1}{\Delta t} u^n + u^n u_{,x}^{n+1} + v^n u_{,y}^{n+1} + p_{,x}^{n+1} &= f_x^{n+1} \\ \frac{1}{\Delta t} v^{n+1} - \frac{1}{\Delta t} v^n + u^n v_{,x}^{n+1} + v^n v_{,y}^{n+1} + p_{,y}^{n+1} &= f_y^{n+1} \\ u_{,y}^{n+1} - v_{,x}^{n+1} + \omega^{n+1} &= 0 \\ \frac{1}{\Delta t} \omega^{n+1} - \frac{1}{\Delta t} \omega^n + u^n \omega_{,x}^{n+1} + v^n \omega_{,y}^{n+1} &= 0 \end{aligned} \quad (4.94)$$

and the first-order (nonlinear) operator form is

$$A_0^f(\mathbf{u}^n) \mathbf{u}^{n+1} + A_1^f(\mathbf{u}^n) \mathbf{u}_{,x}^{n+1} + A_2^f(\mathbf{u}^n) \mathbf{u}_{,y}^{n+1} = \mathbf{f}(\mathbf{u}^n) \quad (4.95)$$

with operator matrices

$$\begin{aligned}
A_0^f(\mathbf{u}^n) &= \begin{bmatrix} 0 & 0 & 0 & 0 \\ 1/\Delta t & 0 & 0 & 0 \\ 0 & 1/\Delta t & 0 & 0 \\ 0 & 0 & 0 & 1 \\ 0 & 0 & 0 & 1/\Delta t \end{bmatrix} & A_1^f(\mathbf{u}^n) &= \begin{bmatrix} 1 & 0 & 0 & 0 \\ u^n & 0 & 1 & 0 \\ 0 & u^n & 0 & 0 \\ 0 & -1 & 0 & 0 \\ 0 & 0 & 0 & u^n \end{bmatrix} \\
A_2^f(\mathbf{u}^n) &= \begin{bmatrix} 0 & 1 & 0 & 0 \\ v^n & 0 & 0 & 0 \\ 0 & v^n & 1 & 0 \\ 1 & 0 & 0 & 0 \\ 0 & 0 & 0 & v^n \end{bmatrix} & \mathbf{f}^f(\mathbf{u}^n) &= \begin{bmatrix} 0 \\ u^n/\Delta t + f_x^{n+1} \\ v^n/\Delta t + f_y^{n+1} \\ 0 \\ \omega^n/\Delta t \end{bmatrix}
\end{aligned} \tag{4.96}$$

An example of a steady fluid solution using this formulation for the flow about a sphere is given in Figure 4.13 and compared with the theoretical solution in Figure 4.14.

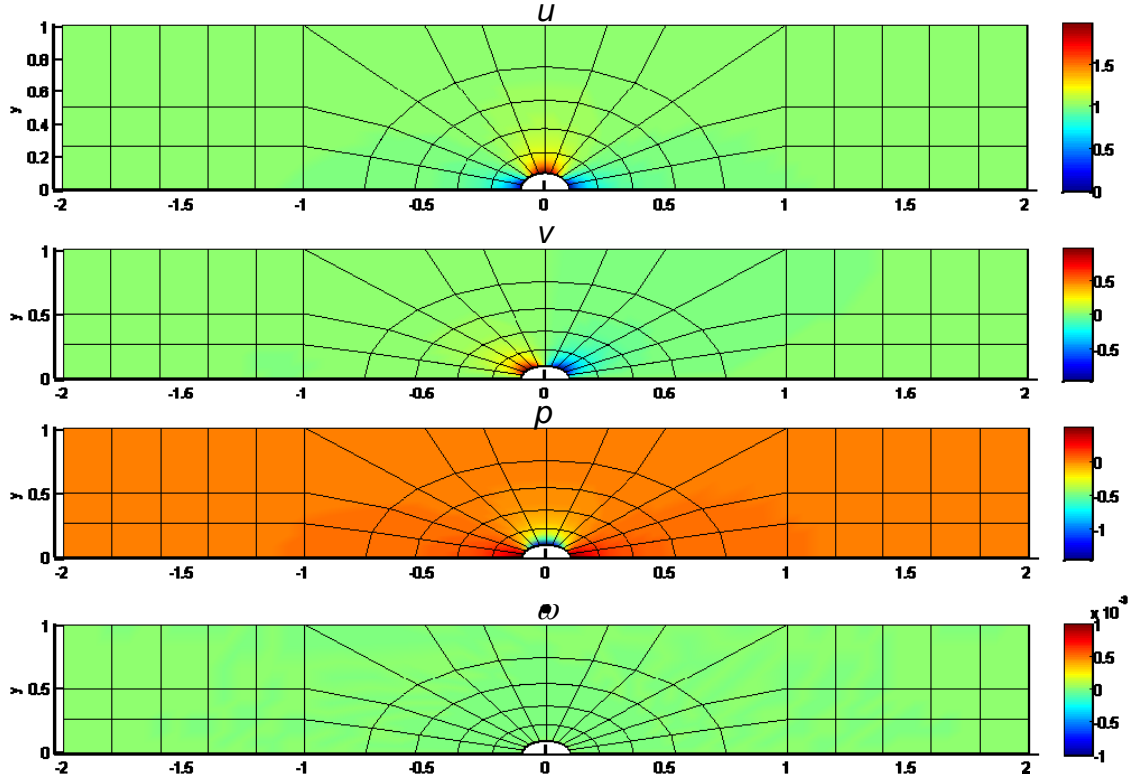


Figure 4.13: LSFEM solution of steady, incompressible Euler flow about a sphere ($p = 8$)

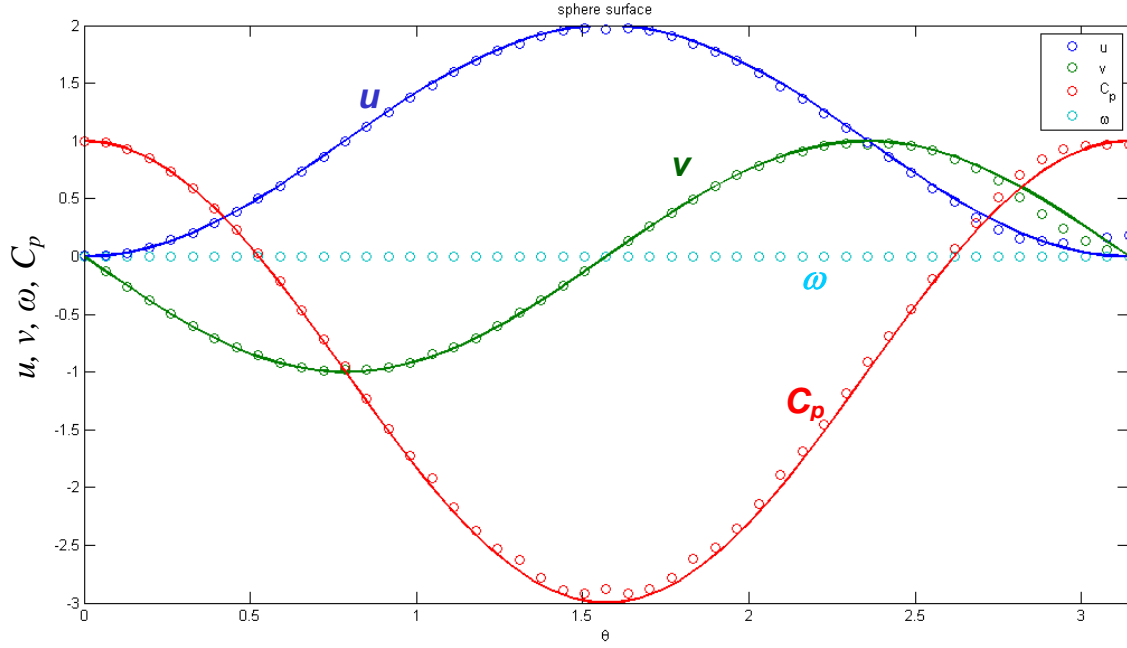


Figure 4.14: Comparison of LSFEM solution with theoretical solution (solid lines) for steady, incompressible Euler flow about a sphere

4.5.6 Transient, Compressible Euler

Neglecting body forces, a compressible Newtonian fluid is governed by the continuity and momentum equations,

$$\frac{D\rho}{Dt} + \rho \nabla \cdot \mathbf{V} = 0 \quad (4.97)$$

$$\nabla : \boldsymbol{\sigma}^f - \rho \frac{D\mathbf{V}}{Dt} = 0 \quad (4.98)$$

where ρ is density, $\boldsymbol{\sigma}^f$ is the fluid stress tensor, and $\mathbf{V} = [u \ v]^T$ is the velocity vector. If

viscous shear forces are neglected then $\sigma_{ij}^f = -p\delta_{ij}$ where p is pressure and δ_{ij} is the

Kronecker delta. These assumptions with the equation of state for an ideal fluid yield the

2D compressible Euler equations in first-order form

$$\begin{aligned}
\rho_{,t} + u\rho_{,x} + v\rho_{,y} + \rho u_{,x} + \rho v_{,y} &= 0 \\
u_{,t} + (u+v)u_{,x} + p_{,x}/\rho &= 0 \\
v_{,t} + (u+v)v_{,y} + p_{,y}/\rho &= 0 \\
p_{,t} + \gamma p(u_{,x} + v_{,y}) + up_{,x} + vp_{,y} &= 0
\end{aligned} \tag{4.99}$$

where γ is the ratio of specific heats. Equation (4.99) in matrix-operator form is

$$A_t^f \mathbf{u}_{,t}^f + A_0^f \mathbf{u}^f + A_1^f \mathbf{u}_{,x}^f + A_2^f \mathbf{u}_{,y}^f = \mathbf{f}^f \tag{4.100}$$

where

$$\begin{aligned}
A_t^f &= \begin{bmatrix} 1 & 0 & 0 & 0 \\ 0 & 1 & 0 & 0 \\ 0 & 0 & 1 & 0 \\ 0 & 0 & 0 & 1 \end{bmatrix} & A_0^f &= \begin{bmatrix} 0 & 0 & 0 & 0 \\ 0 & 0 & 0 & 0 \\ 0 & 0 & 0 & 0 \\ 0 & 0 & 0 & 0 \end{bmatrix} \\
A_1^f &= \begin{bmatrix} u & \rho & 0 & 0 \\ 0 & u & 0 & 1/\rho \\ 0 & 0 & u & 0 \\ 0 & \gamma p & 0 & u \end{bmatrix} & A_2^f &= \begin{bmatrix} v & 0 & \rho & 0 \\ 0 & v & 0 & 0 \\ 0 & 0 & v & 1/\rho \\ 0 & 0 & \gamma p & v \end{bmatrix} & \mathbf{f}^f &= \begin{bmatrix} 0 \\ 0 \\ 0 \\ 0 \end{bmatrix}
\end{aligned} \tag{4.101}$$

$\mathbf{u}^f = [\rho \quad u \quad v \quad p]^T$ is the vector of primitive fluid variables.

4.6 Structural Elasticity Models

This section describes two LSFEM structural models that are used in subsequent analysis: 2D plane stress elasticity and the 1D Euler-Bernoulli beam. The three general classes of 2D elasticity formulations for LSFEM were discussed in Section 2.4.2.2. Though not elliptic, the five-variable plane-stress stress-displacement form is the most convenient for our purposes. The presence of the stress tensor components as degrees of freedom allows for direct coupling with the fluid stresses without the need for intermediate variables or transformations. Additionally, stress is often an important

analysis and design variable and thus it is useful to have the stress tensor as a primary variable in the CSE formulation.

The 1D Euler-Bernoulli (E-B) beam is introduced for its simplicity and the wide variety of analytic solutions that are possible without the complications of dealing with second-order tensors [104]. Example problems for both FSI and CSE system are solved using the E-B beam as a straightforward test and validation tool in the course of method development.

4.6.1 Plane Stress (u - σ formulation)

The non-elliptic, mixed stress-displacement formulation requires the minimum number of degrees of freedom (five) to formulate a first-order approximation for the 2D elasticity equations. The plane elasticity mixed stress-displacement unknowns are the three components of the stress tensor, σ_{ij} , and the two components of the displacement vector, u and v . The 2D kinematic relations for elasticity relate the strain tensor components, ε_{ij} , to the gradients of the displacement

$$\begin{aligned}\varepsilon_{xx} &= u_{,x} \\ \varepsilon_{yy} &= v_{,y} \\ \varepsilon_{xy} &= \frac{1}{2}(u_{,y} + v_{,x})\end{aligned}\tag{4.102}$$

Assuming a plane-stress state and substituting (4.102) into the constitutive relation for isotropic Hookean strain

$$\begin{bmatrix} \sigma_{xx} \\ \sigma_{yy} \\ \sigma_{xy} \end{bmatrix} = \frac{E}{1-\nu^2} \begin{bmatrix} 1 & \nu & 0 \\ \nu & 1 & 0 \\ 0 & 0 & \frac{1}{2}(1-\nu) \end{bmatrix} \begin{bmatrix} \varepsilon_{xx} \\ \varepsilon_{yy} \\ \varepsilon_{xy} \end{bmatrix}\tag{4.103}$$

yields three equations relating stress and displacements

$$\begin{aligned}
\sigma_{xx} &= \frac{E}{1-\nu^2} [u_{,x} + \nu v_{,y}] \\
\sigma_{yy} &= \frac{E}{1-\nu^2} [\nu u_{,x} + v_{,y}] \\
\sigma_{xy} &= \frac{E}{2(1+\nu)} [u_{,y} + v_{,x}]
\end{aligned} \tag{4.104}$$

The two components of the equilibrium equations give the final two equations

$$\begin{aligned}
-\rho u_{,tt} + \sigma_{xx,x} + \sigma_{xy,y} &= -f_x \\
-\rho v_{,tt} + \sigma_{yy,y} + \sigma_{xy,x} &= -f_y
\end{aligned} \tag{4.105}$$

Thus, the 2D plane stress stress-displacement first-order system in matrix-operator form is

$$A_t^s \mathbf{u}_{,tt}^s + A_0^s \mathbf{u}^s + A_1^s \mathbf{u}_{,x}^s + A_2^s \mathbf{u}_{,y}^s = \mathbf{f}^s \tag{4.106}$$

where

$$\begin{aligned}
A_t^s &= \begin{bmatrix} 0 & 0 & 0 & 0 & 0 \\ 0 & 0 & 0 & 0 & 0 \\ 0 & 0 & 0 & 0 & 0 \\ -\rho^s & 0 & 0 & 0 & 0 \\ 0 & -\rho^s & 0 & 0 & 0 \end{bmatrix} & A_0^s &= \begin{bmatrix} 0 & 0 & 1 & 0 & 0 \\ 0 & 0 & 0 & 1 & 0 \\ 0 & 0 & 0 & 0 & 1 \\ 0 & 0 & 0 & 0 & 0 \\ 0 & 0 & 0 & 0 & 0 \end{bmatrix} \\
A_1^s &= \begin{bmatrix} \frac{-E}{1-\nu^2} & 0 & 0 & 0 & 0 \\ \frac{-\nu E}{1-\nu^2} & 0 & 0 & 0 & 0 \\ 0 & \frac{-E}{2(1+\nu)} & 0 & 0 & 0 \\ 0 & 0 & 1 & 0 & 0 \\ 0 & 0 & 0 & 0 & 1 \end{bmatrix} & A_2^s &= \begin{bmatrix} 0 & \frac{-\nu E}{1-\nu^2} & 0 & 0 & 0 \\ 0 & \frac{-E}{1-\nu^2} & 0 & 0 & 0 \\ \frac{-E}{2(1+\nu)} & 0 & 0 & 0 & 0 \\ 0 & 0 & 0 & 0 & 1 \\ 0 & 0 & 0 & 1 & 0 \end{bmatrix} & \mathbf{f}^s &= \begin{bmatrix} 0 \\ 0 \\ 0 \\ -f_x \\ -f_y \end{bmatrix}
\end{aligned} \tag{4.107}$$

where $\mathbf{u}^s = [u \quad v \quad \sigma_{xx} \quad \sigma_{yy} \quad \sigma_{xy}]^T$. The s superscripts are introduced to denote structure domain variables and distinguish them from fluid domain variables in the coupled FSI system.

Note that formulation (4.107) has an odd number of variables and thus can no longer be elliptic, even though elasticity systems are elliptic in nature. Additionally, this formulation is not coercive in H^1 . The selection of this formulation for LSFEM is based primarily on the minimum number of degrees of freedom required and the presence of the stress tensor allowing direct access to traction boundary conditions and stress sensitivity. Less than optimal convergence properties of the LSFEM solution can be expected due to the destruction of ellipticity and the lack of coercivity and are somewhat mitigated by using higher-order p -type elements.

4.6.2 Steady, Linear Euler-Bernoulli Beam

The governing equation for the deflection, v , of an Euler-Bernoulli beam subject to a transverse load per unit length, p_y , is

$$\frac{\partial^2}{\partial x^2} \left(EI \frac{\partial^2 v}{\partial x^2} \right) = p_y \quad (4.108)$$

Introducing

$$\theta = v_{,x} \quad (4.109)$$

$$M_z = EI v_{,xx} = \theta_{,x} \quad (4.110)$$

$$V_y = -M_{z,x} \quad (4.111)$$

where θ is the beam slope, M_z is the internal bending moment, and V_y is the internal shear force allows decomposition of (4.108) into first-order form

$$A_0 \mathbf{u} + A_1 \mathbf{u}_{,x} = \mathbf{f} \quad (4.112)$$

where $\mathbf{u} = \begin{bmatrix} v & \theta & M_z & V_y \end{bmatrix}^T$ and the matrix-operators are

$$A_0 = \begin{bmatrix} 0 & 1 & 0 & 0 \\ 0 & 0 & 1/EI & 0 \\ 0 & 0 & 0 & -1 \\ 0 & 0 & 0 & 0 \end{bmatrix} \quad A_1 = \begin{bmatrix} -1 & 0 & 0 & 0 \\ 0 & -1 & 0 & 0 \\ 0 & 0 & -1 & 0 \\ 0 & 0 & 0 & -1 \end{bmatrix} \quad \mathbf{f} = \begin{bmatrix} 0 \\ 0 \\ 0 \\ P_y \end{bmatrix} \quad (4.113)$$

4.6.3 Transient, Nonlinear Euler-Bernoulli Beam

One of the fluid-structure interaction problems considered later is an airfoil mounted at the tip of a flexible sting. The sting is modeled as a nonlinear Euler-Bernoulli beam where the nonlinear von Karman strain relations account for possible large deflections of the beam. The nonlinear formulation is a total Lagrangian description in which the forces and strains are referenced to the undeformed configuration. Nonlinear Green strain terms are incorporated to model large transverse deflection of the beam. The derivation is based the nonlinear bending of straight beams from [106]. We assume large transverse displacements, moderate rotations, and relatively small axial strains in accordance with the assumptions of [106]. Additionally, the Euler-Bernoulli beam assumption that plane sections remain plane after deformation, equivalent to neglecting the Poisson effect and transverse strains, is also allowed for the long, slender sting in this problem. Because the changes in geometry (specifically, the cross-sectional area of the beam) are small, the distinction between the Piola-Lagrange stress (which expresses forces in the deformed configuration to areas in the reference configuration) and the Cauchy stress (which expresses forces of the deformed configuration to areas in the deformed configuration) is not necessary [106]. A modification to the derived equations which does make the distinction between the Piola-Lagrange and Cauchy stress is

presented at the end of this section. The force and free-body diagram of the beam is given in Figure 4.15.

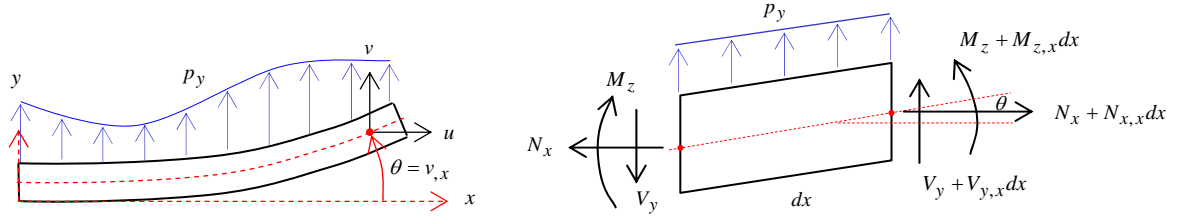


Figure 4.15: Beam free-body diagram

With the Euler-Bernoulli assumption, the angle of rotation and the internal bending moment are given by

$$\theta = v_{,x} \quad (4.114)$$

$$M_z = EI\theta \quad (4.115)$$

where v is the vertical (transverse) displacement, and the product of Young's modulus, E , and the moment of inertia, I , is the effective bending stiffness of the beam. The axial force, N_x , at any cross section of the beam is given by

$$N_x = \int_A \sigma_{xx} dA \quad (4.116)$$

where σ_{xx} is the normal stress and A is the cross sectional area of the beam. Summing the moments about the z -axis yields

$$M_{z,x} + V_y - N_x \theta = 0 \quad (4.117)$$

The nonlinear von Karman strain-displacement relation [106] is

$$\varepsilon_{ij} = \frac{1}{2}(u_{i,j} + u_{j,i}) + \frac{1}{2}(u_{m,i}u_{m,j}) \quad (4.118)$$

which, assuming $u_{,x}^2 \ll u_{,x}$ and $u_{,x}^2 \ll v_{,x}^2$, becomes for the axial dimension

$$\varepsilon_{xx} = u_{,x} + \frac{1}{2} v_{,x}^2 = u_{,x} + \frac{1}{2} \theta^2 \quad (4.119)$$

Spar buckling due to axial compression is a possible failure mode of joined wing configurations. Including an axial tip load, P_{tip} , then the von Karman strain together with the constitutive equation

$$\sigma_{xx} = E\varepsilon_{xx} \quad (4.120)$$

yields the nonlinear relationship between tip load, shear, bending moment, and rotation

$$M_{z,x} + V_y - P_{tip} \theta - \frac{EA}{2} \theta^3 = 0 \quad (4.121)$$

If there are no axial loads (so that the beam is inextensible beam and $u_{,x} = 0$), (4.121)

reduces to

$$M_{z,x} + V_y - \frac{EA}{2} \theta^3 = 0 \quad (4.122)$$

Note that V_y is the shear force perpendicular to the x -axis. The shear force, Q , perpendicular to the neutral axis of the deformed beam is given by

$$Q = -V_y + \frac{EA}{2} \theta^3 \quad (4.123)$$

Finally, summing the forces in the y -direction yields the final equation governing the beam dynamics

$$\rho_y \frac{\partial^2 v}{\partial t^2} - V_{y,x} = p_y \quad (4.124)$$

where ρ_y is the mass per unit length of the sting and p_y is the transverse load per unit length. Substituting (4.122) and (4.115) into (4.124) yields the nonlinear governing equation large deflections, v , of the sting subject only to a transverse load

$$\rho_y \frac{\partial^2 v}{\partial t^2} + \frac{\partial^2}{\partial x^2} \left(EI \frac{\partial^2 v}{\partial x^2} \right) - \frac{\partial}{\partial x} \left[\frac{EA}{2} \left(\frac{\partial v}{\partial x} \right)^3 \right] = p_y \quad (4.125)$$

The nonlinear beam system in first-order matrix operator form is

$$A_t \mathbf{u}_{,t} + A_0 \mathbf{u} + A_1 \mathbf{u}_{,x} = \mathbf{f} \quad (4.126)$$

where $\mathbf{u} = [v \quad \theta \quad M_z \quad V_y \quad \dot{v}]^T$ and the matrix operators (including an axial tip load)

are

$$A_t = \begin{bmatrix} 0 & 0 & 0 & 0 & 0 \\ 0 & 0 & 0 & 0 & 0 \\ 0 & 0 & 0 & 0 & 0 \\ 0 & 0 & 0 & 0 & \rho_y \\ 1 & 0 & 0 & 0 & 0 \end{bmatrix} \quad A_0 = \begin{bmatrix} 0 & 1 & 0 & 0 & 0 \\ 0 & 0 & 1/EI & 0 & 0 \\ 0 & P_{tip} + \frac{1}{2}EA\theta^2 & 0 & -1 & 0 \\ 0 & 0 & 0 & 0 & 0 \\ 0 & 0 & 0 & 0 & -1 \end{bmatrix} \quad A_1 = \begin{bmatrix} -1 & 0 & 0 & 0 & 0 \\ 0 & -1 & 0 & 0 & 0 \\ 0 & 0 & -1 & 0 & 0 \\ 0 & 0 & 0 & 1 & 0 \\ 0 & 0 & 0 & 0 & 0 \end{bmatrix} \quad \mathbf{f} = \begin{bmatrix} 0 \\ 0 \\ 0 \\ p_y \\ 0 \end{bmatrix} \quad (4.127)$$

The system of continuous sensitivity equations is formed by differentiating (4.114), (4.115), (4.121), and (4.124). Thus the nonlinear beam CSEs in first order form are

$${}^L\theta = {}^L v_{,x} \quad (4.128)$$

$${}^L M_z = EI {}^L \theta_{,x} \quad (4.129)$$

$${}^L M_{z,x} + {}^L V_y - P_{tip} {}^L \theta - \frac{3}{2} EA \theta^2 ({}^L \theta) = 0 \quad (4.130)$$

$$\rho_y ({}^L \dot{v}) - {}^L V_{y,x} = {}^L p_y \quad (4.131)$$

$${}^L \dot{v} = {}^L v_{,t} \quad (4.132)$$

As noted above, the sensitivity system is linear, even though the original elasticity equations were nonlinear. In first-order, matrix operator form, (4.128)-(4.132) are

$${}^L A_t = \begin{bmatrix} 0 & 0 & 0 & 0 & 0 \\ 0 & 0 & 0 & 0 & 0 \\ 0 & 0 & 0 & 0 & 0 \\ 0 & 0 & 0 & 0 & \rho_y \\ 1 & 0 & 0 & 0 & 0 \end{bmatrix} \quad {}^L A_0 = \begin{bmatrix} 0 & 1 & 0 & 0 & 0 \\ 0 & 0 & 1/EI & 0 & 0 \\ 0 & P_{tip} + \frac{3}{2}EA\theta^2 & 0 & -1 & 0 \\ 0 & 0 & 0 & 0 & 0 \\ 0 & 0 & 0 & 0 & -1 \end{bmatrix} \quad {}^L A_1 = \begin{bmatrix} -1 & 0 & 0 & 0 & 0 \\ 0 & -1 & 0 & 0 & 0 \\ 0 & 0 & -1 & 0 & 0 \\ 0 & 0 & 0 & 1 & 0 \\ 0 & 0 & 0 & 0 & 0 \end{bmatrix} \quad {}^L \mathbf{f} = \begin{bmatrix} 0 \\ 0 \\ 0 \\ 0 \\ 0 \end{bmatrix} \quad (4.133)$$

Note that, as explained above, the A_t and A_1 CSE matrix operators are the same as the original, nonlinear elasticity system, but that the A_0 matrix for the CSE system is different.

The nonlinear bending strain term $-\frac{EA}{2}\theta^3$ is a stiffening term (the nonlinear bending strain absorbs some of the energy of the transverse load). If the axial tip force is tensile in nature ($P_{tip} > 0$) then the nonlinear effect is further stiffening. If the axial tip force is compressive ($P_{tip} < 0$) then the axial load has a softening effect typical of beam-column buckling. Recall that since this is a total Lagrangian description of the nonlinear beam bending, the forces P_{tip} and V_y are expressed in the original (undeformed) coordinate system. Follower forces are expressed relative to tip of the deformed beam must be resolved into the undeformed coordinates. More detail of modeling the follower force is given in the description of the FSI example problem in Section 7.3.

This nonlinear bending of straight beams was based on the assumptions of large transverse displacements, moderate rotations, and relatively small axial strains [106]. Additionally, we assumed that the post-deformation change in the cross-sectional area of the beam was small so that there was no distinction between the Piola-Lagrange stress and the Cauchy stress. The assumption of small changes in cross-sectional area is related to the small axial strain assumption. In 1D, the Piola-Lagrange stress (or 1st Piola-Kirchhoff stress) is also known as the engineering stress. It is a Lagrangian description in which the force in the present configuration is referenced to the area of the undeformed configuration. The 1D Piola-Lagrange (engineering) stress is

$$P = \sigma_E = \frac{T}{A} \quad (4.134)$$

where the reference areas and lengths are described in Figure 4.16. A convention of upper-case letters for the undeformed configuration and lower-case letters for the deformed configuration is adopted.

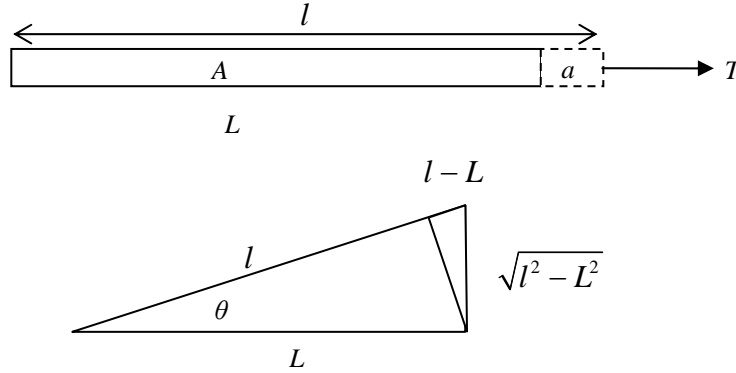


Figure 4.16: 1D stress and strain reference area and configuration definitions

The 1D Cauchy or true stress is

$$\sigma_x = \frac{T}{a} \quad (4.135)$$

In a similar manner, the 1D engineering strain and true strain for axial deformation are defined as

$$\varepsilon_E = \frac{l - L}{L} \quad (4.136)$$

and

$$\varepsilon_T = \ln\left(\frac{L + \Delta L}{L}\right) = \ln(1 + \varepsilon_E) \quad (4.137)$$

respectively. The 1D Lagrangian description of the strain due rotation is the Green strain

$$\varepsilon_G = \frac{1}{2}\theta^2 = \frac{1}{2}\left(\frac{l^2 - L^2}{L^2}\right) \quad (4.138)$$

When expressed relative to the deformed configuration, this yields the 1D Almansi-Hamel strain

$$\varepsilon_A = \frac{1}{2} \left(\frac{l^2 - L^2}{l^2} \right) \quad (4.139)$$

Both (4.138) and (4.139) are based on small angle assumptions. They are not used in the current development which assumes moderate rotations and are merely included for completeness.

Force equilibrium is properly expressed in terms of the Cauchy stress. Note that the 1D engineering and Cauchy stresses are related by

$$\sigma_E = \frac{a}{A} \sigma_x \quad (4.140)$$

The consistent integration of (4.116) to determine the axial force in the Lagrangian reference frame must introduce a factor of $\frac{a}{A}$. Assuming a constant volume of material,

$Vol = LA = la$, yields the relation

$$\frac{a}{A} = \frac{l}{L} = \varepsilon_E + 1 = u_{,x} + 1 \quad (4.141)$$

The modified, consistent form for (4.121) is then

$$M_{z,x} + V_y - (1 + u_{,x}) P_{tip} \theta - (1 + u_{,x}) \frac{EA}{2} \theta^3 = 0 \quad (4.142)$$

Note that under the assumption that $u_{,x}$ is negligible, (4.142) yields the previously derived (4.121). The nonlinear bending model developed in this section is used in Section 7.3.3 for a FSI problem. The axial load due to the fluid is more than two orders of magnitude smaller than the lateral load. Furthermore, typical values for Young's modulus of aerospace materials are 10^7 to 10^9 depending on the units. Thus, the axial

strain will be at least 7 orders of magnitude smaller than the axial stress. For this particular example problem, the modified form (4.142) which makes a distinction between the Piola-Lagrange and Cauchy stresses is not required.

4.6.4 Elastic Mesh Deformation

In a fluid-structure interaction problem, the fluid system is typically posed in an Eulerian frame. As the structure deforms under the fluid forces, the fluid domain changes shape and some method of updating the Eulerian fluid mesh is required for the next time interval or iteration. This section describes two elasticity-based mesh deformation methods for the fluid domain that were formulated and implemented in the course of the FSI analysis development.

The first mesh deformation model is the 2D plane-stress formulation described in Section 4.6.1. If $\nu = 0$, the plane-stress model becomes a spring-node system typical of many mesh deformation schemes. Increasing ν (up to $1/2$) introduces shear which serves to limit the angular distortion of the mesh.

The second fluid domain mesh deformation is based on Yang's first-order least squares displacement-displacement gradient formulation for elasticity systems [141]

$$\mathbf{A}^d \mathbf{u}^d = A_0^d \mathbf{u}^d + A_1^d \mathbf{u}_{,x}^d + A_2^d \mathbf{u}_{,y}^d = 0 \quad (4.143)$$

where $\mathbf{u}^d = [d_1 \ d_2 \ \varphi_1 \ \varphi_2 \ \varphi_3 \ \varphi_4]^T$, the superscript d denotes mesh deformation domain, and

$$\begin{aligned} \varphi_1 &\equiv d_{1,x} & \varphi_3 &\equiv d_{1,y} \\ \varphi_4 &\equiv d_{2,x} & \varphi_2 &\equiv d_{2,y} \end{aligned} \quad (4.144)$$

The dual variables, (4.144), are essentially the gradients of displacements. The elasticity homogeneous equilibrium equation (4.105) can then be written as

$$\begin{aligned}\frac{\partial}{\partial x}(\alpha^d \varphi_1 + \lambda^d \varphi_2) + \frac{\partial}{\partial y}(\mu^d \varphi_3 + \mu^d \varphi_4) &= 0 \quad \text{in } \Omega^d \\ \frac{\partial}{\partial x}(\mu^d \varphi_3 + \mu^d \varphi_4) + \frac{\partial}{\partial y}(\lambda^d \varphi_1 + \alpha^d \varphi_2) &= 0 \quad \text{in } \Omega^d\end{aligned}\tag{4.145}$$

where $\alpha^d = \lambda^d + 2\mu^d$ and λ^d and μ^d are the pseudo-solid Lamé constants,

$$\mu^d = \frac{E^d}{2(1+\nu^d)} > 0\tag{4.146}$$

$$\lambda^d = \frac{E^d \nu^d}{(1+\nu^d)(1-2\nu^d)} > 0\tag{4.147}$$

E^d is Young's modulus, and ν^d is Poisson's ratio ($\nu^d < \frac{1}{2}$) of the pseudo-solid. The matrix-operators are

$$\begin{aligned}A_0^d &= \begin{bmatrix} 0 & 0 & -1 & -1 & 0 & 0 \\ 0 & 0 & 0 & 0 & -1 & 1 \\ 0 & 0 & 0 & 0 & 0 & 0 \\ 0 & 0 & 0 & 0 & 0 & 0 \\ 0 & 0 & 0 & 0 & 0 & 0 \\ 0 & 0 & 0 & 0 & 0 & 0 \end{bmatrix} \\ A_1^d &= \begin{bmatrix} 1 & 0 & 0 & 0 & 0 & 0 \\ 0 & -1 & 0 & 0 & 0 & 0 \\ 0 & 0 & -\alpha & -\lambda & 0 & 0 \\ 0 & 0 & 0 & 0 & -\mu & -\mu \\ 0 & 0 & 0 & 0 & -1 & 0 \\ 0 & 0 & 0 & 1 & 0 & 0 \end{bmatrix} \quad A_2^d = \begin{bmatrix} 0 & 1 & 0 & 0 & 0 & 0 \\ 1 & 0 & 0 & 0 & 0 & 0 \\ 0 & 0 & 0 & 0 & -\mu & -\mu \\ 0 & 0 & -\lambda & -\alpha & 0 & 0 \\ 0 & 0 & 1 & 0 & 0 & 0 \\ 0 & 0 & 0 & 0 & 0 & -1 \end{bmatrix}\end{aligned}\tag{4.148}$$

The pseudo-solid boundary conditions for displacement are

$$\begin{aligned}\{d_1 \quad d_2\}^T &= \{u^s \quad v^s\}^T \quad \text{on } \Gamma_{sf} \\ \{d_1 \quad d_2\}^T &= 0 \quad \text{on } \Gamma - \Gamma_{sf}\end{aligned}\tag{4.149}$$

The pseudo-solid boundary conditions for the displacement gradients are

$$\begin{bmatrix} \alpha n_1 & \lambda n_1 & \mu n_2 & \mu n_2 \\ \lambda n_2 & \alpha n_2 & \mu n_1 & \mu n_1 \end{bmatrix} \begin{Bmatrix} \varphi_1 & \varphi_2 & \varphi_3 & \varphi_4 \end{Bmatrix}^T = \begin{Bmatrix} 0 \\ 0 \end{Bmatrix} \quad \text{on } \Gamma - \Gamma_{sf} \quad (4.150)$$

A clever technique to minimize mesh distortion is to augment the pseudo-solid elasticity model with a curl-free constraint, equivalent to irrotational fluid flow. This is easily done in a weak sense with the addition of another domain residual term that penalizes the “vorticity” of the mesh

$$J_{\omega}^d = \alpha_{\omega}^d \left\| \varphi_3^d - \varphi_4^d \right\|_{L^2}^2 \quad (4.151)$$

where α_{ω}^d is the mesh distortion weighting factor.

4.7 Transient LSFEM

This section describes two methods for implementing transient problems using LSFEM. The first uses a continuous time-space finite element approximation to the dynamic equations. The second discretizes the time domain and employs an implicit backward-difference operator for time before applying the finite element approximation to the spatial domain.

4.7.1 Time-space formulation

The LSFEM code developed in the course of this research is limited to 2D applications. However in the case of 1D domains, transient problems are easily implemented using the second dimension for continuous time approximations. Thus, the system least-squares functional is a continuous time-space integral to which the normal finite element approximation is applied.

Consider, as an example, the axial vibration of a clamped-free bar with no distributed load. The transient equations are

$$\rho_x \frac{\partial^2 u}{\partial t^2} - \frac{\partial}{\partial x} \left(EA \frac{\partial u}{\partial x} \right) = f_x = 0 \quad (4.152)$$

For the states variable $\mathbf{u} = [u \quad \sigma_x \quad \dot{u}]^T$, the first-order form is

$$\begin{bmatrix} 0 & 1 & 0 \\ 0 & 0 & 0 \\ 0 & 0 & 1 \end{bmatrix} \begin{Bmatrix} u \\ \sigma_x \\ \dot{u} \end{Bmatrix} + \begin{bmatrix} -E & 0 & 0 \\ 0 & -A & 0 \\ 0 & 0 & 0 \end{bmatrix} \begin{Bmatrix} u \\ \sigma_x \\ \dot{u} \end{Bmatrix}_{,x} + \begin{bmatrix} 0 & 0 & 0 \\ 0 & 0 & \rho_x \\ -1 & 0 & 0 \end{bmatrix} \begin{Bmatrix} u \\ \sigma_x \\ \dot{u} \end{Bmatrix}_{,t} = \begin{Bmatrix} 0 \\ f_x \\ 0 \end{Bmatrix} \quad (4.153)$$

Figure 4.17 depicts the time-space mesh and boundary conditions for a free vibrating plucked bar in which the initial displacement of the bar is in the first mode shape of a clamped-free bar

$$u(x, t; L) = A_1 \cos(\omega_1 t) \sin\left(\lambda_1 \frac{x}{L}\right) \quad (4.154)$$

where the eigenvalues are

$$\lambda_i = \alpha_i L = \frac{(2i-1)\pi}{2} \quad (4.155)$$

and the natural frequencies are

$$\omega_i = \frac{(2i-1)\pi}{2L} \sqrt{\frac{EA}{\rho_x}} \quad (4.156)$$

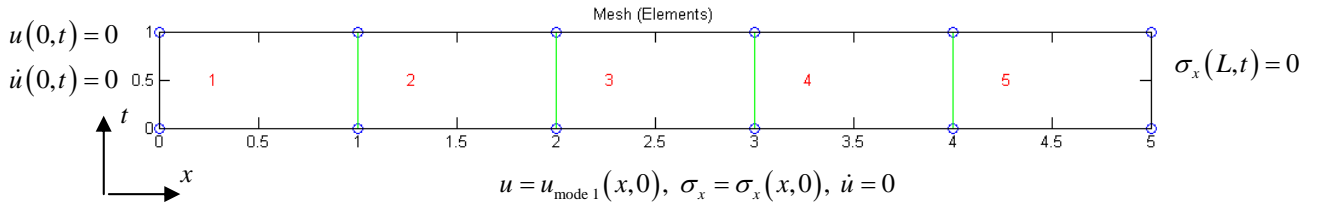


Figure 4.17: Plucked bar time-space mesh and boundary conditions.

The axial stress and velocity are then

$$\sigma(x, t; L) = EA_1 \frac{\lambda_1}{L} \cos(\omega_1 t) \cos\left(\lambda_1 \frac{x}{L}\right) \quad (4.157)$$

$$\dot{u}(x, t; L) = -A_1 \omega_1 \sin(\omega_1 t) \sin\left(\lambda_1 \frac{x}{L}\right) \quad (4.158)$$

The time-space solution for the first quarter period of the plucked bar are plotted in Figure 4.18. The LSFEM solution matches the analytic solution.

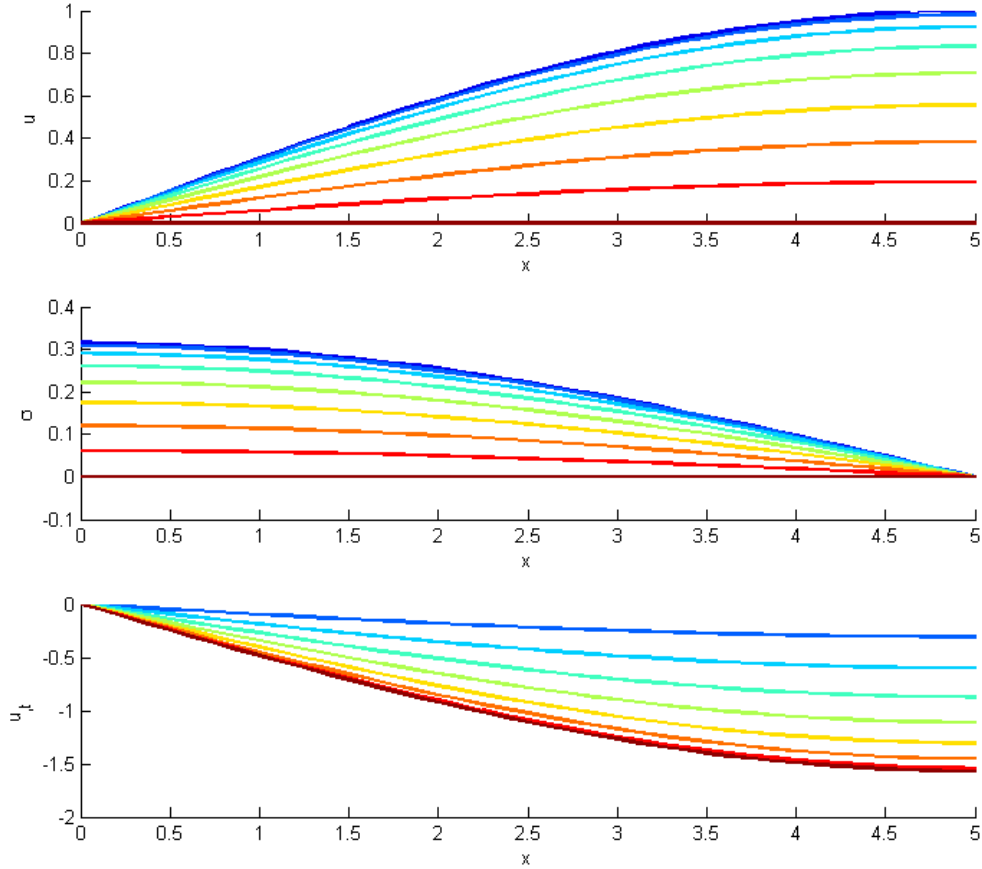


Figure 4.18: Displacement, stress, and velocity during the first quarter period of a clamped-free bar plucked in the first mode shape (initial position *blue* to quarter period *red*)

4.7.2 Continuous Space, Backward-Difference Time Formulation

The second transient formulation implemented in the LSFEM research code discretizes the time domain and employs an implicit backward-difference operator for

time. The usual finite element approximation is then used for the spatial domain. The backward-difference operator is easily derived from a Taylor series representation of time. Higher-order series representations (equivalently more steps backward in time) results in improved accuracy due to the reduced truncation error and permits a larger time step.

Table 4.4: Multipoint backward-difference representations

# of prior points	formula ^{1,2}	truncation error order
2	$u_{,tt}^n = (\Delta t)^{-2} (u^n - 2u^{n-1} + u^{n-2})$	$O[\Delta t]$
3	$u_{,tt}^n = (\Delta t)^{-2} (2u^n - 5u^{n-1} + 4u^{n-2} - u^{n-3})$	$O[(\Delta t)^2]$
5	$u_{,tt}^n = (\Delta t)^{-2} \frac{1}{12} (45u^n - 154u^{n-1} + 214u^{n-2} - 156u^{n-3} + 61u^{n-4} - 10u^{n-5})$	$O[(\Delta t)^4]$
7	$u_{,tt}^n = (\Delta t)^{-2} \frac{1}{180} (938u^n - 4014u^{n-1} + 7911u^{n-2} - 9490u^{n-3} + 7380u^{n-4} + \dots - 3618u^{n-5} + 1019u^{n-6} - 126u^{n-7})$	$O[(\Delta t)^6]$

¹: Δt is assumed to be uniform

²: The n^{th} superscript refers to the n^{th} time step

Consider, as an example, the vibration of a clamped-free Euler-Bernoulli beam with no distributed load. The transient equations are

$$\rho_x \frac{\partial^2 v}{\partial t^2} + \frac{\partial^2}{\partial x^2} \left(EI \frac{\partial^2 v}{\partial x^2} \right) = p_y = 0 \quad (4.159)$$

Discretizing in time and substituting a backward-difference approximation for the deflection acceleration yields

$$\frac{\partial^2}{\partial x^2} \left(EI \frac{\partial^2 v}{\partial x^2} \right) = p_y - \rho_x \nabla_t \nabla_t v \quad (4.160)$$

where ∇_t is the standard first backward (or rearward)-difference operator. Using any of the multipoint backward-difference approximations for deflection from Table 4.4 and moving the current state v^n back to the left hand side yields the implicit, backward-difference time, continuous space formulation for an Euler-Bernoulli beam

$$\frac{\rho_x c^n}{(\Delta t)^2} v^n + \frac{\partial^2}{\partial x^2} \left(EI \frac{\partial^2 v^n}{\partial x^2} \right) = p_y - \frac{\rho_x}{(\Delta t)^2} f(v^{n-1}, \dots, v^{n-n_{pts}}) \quad (4.161)$$

where c^n is the coefficient associated with the first term of the backward-difference approximation and $f(v^{n-1}, \dots, v^{n-n_{pts}})$ is the backward-difference function from Table 4.4 after the leading v^n term has been removed.

The analytic solution for a beam plucked in the first mode shape is

$$\begin{aligned} v(x, t) &= A_1 \cos(\omega t) \left[\cosh\left(\lambda_1 \frac{x}{L}\right) - \cos\left(\lambda_1 \frac{x}{L}\right) - \beta_1 \left[\sinh\left(\lambda_1 \frac{x}{L}\right) - \sin\left(\lambda_1 \frac{x}{L}\right) \right] \right] \\ \theta(x, t) &= A_1 \cos(\omega t) \left[\frac{\lambda_1}{L} \sinh\left(\lambda_1 \frac{x}{L}\right) + \frac{\lambda_1}{L} \sin\left(\lambda_1 \frac{x}{L}\right) - \beta_1 \left[\frac{\lambda_1}{L} \cosh\left(\lambda_1 \frac{x}{L}\right) - \frac{\lambda_1}{L} \cos\left(\lambda_1 \frac{x}{L}\right) \right] \right] \\ M_z(x, t) &= EIA_1 \cos(\omega t) \left[\left(\frac{\lambda_1}{L}\right)^2 \cosh\left(\lambda_1 \frac{x}{L}\right) + \left(\frac{\lambda_1}{L}\right)^2 \cos\left(\lambda_1 \frac{x}{L}\right) - \beta_1 \left[\left(\frac{\lambda_1}{L}\right)^2 \sinh\left(\lambda_1 \frac{x}{L}\right) + \left(\frac{\lambda_1}{L}\right)^2 \sin\left(\lambda_1 \frac{x}{L}\right) \right] \right] \\ V_y(x, t) &= -EIA_1 \cos(\omega t) \left[\left(\frac{\lambda_1}{L}\right)^3 \sinh\left(\lambda_1 \frac{x}{L}\right) - \left(\frac{\lambda_1}{L}\right)^3 \sin\left(\lambda_1 \frac{x}{L}\right) - \beta_1 \left[\left(\frac{\lambda_1}{L}\right)^3 \cosh\left(\lambda_1 \frac{x}{L}\right) + \left(\frac{\lambda_1}{L}\right)^3 \cos\left(\lambda_1 \frac{x}{L}\right) \right] \right] \\ \ddot{v}(x, t) &= -\omega^2 A_1 \cos(\omega t) \left[\cosh\left(\lambda_1 \frac{x}{L}\right) - \cos\left(\lambda_1 \frac{x}{L}\right) - \beta_1 \left[\sinh\left(\lambda_1 \frac{x}{L}\right) - \sin\left(\lambda_1 \frac{x}{L}\right) \right] \right] \end{aligned} \quad (4.162)$$

where the first eigenvalue is $\lambda_1 = 1.87510$, $\beta_1 = 0.734096$, and the natural frequency is

$\omega = (\lambda_1)^2 \sqrt{\frac{EI}{\rho_x L^4}}$. The amplitude coefficient, A_1 , is the maximum lateral deflection of the

beam. The time-space solution for the first quarter period of the plucked bar are plotted in Figure 4.19. The LSFEM solution matches the analytic solution.

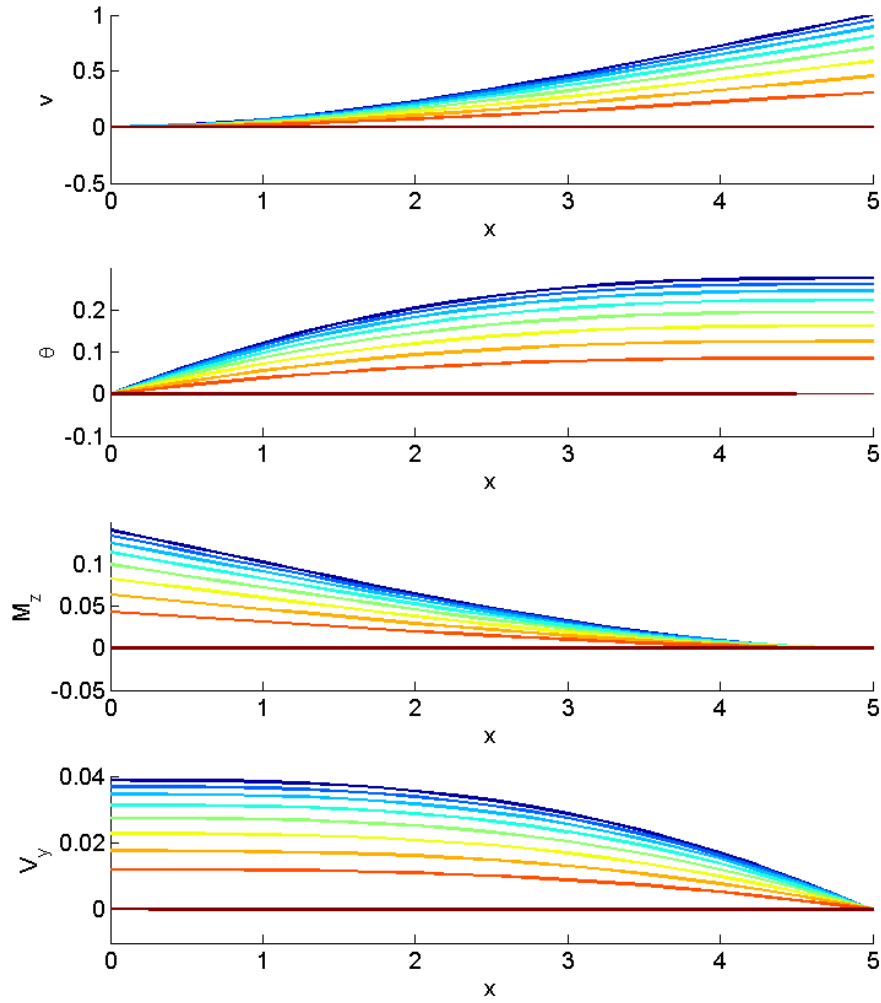


Figure 4.19: First quarter period of a beam plucked in the first mode shape ($\Delta t = 0.02$, $p = 4$, 5 pts backward difference) (initial position *blue* to quarter period *red*)

The stability of time-space finite difference equations is governed by the well-known Courant–Friedrichs–Levy condition[21]. In a discrete finite difference context, the definition of stability is that errors (truncation or round-off) do not grow while marching to the next step [2]. Four parameters affect the numerical stability of the scheme outlined above: time step size, Δt ; finite element polynomial order, p ; number of backward difference points; finite element mesh size, h . To explore the numerical stability of this scheme, we consider a simpler problem and employ the Fourier error

propagation method detailed in [125]. To make the problem tractable, consider the analogous (but lower order) 1D wave equation

$$u_{,t} + cu_{,x} = 0 \quad (4.163)$$

where c is the wave speed. The continuous space, 1-point backward-difference time formulation of (4.163) is

$$\frac{1}{\Delta t}u^n + c\frac{\partial}{\partial x}u^n = \frac{1}{\Delta t}u^{n-1} \quad (4.164)$$

The numerical error, ε , in solving (4.164) is also governed by the same relation so that

$$\frac{1}{\Delta t}\varepsilon^n + c\frac{\partial}{\partial x}\varepsilon^n = \frac{1}{\Delta t}\varepsilon^{n-1} \quad (4.165)$$

We assume that the error at any point in time ($t=0$ is convenient) can be expressed as a Fourier series so that

$$\varepsilon(x,t) = e^{at}e^{ik_mx} \quad (4.166)$$

where k_m is the wave number of the spatial error. Substituting (4.166) into (4.165) and dividing by $\exp(ik_mx)$ yields

$$e^{a(t+\Delta t)} + c\Delta tik_me^{a(t+\Delta t)} = e^{at} \quad (4.167)$$

so that

$$e^{a\Delta t} = \frac{1}{1 + c\Delta tik_m} \quad (4.168)$$

Noting that $\varepsilon^{n+1} = e^{a\Delta t}\varepsilon^n$ motivates the definition of the amplification factor

$$G = |e^{a\Delta t}| = \left| \frac{1}{1 + c\Delta tik_m} \right| = \frac{1}{\sqrt{1 + (c\Delta tk_m)^2}} \quad (4.169)$$

Since $G < 1$, the error will not grow in time and this scheme is always stable for the 1D wave equation. For a finite difference scheme, the spatial wave number is governed by

the spatial mesh step size, Δx . Indeed, the CFL requirement that $\frac{c\Delta t}{\Delta x} \leq 1$ can be inferred from a similar derivation of the amplification factor. For a finite element approximation of the spatial domain, increasing p should increase the frequency (and hence the wavenumber) of the lowest order error in the solution. Some of the conclusions on the stability of the backward difference numerical scheme are counterintuitive compared to conventional finite difference methods. For example, holding all else equal but decreasing the time step in (4.169) will increase the amplification factor closer to 1. Thus, decreasing the time step (which in most finite difference schemes improves stability and accuracy) can decrease stability margin for the discrete time, continuous space formulation.

Now consider the classic wave equation

$$u_{,tt} + cu_{,xx} = 0 \quad (4.170)$$

which is a closer analogue to the transient Euler-Bernoulli beam (4.159). The Fourier stability analysis for (4.170) leads to

$$e^{2a\Delta t} \left(1 - c(k_m \Delta t)^2 \right) = 2e^{a\Delta t} - 1 \quad (4.171)$$

which is a quadratic equation with solutions given by

$$e^{a\Delta t} = \frac{2 \pm \sqrt{c}k_m \Delta t}{2 - c(k_m \Delta t)^2} \quad (4.172)$$

Assuming the quantity $\sqrt{c}k_m \Delta t > 0$ leads to the worst case root. The requirement $G < 1$ gives the stability restrictions in terms of the time step and wave number for the continuous space, backward-difference time numerical scheme as applied to the classic wave equation:

$$k_m \Delta t > \frac{1}{2\sqrt{c}} \quad (4.173)$$

This implies a minimum limit on time step for numerical stability. (The other root leads to $\sqrt{c}k_m \Delta t > -1$ which is always satisfied). Contrast (4.173) with the CFL condition which represents a maximum limit to the step size. Further, as p value increases (or h decreases), the fundamental frequency for the error should increase and the wave number, k_m , increases. Thus, a more accurate finite element solution (due to increased p or finer mesh) will permit a smaller step size. Although these conclusions are only applicable to the wave equation, they match the observations of the analogous transient EB system. Several trends and tentative conclusions, summarized in Table 4.5, are inferred from the behavior of this model problem. These tentative conclusions are supported by the comparisons presented in the Figure 4.20-Figure 4.22 at the end this chapter. Figure 4.20 demonstrates that increasing the number of backward-difference points can decrease stability. Similarly, Figure 4.21 demonstrates that decreasing Δt also decreases stability whereas Figure 4.22 demonstrates that increasing p can restore stability. Further analysis of the stability limits for the discrete time, continuous space representation of the equations derived above is complicated by the large number of terms in the representations of Table 4.4 and is beyond the scope of the present effort. No references to this type of analysis relevant to the present attempt can be found in the literature. The numerical parameter stability requirements for the FSI example problem considered in Chapter 7 which uses this approach are established by using values that are known to be stable from the free vibration verification problems. Further study of the stability limits for this mixed numerical scheme may be a promising avenue for further research.

Table 4.5: Backward difference discrete time stability and accuracy considerations

	Stability	Accuracy	Explanation
Inc Δt	improves stability	decreases accuracy	prevents stability problems due to round-off error in comparison of solutions in close proximity in time
Inc p	improves stability	increases accuracy	improved spatial accuracy eliminates solution error at points in time
Inc num BD pts	decreases stability	increases accuracy	round-off error between adjacent time points dominates
Inc h	improves stability	increases accuracy	improves spatial accuracy

4.8 Fluid-Structure Interface Relations

In a fluid structure interaction problem, the boundary condition (3.2) on the fluid-structure boundary, Γ^{sf} , becomes an interface condition. The interface conditions on Γ^{sf} are based on kinematic and equilibrium conditions along the interface between the structure and fluid domains. If the outward normal vectors for the structure and fluid domains are \mathbf{n}^s and \mathbf{n}^f , then $\mathbf{n}^s = -\mathbf{n}^f$ on Γ^{sf} . Thus for an inviscid fluid, the no-penetration condition (slip wall) is

$$\mathbf{v}^s \cdot \mathbf{n}^s + \mathbf{v}^f \cdot \mathbf{n}^f = 0 \quad \text{on } \Gamma^{sf} \quad (4.174)$$

where \mathbf{v}^s and \mathbf{v}^f are the structure and fluid velocities respectively. For viscous flow, the no slip condition is

$$\mathbf{v}^s - \mathbf{v}^f = 0 \quad \text{on } \Gamma^{sf} \quad (4.175)$$

For steady-state problems, the structure velocity is zero. Equilibrium conditions on the fluid-structure interface result in

$$\boldsymbol{\sigma}^s \cdot \mathbf{n}^s + \boldsymbol{\sigma}^f \cdot \mathbf{n}^f = 0 \quad \text{on } \Gamma^{sf} \quad (4.176)$$

which equates the structure boundary stress vector, $\boldsymbol{\sigma}^s \cdot \mathbf{n}^s$, to the traction forces due to the fluid stress at the interface, written in tensor index notation as

$$\sigma_{ij}^f = -p^f \delta_{ij} + \mu^f (u_{i,j}^f + u_{j,i}^f) + \delta_{ij} \lambda^f u_{i,i}^f \quad (4.177)$$

where μ^f is the fluid viscosity and λ^f is the fluid bulk viscosity.

The interface coupling is incorporated into the LSFEM model by a boundary integral, (4.1), evaluated along Γ^{sf} . Thus the weighted residual is

$$J_{tot} = \alpha^s J^s + \alpha^f J^f + \alpha^{sf} J^{sf} + \alpha^{\Gamma^s} J^{\Gamma^s} + \alpha^{\Gamma^f} J^{\Gamma^f} \quad (4.178)$$

where

$$J^s(\Omega^s) = \|\mathbf{A}^s \mathbf{u}^s - \mathbf{f}^s\|_{L^2}^2 \quad (4.179)$$

$$J^f(\Omega^f) = \|\mathbf{A}^f \mathbf{u}^f - \mathbf{f}^f\|_{L^2}^2 \quad (4.180)$$

$$J^{sf}(\Gamma^{sf}) = \|\boldsymbol{\sigma}^s \cdot \mathbf{n}^s + \boldsymbol{\sigma}^f \cdot \mathbf{n}^f\|_{L^2}^2 + \|\mathbf{v}^s \cdot \mathbf{n}^s + \mathbf{v}^f \cdot \mathbf{n}^f\|_{L^2}^2 \quad (4.181)$$

$$J^{\Gamma^s}(\Gamma^s) = \|\mathbf{B}^s \mathbf{u}^s - \mathbf{g}^s\|_{L^2}^2 \quad (4.182)$$

$$J^{\Gamma^f}(\Gamma^f) = \|\mathbf{B}^f \mathbf{u}^f - \mathbf{g}^f\|_{L^2}^2 \quad (4.183)$$

As discussed in Section 2.2, there are several options for coupling the mesh deformation problem with the fluid-structure interface problem. In the monolithic FSI approach (it is uncertain whether the expression is due to Hubner or Michler as both papers appear at the same time), the structure, fluid, and mesh deformation are fully-coupled and posed as a single, implicit system [64, 84]. Some researchers have employed different finite element formulations for each domain. For example [76] used LSFEM for the fluid solution and a weak-Galerkin FEM for the structure solution. In [101], a unified, higher-order p LSFEM formulation for the structure, fluid, and mesh deformation domains was adopted. In this scheme, the fully-coupled structure-fluid-mesh system takes the form

$$\begin{bmatrix} [K^{ss}] & [K^{sf}] & [K^{sd}] \\ [K^{fs}] & [K^{ff}] & [K^{fd}] \\ [K^{ds}] & [K^{df}] & [K^{dd}] \end{bmatrix} \begin{Bmatrix} U^s \\ U^f \\ U^d \end{Bmatrix} = \begin{Bmatrix} F^s \\ F^f \\ F^d \end{Bmatrix} \quad (4.184)$$

where s denotes the structure domain, f the fluid domain, and d denotes the deformation domain. The diagonal components of the stiffness matrix in (4.184) are constructed on an element basis and assembled into the global system by separate evaluation in each domain. The coupling terms (off-diagonal components) of (4.184) are determined from evaluating the boundary integral along the interface and assembling the boundary element degrees of freedom into the global system based on a global degree of freedom index table.

A serious drawback to using the monolithic formulation with LSFEM was noted by Rasmussen [101]. For a variety of example problems, the LSFEM solution was shown to be extremely sensitive to the boundary and domain weights of the total system residual which takes the form

$$J_{tot} = \alpha^s J^s + \alpha^f J^f + \alpha^d J^d + \alpha^{sfd} J^{sfd} \quad (4.185)$$

The most promising weighting scheme developed in [101] was an iterative residual balancing method that increased the required computations by at least one order of magnitude. This represents a significant computational burden. Since the mesh sensitivity is not required for the local CSE formulation developed for FSI problems in Chapter 7, we avoid the computational expense of using a monolithic LSFEM formulation. The mesh problem is decoupled from the fluid-structure problem and the

fluid domain is remeshed between each time step. No accuracy problems have been noted for this approach for the problems with an analytic solution.

4.9 Summary of the Least-Square Finite Element Method

This chapter described the theory of LSFEM as a variational method and presented a method for implementing higher-order polynomial elements, p -elements, in LSFEM. The specific LSFEM formulations for six fluid models, four elasticity models, and transient LSFEM formulations were also presented. Not all of the LSFEM models developed in this Chapter are employed in subsequent chapters, but they were included for the sake of completeness and for the potential benefit to future researchers.

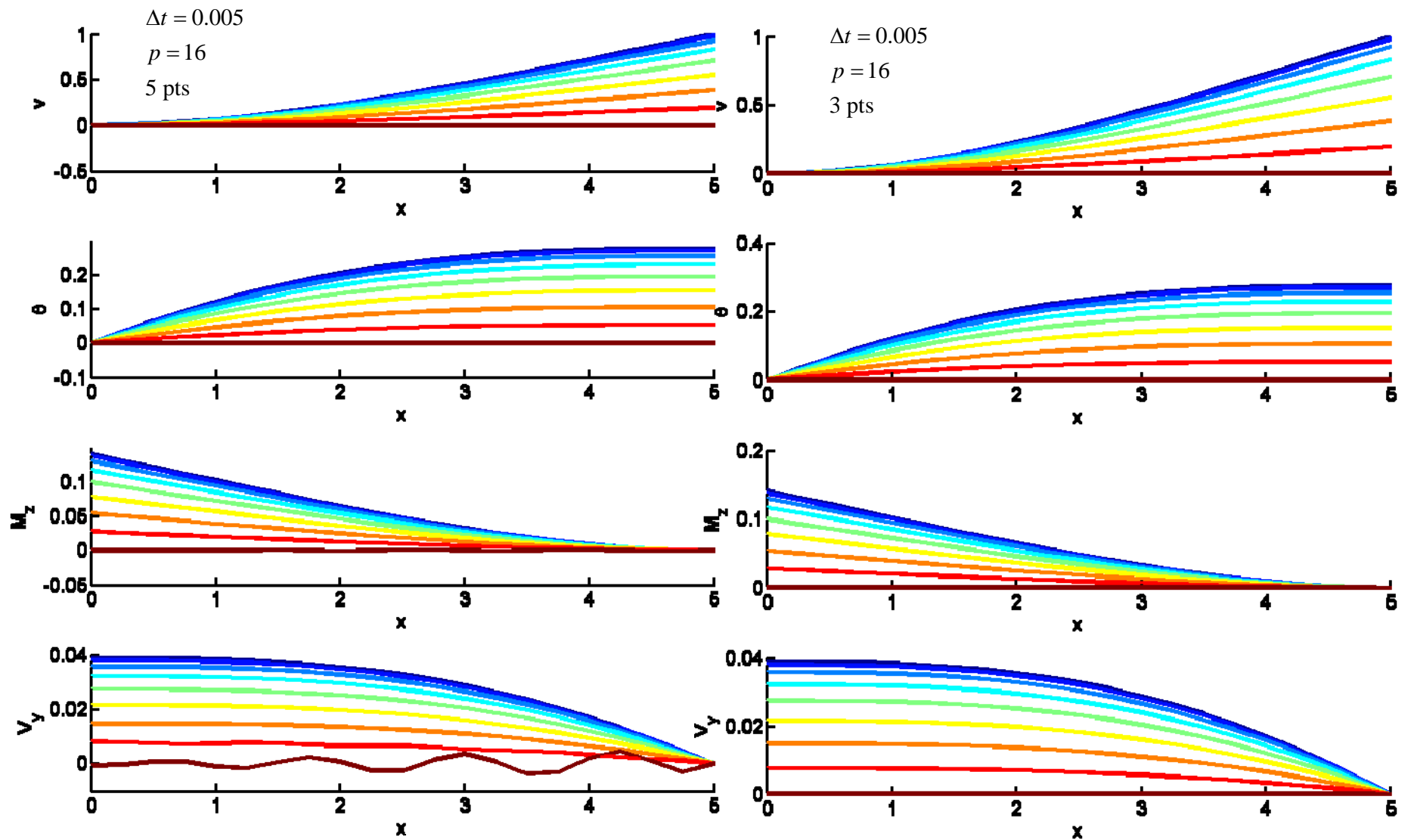


Figure 4.20: Comparison demonstrating effect of number of BD points on numerical stability of quarter period plucked beam solution

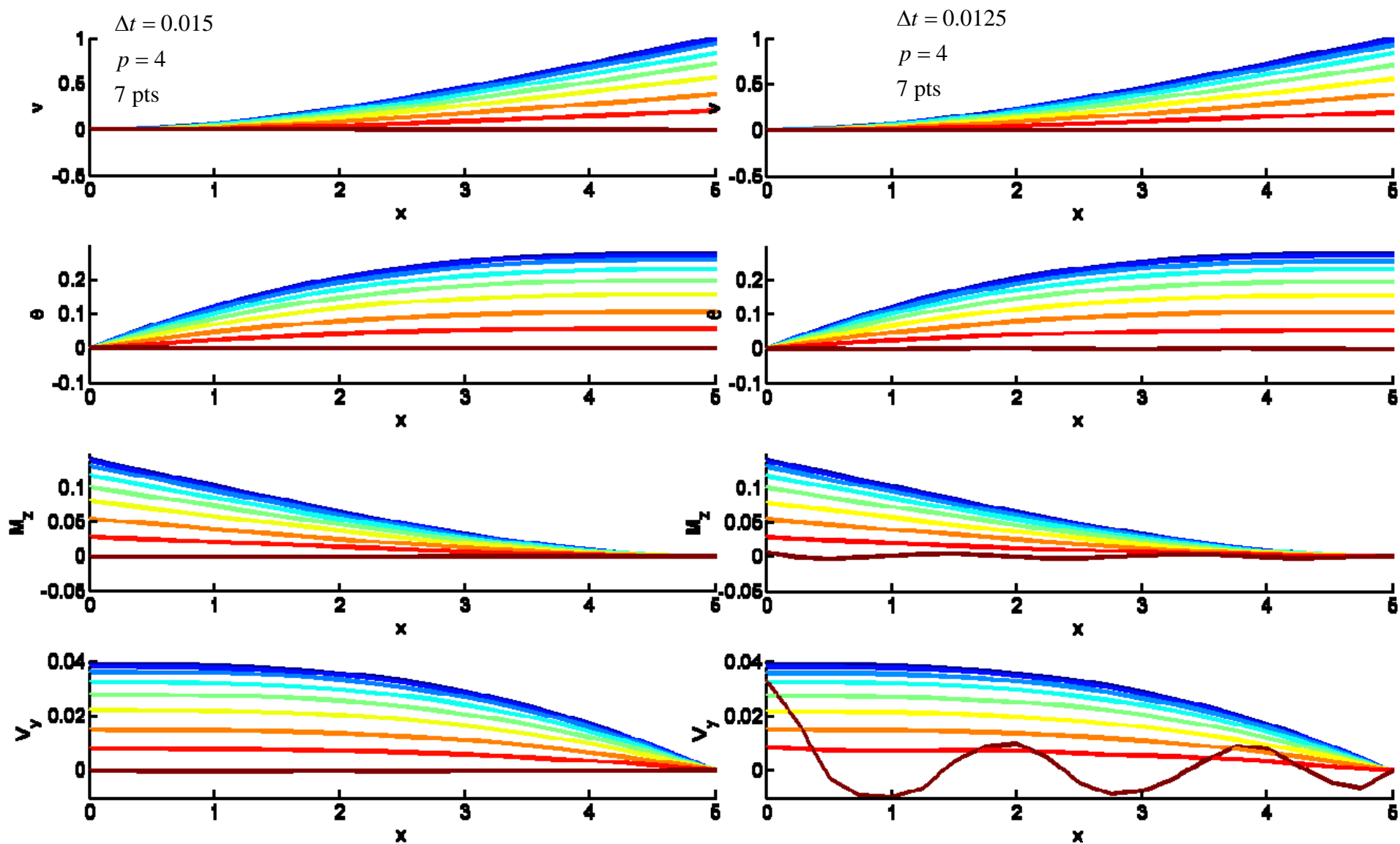


Figure 4.21: Comparison showing rapid deterioration of numerical stability due to too small Δt of quarter period plucked beam solution

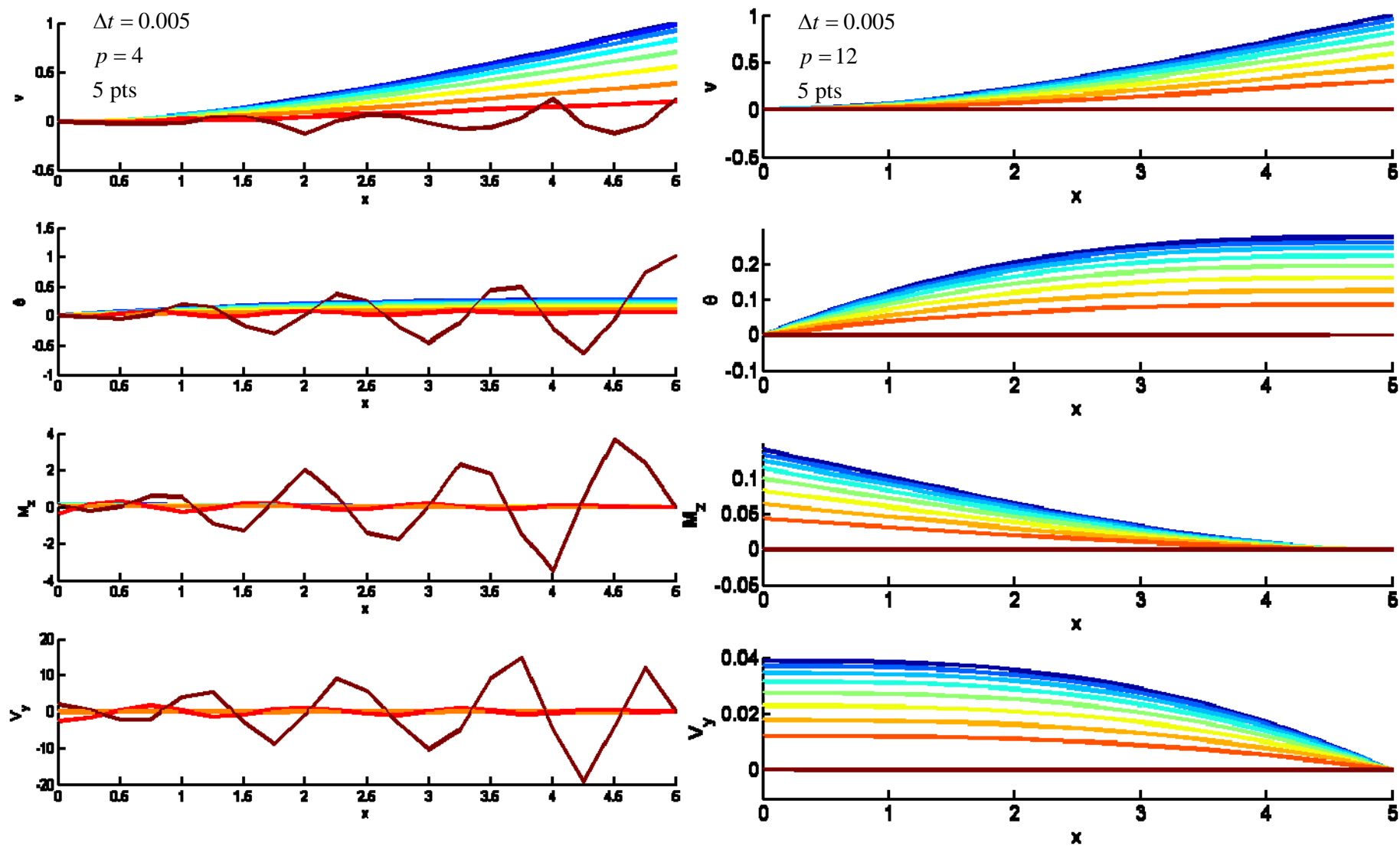


Figure 4.22: Comparison showing improvement of numerical stability due to increased p on quarter period plucked beam solution

5 LS-CSE For Elasticity

Continuous sensitivity solutions for the shape variation to several 2D elasticity examples problems are presented. The example problems were solved using an original LSFEM solver with higher-order p -elements that was implemented in MATLAB[®]. The problems considered here employ both Cartesian and polar coordinate systems and have analytic solutions which permit a closed-form solution for the shape parameter sensitivity. The CSE solutions are also compared to finite difference results.

The first problem (Section 5.1) is a plane elasticity example adapted from Timoshenko and Goodier (T&G). The second problem (Section 5.2) explores several variations of an axially-loaded plate with a hole. The purpose of these example problems is to demonstrate the LS-CSE method in sufficient detail for others to follow and use as validation cases. As noted in Chapter 2, the literature contains precious few examples of continuous sensitivity applications for elasticity.

5.1 Timoshenko and Goodier Example

This is a classic elasticity problem, example 3.24 from [127], in which a simply supported rectangular beam is subject to a surface traction on the upper and lower edges, Figure 5.1. For the current example, the beam length, L , and semi-width, c , are 1 and $\frac{1}{2}$ respectively so that the domain is a unit square. The solution for a loading of $A = B = \frac{1}{2}$, and $\alpha = \pi/L$ (so that the edge traction is a half-sine curve) is plotted in Figure 5.1. The analytic solution for the stress and displacement fields is

$$\sigma_{xx}(x, y) = \sin(\alpha x) [C_1 \alpha^2 \cosh \alpha y + C_2 \alpha^2 \sinh \alpha y + \dots \\ C_3 (y \alpha^2 \cosh \alpha y + 2 \alpha \sinh \alpha y) + C_4 (y \alpha^2 \sinh \alpha y + 2 \alpha \cosh \alpha y)] \quad (5.1)$$

$$\sigma_{yy}(x, y) = -\alpha^2 \sin(\alpha x) [C_1 \cosh \alpha y + C_2 \sinh \alpha y + C_3 y \cosh \alpha y + C_4 y \sinh \alpha y] \quad (5.2)$$

$$\sigma_{xy} = -\alpha \cos \alpha x [C_1 \alpha \sinh \alpha y + C_2 \alpha \cosh \alpha y + \dots \\ C_3 (\cosh \alpha y + y \alpha \sinh \alpha y) + C_4 (\sinh \alpha y + \alpha y \cosh \alpha y)] \quad (5.3)$$

$$u(x, y) = \frac{-1}{\alpha E} \cos(\alpha x) [C_1 \alpha^2 \cosh \alpha y + C_2 \alpha^2 \sinh \alpha y + \dots \\ C_3 (y \alpha^2 \cosh \alpha y + 2 \alpha \sinh \alpha y) + C_4 (y \alpha^2 \sinh \alpha y + 2 \alpha \cosh \alpha y)] + \dots \quad (5.4)$$

$$\frac{-\nu \alpha}{E} \cos(\alpha x) [C_1 \cosh \alpha y + C_2 \sinh \alpha y + C_3 y \cosh \alpha y + C_4 y \sinh \alpha y] \\ v(x, y) = \frac{-\nu}{E} \sin(\alpha x) [C_1 \alpha \sinh \alpha y + C_2 \alpha \cosh \alpha y + \dots \\ C_3 (\alpha y \sinh \alpha y + \cosh \alpha y) + C_4 (\alpha y \cosh \alpha y + \sinh \alpha y)] + \dots \\ \frac{-1}{E} \sin(\alpha x) [C_1 \alpha \sinh \alpha y + C_2 \alpha \cosh \alpha y + \dots \\ C_3 (\alpha y \sinh \alpha y - \alpha \cosh \alpha y) + C_4 (\alpha y \cosh \alpha y - \alpha \sinh \alpha y)] \quad (5.5)$$

where the C_i coefficients are given by the problem loading and geometry

$$C_1 = \frac{(A+B)}{\alpha^2} \frac{\sinh \alpha c + \alpha c \cosh \alpha c}{\sinh 2\alpha c + 2\alpha c} \\ C_2 = -\frac{(A-B)}{\alpha^2} \frac{\cosh \alpha c + \alpha c \sinh \alpha c}{\sinh 2\alpha c - 2\alpha c} \\ C_3 = \frac{(A-B)}{\alpha^2} \frac{\alpha \cosh \alpha c}{\sinh 2\alpha c - 2\alpha c} \\ C_4 = -\frac{(A+B)}{\alpha^2} \frac{\alpha \sinh \alpha c}{\sinh 2\alpha c + 2\alpha c} \quad (5.6)$$

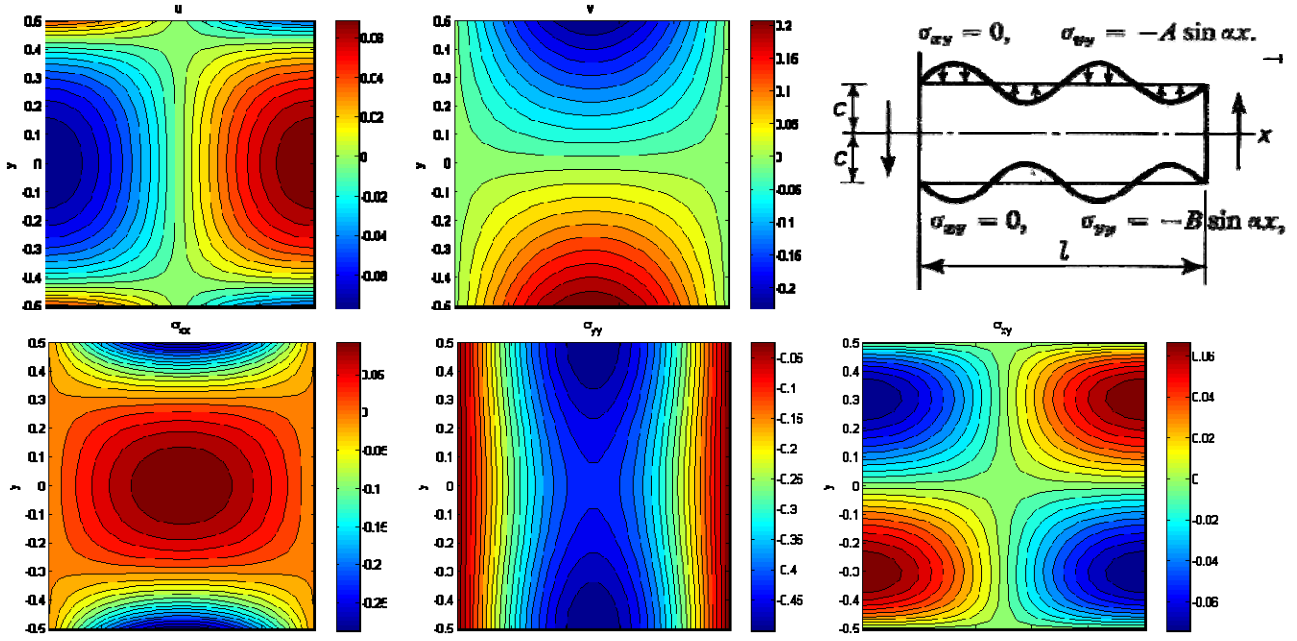


Figure 5.1: Timoshenko and Goodier example 3.24

The closed-form analytic sensitivity to beam length is obtained by differentiating (5.1)-(5.5) with respect to L (through its implicit dependence on α). The left edge of the beam is fixed, and the right edge will vary as L . The domain is parameterized with respect to beam length as so that the material coordinates of the boundaries are given by

$$\begin{aligned}
 \mathbf{X}_{\Gamma_1} &= \{(0, \eta) \mid \eta \in [-c, c]\} \\
 \mathbf{X}_{\Gamma_2} &= \{(\xi L, -c) \mid \xi = x/L\} \\
 \mathbf{X}_{\Gamma_3} &= \{(L, \eta) \mid \eta \in [-c, c]\} \\
 \mathbf{X}_{\Gamma_4} &= \{(\xi L, +c) \mid \xi = x/L\}
 \end{aligned} \tag{5.7}$$

where the Γ_i 's are defined in Figure 5.2. The domain sensitivity to beam length is then

$$\begin{aligned}
 \mathbf{X}_{\Gamma_1, L} &= \{(0, 0)\} \\
 \mathbf{X}_{\Gamma_2, L} &= \{(\xi, 0) \mid \xi = x/L\} \\
 \mathbf{X}_{\Gamma_3, L} &= \{(1, \eta) \mid \eta \in [-c, c]\} \\
 \mathbf{X}_{\Gamma_4, L} &= \{(\xi, 0) \mid \xi = x/L\}
 \end{aligned} \tag{5.8}$$

The boundary data for the elasticity problem is also depicted in Figure 5.2 and is repeated in Table 5.1 where it is compared with the boundary data for the sensitivity problem. The boundary data for the sensitivity problem is derived from

$${}^L\mathbf{u}|_{\Gamma} \equiv \frac{\partial \mathbf{u}}{\partial L} \Big|_{\mathbf{x}=\Gamma} = \frac{D\mathbf{u}}{DL} \Big|_{\Gamma} - \nabla \mathbf{u} \cdot \frac{\partial \mathbf{x}_{\Gamma(L)}}{\partial L} \quad (5.9)$$

where the total derivative for the constrained variables is zero for the sensitivity problem.

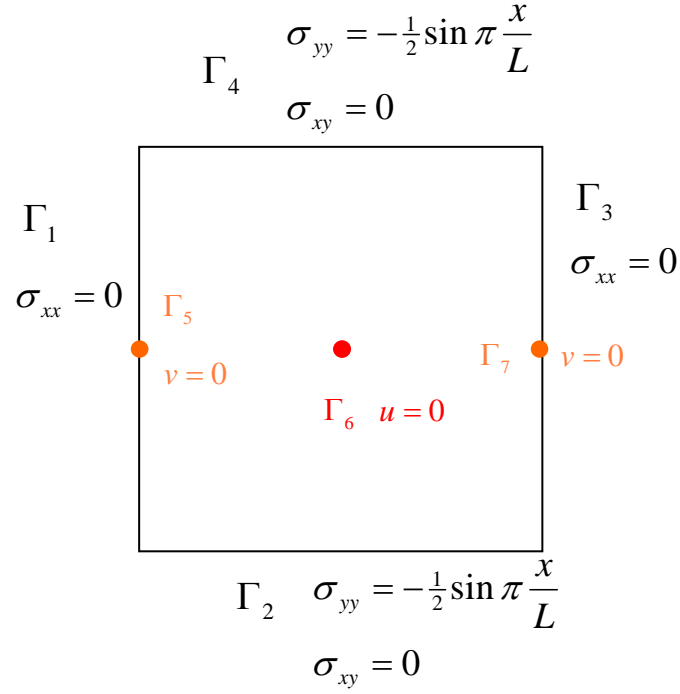


Figure 5.2: Timoshenko and Goodier example 3.24 boundary conditions

Table 5.1: Boundary Data for Timoshenko and Goodier example 3.24 elasticity and sensitivity problems

Boundary	Elasticity Problem	Sensitivity Problem
Γ_1	$\sigma_{xx} = 0$	$\sigma_{xx} = 0$
$\Gamma_2 \& \Gamma_4$	$\sigma_{yy} = -\frac{1}{2} \sin \pi \frac{x}{L}$ $\sigma_{xy} = 0$	${}^L\sigma_{yy} = -x\sigma_{yy,x} = \frac{1}{2} x\pi \cos \pi x$ ${}^L\sigma_{xy} = 0$
Γ_3	$\sigma_{xx} = 0$	${}^L\sigma_{xx} = -\sigma_{xx,x}$
$\Gamma_5 \& \Gamma_7$	$v = 0$	${}^Lv = -v_{,x} = 0$
Γ_6	$u = 0$	${}^Lu = -\frac{1}{2} u_{,x}$

The LSFEM solution, computed on a four element mesh for $p = 12$, is plotted in Figure 5.2 and can compared to the analytic solution in Figure 5.1. The L_2 residual error norm for the LSFEM solution is on the order of 10^{-11} and the absolute error difference between the LSFEM solution and the analytic stress field is on the order of 10^{-10} . The detail and accuracy of the higher-order p -value on a fairly coarse mesh is an extraordinary testament of the merits of p -type elements in the LSFEM solution.

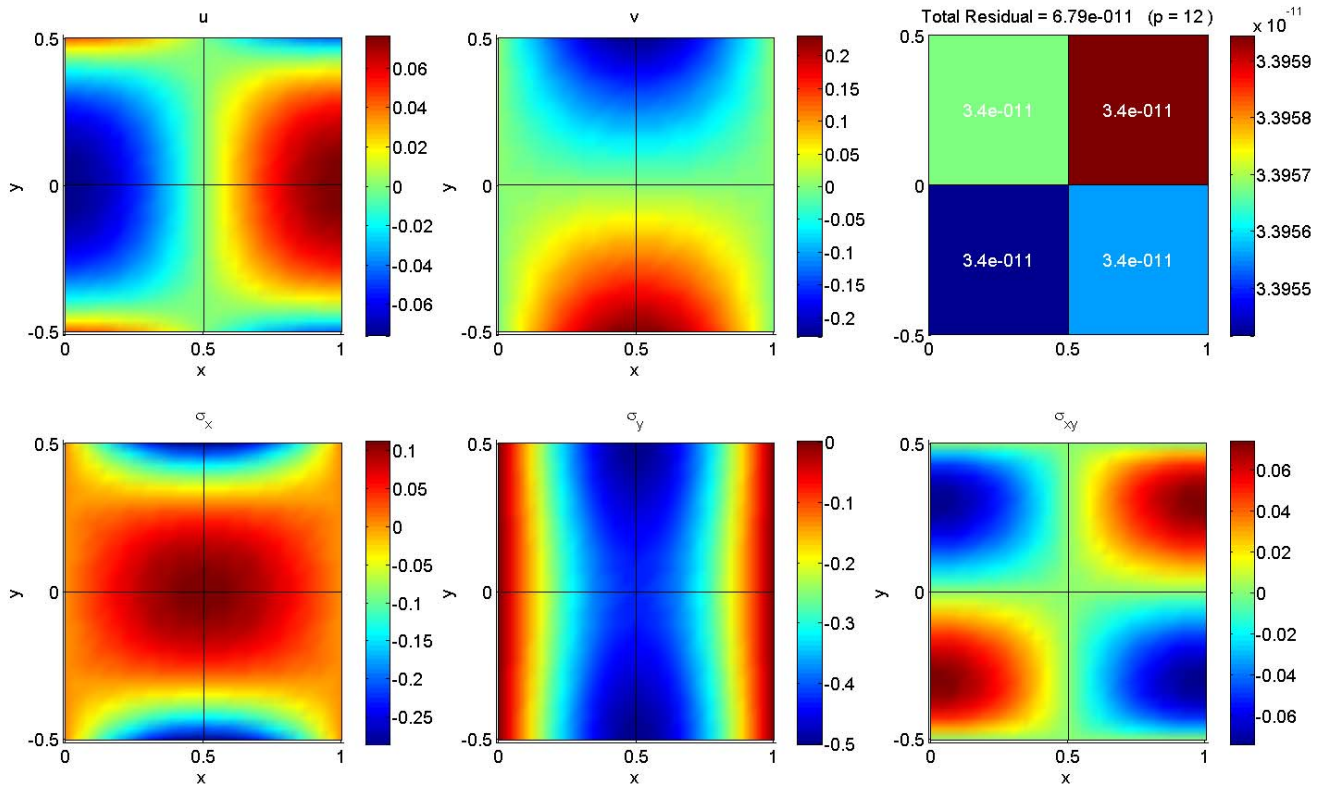


Figure 5.3: T&G LSFEM solution and residual ($p = 12$)

The least-squares CSE solution, computed on the same computational four-element mesh used for the original problem, is plotted in Figure 5.4 and compared to the analytic sensitivities Figure 5.5. Again, a p -value of 12 was used for the least-squares CSE solution. The L_2 residual error norm for the LSFEM solution is on the order of 10^{-10} , an order of magnitude reduction in accuracy from the original solution. This matches conclusions made by previous researchers that a more refined mesh is commonly needed for the CSE system [120]. In practice, we take advantage of the p -element implementation and simply increase the p -order while maintaining the same computational mesh.

The total material analytic derivative is computed by adding the transport term associated with the domain parameterization given by (5.7) to the analytic local sensitivity. The material derivative for the entire domain is plotted in Figure 5.6 which should be compared to the local sensitivity in Figure 5.5. The LS-CSE, analytic sensitivities, and finite difference calculations are further compared in Figure 5.7 and Figure 5.8. Note that finite difference derivatives are by nature total derivatives and that they match the LS-CSE total sensitivity calculations. Additionally, the difference between the local and total derivative values is clearly evident by comparing Figure 5.5 and Figure 5.6. The potential pitfalls in neglecting the distinction between the local and total derivative was discussed in Section 3.3.2.

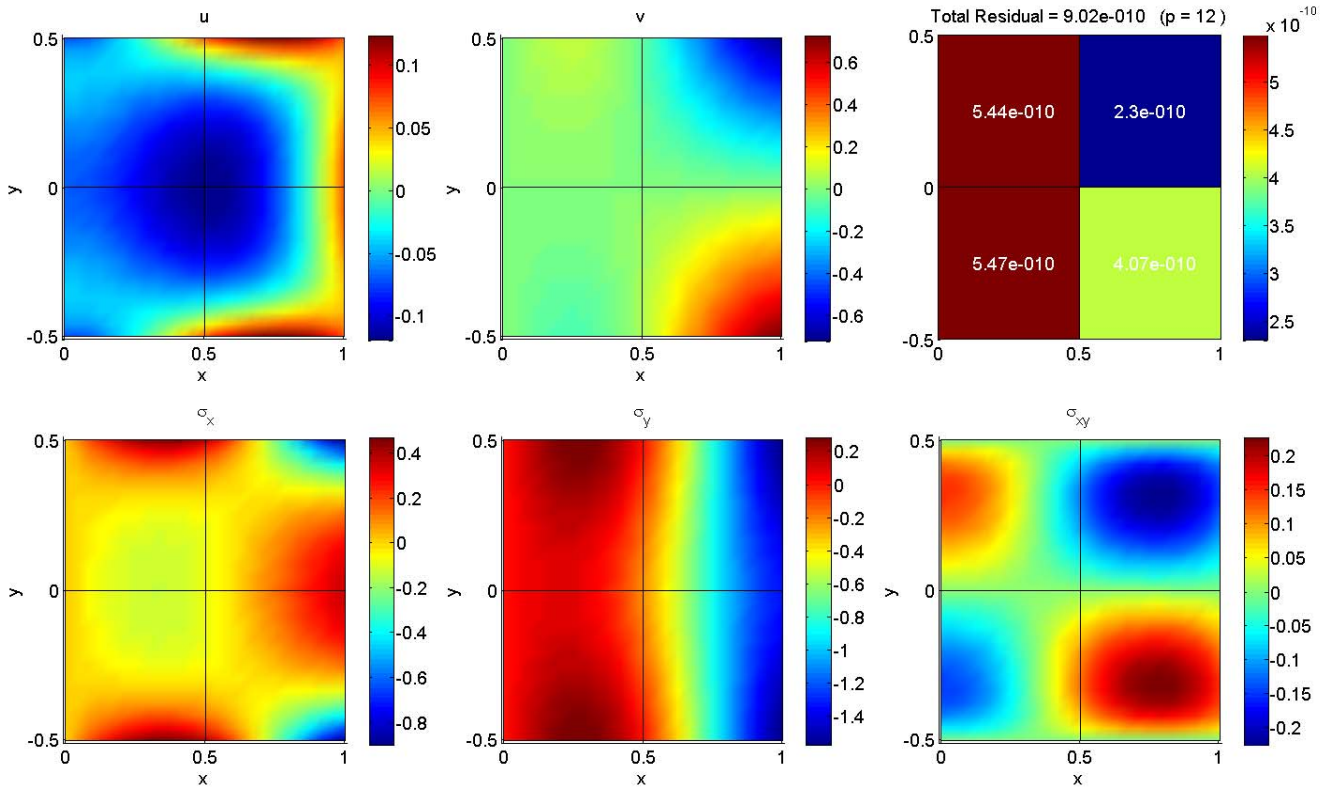


Figure 5.4: T&G CSE solution and residual ($p = 12$) for sensitivity to beam length

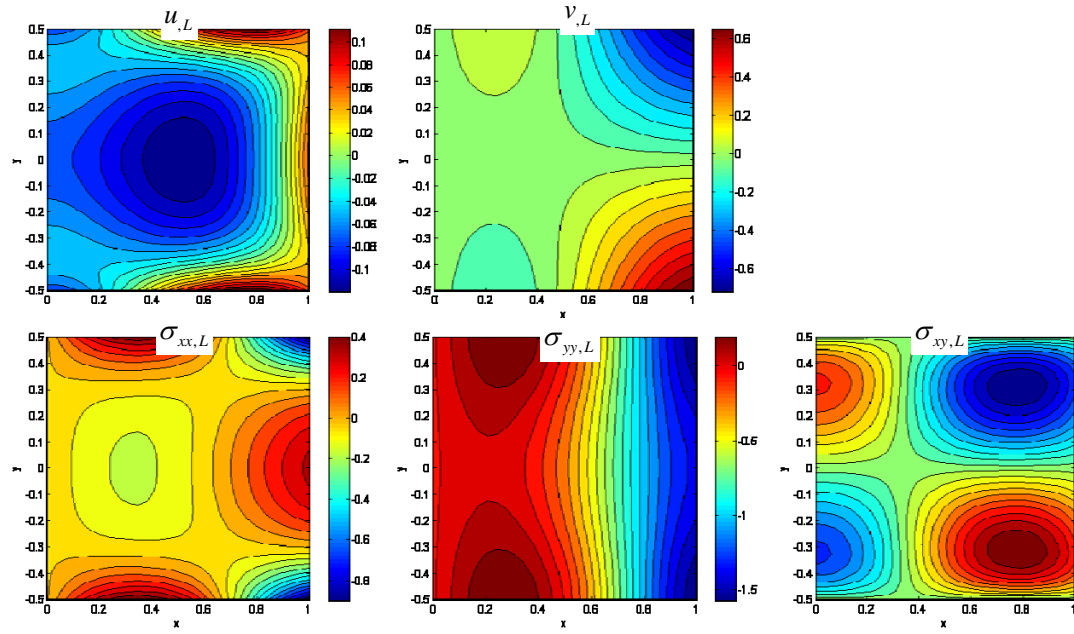


Figure 5.5: T&G analytic local sensitivity to beam length

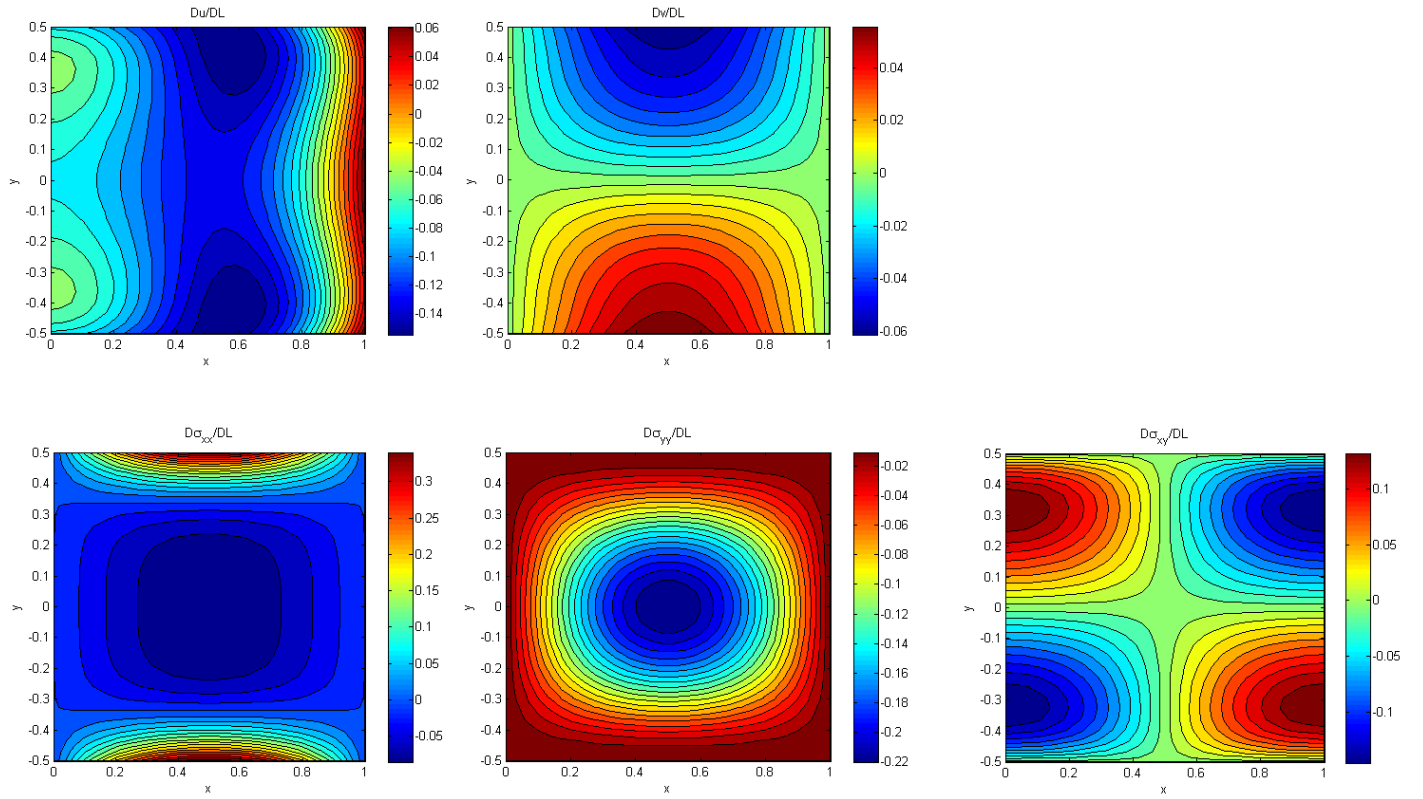


Figure 5.6: T&G CSE analytic total sensitivity to beam length

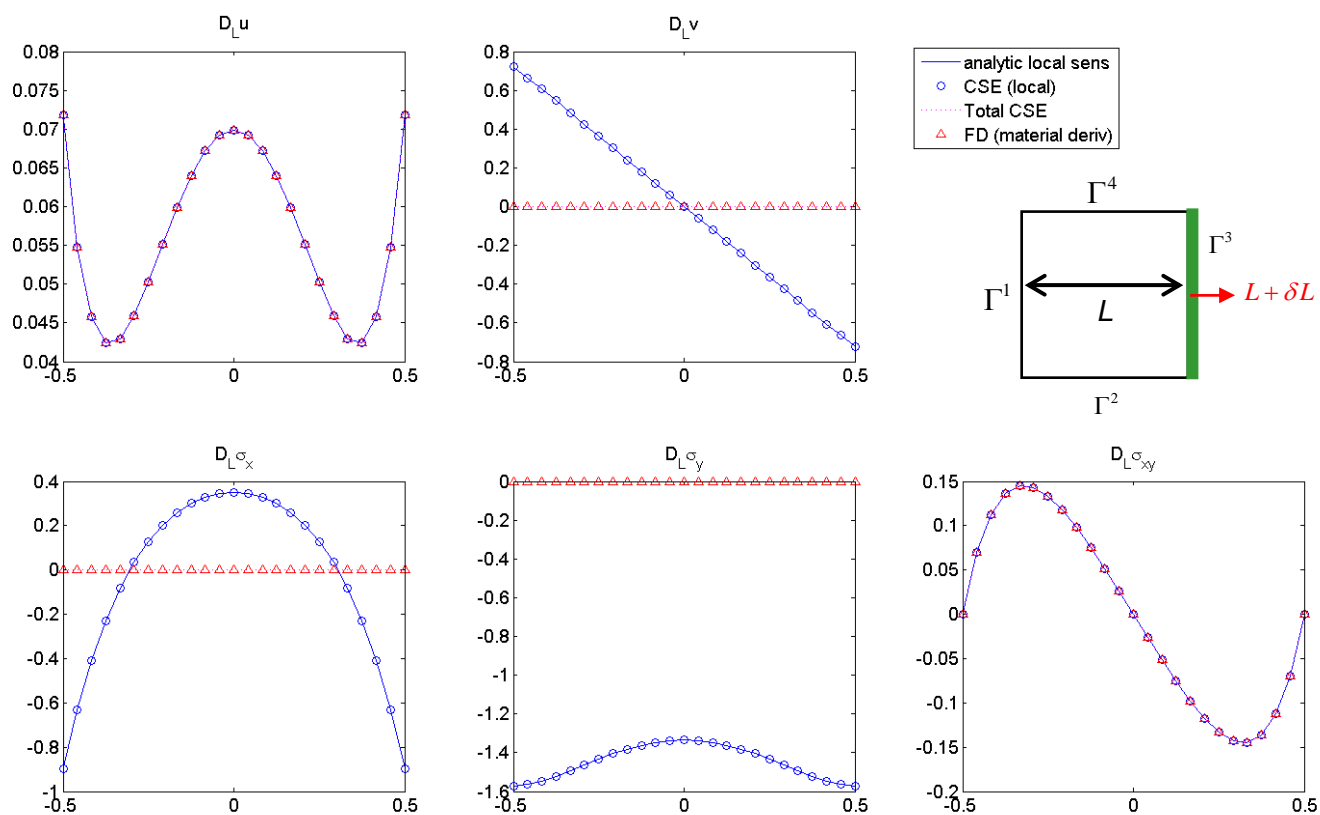


Figure 5.7: Comparison of T&G LS-CSE and analytic derivatives for on boundary Γ_3

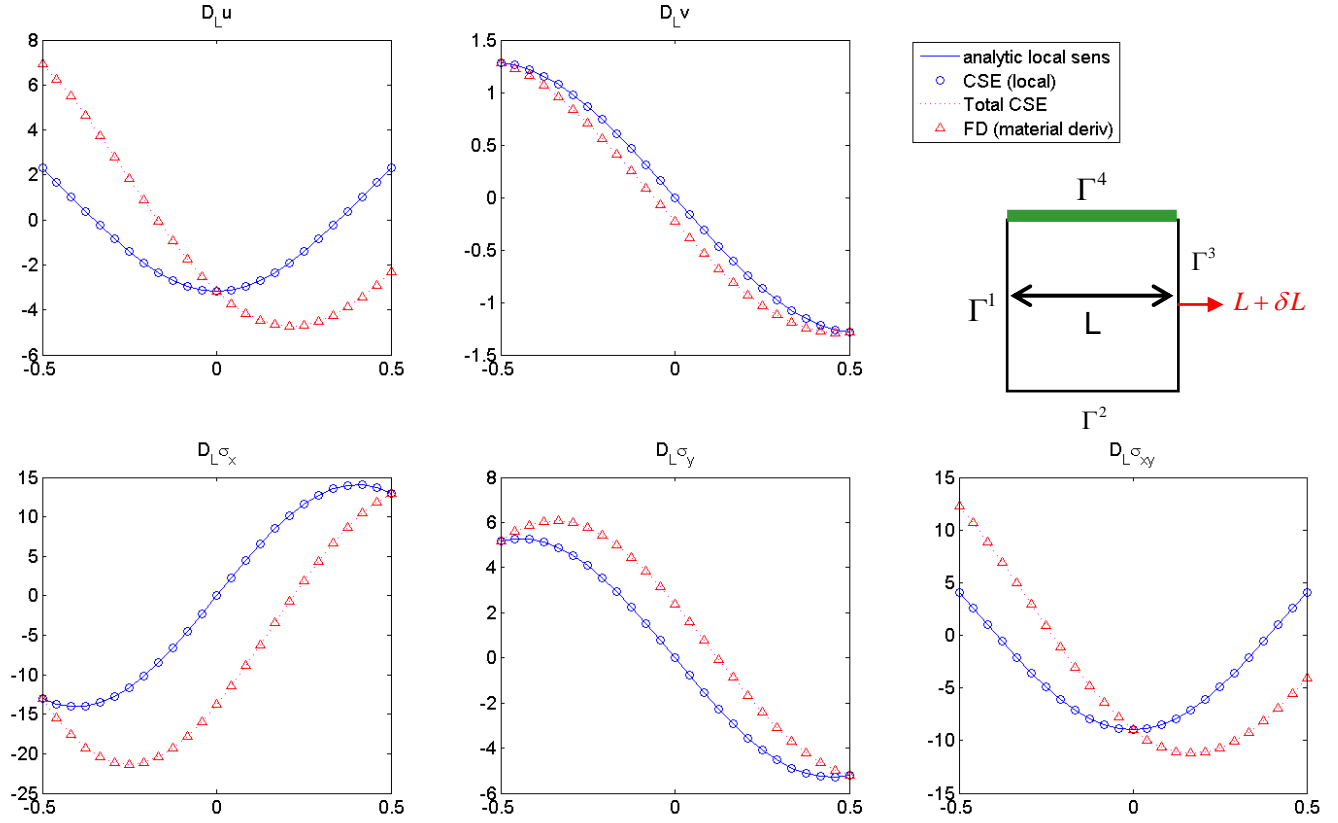


Figure 5.8: Comparison of T&G LS-CSE and analytic derivatives for on Boundary Γ_4

5.2 Plate with a hole

Determining the stress concentration for a thin plate with an unstressed hole is a classic problem in strength of materials and a common exercise in FEM analysis. An analytic solution exists for a circular hole in an infinite plate subject to uniaxial tension [124], and results for finite plates under biaxial loading with a variety of hole dimensions are plotted as a function of load and plate/hole dimensions [91, 111]. To illustrate the least-square continuous sensitivity method, we consider the shape optimization of an elliptic cut-out in a biaxially loaded plate, Figure 5.9. The objective of the optimization is to obtain a uniform distribution of tangential stress along the hole. The problem was

posed and solved by Bhaskaran and Berkooz [18] using a sensitivity equation method, but details of the sensitivity calculations were not included in the paper. We first present details of the LS-CSE solution to an infinite plate for which an analytic solution exists, and then use the CSE solution to optimize the problem considered in [18]. The objective is to provide sufficient detail in the derivation and results such that this problem can serve as a verification benchmark for structural sensitivity analysis.

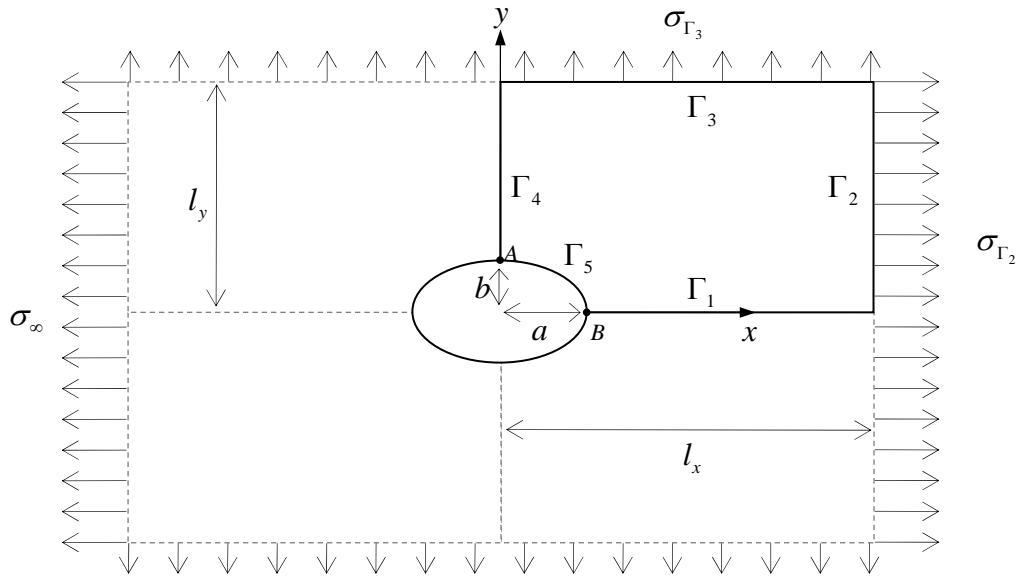


Figure 5.9: Plate with an elliptical hole

Table 5.2: Boundary conditions for plate with a circular hole

Boundary	Boundary Condition
Γ_1	$v = 0, \quad \sigma_{xy} = 0$ plate symmetry
Γ_2	σ_{xx} & σ_{xy} analytic solution
Γ_3	σ_{yy} & σ_{xy} analytic solution
Γ_4	$u = 0, \quad \sigma_{xy} = 0$ plate symmetry
Γ_5	$\sigma_n = 0, \quad \sigma_\tau = 0$ stress free hole

5.2.1 Infinite Plate Analytic Solution

Consider first an infinite plate with a circular hole, $a = b = 1/4$ subject to a uniaxial load in the x -direction, $\sigma_{\Gamma_2} = \sigma_\infty = 10$. By virtue of biaxial symmetry, only a quadrant of the domain can be used as the computational domain (boundary conditions are given in Table 5.2). To obtain LSFEM results that can be compared to the analytic solution, the analytic normal and tangential stress distribution on boundaries Γ_2 and Γ_3 are imposed as boundary conditions (take $l_x = l_y = 4a = 1$). We first consider the solution of the elasticity system and then the solution to the CSE system. The analytic stress and displacement solutions for a circular hole are [124]

$$u(r, \theta) = \frac{\sigma_\infty a}{8G} \left[\frac{r}{a} (\kappa + 1) \cos \theta + 2 \frac{a}{r} ((1 + \kappa) \cos \theta + \cos 3\theta) - 2 \frac{a^3}{r^3} \cos 3\theta \right] \quad (5.10)$$

$$v(r, \theta) = \frac{\sigma_\infty a}{8G} \left[\frac{r}{a} (\kappa - 3) \sin \theta + 2 \frac{a}{r} ((1 - \kappa) \sin \theta + \sin 3\theta) - 2 \frac{a^3}{r^3} \sin 3\theta \right] \quad (5.11)$$

$$\sigma_{xx}(r, \theta) = \sigma_\infty \left[1 - \frac{a^2}{r^2} \left(\frac{3}{2} \cos 2\theta + \cos 4\theta \right) + \frac{3}{2} \frac{a^4}{r^4} \cos 4\theta \right] \quad (5.12)$$

$$\sigma_{yy}(r, \theta) = \sigma_\infty \left[-\frac{a^2}{r^2} \left(\frac{1}{2} \cos 2\theta - \cos 4\theta \right) - \frac{3}{2} \frac{a^4}{r^4} \cos 4\theta \right] \quad (5.13)$$

$$\sigma_{xy}(r, \theta) = \sigma_\infty \left[-\frac{a^2}{r^2} \left(\frac{1}{2} \sin 2\theta + \sin 4\theta \right) + \frac{3}{2} \frac{a^4}{r^4} \sin 4\theta \right] \quad (5.14)$$

where $\kappa = (3 - \nu)/(1 + \nu)$ and the modulus of rigidity, $G = E/(2(1 + \nu))$. We take Poisson's ratio, $\nu = 1/3$, and non-dimensionalize the equations so that $E = 1$. The LSFEM solution for an 18-element mesh with 8th order polynomials ($p = 8$) is given in Figure

5.10. The solution along the hole, Γ_5 , is compared with the analytic solution in Figure 5.11. One of the advantages of an LSFEM approach is that the solution permits a readily available error estimate in the form of the residual. Both the residual and the error norm are on the order of 10^{-4} for this relatively coarse mesh and moderate p -value. The peak normal stress at the apex of the hole is 30, leading to a stress concentration factor of 3, which matches the result obtained from strength of materials [91].

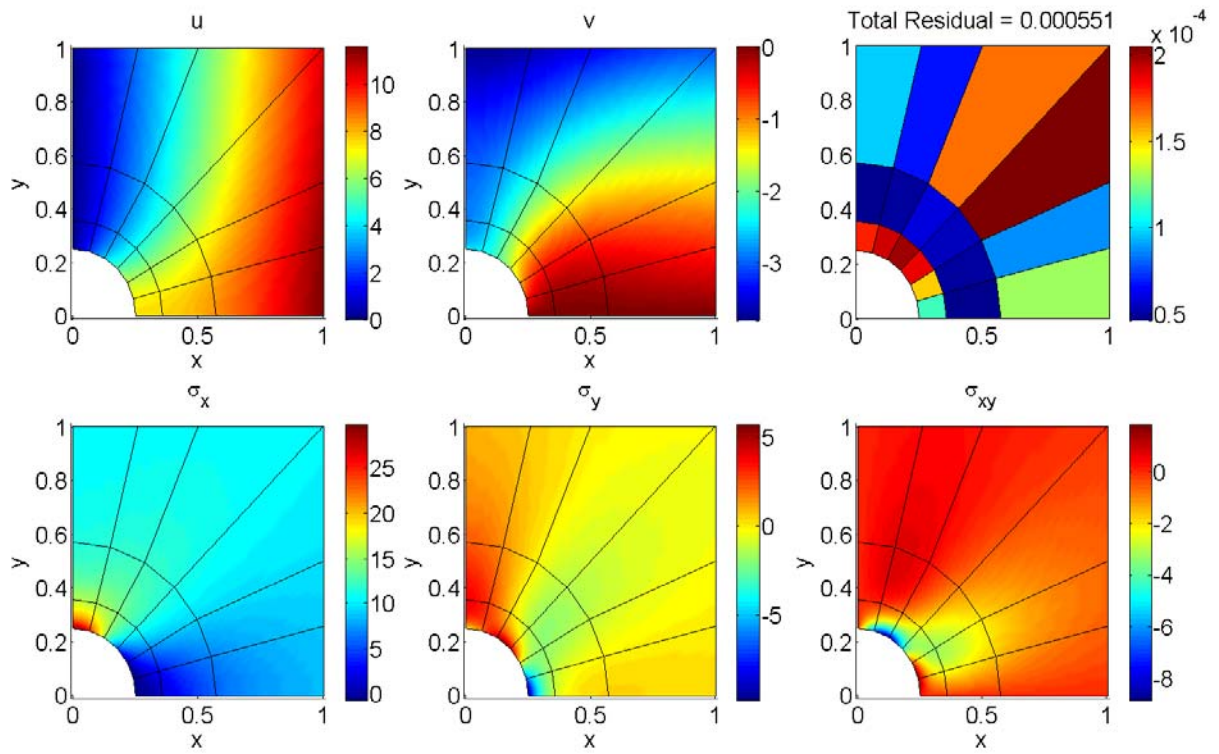


Figure 5.10 LSFEM Solution ($p = 8$) for Displacements (u, v) , Stresses $(\sigma_x, \sigma_y, \sigma_{xy})$, and Residual Error Norm of a Quarter Plate with a Circular Hole Subject to Normal- x Stress Value of 10.

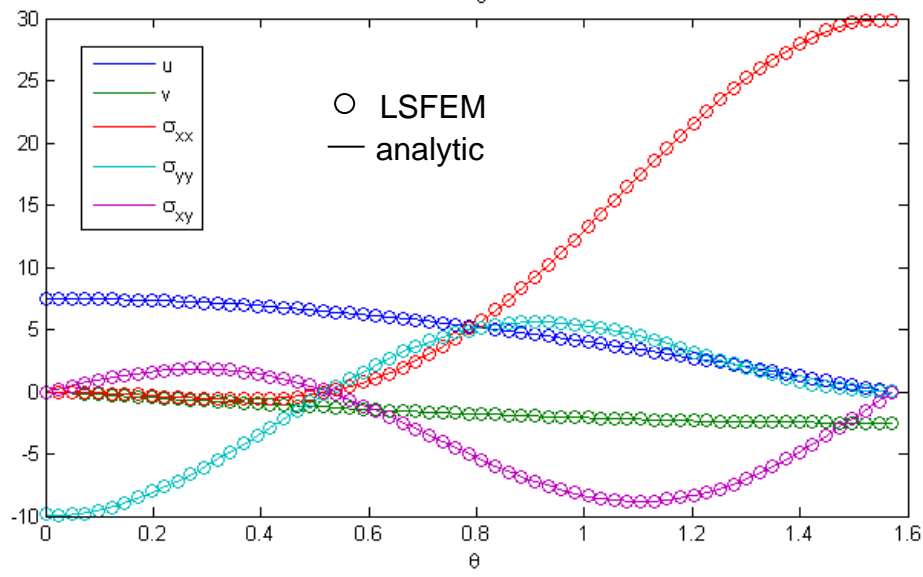


Figure 5.11 Comparison of LSFEM and Analytic Solution Along the Hole ($p = 8$)

Since the elasticity equations are linear, the LS-CSE first-order matrix operators are identical to the elasticity system operators. The boundary conditions at the hole remain the same (stress free) regardless of hole radius, hence the total material derivative of radial and shear along the hole is zero. Thus, the CSE boundary conditions along the hole are determined only by the transport term in (3.13). Taking hole radius, a , as the shape parameter, the Γ_1 , Γ_4 , and Γ_5 boundaries change with the hole. The hole coordinates are easily parameterized in polar coordinates as

$$X_{\Gamma_5} = \left\{ \begin{pmatrix} a & \theta \end{pmatrix}^T \right\}_{(r\theta)} \quad (5.15)$$

so that

$$X_{\Gamma_5,a} = \left\{ \begin{pmatrix} 1 & 0 \end{pmatrix}^T \right\}_{(r\theta)} \quad (5.16)$$

Similarly, in Cartesian coordinates,

$$X_{\Gamma_1} = \left\{ \left(\begin{bmatrix} 1-\xi & \xi \end{bmatrix} \begin{Bmatrix} a \\ 1 \end{Bmatrix} \right)^T \middle| \xi \in [0,1] \right\}_{(xy)} \quad (5.17)$$

$$X_{\Gamma_4} = \left\{ \left(\begin{bmatrix} 0 & 1-\xi & \xi \end{bmatrix} \begin{Bmatrix} b \\ 1 \end{Bmatrix} \right)^T \middle| \xi \in [0,1] \right\}_{(xy)} \quad (5.18)$$

Then, for a circular hole with $a = b$

$$X_{\Gamma_1,a} = \left\{ (1-\xi \ 0)^T \middle| \xi \in [0,1] \right\}_{(xy)} \quad (5.19)$$

$$X_{\Gamma_4,a} = \left\{ (0 \ 1-\xi)^T \middle| \xi \in [0,1] \right\}_{(xy)} \quad (5.20)$$

Now, differentiating the boundary conditions along Γ_1 and Γ_4 and evaluating the convection term with (5.19) and (5.20) yields the CSE boundary conditions for the Γ_1 and Γ_4 boundaries

$$\left\{ \begin{matrix} {}^a v(\xi) \\ {}^a \sigma_{xy}(\xi) \end{matrix} \right\}_{\Gamma_1} = \frac{D \{v \ \sigma_{xy}\}_{\Gamma_1}^T}{Da} - \left\{ \begin{matrix} \nabla v \\ \nabla \sigma_{xy} \end{matrix} \right\} \cdot \frac{\partial X_{\Gamma_1}}{\partial a} = 0 - \left\{ \begin{matrix} (1-\xi)v_{,x} \\ (1-\xi)\sigma_{xy,x} \end{matrix} \right\}_{\xi \in [0,1]} = 0 \quad (5.21)$$

$$\left\{ \begin{matrix} {}^a u(\xi) \\ {}^a \sigma_{xy}(\xi) \end{matrix} \right\}_{\Gamma_4} = \frac{D \{u \ \sigma_{xy}\}_{\Gamma_4}^T}{Da} - \left\{ \begin{matrix} \nabla u \\ \nabla \sigma_{xy} \end{matrix} \right\} \cdot \frac{\partial X_{\Gamma_4}}{\partial a} = 0 - \left\{ \begin{matrix} (1-\xi)u_{,y} \\ (1-\xi)\sigma_{xy,y} \end{matrix} \right\}_{\xi \in [0,1]} = 0 \quad (5.22)$$

For Γ_5 , the gradients in the convection term must be calculated from the gradients of the LSFEM solution and are not available by inspection as they are for Γ_1 and Γ_4 . The Γ_5 CSE boundary conditions are

$$\left\{ \begin{matrix} {}^a \sigma_{rr} \\ {}^a \sigma_{r\theta} \end{matrix} \right\}_{\Gamma_5} = \frac{D \{\sigma_{rr} \ \sigma_{r\theta}\}_{\Gamma_5}^T}{Da} - \nabla_{(r\theta)} \left\{ \begin{matrix} \sigma_{rr} \\ \sigma_{r\theta} \end{matrix} \right\} \cdot \frac{\partial}{\partial a} \{X_{\Gamma_5}\}_{(r\theta)} = \left\{ \begin{matrix} -\sigma_{rr,r} \\ -\sigma_{r\theta,r} \end{matrix} \right\} \quad (5.23)$$

where it should be noted that the gradient operator and boundary set definition must be expressed in the same coordinate system. The radial, shear, and tangential stress components along the hole are given by

$$\begin{bmatrix} \sigma_{rr} & \sigma_{r\theta} \\ \sigma_{\theta r} & \sigma_{\theta\theta} \end{bmatrix} = \begin{bmatrix} \cos \theta & \sin \theta \\ -\sin \theta & \cos \theta \end{bmatrix} \begin{bmatrix} \sigma_{xx} & \sigma_{xy} \\ \sigma_{yx} & \sigma_{yy} \end{bmatrix} \begin{bmatrix} \cos \theta & -\sin \theta \\ \sin \theta & \cos \theta \end{bmatrix} \quad (5.24)$$

Using this coordinate transformation and the polar coordinate gradient operator

$$\nabla_{(r\theta)} \equiv \left\langle \frac{\partial}{\partial r} \quad \frac{1}{r} \frac{\partial}{\partial \theta} \right\rangle \quad (5.25)$$

the radial gradients of the normal and shear stress components are

$$\sigma_{rr,r} = \sigma_{xx,r} \cos^2(\theta) + \sigma_{yy,r} \sin^2(\theta) + 2\sigma_{xy,r} \sin(\theta)\cos(\theta) \quad (5.26)$$

$$\sigma_{r\theta,r} = -(\sigma_{xx,r} - \sigma_{yy,r}) \sin \theta \cos \theta + \sigma_{xy,r} (\cos^2 \theta - \sin^2 \theta) \quad (5.27)$$

Expressing the radial gradient through the chain rule $\frac{d}{dr}(\cdot) = \frac{\partial(\cdot)}{\partial x} \frac{\partial x}{\partial r} + \frac{\partial(\cdot)}{\partial y} \frac{\partial y}{\partial r}$ and

noting that $x_{,r} = \cos \theta$ and $y_{,r} = \sin \theta$ yields the final radial and tangential stress CSE

boundary conditions in terms of Cartesian components

$$\begin{aligned} {}^a \sigma_{rr} = -\sigma_{rr,r} = & -(\sigma_{xx,x} \cos \theta + \sigma_{xx,y} \sin \theta) \cos^2 \theta - (\sigma_{yy,x} \cos \theta + \sigma_{yy,y} \sin \theta) \sin^2 \theta + \dots \\ & - 2(\sigma_{xy,x} \cos \theta + \sigma_{xy,y} \sin \theta) \cos \theta \sin \theta \end{aligned} \quad (5.28)$$

$$\begin{aligned} {}^a \sigma_{r\theta} = -\sigma_{r\theta,r} = & [(\sigma_{xx,x} - \sigma_{yy,x}) \cos \theta + (\sigma_{xx,y} - \sigma_{yy,y}) \sin \theta] \cos \theta \sin \theta + \dots \\ & - (\sigma_{xy,x} \cos \theta + \sigma_{xy,y} \sin \theta) (\cos^2 \theta - \sin^2 \theta) \end{aligned} \quad (5.29)$$

The spatial derivatives of the Cartesian stress components required in (5.28) and (5.29) come from the gradients of the shape functions of the LSFEM solution. The analytic and

LSFEM-derived boundary conditions for the hole in the CSE problem are compared in Figure 5.12.

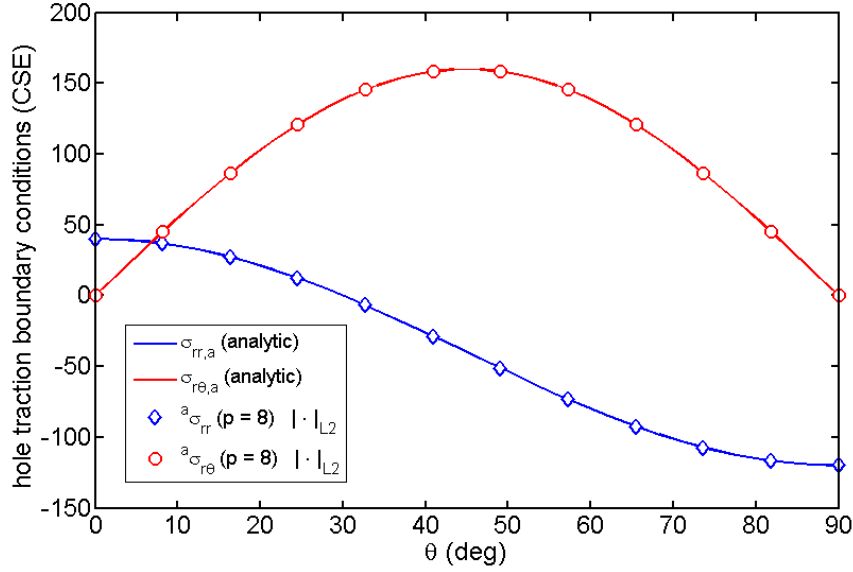


Figure 5.12 Comparison of analytic and LSFEM-derived sensitivity boundary conditions

Analytic sensitivities are readily obtained by differentiating (5.10)-(5.14) with respect to hole radius, a . The analytic sensitivities are

$$u_{,a} = \frac{\sigma_{\infty}}{8G} \left[4 \frac{a}{r} \left((1 + \kappa) \cos \theta + \cos 3\theta \right) - 8 \frac{a^3}{r^3} \cos 3\theta \right] \quad (5.30)$$

$$v_{,a} = \frac{\sigma_{\infty}}{8G} \left[4 \frac{a}{r} \left((1 - \kappa) \sin \theta + \sin 3\theta \right) - 8 \frac{a^3}{r^3} \sin 3\theta \right] \quad (5.31)$$

$$\sigma_{xx,a} = \sigma_{\infty} \left[-\frac{a}{r^2} (3 \cos 2\theta + 2 \cos 4\theta) + 6 \frac{a^3}{r^4} \cos 4\theta \right] \quad (5.32)$$

$$\sigma_{yy,a} = \sigma_{\infty} \left[-\frac{a}{r^2} (\cos 2\theta - 2 \cos 4\theta) - 6 \frac{a^3}{r^4} \cos 4\theta \right] \quad (5.33)$$

$$\sigma_{xy,a} = \sigma_{\infty} \left[-\frac{a}{r^2} (\sin 2\theta + 2 \sin 4\theta) + 6 \frac{a^3}{r^4} \sin 4\theta \right] \quad (5.34)$$

The LS-CSE solution for the same 18-element mesh ($p = 8$) is given in Figure 5.13. The local sensitivity solution for tangential stress along the hole is compared with the analytic solution in Figure 5.14. The finite difference and the total sensitivity calculated from the LS-CSE solution are also plotted in Figure 5.14. Note that as in the bar example given previously, the local and total derivatives yield significantly different results. The tangential stress along the hole of an infinite plate does not depend on the hole radius so the total sensitivity of the tangential stress at material points on the hole boundary is zero as expected.

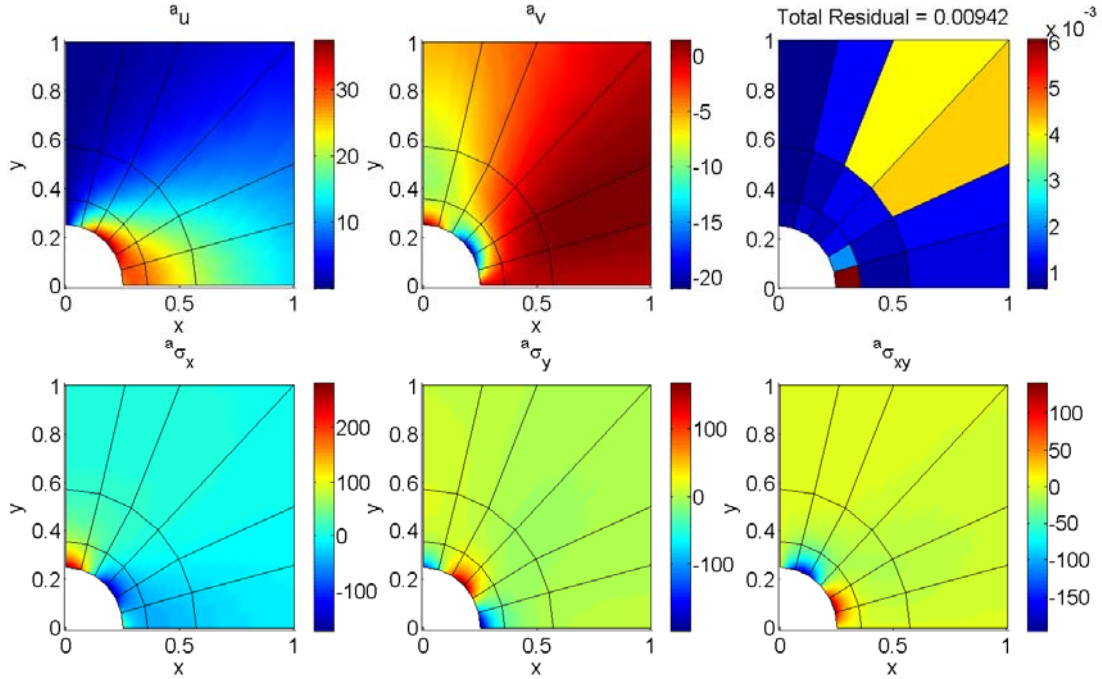


Figure 5.13 LS-CSE Solution ($p = 8$) and Residual Error Norm for the Sensitivity of Field Variables to Hole Radius, a , for a Quarter Plate with a Circular Hole

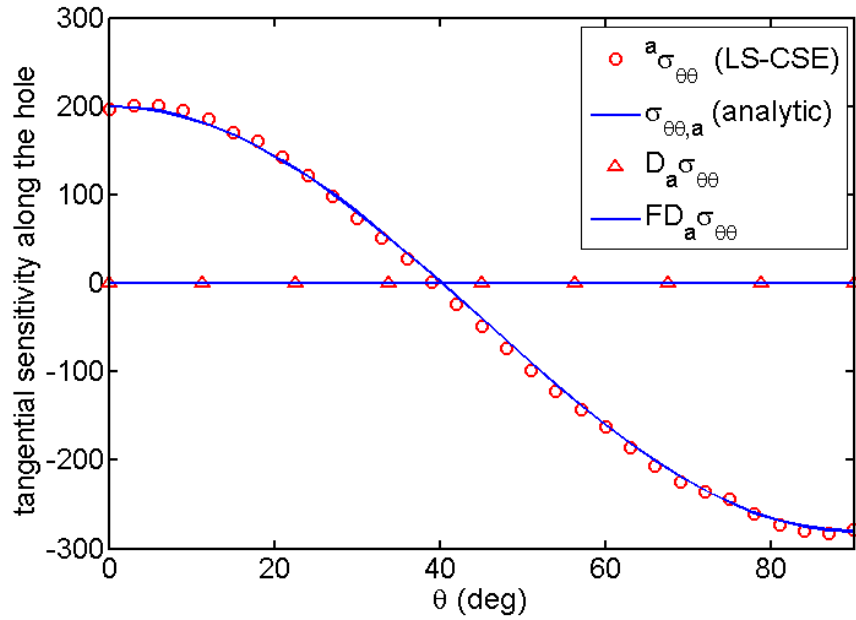


Figure 5.14 Comparison of Analytic, Finite Difference, and LS-CSE Solutions along the Hole Boundary for Tangential Stress Sensitivity to Hole Radius, a

Figure 5.15 plots the p -convergence for both the elasticity and sensitivity problems as well as the convergence of the maximum stress within the plate normalized by the loading stress. Note that for $p = 8$, the stress concentration approaches asymptotically the theoretical stress concentration factor of 3. The residual and the error norm for the $p = 8$ sensitivity solution given in Figure 5.13 and Figure 5.14 are both on the order of 10^{-2} ; two orders of magnitude greater than the original LSFEM problem at the same p -value. A polynomial order of 11 yields the equivalent 10^{-4} error for the LS-CSE problem as compared to the original LSFEM residual at $p = 8$. CSE systems typically have steeper gradients in the vicinity of a boundary subject to shape variation than the original problem and often require a higher p -value (or finer mesh) than the original system—a result previously observed [120, 135]. It is convenient to use the same mesh for both the original system and the sensitivity system and to obtain the more

refined solution through higher-order p -elements. This is a distinct advantage of higher-order FEM, since p -refinement allows a straightforward means to achieve a refined solution without needing a refined mesh.

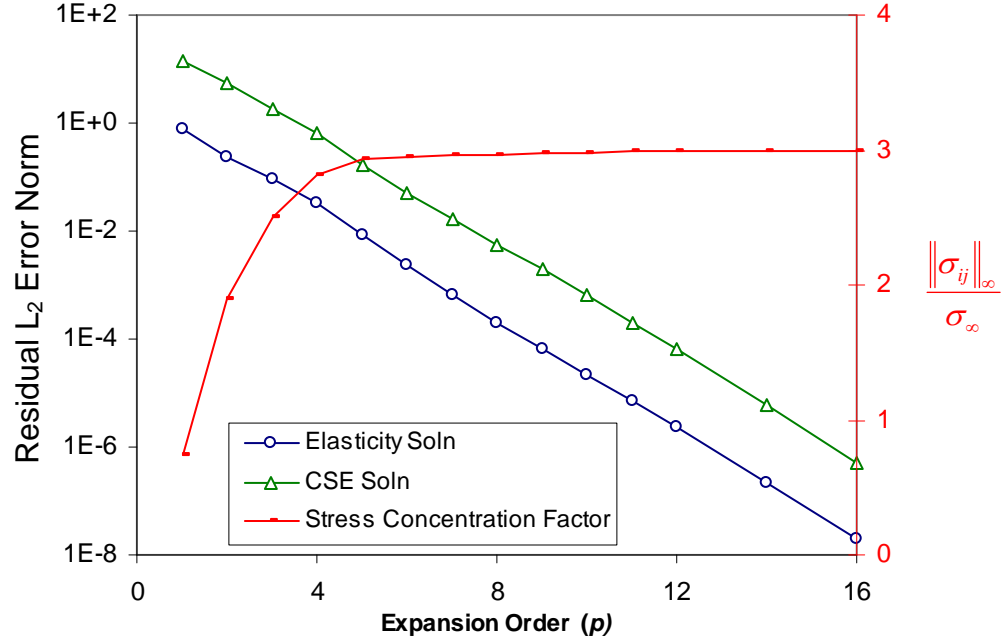


Figure 5.15 Elasticity and Sensitivity Problem p -convergence and Stress-Concentration Convergence for a Uniaxially Loaded Plate with a Circular Hole

5.2.2 Shape Optimization of a Biaxially-Loaded Plate with a Hole

Bhaskaran and Berkooz posed a shape optimization problem based on the plate with a hole which seeks the optimum dimensions of an elliptical hole to obtain a uniform distribution of the tangential stress along the hole [18]. The semi-major axis of the ellipse is constrained to be one-fifth of the edge of the square plate, and the semi-minor axis is taken as the design parameter. The applied loads are $\sigma_{xx} = 1$ MPa and $\sigma_{yy} = 0.75$ MPa. The objective function to be minimized is

$$J = \int_{\Gamma_5} \left(\sigma_{\theta\theta} - \bar{\sigma}_{\theta\theta} \right)^2 dE \quad (5.35)$$

where E is the eccentric anomaly of the elliptical hole and the mean tangential stress along the hole is

$$\bar{\sigma}_{\theta\theta} = \frac{2}{\pi} \int_0^{\pi/2} \sigma_{\theta\theta} dE \quad (5.36)$$

Bhaskaran and Berkooz posed the objective function as an integral over arc length. Evaluating the objective function (5.35) with respect to eccentric anomaly instead of arc length is equivalent to Bhaskaran and Berkooz but is simpler to implement since the sensitivity of the arc length (which is a function of semi-minor axis of the ellipse) does not have to be calculated. The only boundaries defined in Figure 5.9 that depend on the semi-minor axis are Γ_4 and Γ_5 . The first is parameterized by (5.18) and Γ_5 is given (in Cartesian coordinates) by

$$X_{\Gamma_5} = \left\{ \begin{pmatrix} a \cos E & b \sin E \end{pmatrix}^T \right\} \quad (5.37)$$

so that

$$X_{\Gamma_5, b} = \left\{ \begin{pmatrix} 0 & \sin E \end{pmatrix}^T \right\} \quad (5.38)$$

The objective function material gradient with respect to the semi-minor axis is

$$D_b J = 2 \int_{\Gamma_5} \left(\sigma_{\theta\theta} - \bar{\sigma}_{\theta\theta} \right) \left(D_b \sigma_{\theta\theta} - D_b \bar{\sigma}_{\theta\theta} \right) dE \quad (5.39)$$

where for the parameterization given by (5.37)

$$D_b \sigma_{\theta\theta} = {}^b \sigma_{\theta\theta} + \sin E \sigma_{\theta\theta, y} \quad (5.40)$$

$$D_b \bar{\sigma}_{\theta\theta} = \frac{2}{\pi} \int_0^{\pi/2} {}^b \sigma_{\theta\theta} dE + \frac{2}{\pi} \int_0^{\pi/2} \sin E \sigma_{\theta\theta, y} dE \quad (5.41)$$

The tangential stress sensitivity, ${}^b\sigma_{\theta\theta}$, is determined from the solution to the LS-CSE system. The CSE problem has homogeneous boundary conditions on every boundary except Γ_5 which are given by

$$\begin{Bmatrix} {}^b\sigma_{rr} \\ {}^b\sigma_{r\theta} \end{Bmatrix} = 0 - \nabla \begin{Bmatrix} \sigma_{rr} \\ \sigma_{r\theta} \end{Bmatrix} \cdot \begin{Bmatrix} 0 \\ \sin E \end{Bmatrix} = \begin{Bmatrix} -\sigma_{rr,y} \sin E \\ -\sigma_{r\theta,y} \sin E \end{Bmatrix} \quad (5.42)$$

The analytic stress concentration factors for an infinite biaxially-loaded plate are based on the maximum normal stresses σ_A and σ_B [91]

$$K_{tA} \equiv \frac{\sigma_A}{\sigma_{\Gamma_2}} = \frac{\sigma_{\Gamma_3}}{\sigma_{\Gamma_2}} \left[1 + \frac{2}{b/a} \right] - 1 \quad (5.43)$$

$$K_{tB} \equiv \frac{\sigma_B}{\sigma_{\Gamma_2}} = 1 + \frac{2b}{a} - \frac{\sigma_{\Gamma_3}}{\sigma_{\Gamma_2}} \quad (5.44)$$

where the points A and B are the apex and shoulder points indicated in Figure 5.9. Equating the stress concentration at these two points yields the desired uniform tangential stress around the ellipse and requires that

$$\frac{b}{a} = \frac{\sigma_{\Gamma_3}}{\sigma_{\Gamma_2}} \quad (5.45)$$

which yields an optimum semi-minor axis of 0.75 for the given loading. For an infinite plate, this yields a uniform stress concentration value of 1.75 around the hole. Various finite-width corrections [91] for semi-infinite plates under uniaxial loading yield approximate values 3% higher for stress concentrations for hole-to-edge ratios of 0.2. This implies a uniform tangential stress of 1.8 MPa for the present case which is very close to the 1.797 MPa result obtained from the simple line-search optimization based on the LS-CSE objective gradient of (5.39). The convergence history for the tangential stress is plotted in Figure 5.16 along with values of the objective function as a function of

eccentric anomaly along the hole. Values of the objective function and total objective function gradient are also summarized in Table 5.3. Note also that the residual error of 10^{-3} is comparable to the accuracy obtained in achieving a uniform stress distribution. This highlights that advantage of the built-in error estimate of the LSFEM approach.

Table 5.3: Plate with a elliptical hole optimization

b	J	$D_b J$	$\bar{\sigma}_{\theta\theta}$
1.0	1.56 E-1	1.960	1.814
0.804	6.00 E-3	0.363	1.799
0.764	2.88 E-4	0.140	1.797
0.75	9.22 E-5	-0.0118	1.797

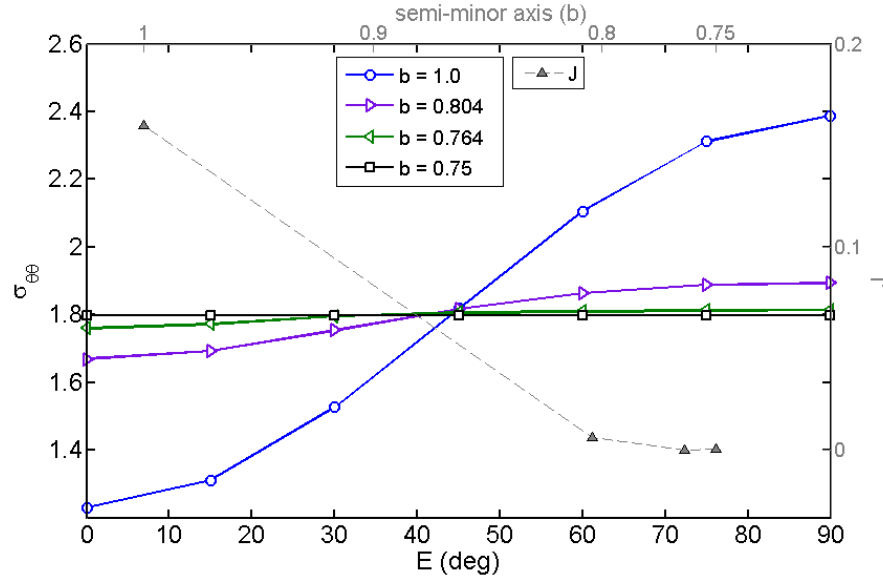


Figure 5.16 Tangential stress optimization convergence to uniform value ($\bar{\sigma}_{\theta\theta} = 1.797$) as a function of eccentric anomaly (E) and Objective function value as a function of semi-minor axis (b)

5.3 Summary

This chapter demonstrated the LS-CSE method for several 2D elasticity problems. Continuous sensitivity was first introduced for elasticity systems, but, as noted in Chapter 2, there is a dearth of applications of the method to actual problems. This may be in part that the derivation of the continuous sensitivity equations in the literature tends to obscure the simplicity of the continuous sensitivity system when posed in local derivative form. The local derivative form also leads to simpler boundary conditions for elasticity problems. Another advantage of the local derivative form demonstrated in these examples, is that only the boundary parameterization for shape variation problems need be described. This avoids having to define a parameterization or transformation function for the entire domain unless the material derivatives are also desired. The conversion from local to total sensitivity solution was demonstrated in each of the example problems and compared to analytic and finite difference sensitivities. Additionally, the LS-CSE results were used to demonstrate the optimization of an example problem from the literature.

The next chapter will demonstrate the LS-CSE method for several different fluid problems before we turn to the sensitivity analysis of FSI problems in a subsequent chapter.

6 LS-CSE For Fluids

This chapter presents two fluid flow problems together with flow sensitivity problems. This first problem (Section 6.1) is that of Stokes flow about a sphere which has an analytic solution and analytic sensitivity. The second problem (Section 6.2) is potential flow about an airfoil that is further studied in the FSI problems of the next Chapter.

6.1 Sphere in Stokes Flow

We now consider Stokes flow about an immersed sphere, a problem originally posed and solved by Stokes, c. 1851, using a stream function approach. The description and analytic solution are from [133], section 3.9-2. For sensitivity calculations, we take the sphere radius as the shape parameter.

The stream function for creeping flow past a sphere in polar coordinates is

$$\psi(r, \theta) = \frac{1}{4} U_{\infty} a^2 \sin^2 \theta \left(\frac{a}{r} - \frac{3r}{a} + \frac{2r^2}{a^2} \right) \quad (6.1)$$

The radial and tangential velocity components are determined from

$$u_r = \frac{1}{r^2 \sin \theta} \frac{\partial \psi}{\partial \theta} \quad (6.2)$$

$$u_{\theta} = \frac{-1}{r \sin \theta} \frac{\partial \psi}{\partial r} \quad (6.3)$$

Thus

$$u_r = U_{\infty} \cos \theta \left(1 + \frac{a^3}{2r^3} - \frac{3a}{2r} \right) \quad (6.4)$$

$$u_{\theta} = U_{\infty} \sin \theta \left(-1 + \frac{a^3}{4r^3} + \frac{3a}{4r} \right) \quad (6.5)$$

Additionally,

$$p = p_\infty - \frac{3\mu a U_\infty}{2r^2} \cos \theta \quad (6.6)$$

so that the analytic sensitivity to the sphere radius a is

$$u_{r,a} = U_\infty \cos \theta \left(\frac{3a^2}{2r^3} - \frac{3}{2r} \right) \quad (6.7)$$

$$u_{\theta,a} = U_\infty \sin \theta \left(\frac{3a^2}{4r^3} + \frac{3}{4r} \right) \quad (6.8)$$

$$p_{,a} = -\frac{3\mu U_\infty}{2r^2} \cos \theta \quad (6.9)$$

Vorticity is determined by taking the curl of velocity in curvilinear coordinates [74]

which in 2D polar coordinates reduces to

$$\omega = u_{\theta,r} - \frac{1}{r} u_{r,\theta} \quad (6.10)$$

Thus, the vorticity is given by

$$\omega = U_\infty \sin \theta \left(\frac{1}{r} - \frac{9a}{4r^2} - \frac{a^3}{4r^4} \right) \quad (6.11)$$

and the vorticity sensitivity to the sphere radius is

$$\omega_{,a} = U_\infty \sin \theta \left(-\frac{9}{4r^2} - \frac{3a^2}{4r^4} \right) \quad (6.12)$$

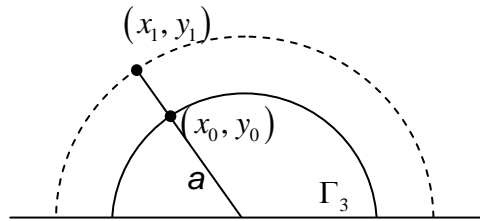


Figure 6.1: Sphere surface boundary parameterization and description.

The domain is parameterized with respect to sphere radius so that the material coordinates of the sphere surface boundary, Γ_3 , are given by

$$\mathbf{X}_{\Gamma_3} = \{(r, \theta) | r = a\} \quad (6.13)$$

The Γ_3 material coordinate sensitivity to a is then

$$\mathbf{X}_{\Gamma_3, a} = \{(1, 0)\} \quad (6.14)$$

The computational mesh for the flow and sensitivity problems is a half-sphere domain based on the symmetry of the problem, Figure 6.2 and Figure 6.3, which also includes descriptions of the boundary conditions.

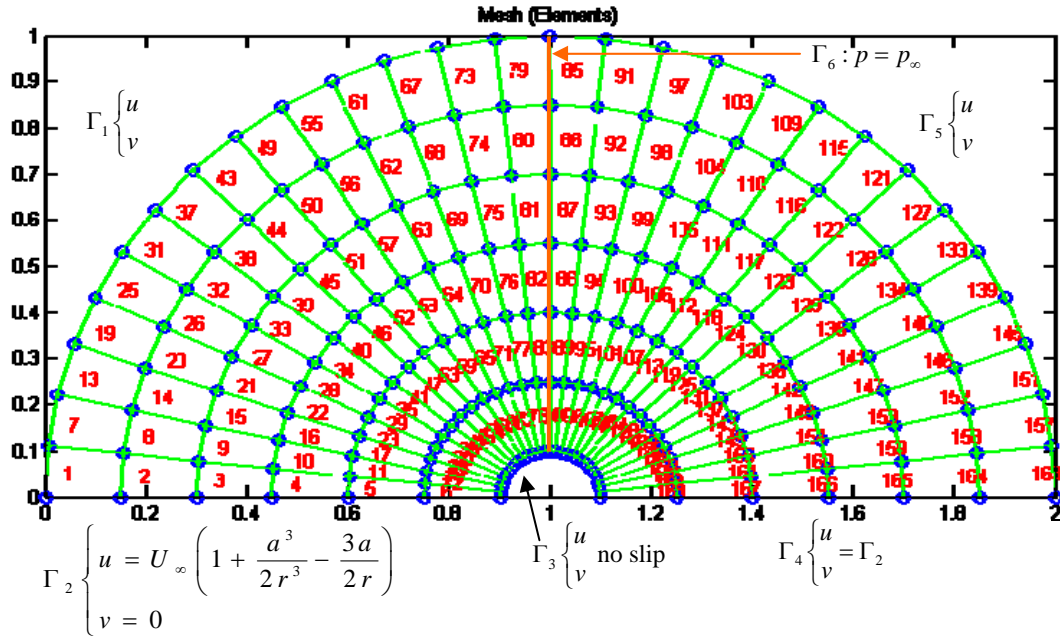
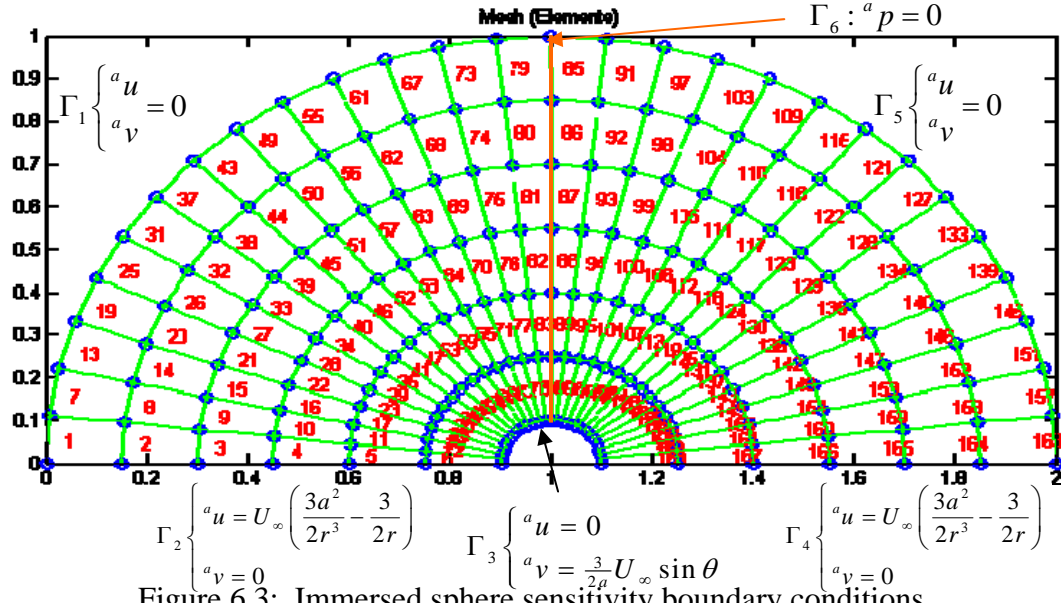


Figure 6.2: Immersed sphere computational mesh and boundary conditions



The LSFEM solution and analytic solutions are plotted in Figure 6.4 and Figure 6.5 and the sensitivities are plotted in Figure 6.6 and Figure 6.7. Another comparison of Stokes' flow is given in the next Section 7.2 in the context of an FSI solution.

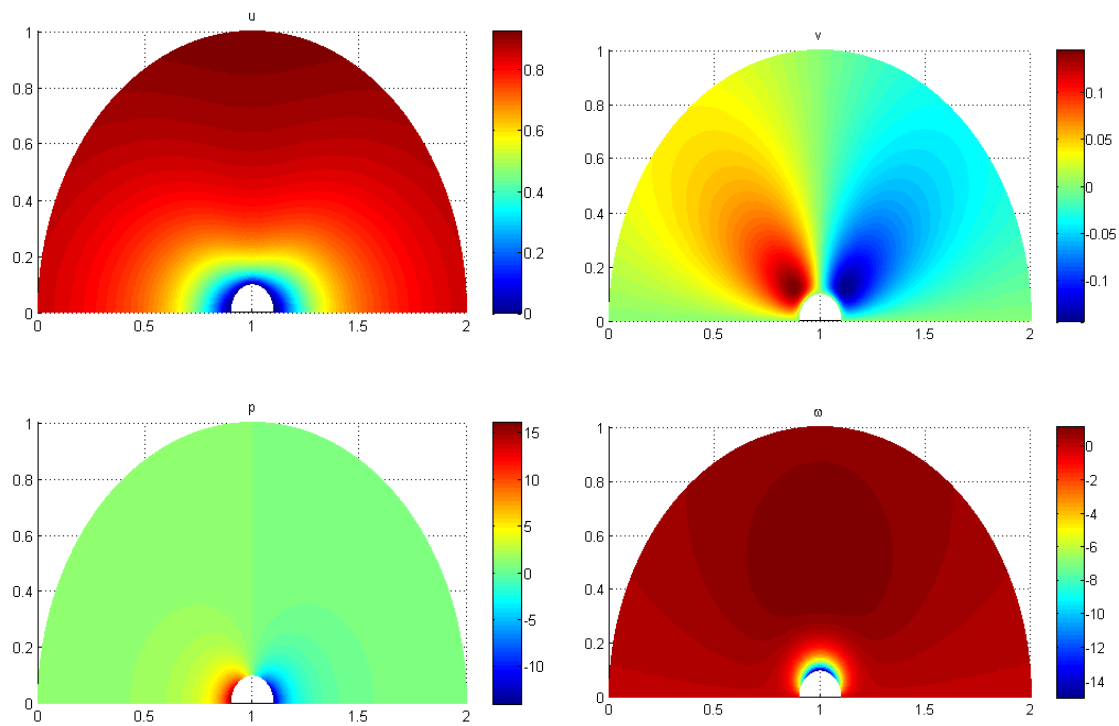


Figure 6.4: Sphere immersed in Stokes flow analytic solution

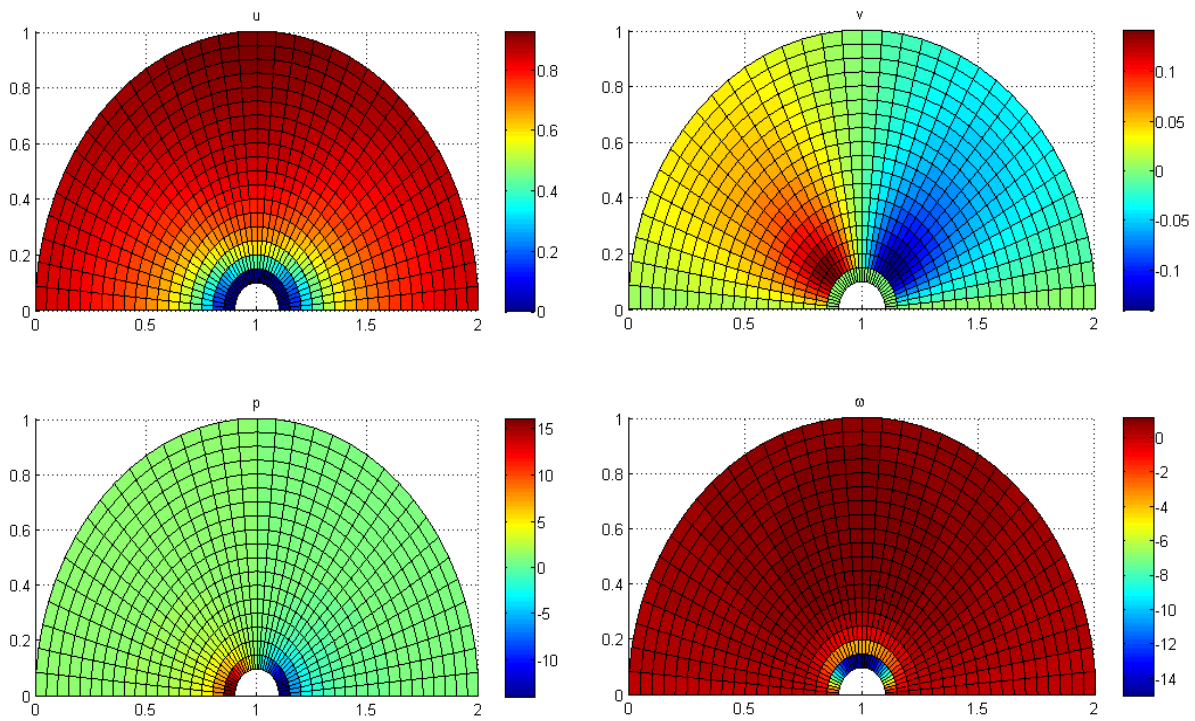


Figure 6.5: LSFEM solution for sphere immersed in Stokes Flow

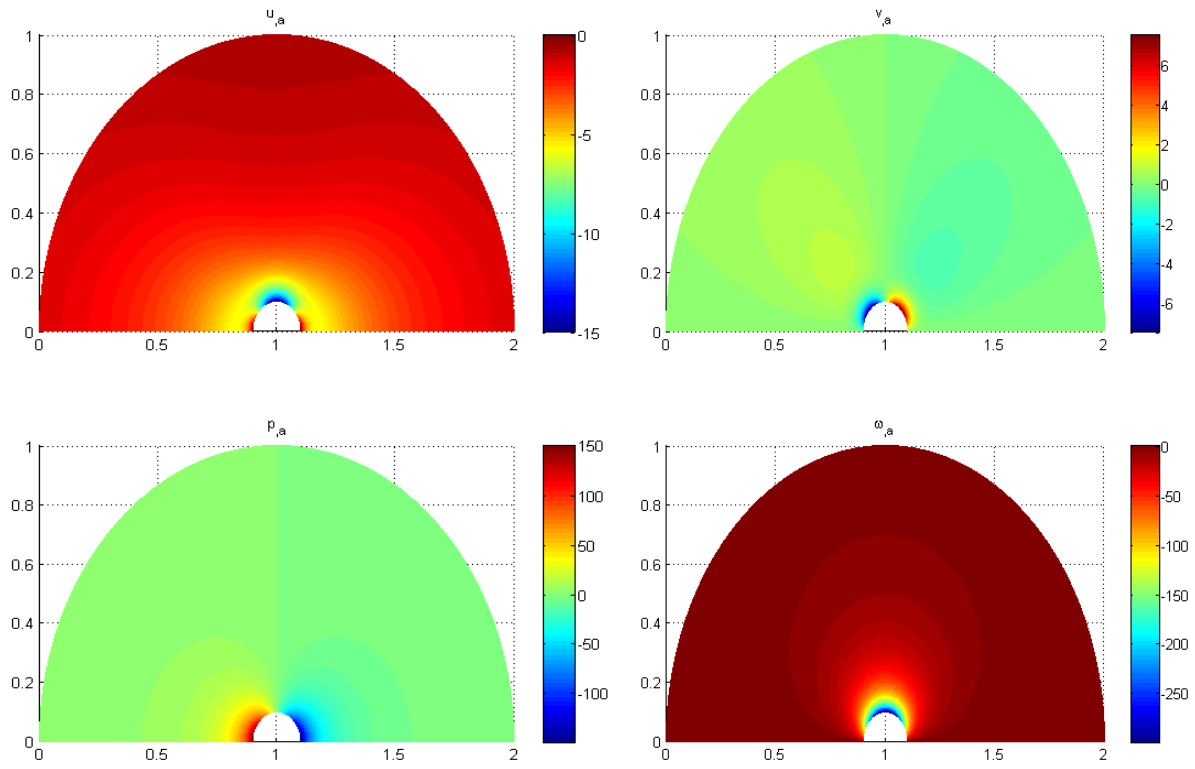


Figure 6.6: Sphere immersed in Stokes flow analytic sensitivity

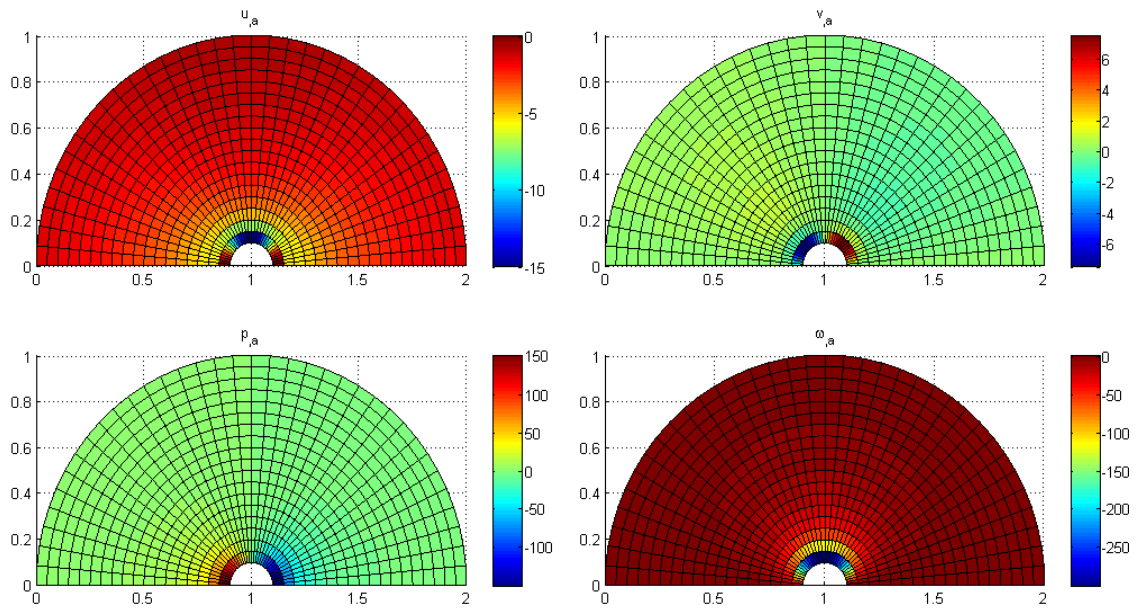


Figure 6.7: LS-CSE for sphere immersed in Stokes flow

6.2 Airfoil in potential flow

The LSFEM linear potential flow solution for a NACA 0012 airfoil at 10 deg angle of attack is given in Figure 6.8. Note that this is a zoom image of the computational mesh which extends out to a radius of 15 chord lengths in all directions, Figure 6.9. The velocity components along the upper and lower surface of the airfoil are compared with a vortex panel solution from [43] in Figure 6.10. The C_p values for the pressure derived from Bernoulli's equation is also compared with the vortex panel solution in Figure 6.11. The freestream flow boundary conditions are a function of angle of attack:

$$\begin{aligned} u_\infty &= U_\infty \cos \alpha \\ v_\infty &= U_\infty \sin \alpha \end{aligned} \quad (6.15)$$

where U_∞ is the freestream velocity and α is the angle of attack of the airfoil. The boundary conditions on the surface of the airfoil are

$$\mathbf{u} \cdot \hat{n} = 0 \quad (6.16)$$

where \hat{n} is the outward surface normal unit vector and $\mathbf{u} = \{u \ v\}^T$ are the velocity components and primary variables.

The flow sensitivity to angle of attack will be of interest in some of the Chapter 7 example FSI problems. The boundary conditions for the CSE problem are

$$\begin{aligned} {}^\alpha u_\infty &= -U_\infty \sin \alpha \\ {}^\alpha v_\infty &= U_\infty \cos \alpha \end{aligned} \quad (6.17)$$

and

$${}^\alpha \mathbf{u} \cdot \hat{n} = 0 \quad (6.18)$$

The angle of attack CSE solution is plotted in Figure 6.12 and Figure 6.13.

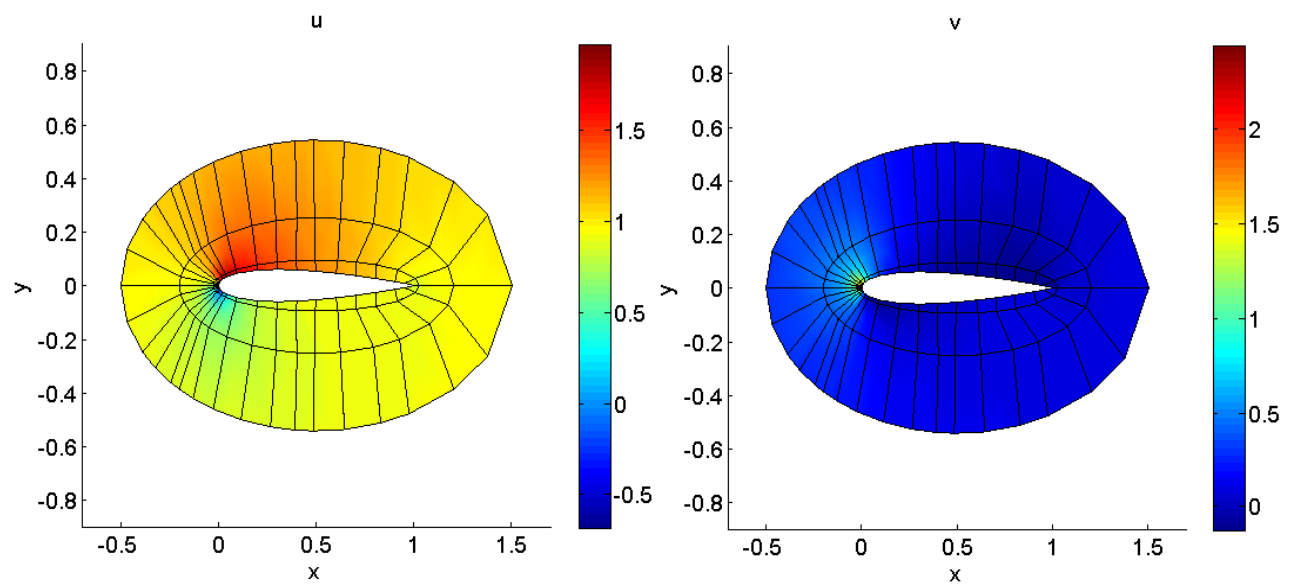


Figure 6.8: Velocity component solution for potential flow about NACA 0012 airfoil at 10 deg AOA ($p = 12$)

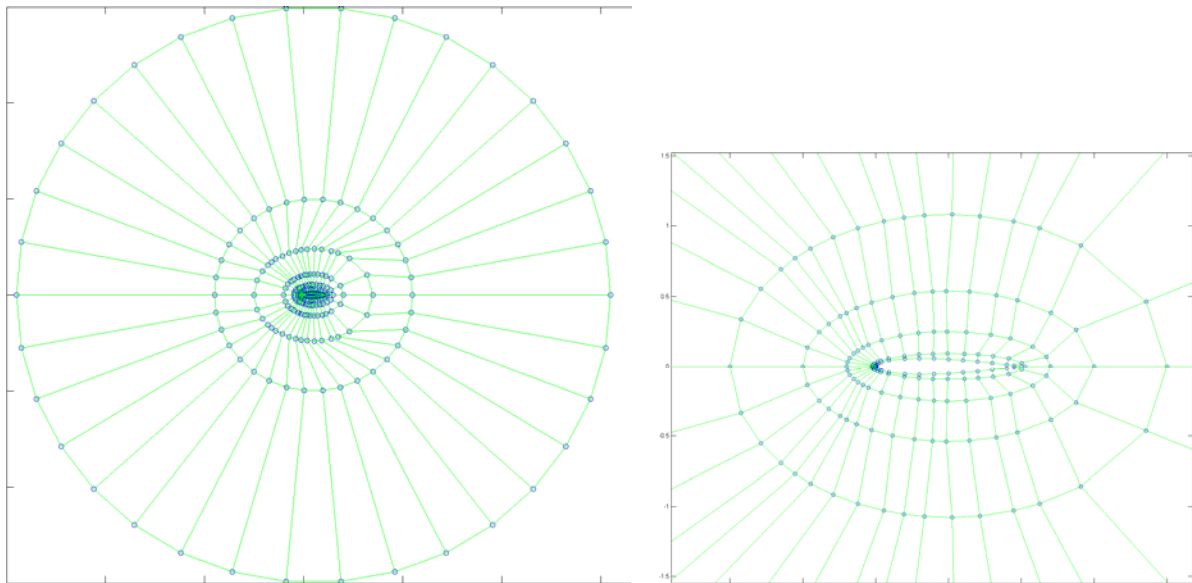


Figure 6.9: NACA 0012 airfoil 238 element computational mesh (full mesh, left; close-up of airfoil, right)

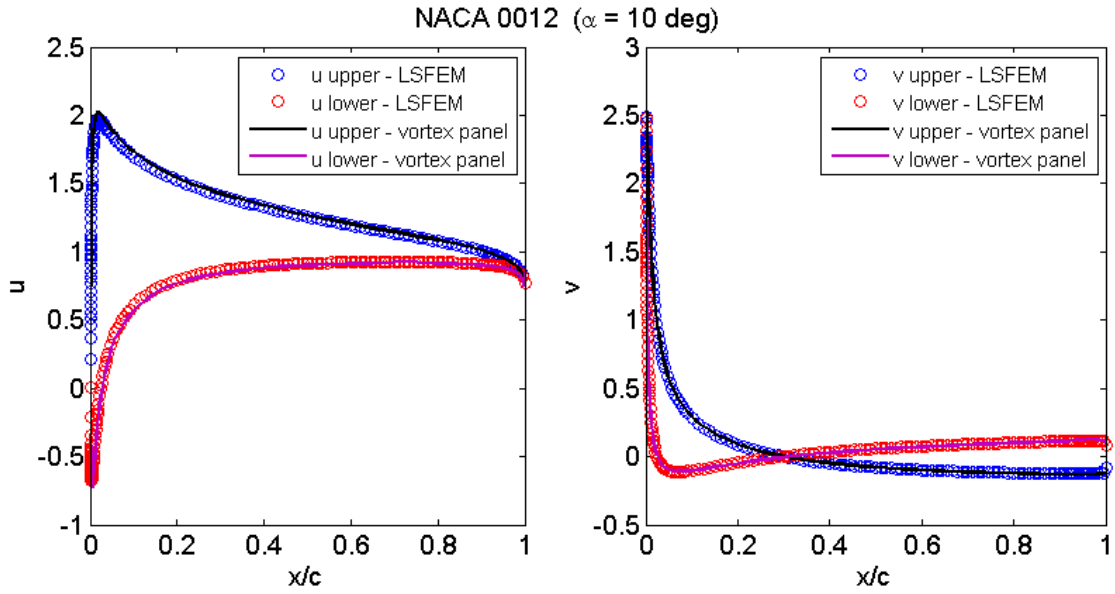


Figure 6.10: Comparison of flow solution at airfoil surface to vortex panel solution ($p =$
12)

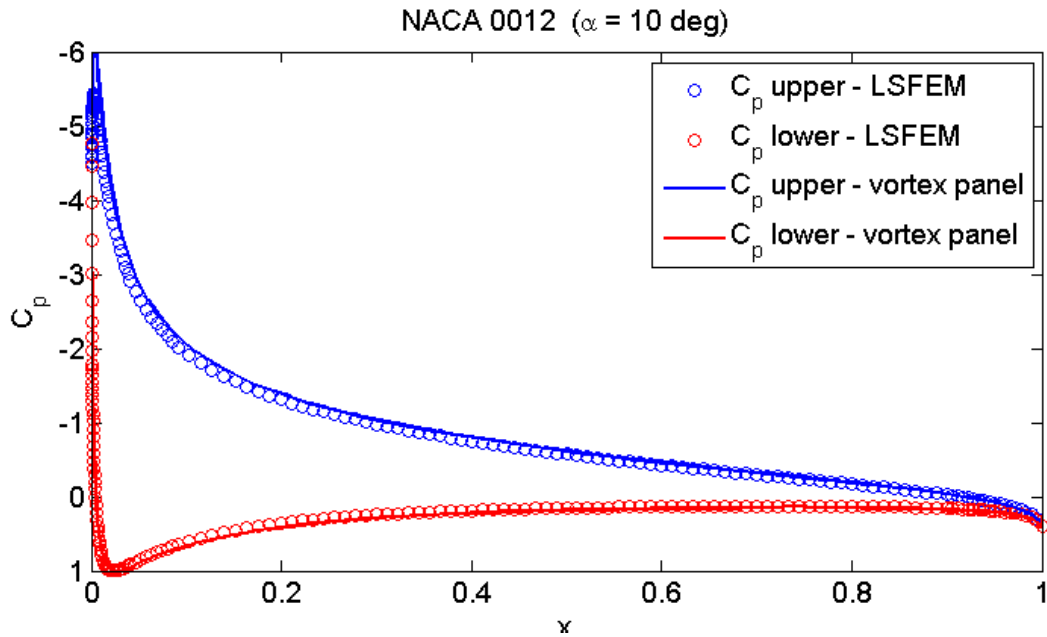


Figure 6.11: C_p for LSFEM and vortex panel for NACA 0012 airfoil

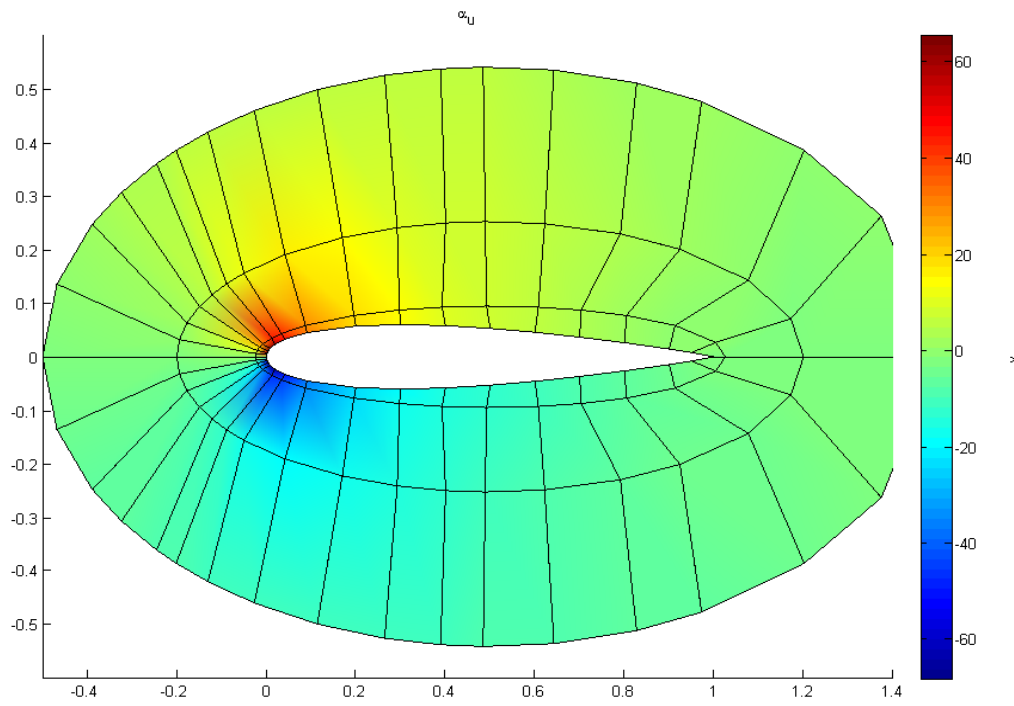


Figure 6.12: Potential flow u component velocity sensitivity to angle of attack for NACA 0012 airfoil.

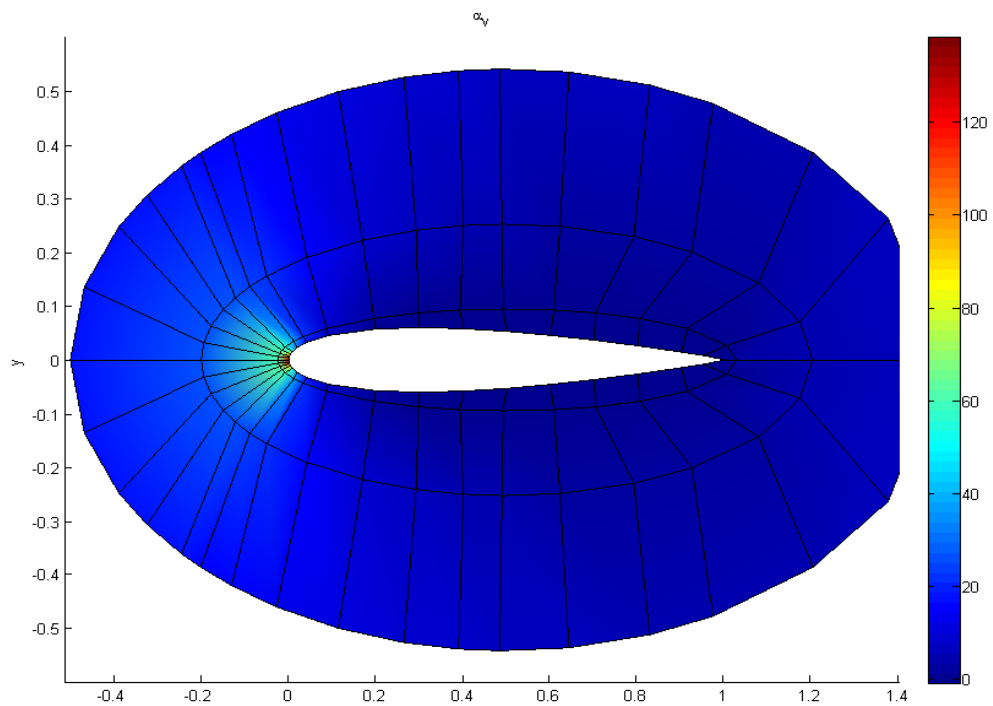


Figure 6.13: Potential flow v component velocity sensitivity to angle of attack for NACA 0012 airfoil.

We now compare the steady, compressible solution for flow about a NACA 0012 airfoil using two different models. The first is the nonlinear, compressible potential model developed in Section 4.5.2. In the second, pressure is determined through Bernoulli's equation of the vortex panel solution (which has already been compared and is equivalent to an incompressible solution of the linear potential flow equation in which the speed of sound becomes infinite). The pressure is then corrected for compressibility using the Prandtl-Glauert compressibility correction (4.73). The results are plotted in Figure 6.14 for a 10 deg angle of attack flow at 0.5 M. Eight nonlinear iterations using direct substitution are required for the compressible potential solution. The agreement is very good except for the very tip of the leading edge of the airfoil. The LS residual in the elements at the leading edge is an order of magnitude greater than the residual in the elements along the rest of the surface of the airfoil. The LE residual improves with increased p , but the solution in Figure 6.14 is the highest p within the given desktop computer memory limits. It is expected that further h (mesh size) or p refinement would improve the convergence of the LE solution the compressibility-corrected linear potential solution and the vortex panel solution. The very close agreement of the compressibility-corrected linear potential solution with the more computationally expensive FPE solution motivates a strategy for employing the compressibility-corrected linear potential solution for computationally expensive FSI problems. The next chapter presents LS-CSE sensitivity solutions for FSI including linear potential flow, compressibility-corrected flow, and full potential equation flow.

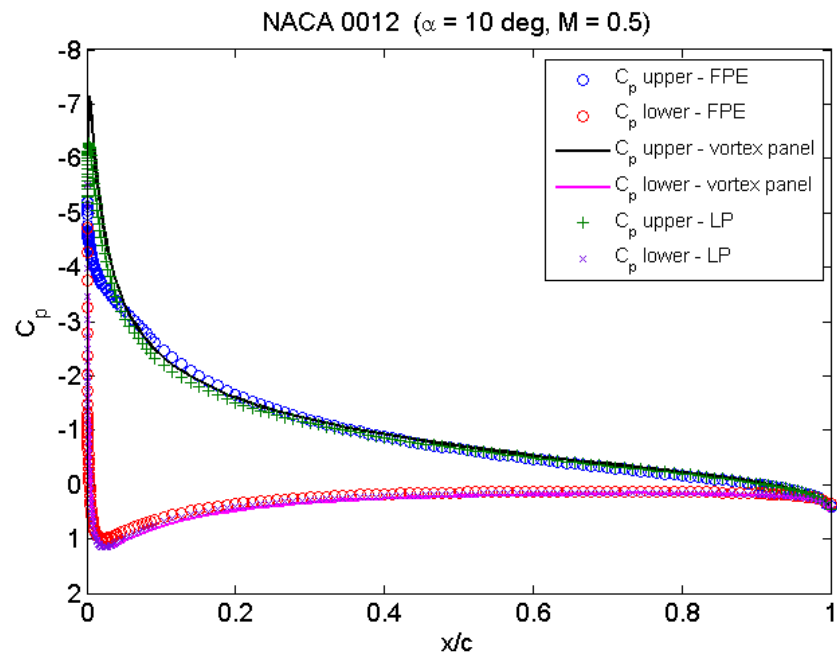


Figure 6.14: Steady, compressible flow solution (0.5 M) for the nonlinear potential model (8 nonlinear iterations) and the linear potential solution and vortex panel data corrected for compressibility

7 LS-CSE For Transient FSI

The least-squares continuous sensitivity method is now applied to calculate the shape design sensitivities for a series of fluid-structure example problems. The first two examples employ a monolithic (fully-coupled) fluid-structure analysis and sensitivity formulation. Section 7.1, the Golden Piston, is a simple, steady problem with closed form solutions for both the analysis and sensitivity problems that serves to illustrate all aspects of the fluid-structure interaction calculations. Section 7.2, a flexible beam immersed in channel flow, is a more complicated problem that was previously reported in [135]. Section 7.3 describes the analysis and sensitivity of an airfoil mounted on a flexible sting that is motivated by the gust response of a joined wing configuration. The steady solution, Section 7.3.1, considers both linear potential and compressible potential fluid equations and is compared with an analytic solution. A typical section aeroelastic model that is used for validation of the transient solutions that follow is described in Section 7.3.2. The transient gust response model is also described in this section. The full potential transient FSI with nonlinear structural gust response is detailed in Section 7.3.3. This includes structural buckling, a characteristic of joined wing configurations. Finally, the nonlinear, transient compressible FSI solution is compared with the linear potential solution corrected for compressibility in Section 7.3.4. The close agreement between these approaches should permit significant computational savings in future analysis since the nonlinear, compressible fluid solution can be modeled from the linear potential fluid solution.

The series of example problems considered in Section 7.3 contain all the aspects of more complex fluid-structure interaction problems, but are relatively small scale which

makes them interesting examples for the study of various phenomena including compressibility, geometric nonlinear stiffening, buckling, and the sensitivity of each of these responses to design parameters. In addition to validating the use of linear potential fluid corrected for compressibility, the model problem is itself a promising test case for the verification and validation of other fluid-structure interaction solvers.

7.1 Golden Piston

The Golden Piston problem consists of an inflexible pressure vessel with a flexible bar (piston) at one end that can compress in response to the static pressure in the pressure vessel, Figure 7.1. As the piston moves to the right, the fluid-structure interface moves right, increasing the volume of the chamber with a corresponding drop in the static pressure. The fluid variables are pressure, p , and the structure variables are displacement and stress, u and σ . The fluid-structure interface condition is the equilibrium condition between the fluid forces and the structure forces at the tip of the bar

$$\Gamma^{sf} : \{p = -\sigma_x\} \quad (7.1)$$

Ω^f Ω^s

$\mathbf{u}^f = \{p\}$ pressure vessel bar A, E $\mathbf{u}^s = \{u \ \sigma\}^T$

L_f x_0 L_s x_1

$\Gamma^{sf} : \{p = -\sigma_x\}$

$p = p_0 \left(\frac{L_f}{L_f + u} \right)$ $\sigma_{x,x} + \frac{1}{A} f_x = 0$

Boyle's Law $u_{,x} - \frac{1}{E} \sigma_x = 0$

Figure 7.1: Golden Piston problem description

The analytic solution for the displacement of the interface, pressure, and stress is

$$u_{x_0} = u|_{x_0} = -\frac{1}{2}L_f + \sqrt{\frac{1}{4}L_f^2 + \frac{p_0}{E}L_sL_f} \quad (7.2)$$

$$p = p_0 \frac{L_f}{L_f + u_{x_0}} \quad (7.3)$$

$$\sigma_x = -p \quad (7.4)$$

where p_0 is the initial pressure in the chamber, L_f is the length of the pressure vessel, L_s is the length of the bar, and E and A are the modulus and cross section of the bar. For $E = L_s = L_f = p_0 = 1$ with no body forces, the analytic solution for pressure, stress, and interface displacement is

$$u_{x_0} = -\sigma = p = \frac{1}{\phi} \quad (7.5)$$

where ϕ is the famous golden ratio or golden mean: $\phi = \frac{1+\sqrt{5}}{2} = 1.618\dots$. Hence the moniker for the problem. Taking bar length as the shape design parameter, the analytic sensitivities to bar length are

$$u_{x_0, L_s} = \frac{1}{2} \left[\frac{1}{4}L_f^2 + \frac{p_0}{E}L_sL_f \right]^{-\frac{1}{2}} \frac{p_0}{E}L_f \quad (7.6)$$

$$p_{, L_s} = \frac{-p_0^2 L_f^2}{2E \left(\frac{1}{2}L_f + \sqrt{\frac{1}{4}L_f^2 + \frac{p_0}{E}L_sL_f} \right)^2 \sqrt{\frac{1}{4}L_f^2 + \frac{p_0}{E}L_sL_f}} \quad (7.7)$$

$$\sigma_{x, L_s} = \frac{p_0^2 L_f^2}{2E \left(\frac{1}{2}L_f + \sqrt{\frac{1}{4}L_f^2 + \frac{p_0}{E}L_sL_f} \right)^2 \sqrt{\frac{1}{4}L_f^2 + \frac{p_0}{E}L_sL_f}} \quad (7.8)$$

The fully-coupled total residual for the FSI problem is

$$J_{tot} = \alpha^s J^s + \alpha^f J^f + \alpha^{sf} J^{sf} + \sum_{i \in \{\Gamma_{weak}\}} \alpha^{\Gamma_i} J^{\Gamma_i} \quad (7.9)$$

where α are the weighting factors for each of the component residuals (s : structure, f : fluid, sf : fluid-structure interface relations) and the last term is the boundary residual for

any weakly (integral) enforced boundary conditions. The monolithic LSFEM model then has the form

$$\begin{bmatrix} \alpha^s \mathbf{K}^s & 0 \\ 0 & \alpha^f \mathbf{K}^f \end{bmatrix} + \alpha^{sf} \mathbf{K}^{sf} \mathbf{u} = \begin{Bmatrix} \alpha^s \mathbf{F}^s \\ \alpha^f \mathbf{F}^f \end{Bmatrix} + \alpha^{sf} \mathbf{G}^{sf} \quad (7.10)$$

For a single, linear bar element ($p = 1$) and a single fluid element, the monolithic system is

$$\begin{bmatrix} 1 & \frac{1}{2} & -1 & \frac{1}{2} & 0 \\ \frac{1}{2} & \frac{4}{3} & -\frac{1}{2} & -\frac{5}{6} & 0 \\ -1 & -\frac{1}{2} & 1 & -\frac{1}{2} & 0 \\ \frac{1}{2} & -\frac{5}{6} & -\frac{1}{2} & \frac{4}{3} & 0 \\ 0 & 0 & 0 & 0 & L_f + u_1 \end{bmatrix} \begin{Bmatrix} u_1 \\ \sigma_1 \\ u_2 \\ \sigma_2 \\ p_1 \end{Bmatrix} + \alpha^{sf} \begin{bmatrix} 0 & 0 & 0 & 0 & 0 \\ 0 & 1 & 0 & 0 & 1 \\ 0 & 0 & 0 & 0 & 0 \\ 0 & 0 & 0 & 0 & 0 \\ 0 & 1 & 0 & 0 & 1 \end{bmatrix} \begin{Bmatrix} u_1 \\ \sigma_1 \\ u_2 \\ \sigma_2 \\ p_1 \end{Bmatrix} + \alpha^{\Gamma_2} \begin{bmatrix} 0 & 0 & 0 & 0 & 0 \\ 0 & 0 & 0 & 0 & 0 \\ 0 & 0 & 1 & 0 & 0 \\ 0 & 0 & 0 & 0 & 0 \\ 0 & 0 & 0 & 0 & 0 \end{bmatrix} \begin{Bmatrix} u_1 \\ \sigma_1 \\ u_2 \\ \sigma_2 \\ p_1 \end{Bmatrix} = \begin{Bmatrix} 0 \\ 0 \\ 0 \\ 0 \\ p_0 L_f \end{Bmatrix} \quad (7.11)$$

where the Γ_2 boundary is the bar's fixed right end. The last term on the left-hand side is the weak boundary system which may be enforced directly instead of including it in (7.11). Since the original monolithic system is nonlinear (due to the fluid force dependence on interface displacement), the LS-CSE finite element model takes a different form. The linear LS-CSE system is

$$\begin{bmatrix} 1 & \frac{1}{2} & -1 & \frac{1}{2} & 0 \\ \frac{1}{2} & \frac{4}{3} & -\frac{1}{2} & -\frac{5}{6} & 0 \\ -1 & -\frac{1}{2} & 1 & -\frac{1}{2} & 0 \\ \frac{1}{2} & -\frac{5}{6} & -\frac{1}{2} & \frac{4}{3} & 0 \\ \frac{p_0 L_f}{(L_f + u_1)^2} & 0 & 0 & 0 & 1 \end{bmatrix} \begin{Bmatrix} {}^L u_1 \\ {}^L \sigma_1 \\ {}^L u_2 \\ {}^L \sigma_2 \\ {}^L p_1 \end{Bmatrix} + \alpha^{sf} \begin{bmatrix} 0 & 0 & 0 & 0 & 0 \\ 0 & 1 & 0 & 0 & 1 \\ 0 & 0 & 0 & 0 & 0 \\ 0 & 0 & 0 & 0 & 0 \\ 0 & 1 & 0 & 0 & 1 \end{bmatrix} \begin{Bmatrix} {}^L u_1 \\ {}^L \sigma_1 \\ {}^L u_2 \\ {}^L \sigma_2 \\ {}^L p_1 \end{Bmatrix} + \alpha^{\Gamma_2} \begin{bmatrix} 0 & 0 & 0 & 0 & 0 \\ 0 & 0 & 0 & 0 & 0 \\ 0 & 0 & 1 & 0 & 0 \\ 0 & 0 & 0 & 0 & 0 \\ 0 & 0 & 0 & 0 & 0 \end{bmatrix} \begin{Bmatrix} {}^L u_1 \\ {}^L \sigma_1 \\ {}^L u_2 \\ {}^L \sigma_2 \\ {}^L p_1 \end{Bmatrix} = \begin{Bmatrix} 0 \\ 0 \\ u_{2,x} \\ 0 \\ 0 \end{Bmatrix} \quad (7.12)$$

where, as before, the weak boundary matrix associated with the bar's fixed end may be enforced directly. The numerical solution to (7.11) is

$$\begin{Bmatrix} u_1 \\ \sigma_1 \\ u_2 \\ \sigma_2 \\ p_1 \end{Bmatrix} = \begin{Bmatrix} 0.618 \\ -0.618 \\ 0 \\ -0.618 \\ 0.618 \end{Bmatrix} \quad (7.13)$$

which matches the analytic solution (7.5) (note that one of the properties of the golden ratio is that $\frac{1}{\phi} = \phi - 1$). The solution to the LS-CSE system (7.12) is

$$\begin{Bmatrix} {}^L u_1 \\ {}^L \sigma_1 \\ {}^L u_2 \\ {}^L \sigma_2 \\ {}^L p_1 \end{Bmatrix} = \begin{Bmatrix} .4472 \\ .1708 \\ .6180 \\ .1708 \\ -.1708 \end{Bmatrix} \quad (7.14)$$

which again matches (7.6)-(7.8).

This is an interesting problem in that it is small enough to be solved by hand and yet it illustrates all of the aspects of a monolithic, fully-coupled FSI system with weak boundary enforcement. In addition, the FSI problem is nonlinear and results in a good demonstration of the sensitivity solution to a nonlinear FSI problem. Further, the analytic solution is readily compared with the FEM solution. We now turn to the sensitivity analysis of another FSI problem with an analytic FSI solution.

7.2 Flexible beam in a channel

The example FSI problem in Figure 7.2 has a closed-form analytic solution [130]. A flexible 1D Euler-Bernoulli beam divides two channels with pressure-driven Stokes flow. A difference in flow rates for the two channels results in a differential pressure load and deflection of the beam.

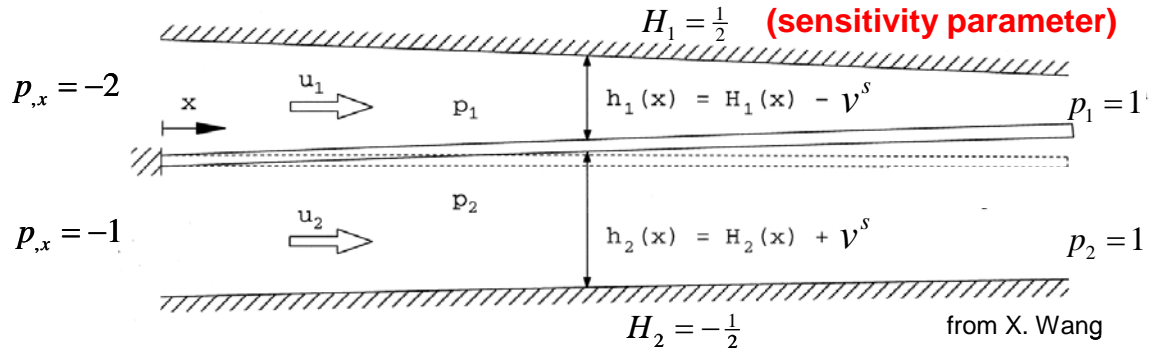


Figure 7.2: Beam immersed in a channel flow (X. Wang)

The FSI problem boundary conditions are given in Table 7.1. The fluid-structure interface is coupled with the fluid and structure domain residuals to form a fully-coupled, monolithic FSI problem. The fluid mesh deformation problem is decoupled from the FSI problem. This maintains the parallel structure of the sensitivity system with the FSI solution. Including the mesh deformation in the FSI problem would result in calculating the mesh sensitivity during the CSE; a computational expense that is not required when the sensitivity problem is posed in local derivative form.

Table 7.1: Beam in channel flow boundary conditions

Boundary	Constrained dofs	
inlet	$u = \frac{-1}{2\mu} (yh - y^2) p_{,x} ; \omega = -u_{,y}$	fully-developed Poiseuille flow
outlet	$v = 0 \quad p = 1$	uniform outflow
walls	$u_t = u^f \cos \theta^s + v^f \sin \theta^s = 0$ $u_n = -u^f \sin \theta^s + v^f \cos \theta^s = 0$	no slip wall
beam-fluid interface	$V_{y,x}^s + (p_1^f - p_2^f) = 0$	force equilibrium
mesh	$\mathbf{d}_i = \left(0 \quad w \frac{1}{h_i} [h_i - y] \right)$	vertically scaled deformation (de-coupled from FSI solution)

The slip wall (fluid-structure interface) relation in terms of the fluid tangential and normal velocities

$$\begin{aligned} u_t &= u^f \cos \theta^s + v^f \sin \theta^s = 0 \\ u_n &= -u^f \sin \theta^s + v^f \cos \theta^s = 0 \end{aligned} \tag{7.15}$$

where θ^s is the beam rotation and the f superscript represents fluid variables. This is a nonlinear fluid-structure coupling term which appears in the FSI problem through the boundary integral evaluation. However, because of the small deflections of the structure, a single iteration results in a converged solution (note that both the fluid and structure equations are linear). The total fluid residual after a single iteration is on the order of 10^{-13} . Referring to Figure 7.3, the greatest fluid residual is in the vicinity of the inlet where the mesh does not change. Subsequent iterations with the deformed mesh does not change the level of the residual in either the fluid or structure. The LSFEM FSI solution for the problem parameters given Table 7.2 is plotted in Figure 7.3. The beam deflection is compared to the analytic solution [130] in Figure 7.4

Table 7.2: Immersed Beam Problem Parameters

$EI = 10^3$	beam stiffness
$\mu = \frac{1}{10}$	fluid viscosity
$p_{,x} = -10$	top channel pressure gradient
$p_{,x} = -5$	bottom channel pressure gradient

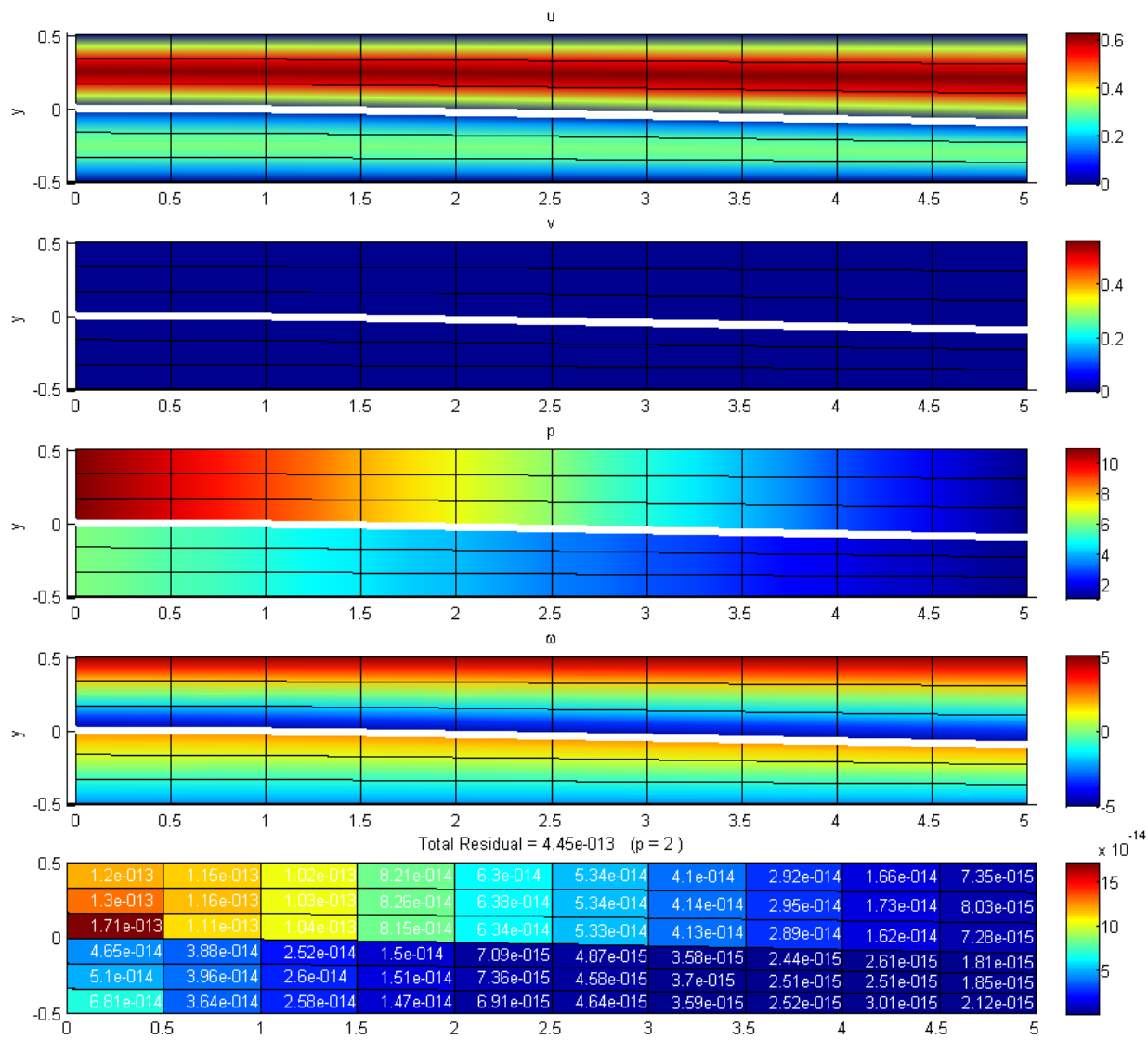


Figure 7.3: LSFEM FSI solution ($p = 2$) showing beam deflection

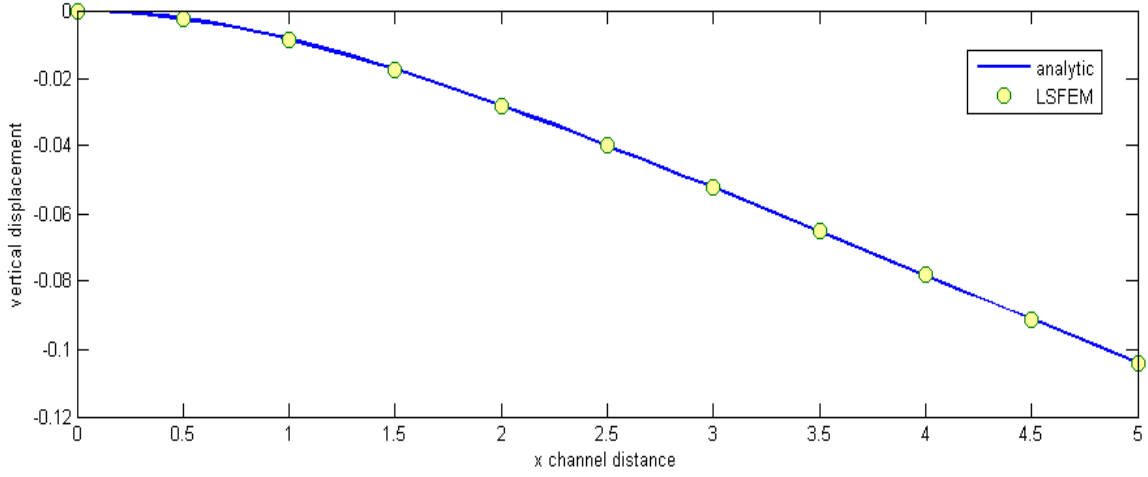


Figure 7.4: LSFEM and analytic solution for beam deflection

Taking the upper channel height as a shape design parameter. We compute the sensitivity of the fluid domain flow and the beam deflection to the upper channel height given that the flow rate through the upper channel is constant as the channel height changes. The upper channel wall is parameterized as the Cartesian ordered pair

$$X_{\Gamma_1^{top}} = \{(\xi \quad H_1) \mid \xi \in [0, L]\} \quad (7.16)$$

where L is the length of the channel. Then

$$\frac{\partial}{\partial H_1} X_{\Gamma_1^{top}} = \{(0 \quad 1)\} \quad (7.17)$$

Since the upper wall remains a no slip wall with variations in H_1 , the upper wall CSE boundary condition reduces to

$$\begin{Bmatrix} {}^H u^f \\ {}^H v^f \end{Bmatrix} = 0 - \begin{Bmatrix} \nabla u^f \\ \nabla v^f \end{Bmatrix} \cdot \frac{\partial X_{\Gamma_1^{top}}}{\partial H_1} = \begin{Bmatrix} -u_{,y}^f \\ -v_{,y}^f \end{Bmatrix} \quad (7.18)$$

Similarly, parameterizing the upper inlet by

$$X_{\Gamma_1^{inlet}} = \{(0 \quad 2\xi H_1) \mid \xi = y \in [0, \frac{1}{2}]\} \quad (7.19)$$

and noting that the inlet fully-developed velocity profile and vorticity are functions of the channel height yields the upper inlet CSE boundary conditions

$$\begin{Bmatrix} u^f \\ \omega^f \end{Bmatrix} = \frac{D\{u^f \omega^f\}}{DH_1} - \begin{Bmatrix} \nabla u^f \\ \nabla \omega^f \end{Bmatrix} \cdot \frac{\partial X_{\Gamma_{inlet}}}{\partial H_1} = \frac{1}{2\mu} \begin{Bmatrix} -yp_{,x} \\ p_{,x} \end{Bmatrix} - \begin{Bmatrix} -2yu_{,y}^f \\ -2y\omega_{,y}^f \end{Bmatrix} \quad (7.20)$$

The upper outlet boundary conditions are handled in the same manner, however the y -component gradient of both v^f and p^f are zero and the uniform outflow does not change, so the outlet boundary conditions reduce to zero. No other boundaries are affected by a variation in upper channel height and thus the remaining CSE boundary conditions are homogeneous.

The least-squares CSE solution is given in Figure 7.5 and the beam deflection is compared to a pseudo-analytic sensitivity in Figure 7.6. Although there is an analytic solution for beam deflection in the form of a solution to a differential equation in [130], an analytic sensitivity for the solution to channel height is not available in closed-form. However, a pseudo-analytic sensitivity is determined by calculating the transverse deflection of the beam to a pseudo-pressure load. The pseudo-pressure load is the differential pressure change in a channel of constant flow rate due to a variation in channel height. The average relative difference between the CSE and pseudo-analytic sensitivity is 2% and the maximum is less than 6% at the tip of the beam. The transverse pseudo-load is integrated along the length of the clamped beam explaining why the relative sensitivity difference increases towards to tip. Note that a p -value of 12 (an order of magnitude higher) was needed for the CSE system to achieve an equivalent residual level to the parent FSI problem. Examining the element residual plot in Figure 7.5, it is clear that the mesh is far from optimally graded. Nevertheless, the need for a more

refined solution to the CSE system is an observation previously made with regard to other systems [120]. It is convenient to use the same mesh for both the FSI system and the sensitivity system. This is a distinct advantage of higher-order FEM, since p -refinement allows a straightforward means to achieve a refined solution without needing a refined mesh.

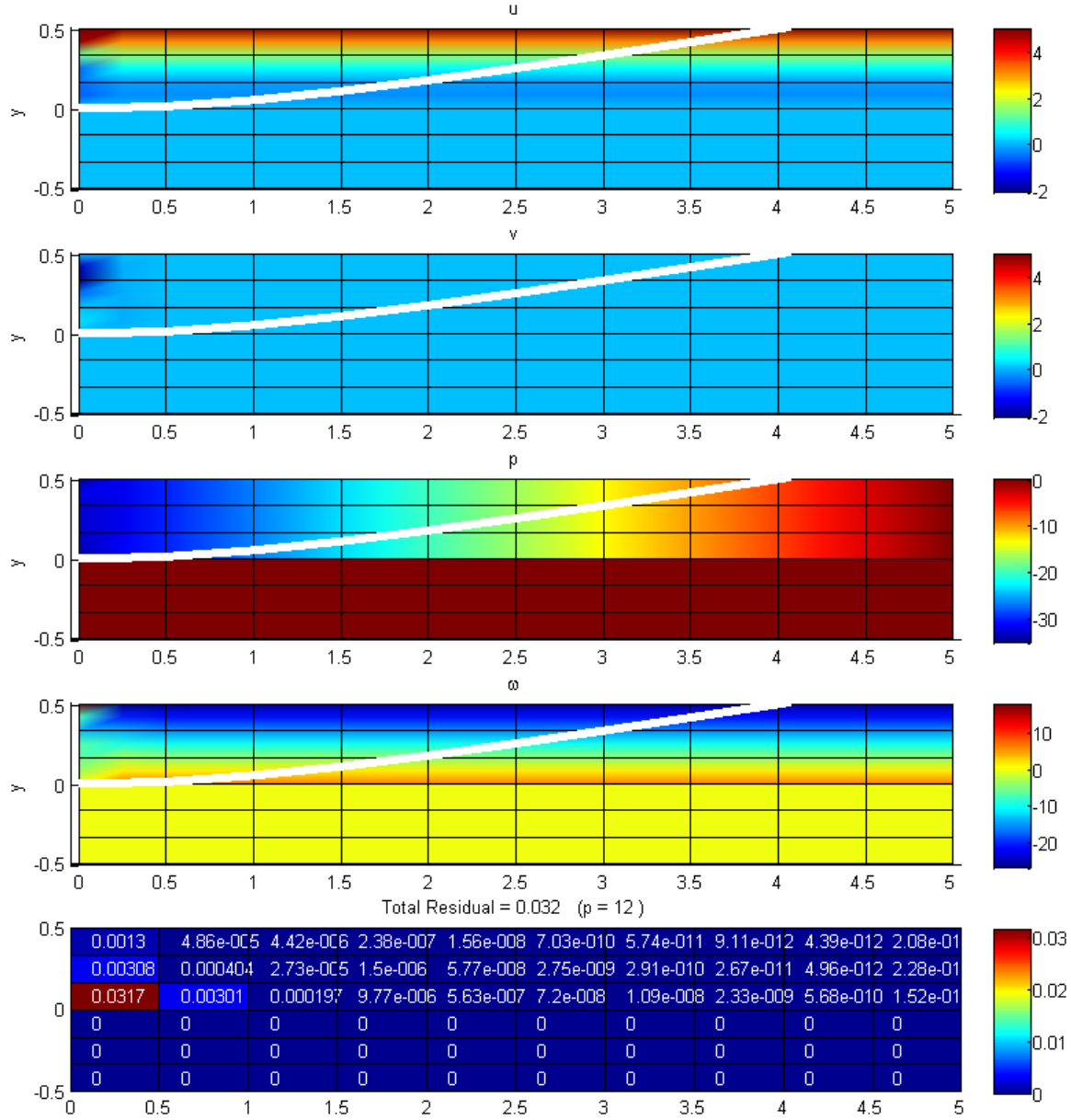


Figure 7.5: LS CSE solution ($p = 12$) showing beam deflection sensitivity

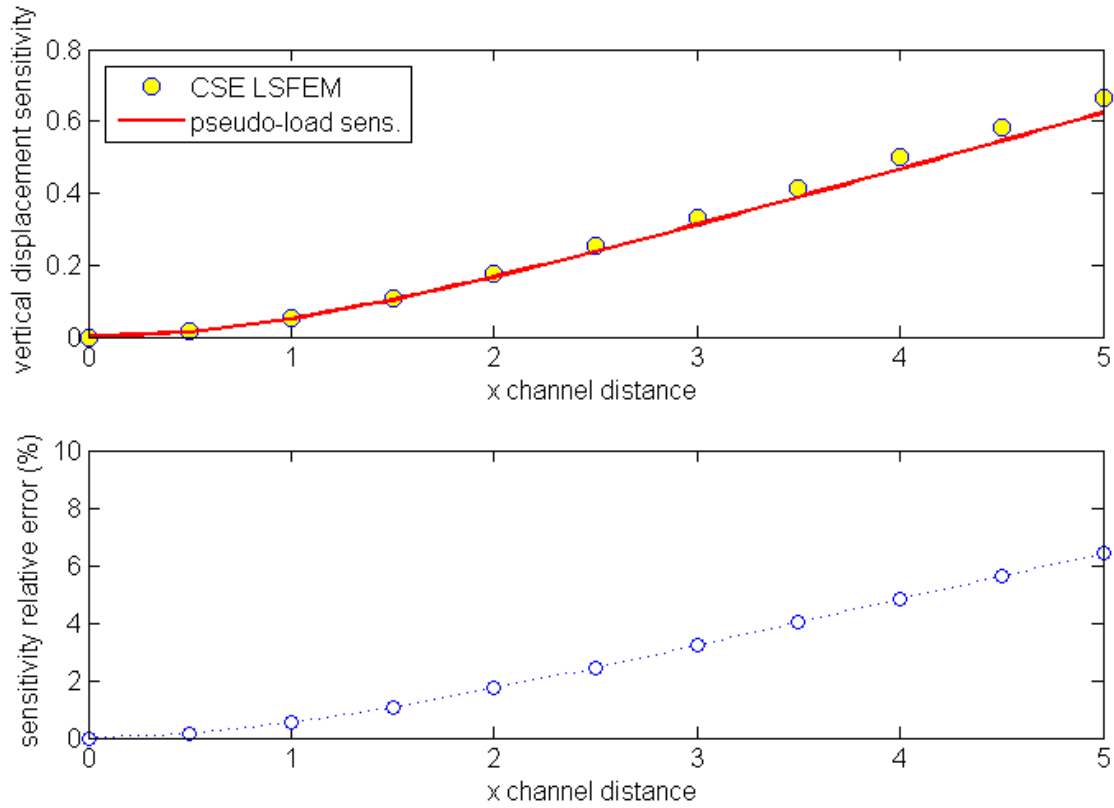


Figure 7.6: LS-CSE beam deflection sensitivity and relative error

We next consider a FSI problem motivated by the joined wing of particular interest to the sponsor.

7.3 Airfoil on a Sting

The analysis and sensitivity for a series of FSI models is now considered for a basic example traceable to the joined wing which exhibits nonlinear gust characteristics. This includes a nonlinear, geometric softening of the structure that leads to buckling in the aft wing of a joined wing. We consider the steady solution, for which an analytic solution exists, as well as transient solutions which are validated using typical section

aerodynamics. We also compare compressible and incompressible solutions using nonlinear full potential and linear potential flow models.

Consider a NACA 0012 airfoil mounted on a flexible sting (Figure 7.7). The sting is modeled as a nonlinear Euler-Bernoulli beam capable of large deflections. At a positive angle of attack, the airfoil generates lift, deflecting the beam in the fluid resulting in an increased angle of attack. Equilibrium deflection of the sting occurs when the force and moments generated by the lifting airfoil balance the internal sting force and moments resisting the bending. The transient response to a discrete gust front flowing past the airfoil is modeled and evaluated.

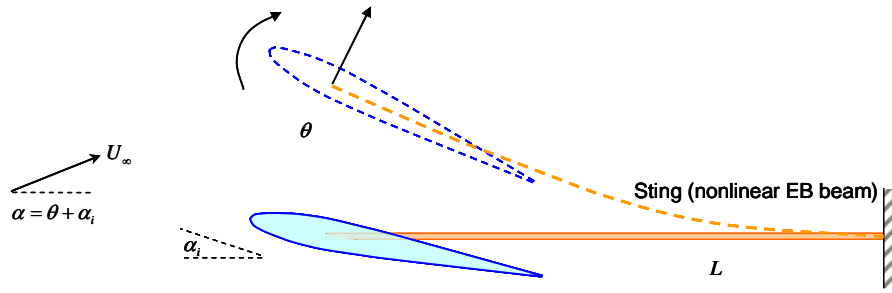


Figure 7.7: Flexible sting mounted airfoil

For the sensitivity problem, we consider beam length, airfoil angle of incidence, and airfoil chord length as shape parameters. Both the fluid and structure sensitivities are calculated for the FSI response. As a primary example of the approach, take the sting length as a shape parameter. The left and right boundaries of the sting, the *tip* and *root*, are naturally parameterized with respect to beam length as

$$\mathbf{X}_{tip} = \{0\} \quad , \quad \mathbf{X}_{root} = \{L\} \quad (7.21)$$

To convert the local sensitivities into a total derivative, we must define a domain transformation function that is compatible with the FSI boundary data. An obvious choice which does not unnecessarily complicate the fluid sensitivity boundary conditions

is represented in Figure 7.8. Below we consider chord length as a fluid domain shape parameter which will involve more complicated fluid sensitivity boundary conditions. For the domain variation depicted in Figure 7.8, define the material points of the domain by

$$\mathbf{X}_\Omega(x) = \{\xi L \mid \xi = x/L; \xi \in [0,1]\} \quad (7.22)$$

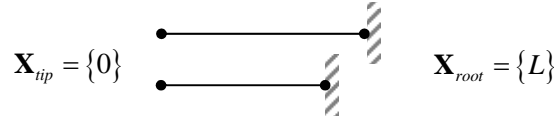


Figure 7.8: Sting length boundary parameterization

We first consider a steady solution for both compressible and incompressible potential fluid flow in the next section.

7.3.1 Steady Solution (Linear and Compressible Potential, Linear Structure)

The analytic solution to the steady airfoil on a sting problem described above is based on fluid-structure force equilibrium. The fluid force (lift per unit span) is given by

$$F_f = q_\infty c C_{L_\alpha} \alpha = q_\infty c C_{L_\alpha} (\theta_{tip} + \alpha_i) \quad (7.23)$$

where $q_\infty = \frac{1}{2} \rho_\infty V_\infty^2$ is the dynamic pressure, c is the chord length, and C_{L_α} is the lift curve slope. The angle of attack α is the sum of the airfoil angle of incidence α_i (“installed AOA”) and the beam tip deflection, θ_{tip} . On the basis of disturbed potential flow for thin airfoils [126], the compressibility corrected lift curve slope is

$$C_{L_\alpha} = \frac{2\pi}{\beta} \quad (7.24)$$

where

$$\beta = \sqrt{1 - M_\infty^2} \quad (7.25)$$

is the compressibility correction factor and M_∞ is the freestream Mach number. When applied to the pressure coefficient

$$C_p = \frac{C_{p,0}}{\beta} \quad (7.26)$$

the compressibility correction is the well-known Prandtl-Glauert rule. Corrections that provide more accurate results for transonic Mach numbers were given in Section 4.5.2.

For the steady deflection of the airfoil on a sting, the fluid force is in equilibrium with the structure internal shear at the tip

$$F_f = -V_y \Big|_{tip} \quad (7.27)$$

where the negative sign is due to the sign convention on the “negative face” of the beam. The equilibrium balance (7.27) is valid for small deflections, but a modification to this relation will be necessary below to accurately model the geometric nonlinearity of large deflections.

Since the NACA 0012 airfoil is symmetric and the airfoil is mounted to the tip of the sting at the aerodynamic center of the airfoil, the moment at the tip of the sting is zero. The equilibrium tip rotation of the sting is then

$$\theta_{tip} = \frac{F_f L^2}{2EI} \quad (7.28)$$

and the equilibrium fluid force is

$$F_f = \left(1 - \frac{q_\infty c \pi L^2}{\beta EI} \right)^{-1} \frac{q_\infty c 2\pi}{\beta} \alpha_i \quad (7.29)$$

The divergence dynamic pressure is the speed at which (7.29) becomes singular. For the incompressible case, the divergence dynamic pressure is

$$q_D = \frac{EI}{c\pi L^2} \quad (7.30)$$

For the compressible case, the divergence Mach number is

$$M_D = \sqrt{\frac{1}{2} - \sqrt{\frac{1}{4} - \frac{4(EI)^2}{\rho_\infty^2 a^4 (c\pi L^2)^2}}} \quad (7.31)$$

We also use the beam stiffness, EI , to tune the problem for a desired angular deflection of the tip, θ_{tip} , for a given freestream velocity through

$$EI = \frac{q_\infty c\pi L^2}{\beta} \left(\frac{\alpha_i}{\theta_{tip}} + 1 \right) \quad (7.32)$$

Leading to the ratio of dynamic to divergence pressure of

$$\frac{q_\infty}{q_D} = \frac{\theta_{tip}}{\theta_{tip} + \alpha_i} \quad (7.33)$$

For a 3 deg angle of incidence and 10 deg steady tip deflection, this yields a stability margin of 23%.

Table 7.3: Sting-mounted airfoil FSI problem boundary conditions

Boundary	Constrained dofs	
fluid IC	$\theta = 10^\circ \quad \dot{v} = 0$	steady equilibrium
beam IC	$\dot{v} = 0$	steady equilibrium
beam root BC	$v = 0 \quad \theta = 0 \quad \dot{v} = 0$	clamped
beam tip interface	$V_y(t) = -F_f(\theta, \dot{v}, V_g(t)) \quad M_z = 0$	fluid-structure interface (force equilibrium)

Table 7.4: Sting-mounted airfoil CSE problem boundary conditions

Boundary	Constrained dofs	
beam IC	${}^L\dot{v} = 0$	steady equilibrium
beam root BC	${}^L v = -v_{,x} \quad {}^L\theta = -\theta_{,x} \quad {}^L\dot{v} = -\dot{v}_{,x}$	clamped
beam tip interface	${}^L V_y(t) = -{}^L F_f \quad {}^L M_z = 0$	fluid-structure interface (force equilibrium)

The fluid forces for the LSFEM solution are calculated by integrating the pressure difference across the top and bottom of the airfoil in the airfoil coordinate system depicted in Figure 7.9.

$$F_{x_a} = - \int_{LE}^{TE} p_u \cos \beta d\xi_u + \int_{LE}^{TE} p_l \cos \beta d\xi_l \quad (7.34)$$

$$F_{y_a} = \int_{LE}^{TE} p_u \sin \beta d\xi_u + \int_{LE}^{TE} p_l \sin \beta d\xi_l \quad (7.35)$$

where p_l and p_u are the fluid pressures on the lower and upper surface of the airfoil respectively and β is the surface normal angle shown in Figure 7.9.

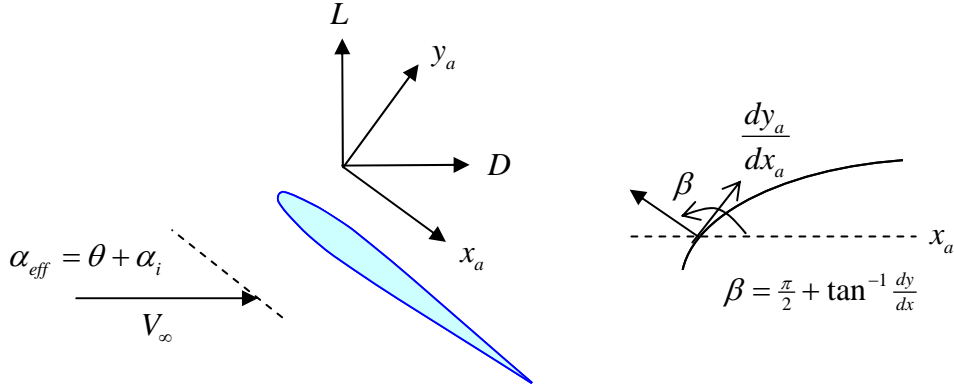


Figure 7.9: Airfoil coordinate system for integrating fluid forces

The conventional lift and pressure drag forces are then

$$F_{lift} = F_{y_a} \cos \alpha_{eff} - F_{x_a} \sin \alpha_{eff} \quad (7.36)$$

$$F_{drag} = F_{x_a} \cos \alpha_{eff} + F_{y_a} \sin \alpha_{eff} \quad (7.37)$$

In the linear potential flow formulation derived in Section 4.5.1, the variables are the velocity components, u and v . For the compressible potential flow formulation derived in Section 4.5.2, the velocity potential function, ϕ is also a primary variable. The local pressure at the airfoil surface is not a variable in either of these formulations and is determined by Bernoulli's equation

$$p = p_0 - \frac{1}{2} \rho_\infty (u^2 + v^2) \quad (7.38)$$

where $p_0 \equiv 1$ and $\rho_\infty \equiv 2$. For the sting length sensitivity problem, the lift sensitivity equation is derived by differentiating the interface conditions with respect to the sensitivity parameter. Thus

$${}^L F_{lift} = {}^L F_{y_a} \cos \alpha_{eff} - {}^L F_{x_a} \cos \alpha_{eff} - F_{y_a} \sin \alpha_{eff} {}^L \theta_{tip} - F_{x_a} \cos \alpha_{eff} {}^L \theta_{tip} \quad (7.39)$$

where

$${}^L F_{x_a} = - \int_{LE}^{TE} {}^L p_u \cos \beta d\xi_u + \int_{LE}^{TE} {}^L p_l \cos \beta d\xi_l \quad (7.40)$$

$${}^L F_{y_a} = \int_{LE}^{TE} {}^L p_u \sin \beta d\xi_u + \int_{LE}^{TE} {}^L p_l \sin \beta d\xi_l \quad (7.41)$$

in terms of the fluid pressure sensitivity ${}^L p$. Note that the angle β is not a function of the length of the sting. The fluid pressure sensitivity is determined by differentiating Bernoulli's equation with respect to the sensitivity parameter. Thus, in the present case, the sensitivity of Bernoulli's equation is

$${}^L p = -2({}^L uu + {}^L vv) \quad (7.42)$$

which is in terms of both the velocity sensitivity variables and the original velocity variables.

The velocity sensitivity for the steady FSI problem with a 10 deg sting tip rotation is plotted in Figure 7.10. The coefficient of pressure sensitivity for the same conditions is plotted Figure 7.11.

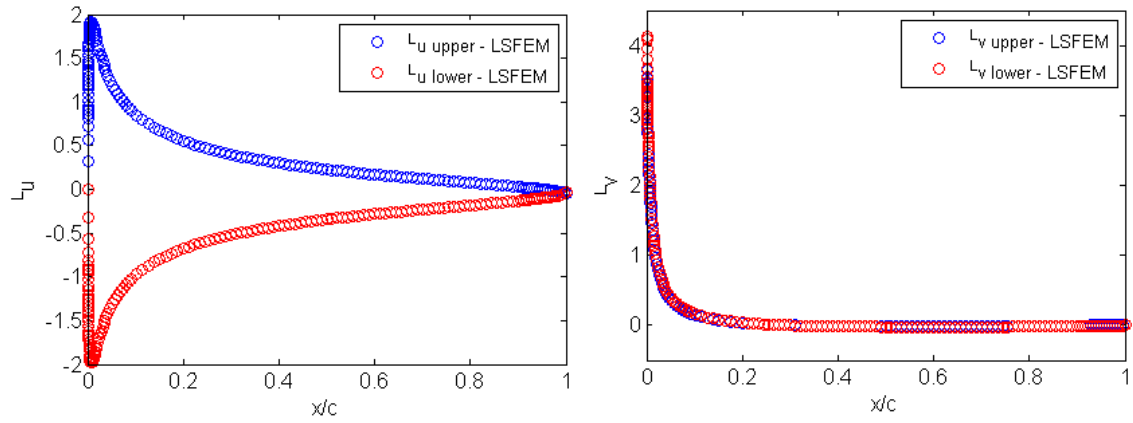


Figure 7.10: Steady LS-CSE velocity sensitivity for NACA 0012 airfoil on a sting (10 deg effective angle of attack)

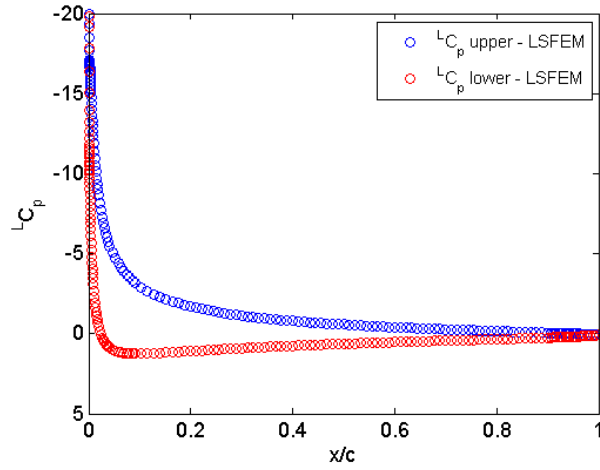


Figure 7.11: Steady LS-CSE pressure coefficient sensitivity for NACA 0012 airfoil on a sting (10 deg effective angle of attack)

Table 7.5: Airfoil on a Sting Problem Parameters

$EI = 102.1018$	beam stiffness
$\rho_y = 0.8185$	sting mass per unit length
$\omega_{beam} = \frac{\pi}{2}$	sting fundamental freq
$\alpha_i = 3\text{deg}$	angle of incidence
$L = 5$	beam length
$q_\infty = 1$	dynamic pressure
$c = 1$	chord length

The complete coupled fluid-structure model problem boundary and initial conditions for the steady FSI problem are given in Table 7.3 and the corresponding boundary and initial conditions for the CSE problem are given in Table 7.4. The steady solution to the incompressible FSI problem is depicted in Figure 7.12 for the problem parameters in Table 7.5. The fluid solution is given at a p -value of 12 on a 238 element mesh. The structure solution is based on a p -value of 4 on a 5 element mesh.

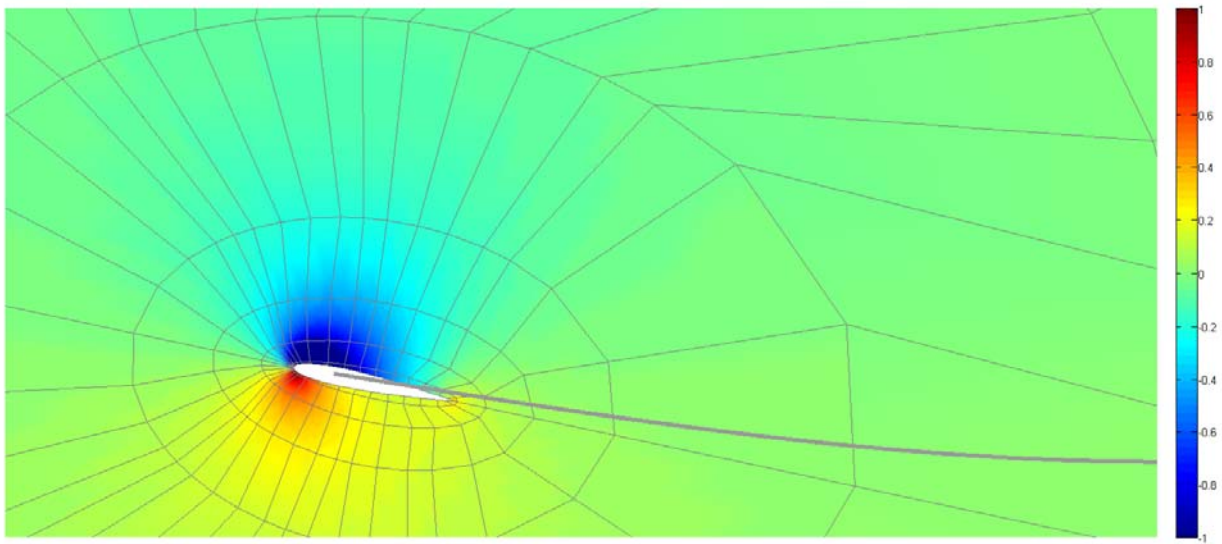


Figure 7.12: Steady LSFEM pressure solution for NACA 0012 airfoil on a sting (tip rotation 10 deg)

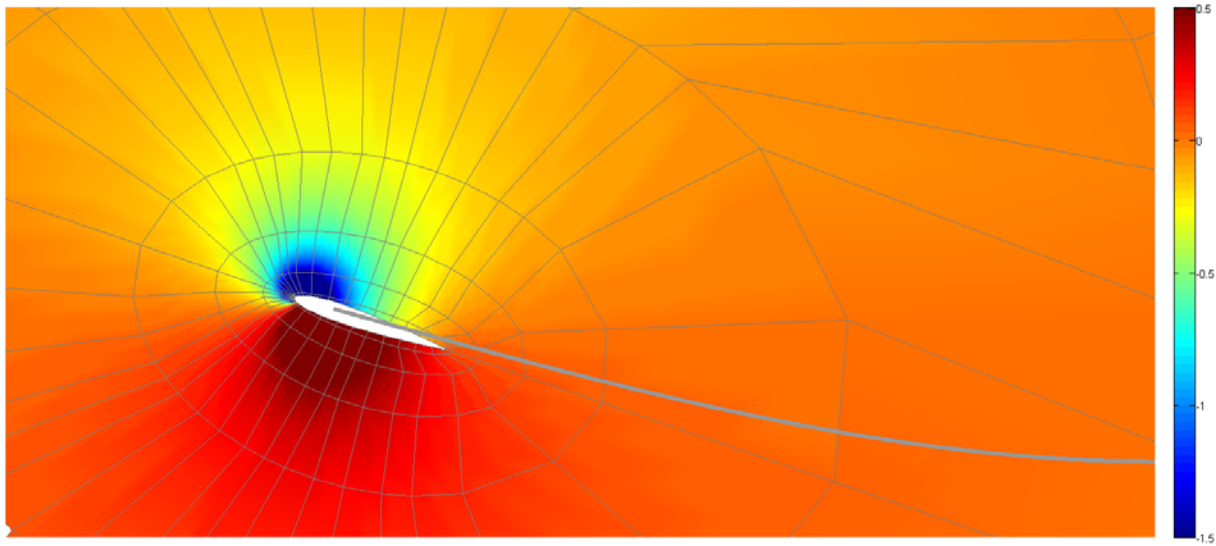


Figure 7.13: Steady LSFEM pressure solution for NACA 0012 airfoil on a sting

The analytic beam solution is given by solving the clamped beam Euler-Bernoulli beam equations with the analytic fluid force given by (7.29). The analytic beam steady solution is

$$v(x; L) = \frac{F_f x^3}{6EI} - \frac{F_f L^2 x}{2EI} + \frac{F_f L^3}{3EI} \quad (7.43)$$

$$\theta(x; L) = \frac{F_f x^2}{2EI} - \frac{F_f L^2}{2EI} \quad (7.44)$$

$$M_z(x; L) = F_f x \quad (7.45)$$

$$V_y(x, L) = -F_f \quad (7.46)$$

A comparison of the analytic beam solution and the LSFEM solution is given in Figure 7.14.

The analytic steady equilibrium sensitivity tip rotation of the sting is determined in the same manner as (7.28)

$${}^L\theta_{tip} = \frac{{}^L F_f L^2}{2EI} + \frac{F_f L}{EI} \quad (7.47)$$

The same result could have been achieved by differentiating (7.44) evaluated at the tip ($x = 0$) with respect to beam length (and including the implicit dependence of F_f on L).

$$-\theta_{,L}(L) = \frac{F_{f,L}L^2}{2EI} + \frac{F_f L}{EI} \quad (7.48)$$

Note that an upward deflection of the beam at the tip is a negative rotation (defined as the slope of the beam). Equation (7.47) then gives the analytic equilibrium fluid force sensitivity by the same manner as (7.29)

$${}^L F_f = \left(1 - \frac{q_\infty c \pi L^2}{\beta EI}\right)^{-1} \frac{q_\infty c 2\pi F_f L}{\beta EI} \quad (7.49)$$

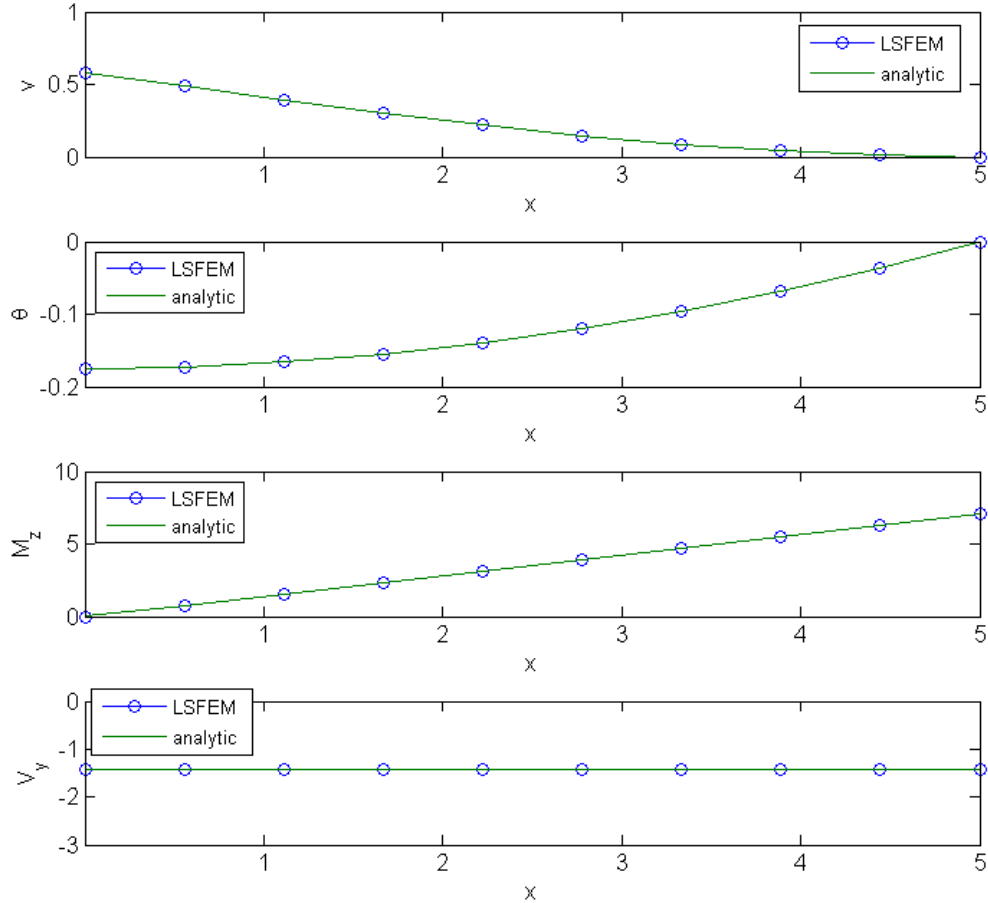


Figure 7.14: Comparison of steady, linear potential FSI solution with analytic solution

The analytic beam sensitivity solution can be determined by differentiating (7.43) through (7.46) with respect to beam length.

$$v_{,L}(x;L) = \frac{{}^L F_f x^3}{6EI} - \frac{{}^L F_f L^2 x}{2EI} - \frac{F_f Lx}{EI} + \frac{{}^L F_f L^3}{3EI} + \frac{F_f L^2}{EI} \quad (7.50)$$

$$\theta_{,L}(x;L) = \frac{{}^L F_f x^2}{2EI} - \frac{{}^L F_f L^2}{2EI} - \frac{F_f L}{EI} \quad (7.51)$$

$$M_{z,L}(x;L) = {}^L F_f x \quad (7.52)$$

$$V_{y,L}(x;L) = -{}^L F_f \quad (7.53)$$

The LS-CSE solution and analytic sensitivities for beam length are compared in Figure 7.15.

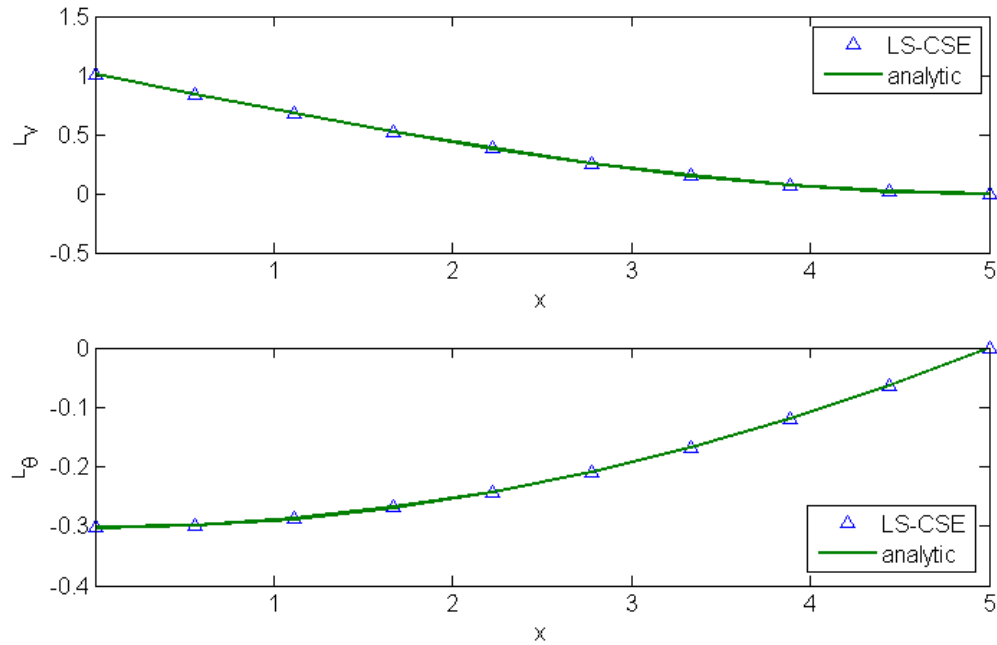


Figure 7.15: Steady, linear potential LS-CSE solution with analytic sensitivity

The same approach that used for determining analytic CSE solutions to beam length can be used for the sensitivity to chord length and angle of incidence. The equilibrium force sensitivity to chord length is

$${}^c F_f = 2\eta(\theta_{tip} + \alpha_i) + 2c\eta {}^c \theta_{tip} = \left(1 - \frac{c\eta L^2}{EI}\right)^{-2} \frac{2c\eta^2 L^2 \alpha_i}{EI} + \left(1 - \frac{c\eta L^2}{EI}\right)^{-1} 2\eta \alpha_i \quad (7.54)$$

where $\eta = \frac{q_\infty \pi}{\beta}$. As expected, (7.54) matches the result obtained by differentiating (7.29)

with respect to c

$$F_{f,c} = -\left(1 - \frac{c\eta L^2}{EI}\right)^{-2} \left(-\frac{\eta L^2}{EI}\right) 2c\eta \alpha_i + \left(1 - \frac{c\eta L^2}{EI}\right)^{-1} 2\eta \alpha_i = {}^c F_f \quad (7.55)$$

The tip rotation sensitivity to chord length is

$${}^c \theta_{tip} = \frac{{}^c F_f L^2}{2EI} \quad (7.56)$$

which also matches the expected result obtained by differentiating (7.28).

The equilibrium force sensitivity to angle of incidence is

$$\alpha_i F_f = 2\eta c (\alpha_i \theta_{tip} + 1) = \left(1 - \frac{c\eta L^2}{EI}\right)^{-1} 2c\eta \quad (7.57)$$

Again, this matches the result obtained by differentiating (7.29) with respect to α_i

$$F_{f,\alpha_i} = \left(1 - \frac{c\eta L^2}{EI}\right)^{-1} 2c\eta = \alpha_i F_f \quad (7.58)$$

The tip rotation sensitivity to angle of incidence is

$$\alpha_i \theta_{tip} = \frac{\alpha_i F_f L^2}{2EI} \quad (7.59)$$

which also matches the expected result obtained by differentiating (7.28). The LS-CSE solution ($p = 12$) for pressure sensitivity to angle of incidence is plotted in Figure 7.16.

Note that the sting rotation sensitivity is depicted to scale. The sting tip sensitivity is for the parameters in Table 7.5 is 3.33 radians per radian of incidence. This corresponds to slightly more than 190 degs of change in tip rotation for every degree change in angle of

incidence. The sting transverse deflection sensitivity (which is more than 11 units of length) is not plotted to scale in Figure 7.16. The airfoil coordinate forces for the angle of incidence sensitivity problem are integrated along upper and lower surface as they were for the FSI and length sensitivity problems. The lift sensitivity calculation for angle of incidence is similar to (7.39) except

$${}^{\alpha_i}F_{lift} = {}^{\alpha_i}F_{y_a} \cos \alpha_{eff} - {}^{\alpha_i}F_{x_a} \cos \alpha_{eff} - F_{y_a} \sin \alpha_{eff} ({}^{\alpha_i}\theta_{ip} + 1) - F_{x_a} \cos \alpha_{eff} ({}^{\alpha_i}\theta_{ip} + 1) \quad (7.60)$$

The integration of the pressure sensitivity and (7.60) yield a LS-CSE lift sensitivity value of 26.3 for a ${}^{\alpha_i}\theta_{ip} = 3.33$. This is within 3% of the analytic sensitivity predicted by (7.57) of 27.2. Note that the nonlinear Euler-Bernoulli beam

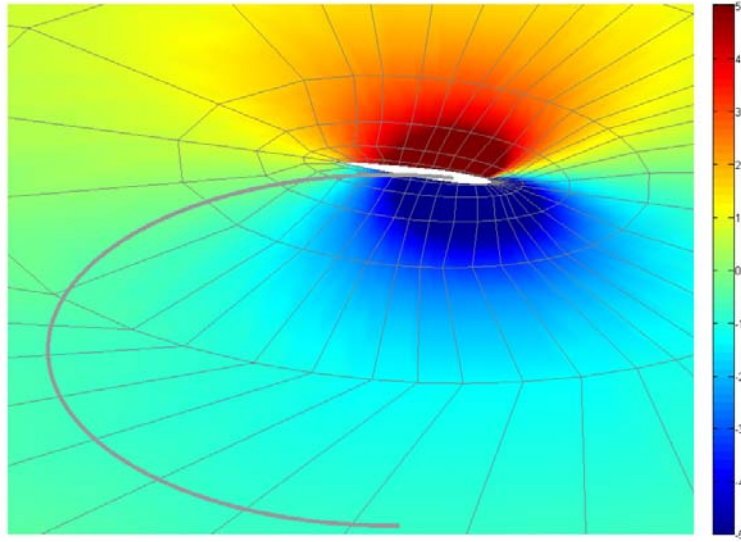


Figure 7.16: LS-CSE solution ($p = 12$) for pressure sensitivity to angle of incidence. (Sting rotation sensitivity is plotted to scale; sting transverse deflection sensitivity is not to scale).

The effect of compressibility on the equilibrium solution for the beam is plotted in Figure 7.17. The $M = 0$ solution is based on a LSFEM solution of the linear potential equations. The $M = 0.5$ is from a LSFEM solution of the steady, compressible potential

equations. Note that linear potential solution corrected for compressibility (not depicted in Figure 7.17) gives a numerical solution that is equal to the compressible potential solution. The compressibility effect at 0.5 M is 15% increase in the lift curve slope. However, as a result of the “positive feedback” interaction between the fluid and structure, this results in an equilibrium force increase of almost 240% and the equivalent increase in tip deflection and rotation.

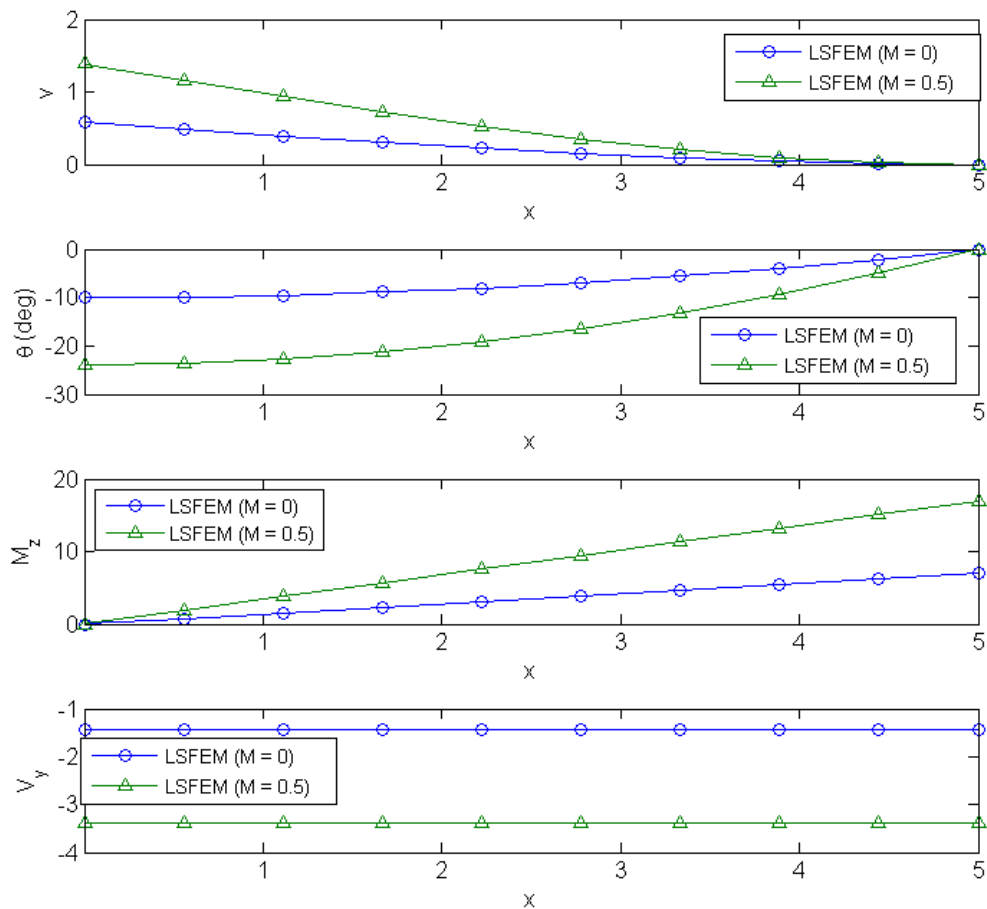


Figure 7.17: Comparison of steady linear potential solution and compressible potential solution ($M = 0.5$) for NACA 0012 airfoil on a sting

7.3.2 Typical Section and Gust Models

Before presenting transient FSI solutions, we describe the gust model that is used in the next two sections as well as the unsteady typical section model that is used to validate the transient solutions. The vertical gust is modeled using the usual discrete gust idealization of a *one-minus-cosine* pulse [62]. V_g is the time-dependent gust velocity given by

$$V_g(t) = \begin{cases} \frac{1}{2} V_{g,\max} \left(1 - \cos \frac{2\pi(t-\tau_0)}{T_g} \right) & \tau_0 \leq t \leq T_g \\ 0 & o.w. \end{cases} \quad (7.61)$$

where $V_{g,\max}$ is the maximum amplitude of the gust, τ_0 is the start of the gust, and T_g is the duration of the gust. The effect of the vertical gust is to change the apparent angle of attack at the airfoil, Figure 7.18. In the FSI model, this is done by changing the far field angle of attack. This treatment will not capture the gust load alleviation effect that results from the finite time interval required for the entire airfoil to experience the gust (*i.e.* the leading edge will “see” the gust angle of attack before the trailing edge), but it is an acceptable simplification, particularly since we are primarily interested in sensitivity analysis. If the magnitude of the vertical gust is small relative to the forward velocity of the airfoil, then the gust angle of attack is

$$\alpha_g = \frac{V_{gust}}{U_\infty} \quad (7.62)$$

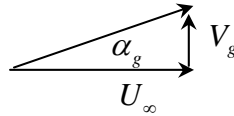


Figure 7.18: Vertical gust relation

The typical section fluid force model is based on a quasi-steady form of Theodorsen's unsteady, thin-airfoil theory [19, 44, 54, 63]. The Theodorsen lift relation for an oscillating airfoil with pitch and plunge is

$$L = C_{L_\alpha} \rho_\infty U_\infty \frac{c}{2} C(k) \left[\dot{h} + U_\infty \alpha - \frac{1}{4} c \dot{\theta} \right] + \pi \rho_\infty \frac{1}{4} b^2 \left(\ddot{h} + U_\infty \dot{\alpha} - \frac{1}{2} c \ddot{\theta} \right) \quad (7.63)$$

where $C(k)$ is the complex valued Theodorsen function dependent upon the reduced frequency, $k = \frac{c\omega}{2U_\infty}$. The first half of the right-hand side of (7.63) is known as the circulatory lift and the expression in brackets represents the apparent angle of attack for an airfoil with plunge rate, \dot{h} , and pitch rate, $\dot{\theta}$. The latter half of the Theodorsen lift relation is an inertial load that represents the apparent mass of the volume of air that must be displaced by the moving airfoil. If the effect of unsteady trailing vortices in the wake is neglected, then the Theodorsen lift relation can be treated as a quasi-steady model. This is equivalent to a reduced frequency of $k = 0$ for which $C(k) = 1$. This is a reasonable assumption for our present gust response model.

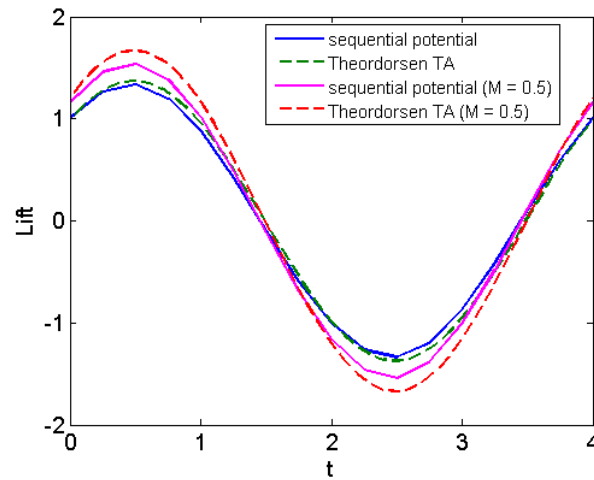


Figure 7.19: Comparison of time-sequential linear potential fluid and quasi-steady thin airfoil (TA) typical section solutions for an oscillating airfoil with pitch and plunge

A comparison of the compressibility corrected time-sequential linear potential fluid model described in Section 4.5.2 with the quasi-steady typical section model described in this section is plotted in Figure 7.19. The incompressible solutions are a very close match. The compressible solution agreement is not as exact in magnitude but the agreement is still reasonable. Note that the compressibility corrections for the typical section model and for the potential solution are applied differently. The compressibility correction for the typical section is handled through the effect on the lift curve slope in accordance with (7.24). In contrast, the compressibility factor for the potential flow solution is applied to the derived pressure values on the surface of the airfoil before it is integrated to give the lift. Additionally, there is no compressibility factor applied to the apparent mass term in the Theodorsen lift relation which may explain why the typical section model overstates the lift determined by the compressibility-corrected potential solution.

7.3.3 Potential Transient FSI (Nonlinear Structure)

The transient, nonlinear gust response is now solved using the linear potential fluid model. Nonlinear, compressible potential flow is employed in the next section. The nonlinear Euler-Bernoulli beam is modeled using the five degree of freedom transient formulation described in Section 4.6.3. It is a total Lagrangian description in which the fluid forces are expressed in the undeformed coordinate system. This is naturally done since the lift and drag forces, by convention perpendicular and parallel to the free stream velocity, are already resolved in the original, undeformed coordinate system (see Figure 7.9). The resolution of the airfoil coordinate forces F_{x_a} and F_{y_a} into the lift and drag forces, (7.36) and (7.37), takes into account the rotation of the sting at each time step.

This models the effect of a follower force in that applied load is recalculated at each iteration to reflect the change in geometry of the structure. This completely valid though nontraditional approach is somewhat unique in that the follower forces that depend on the deformed geometry are applied to a total Lagrangian model that is expressed relative to the undeformed coordinate system.

An iterative FSI coupling method is used to sequence between the fluid and structure solution domains. The fluid-structure interface conditions for the transient FSI problem with large deflection and geometric nonlinearities remain the same. The lift from the airfoil is in equilibrium with the beam internal shear at the tip of the sting. Recall from nonlinear bending derivation Section 4.6.3 that V_y is the shear force perpendicular to the x -axis. Thus, the fluid-structure interface conditions are

$$F_L = -V_y \Big|_{tip} \quad (7.64)$$

$$F_D = P_{tip} \quad (7.65)$$

$$M_f = M_z \Big|_{tip} \quad (7.66)$$

where F_L and F_D are the lift and drag forces respectively. As usual, the appropriate sensitivity derivatives of the fluid-structure interface conditions yield the fluid-structure sensitivity equation interface relations. So the length sensitivity interface conditions are

$${}^L F_L = -{}^L V_y \Big|_{tip} \quad (7.67)$$

$${}^L F_D = {}^L P_{tip} \quad (7.68)$$

$${}^L M_f = {}^L M_z \Big|_{tip} \quad (7.69)$$

Recall the assumptions from Section 4.6.3 of large lateral deflections, moderate to large rotations, and small axial strains. Typical L/D ratios for airfoils are 120 or 150 to 1, so that the lateral force is more than two orders of magnitude greater than the axial load.

Furthermore, typical values for Young's modulus of aerospace materials are 10^7 to 10^9 depending on the units. Thus, the axial strain will be at least 7 orders of magnitude smaller than the axial stress. The current example problem fits within the assumptions of the nonlinear beam bending from Section 4.6.3. The geometric nonlinearities are captured by the Green strain term and an updated Lagrangian description¹ is not applicable for this problem.

In addition to the nonlinear gust load and the compressive pressure drag load, an additional compressive tip load is applied to the beam which acts in phase with the gust. This compressive tip load is motivated by the internal load in the aft wing of a joined wing configuration that results from the gust loading on the forward wing [20, 38]. The total compressive tip load is thus given by

$$P_{tip} = \begin{cases} D - P_a \left(1 - \cos \frac{2\pi(t - \tau_0)}{T_g} \right) & \tau_0 \leq t \leq T_g \\ D & o.w. \end{cases} \quad (7.70)$$

where P_a is the peak amplitude of the compressive load. For the results given below, P_a is chosen so that, at peak deflection, the compressive load is equal to approximately 25% of the magnitude of the aerodynamic load (due to the very large magnitude of Young's modulus, see above, this still results in relatively small axial strain). As with the joined wing, this additional compressive load leads to a geometric softening and a potential for buckling of the sting. The nonlinear effect of the compressive tip load is obvious in the nonlinear beam response to the 1 sec *one-minus-cosine* gust plotted in Figure 7.20.

¹ The updated Lagrangian method accounts for large rigid body rotations of line elements, which produce no strain.

Taking beam length as a shape design parameter, we solve the continuous sensitivity system for the fluid and structure state variable sensitivities to beam length. The fluid potential sensitivity is given by (4.63), the nonlinear structure sensitivity by (4.132), and the sensitivity boundary conditions by Table 7.4. Since the beam tip does not move under the domain parameterization adopted for this problem, the local and total derivative sensitivities at the tip of the beam are identical. A comparison of the LS-CSE solution and the finite difference sensitivity for the nonlinear, transient gust response is plotted in Figure 7.21. The fluid solution is based on a $p = 12$ LSFEM solution for a 238 element mesh. The $p = 4$ structure solution is solved a mesh with 5 spatial elements and 24 time elements. The temporal beam mesh is at least an order of magnitude finer in the vicinity of the gust than it is for the steady region.

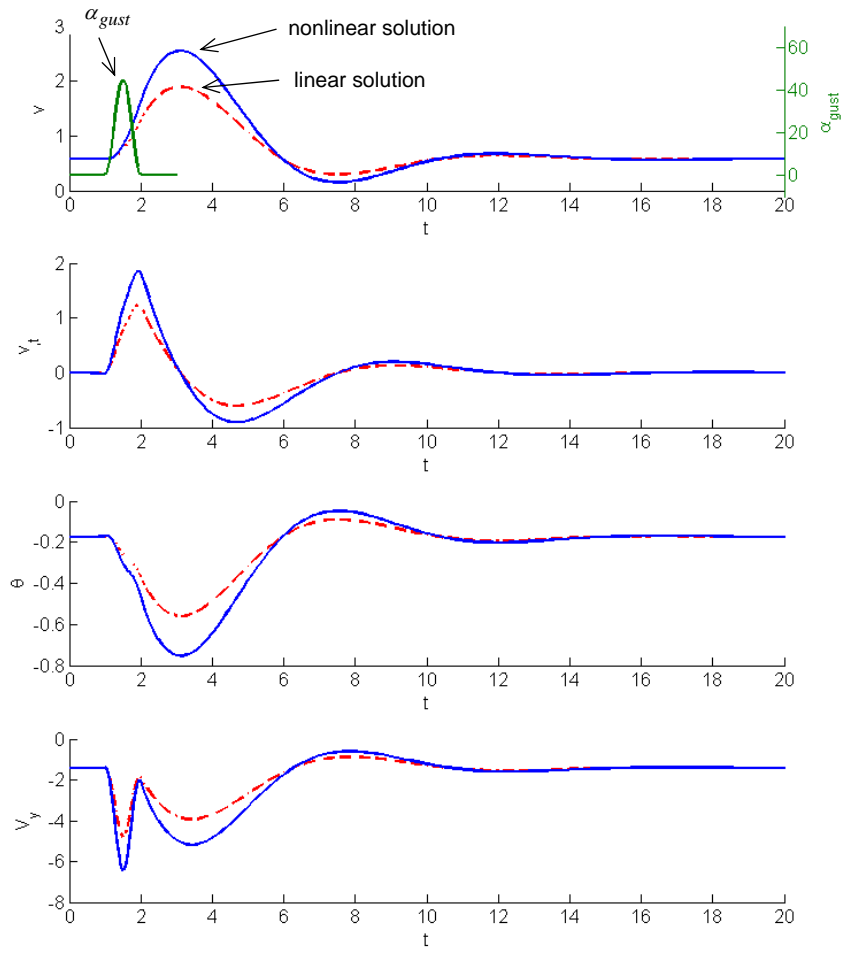


Figure 7.20: Nonlinear transient response for beam tip deflection, velocity, rotation, and internal shear to a 1 sec *one-minus-cosine* gust

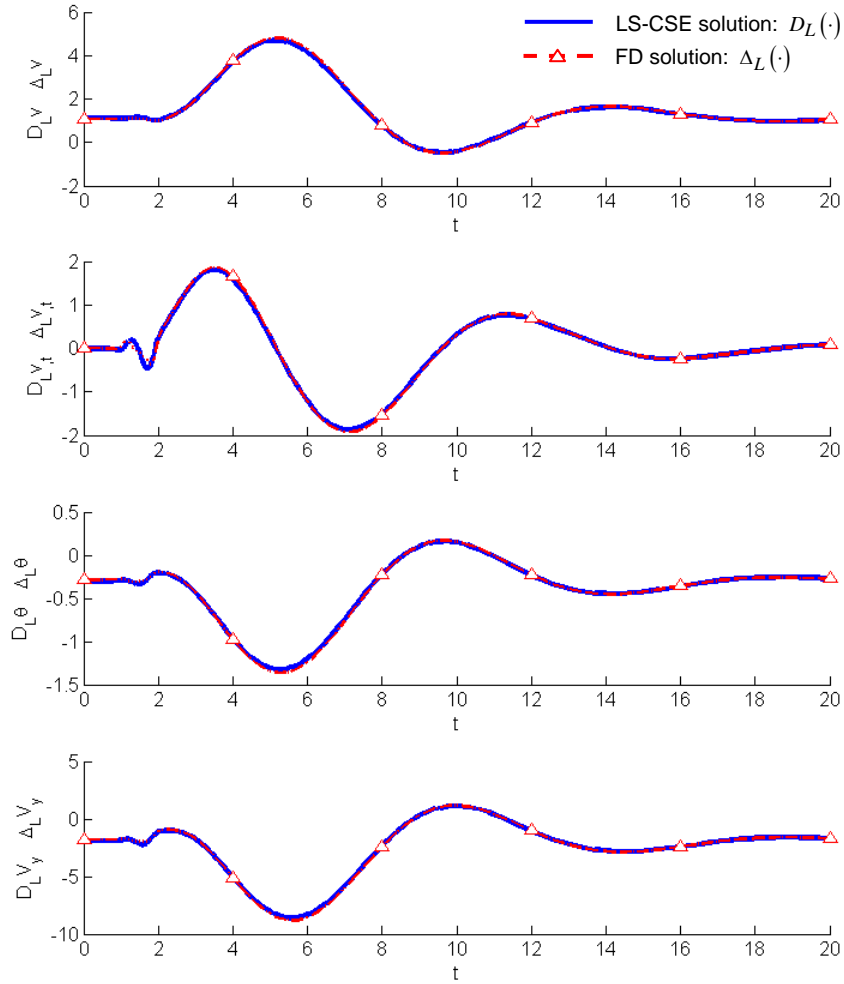


Figure 7.21: Comparison of finite difference and LS-CSE solution for beam deflection, velocity, rotation, and internal shear sensitivity to the beam length for a 1 sec *one-minus-cosine* gust

Since the LS-CSE solution yields the design parameter sensitivity of all the state variables, single or multi-variable optimization methods requiring gradient information can be accomplished with respect to any of the state variables. For example, a multi-objective optimization to minimize the beam root bending moment while maintaining

limits on maximum deflection and rotation of the sting is possible with the sensitivity data obtained from the LS-CSE solution.

As another example of a possible use of the sensitivity solution, consider the extrapolation of the nonlinear beam deflection for the transient gust problem at a particular point in time. For example, at $t = 3$, the beam tip deflection and rotation of the FSI solution in Figure 7.20 is close to a maximum. The LS-CSE solution of the entire beam at $t = 3$ is given in Figure 7.22. Note that the entire transient CSE problem does not have to be solved if only the sensitivity at a point in time is desired (a finite difference sensitivity calculation would require time marching). The CSE boundary conditions for the sensitivity at $t = 3$ only depend on the nonlinear FSI solution at $t = 3$ and not on any of the prior history of the transient CSE system. From a first-order Taylor series approximation, the extrapolated beam deflection and rotation at any point in time is

$$v(x; L_0 + \delta L) \approx v(x; L_0) + D_L v(x; L_0) \delta L \quad (7.71)$$

and

$$\theta(x; L_0 + \delta L) \approx \theta(x; L_0) + D_L \theta(x; L_0) \delta L \quad (7.72)$$

where L_0 is the nominal beam length and the total material sensitivity is given by (3.12).

Explicitly, the total sensitivity for deflection is

$$D_L v(x; L_0) = {}^L v(x; L_0) + v_{,x}(x; L_0) \frac{x}{L_0} \quad (7.73)$$

where ${}^L v$ is the LS-CSE solution sensitivity variable, and the spatial gradient of deflection in the convection term comes from the nonlinear FSI solution. The extrapolated deflections and rotations at $t = 3$ sec for a 3% and 6% longer beam are calculated and compared with the actual beam deflections and rotations in Figure 7.23.

The agreement for a 3% longer beam is fairly close and the extrapolation for a 6% longer beam is noticeably more inaccurate. This is due to the limited accuracy of the first-order Taylor series to a system that is not affine. For the parameters modeled in this FSI system, the static margin for divergence is less than 10% for a 6% longer beam compared to 30% for the original beam. This results in increasingly large deflections for relatively small perturbations in beam length.

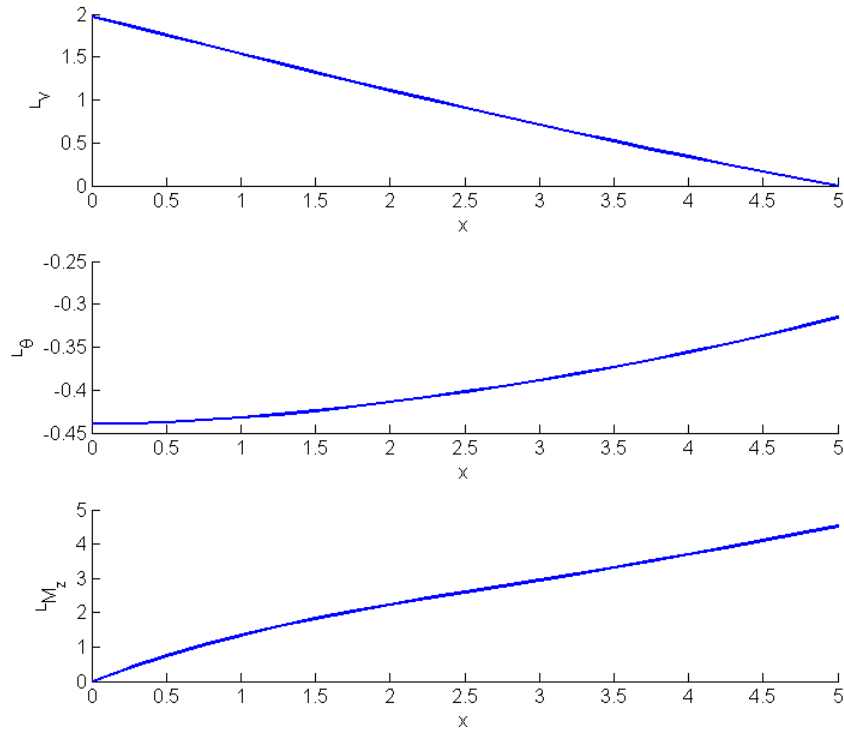


Figure 7.22: Beam deflection, rotation, and internal moment sensitivity to the nonlinear gust response at $t = 3$

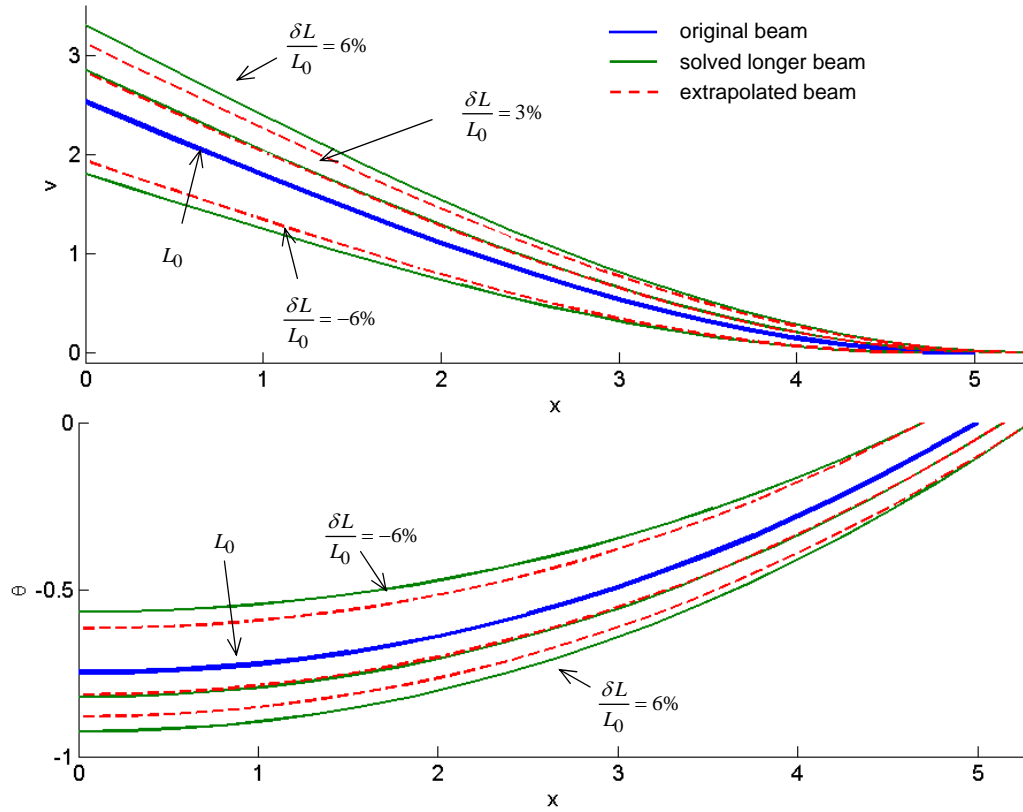


Figure 7.23: Extrapolated and actual beam deflection and rotation to *one-minus-cosine* gust ($t = 3$ sec) for a 3% and 6% longer sting

7.3.4 Compressible Transient FSI (Nonlinear Fluid, Nonlinear Structure)

The nonlinear, transient gust response of the sting-mounted NACA 0012 airfoil is now solved for a compressible fluid. The transient structure is modeled using the time-space, nonlinear Euler-Bernoulli beam formulation detailed in Section 4.7.1. This is coupled with the nonlinear, quasi-steady compressible potential LSFEM fluid developed and validated in Section 4.5.2. The sequential coupling method for the FSI problem is depicted in Figure 7.24. Note there are four loops. Two loops for nonlinear convergence of the fluid and structure, a coupling loop for the FSI system, and an outer time loop for

the transient problem. This numerical architecture is not the most efficient, but it was straightforward to implement within the existing pieces of the developed research code. The sensitivity system uses the same architecture framework, however the nonlinear iterations are not required. The FSI loop is still necessary to converge the fluid and structure solution. Additionally, time marching is not required for the sensitivity problem if the sensitivity is only desired at a single point in time. Thus, as with the other example problems considered in this dissertation, the sensitivity problem is relatively simple to solve once the underlying FSI problem has been solved.

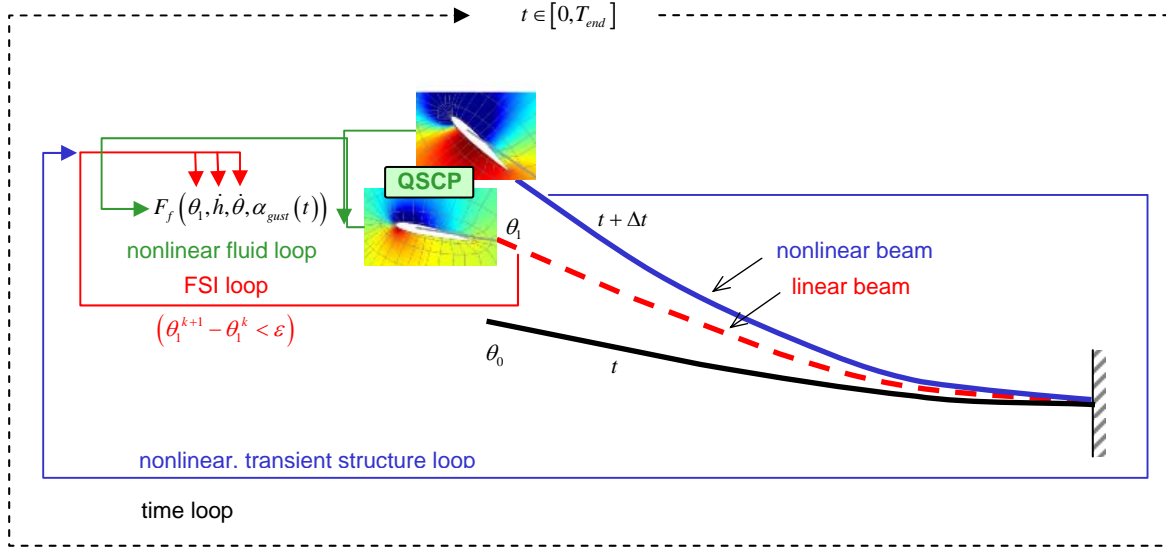


Figure 7.24: Sequential FSI coupling solution architecture for nonlinear, compressible fluid and nonlinear structure.

A Mach number of 0.5 is used for the compressible flow in this section. Recall that the primary effect of compressibility is to increase the pressure difference between the upper and lower surfaces of the airfoil and hence the total lift. The effect is obvious in the steady FSI and CSE solutions for incompressible and compressible flow given in Table 7.6 (which is based on the problem parameters in Table 7.5). Note that the tip

deflection and rotation more than double when compressibility is included. Additionally, note that compressibility increases the tip deflection and rotation sensitivity five-fold.

Table 7.6: Steady FSI and CSE solutions for incompressible and compressible flow

		Incompressible	Compressible
FSI	F_f	1.426	3.399
	θ_{tip}	10.0 deg	23.8 deg
	v_{tip}	0.5818	1.387
CSE	$^L F_f$	1.901	10.8
	$^L \theta_{tip}$	17.3 deg L ⁻¹	85.3 deg L ⁻¹
	$^L v_{tip}$	1.125	5.241

For the compressible gust response, the amplitude of the gust is decreased relative to the gust model used in the previous section so that the increased lift due to compressibility does not result in excessive sting rotation. This makes physical sense as well since the ratio of gust vertical velocity to free-stream velocity will decrease as the Mach number increases. The transient gust response is plotted in Figure 7.25 for both the compressible and incompressible fluid. The response for a linear beam in a compressible fluid is also plotted.

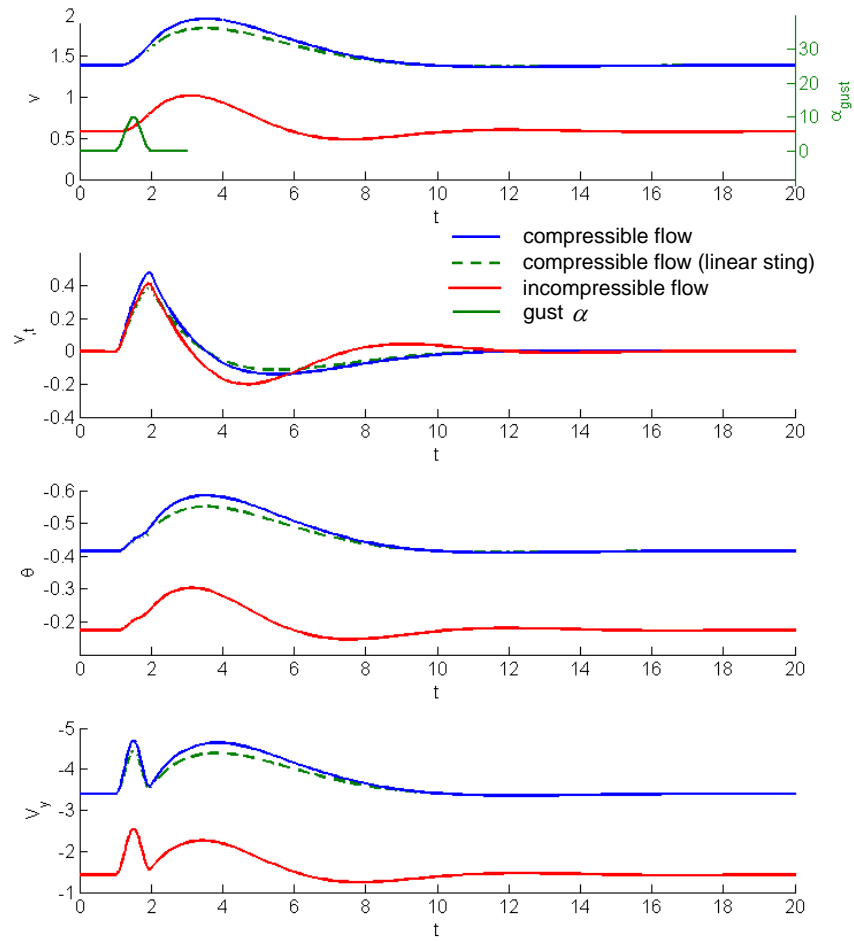


Figure 7.25: Transient, nonlinear gust response of sting tip to *one-minus-cosine* gust (peak α_{gust} magnitude of 10 deg) for compressible and incompressible fluid

The transient tip sensitivity solution is plotted in Figure 7.26. Note the difference in sensitivity for all sting variables during the course of the gust is much less than the difference in sensitivity between the compressible and incompressible flow solutions. This is not surprising. Additionally, as noted previously, the CSE system need not be solved in a transient method if the sensitivity is only at a particular point in time, *e.g.* at the peak sting deflection.

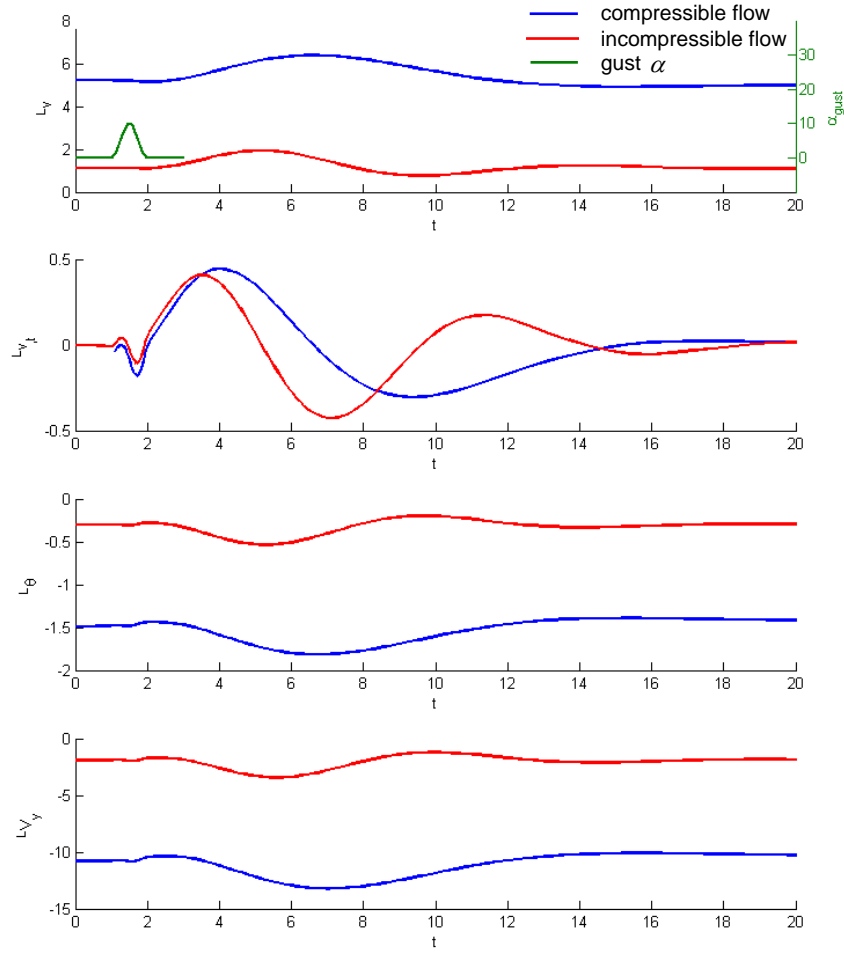


Figure 7.26: Transient, gust CSE of sting tip for *one-minus-cosine* gust (peak α_{gust} magnitude of 10 deg) based on compressible and incompressible FSI solution

The FSI solution at initial equilibrium ($t = 0$ sec) and at peak deflection ($t = 3.5$ sec) is given Figure 7.27. The pressure sensitivity to beam length is plotted in Figure 7.28. As expected, an increase in beam length results in an increased sting deflection which reduces the pressure field from the stagnation point around the leading edge of the airfoil. This in turn increases the lift generated by the airfoil. The tip rotation sensitivity at peak deflection is more than 85 deg per unit beam length which corresponds to the tip rotation sensitivity evident in Figure 7.28. Note that the sting rotation sensitivity in

Figure 7.28 is plotted to scale but that the sting transverse deflection sensitivity is not to scale.

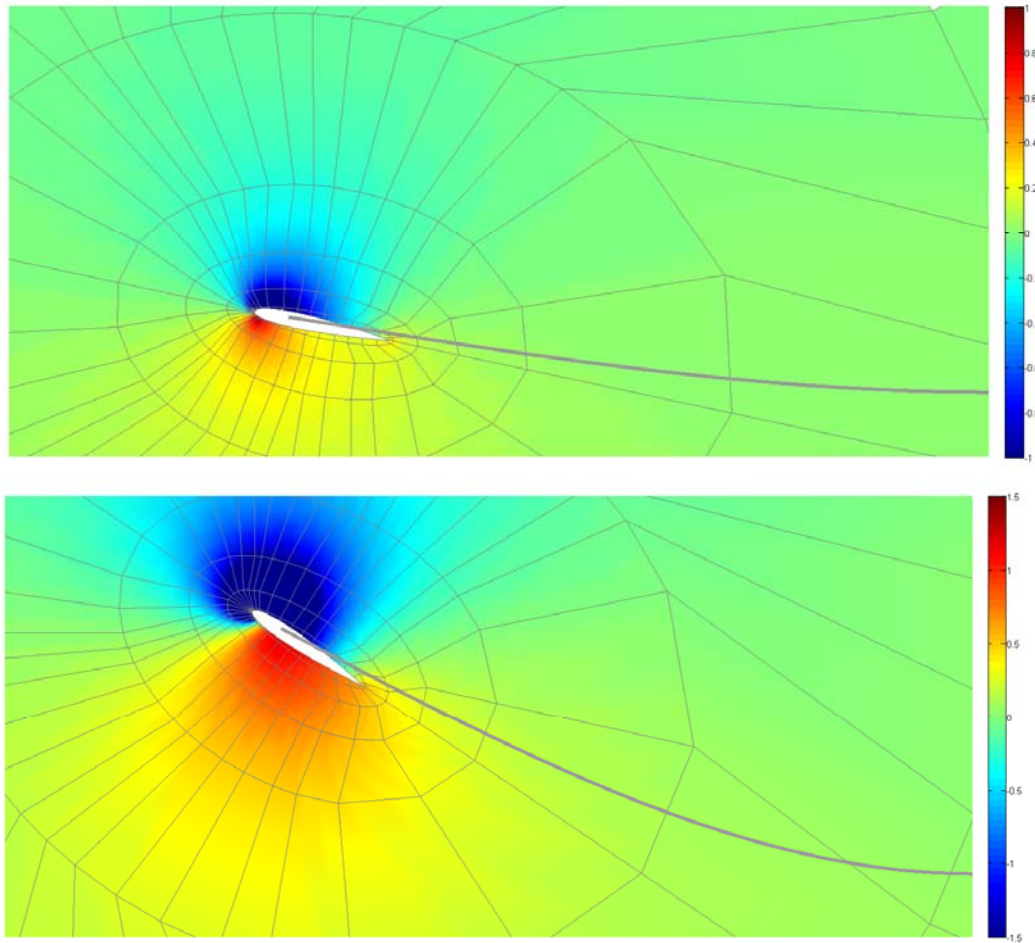


Figure 7.27: Nonlinear compressible FSI (0.5 M) pressure field and structure deformation to *one-minus-cosine gust* ($t = 0$ sec top, $t = 3.5$ sec bottom)

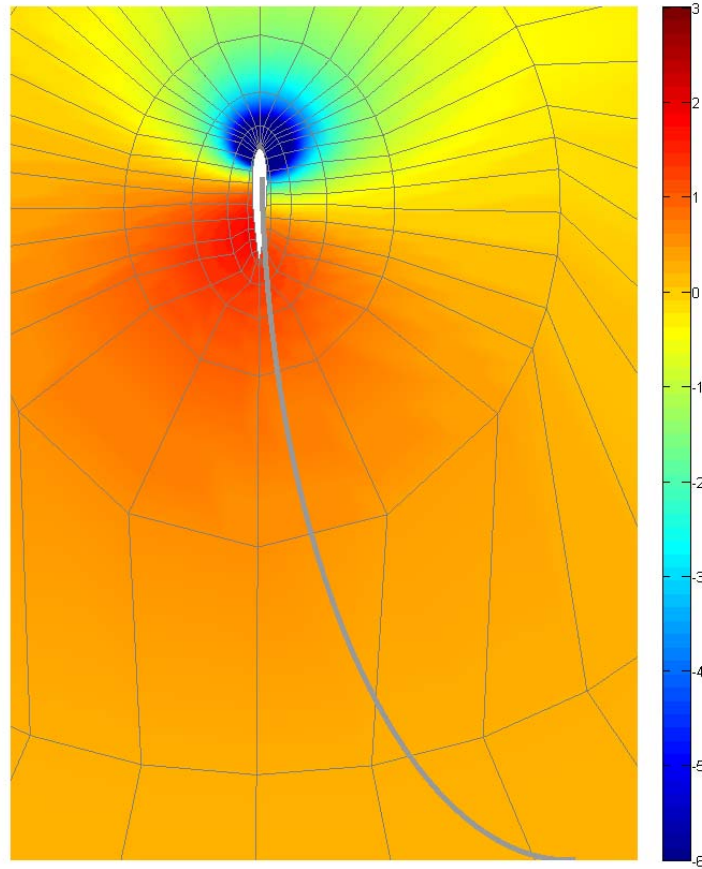


Figure 7.28: CSE pressure sensitivity to beam length with structure deformation sensitivity depicted ($t = 3.5$ sec). (Sting rotation sensitivity is plotted to scale; sting transverse deflection sensitivity is not to scale).

7.4 Summary of LS-CSE for Transient FSI

The least-squares finite element method was originally pursued for the fluid-structure interaction problem for the reasons summarized in Section 1.2. The LSFEM approach did provide a single numerical framework for both the fluid and structure systems in first-order form, which permitted direct coupling between the fluid and structure interface. This was particularly useful in establishing the monolithic formulations of the FSI parent problem. However, as also noted in the previous

applications of LSFEM to FSI [71, 101], the LSFEM FSI solution was plagued by sensitivity of the solution to the residual weights for the domain and interface functionals. Thus, only the first two example problems of the section were solved in monolithic form. The sequential iteration method used in Section 7.3 was adopted primarily to avoid the domain and interface weighting problem.

Despite the relative simplicity of the FSI models used in this chapter, the coupled fluid-structure problems incorporated compressibility and geometric nonlinearity with buckling potential and exhibited rather complex transient responses. The real significance of the current work, though, is in the definition of the coupled sensitivity system and the determination of the CSE boundary conditions. The present work adopted a local derivative form for the interface. The continuous sensitivity approach in local derivative form has an advantage over the CSE FSI approach of Pelletier *et al.* in not having to compute/invert the mesh Jacobian for shape variation problems which results in a significant computational savings for the present approach. Additionally, our approach decoupled the mesh deformation problem from both the FSI analysis and sensitivity problems.

Fluid-structure interaction problems are not simple to solve. However, once a valid solution is obtained for the fluid-structure system and the appropriate sensitivity boundary conditions are derived, the sensitivity analysis is straightforward and avoids many of the numerical complications of the parent fluid-structure problem. This is one of the great advantages of the continuous sensitivity approach: the sensitivity of even a complicated nonlinear, transient, coupled problem is a simple, linear, boundary value problem that need only be solved at a particular point in time.

We have demonstrated the continuous sensitivity solution to a single design variable for several linear, nonlinear, and transient FSI problems. The next chapter examines several practical consideration for CSE including multiple design parameters, non-shape variation sensitivity problems, and using commercial “black box” software to solve the CSE problem.

8 Practical Considerations for CSE

The previous chapters have theoretically posed and derived the continuous sensitivity equations for structural systems, fluid systems, and coupled fluid-structure systems. Further, the analytic and least-squares finite element solutions of the CSEs demonstrate the efficacy of the continuous sensitivity method and the avoidance of common shortcomings of other design sensitivity methods, particularly for shape design problems. The problem descriptions and solutions have been given in sufficient detail that they may serve as benchmarks and validation of future implementation of design sensitivity approaches.

In this chapter, several topics are introduced that discuss practical considerations or limitations to the continuous sensitivity approach. The treatment of problems involving multiple and large numbers of design variables is discussed in Section 8.1. The simplicity of the CSE method for non-shape design parameters is then demonstrated in Section 8.2. Adjoint methods are often employed for problems where the number of design variables is greater than the number of constraint or objective functions, and an adjoint continuous sensitivity method is derived in Section 8.3. Perhaps most significantly, the author introduces the conditions on the continuous system operators that must be met in order to use numerical system solvers for CSE in a “black box” manner in Section 8.4. This includes a proof of the equivalence of the nonlinear Newton-Raphson tangent stiffness matrix and sensitivity system matrix for the Galerkin method. Unfortunately, this equivalence does not apply to the least-squares finite element method.

8.1 Multiple Design Variables

The continuous sensitivity method calculates the design sensitivity for the system

$$\mathbf{A}\mathbf{u}(b) = \mathbf{f}(b) \quad (3.1)$$

by solving the CSEs associated with (3.1) for the sensitivity variables, ${}^b\mathbf{u}$

$${}^b\mathbf{A}({}^b\mathbf{u}) = {}^b\mathbf{f} \quad (8.1)$$

If the sensitivities to another design parameter, c , are desired, then another CSE system

$${}^c\mathbf{A}({}^c\mathbf{u}) = {}^c\mathbf{f} \quad (8.2)$$

must be defined and solved. Thus, there is a CSE system, along with its domain parameterization (for shape problems) and boundary conditions, for each design parameter. For large-scale problems with lots of design variables, the challenge, particularly for shape optimization, is in specifying the shape parameter domain definitions. One useful approach for dealing with multiple design variables is the adjoint method which is described in the Section 8.3. We first examine a conventional CSE approach to a two design variable example.

Consider, as a simple but illustrative example, a two-design parameter version of the 1D elastic bar example from Section 3.3. The bar is divided into two sections, as shown in Figure 8.1, and the lengths of each section are taken as independent design variables.

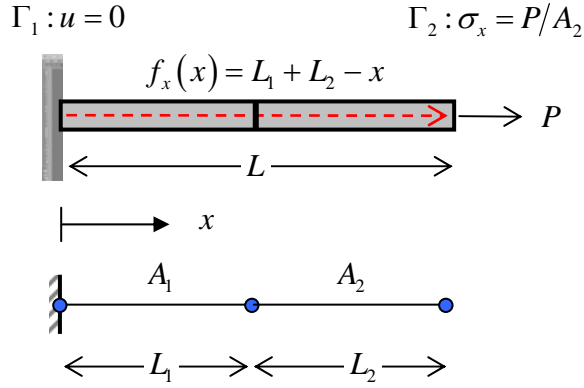


Figure 8.1: Two-section bar sensitivity example

The field equations governing the stress and displacement are the same as given by (3.20-3.21), but the solution to the field equations must be integrated separately for each sub-domain, Ω_1 and Ω_2 . This mimics the treatment of plate, skin, spar, or rib sub-domains in a built-up structure. In addition to the boundary conditions on Γ_1 and Γ_2 given in Figure 8.1, there is a domain interface condition (continuity of displacement and force equilibrium) at $\Omega_1 \cap \Omega_2$ that requires

$$u(L_1)_{\Omega_1} - u(L_1)_{\Omega_2} = 0 \quad (8.3)$$

$$\sigma_x(L_1)_{\Omega_1} A_1 - \sigma_x(L_1)_{\Omega_2} A_2 = 0 = 0 \quad (8.4)$$

This is naturally handled in the FEM assembly of sub-structures, *i.e.* by directly enforcing the continuity of nodal variables. It is included here explicitly to illustrate the CSE method over multiple sub-domains. The problem sub-domains from Figure 8.1 are parameterized by

$$\mathbf{X}_{\Omega_1}(x) = \{\xi L_1; \xi \in [0,1]\}, \quad \mathbf{X}_{\Omega_2}(x) = \{L_1 + \xi L_2; \xi \in [0,1]\} \quad (8.5)$$

The field equations may be directly integrated to yield the stress and displacement solutions

$$\sigma_x(x; L_1, L_2) = \begin{cases} \frac{x^2 - L_1^2}{2A_1} - \frac{(L_1 + L_2)(x - L_1)}{A_1} + \frac{L_2^2}{2A_1} + \frac{P}{A_1} & \text{for } x \in [0, L_1] \\ \frac{x^2 - (L_1 + L_2)^2}{2A_2} - \frac{(L_1 + L_2)(x - L_1 - L_2)}{A_2} + \frac{P}{A_2} & \text{for } x \in [L_1, L_1 + L_2] \end{cases} \quad (8.6)$$

and

$$u(x; L_1, L_2) = \begin{cases} \frac{x^3}{6EA_1} - \frac{(L_1 + L_2)x^2}{2EA_1} + \left[-\frac{L_1^2}{2EA_1} + \frac{(L_1 + L_2)L_1}{EA_1} + \frac{L_2^2}{2EA_1} \right] x + \frac{P}{EA_1} x & \text{for } x \in [0, L_1] \\ \frac{x^3 - L_1^3}{6EA_2} - \frac{L_1x^2}{2EA_2} - \frac{L_2x^2}{2EA_2} - \frac{L_1^2L_2}{2EA_2} + \frac{L_1^2x}{2EA_2} + \frac{L_1L_2x}{EA_2} + \frac{L_2^2x}{2EA_2} - \frac{L_1L_2^2}{2EA_2} + \dots & \\ \frac{Px}{EA_2} - \frac{PL_1}{EA_2} + \frac{L_1^3}{6EA_1} + \frac{L_1^2L_2}{2EA_1} + \frac{L_1L_2^2}{2EA_1} + \frac{PL_1}{EA_1} & \text{for } x \in [L_1, L_1 + L_2] \end{cases} \quad (8.7)$$

For no tip load, $P = 0$, the analytic (local) sensitivities of stress and displacement to segment length L_1 are then

$$\sigma_{x, L_1}(x) = \begin{cases} \frac{L_1}{A_1} + \frac{L_2}{A_1} - \frac{x}{A_1} & \text{for } x \in [0, L_1] \\ \frac{L_1}{A_2} + \frac{L_2}{A_2} - \frac{x}{A_2} & \text{for } x \in [L_1, L_1 + L_2] \end{cases} \quad (8.8)$$

and

$$u_{, L_1}(x) = \begin{cases} \frac{L_1x}{EA_1} + \frac{L_2x}{EA_1} - \frac{x^2}{2EA_1} & \text{for } x \in [0, L_1] \\ -\frac{x^2}{2EA_2} - \frac{L_1^2 + L_2^2}{2EA_2} - \frac{L_1L_2}{EA_2} + \frac{(L_1 + L_2)x}{EA_2} + \dots & \\ \frac{L_1^2 + L_2^2}{2EA_1} + \frac{L_1L_2}{EA_1} & \text{for } x \in [L_1, L_1 + L_2] \end{cases} \quad (8.9)$$

which is the same result obtained in (3.24-3.25) if the substitutions $L = L_1 + L_2$ and $A_1 = A_2$ are made. Similarly, the sensitivities of stress and displacement to segment length L_2 are

$$\sigma_{x,L_2}(x) = \begin{cases} \frac{L_1}{A_1} + \frac{L_2}{A_1} - \frac{x}{A_1} & \text{for } x \in [0, L_1] \\ \frac{L_1}{A_2} + \frac{L_2}{A_2} - \frac{x}{A_2} & \text{for } x \in [L_1, L_1 + L_2] \end{cases} \quad (8.10)$$

and

$$u_{,L_2}(x) = \begin{cases} \frac{L_1 x}{EA_1} + \frac{L_2 x}{EA_1} - \frac{x^2}{2EA_1} & \text{for } x \in [0, L_1] \\ -\frac{x^2}{2EA_2} - \frac{L_1^2}{2EA_2} + \frac{(L_1 + L_2)x}{EA_2} - \frac{L_1 L_2}{EA_2} + \frac{L_1^2}{2EA_1} + \frac{L_1 L_2}{EA_1} & \text{for } x \in [L_1, L_1 + L_2] \end{cases} \quad (8.11)$$

which again gives the same result obtained in (3.24-3.25) with the appropriate substitutions.

The corresponding CSEs are (taking the cross-sectional area as a constant in each segment)

$${}^{L_i}\sigma_{x,x} + \frac{1}{A_i} {}^{L_i}f_x = 0 \quad (8.12)$$

$${}^{L_i}u_{,x} - \frac{1}{E} {}^{L_i}\sigma_x = 0 \quad (8.13)$$

where the index $i = 1, 2$ for each segment (Einstein summation is NOT implied on the repeated index). The sensitivity body forces are

$${}^{L_1}f_x = f_{x,L_1} = 1 \quad (8.14)$$

and

$${}^{L_2}f_x = f_{x,L_2} = 1 \quad (8.15)$$

Parameterize the boundaries with respect to segment lengths by

$$\mathbf{X}_{\Gamma_1} = \{0\} \quad , \quad \mathbf{X}_{\Gamma_2} = \{L_1 + L_2\} \quad (8.16)$$

The bar remains fixed at the base regardless of segment length, so the total derivative of displacement at the origin is zero. Additionally, based on the parameterization of (3.39), the material point at the base of the bar does not move with changes in bar length, that is

$\mathbf{X}_{\Gamma_1, L_1} = 0$. Thus, the displacement sensitivity boundary condition is zero at the origin.

Since the load at the tip of the bar vanishes, the gradient of the axial stress is zero and the total derivative at the tip is also zero. To summarize, the CSE boundary conditions are

$${}^{L_1}u = 0 \quad \text{at } x = 0 \quad (8.17)$$

$${}^{L_1}\sigma_x = 0 \quad \text{at } x = L \quad (8.18)$$

In addition, the sensitivity interface condition at $\Omega_1 \cap \Omega_2$ is

$${}^{L_1}u(L_1)_{\Omega_1} - {}^{L_1}u(L_1)_{\Omega_2} = 0 \quad (8.19)$$

$${}^{L_1}\sigma_x(L_1)_{\Omega_1} A_1 - {}^{L_1}\sigma_x(L_1)_{\Omega_2} A_2 = 0 \quad (8.20)$$

Again, this is naturally handled in the FEM assembly of sub-structures. The explicit treatment here is illustrative in the integration of the field equations for the analytic solution to the CSEs. Note that the CSEs, (3.37) and (3.38), for each design parameter, L_1 and L_2 (and the boundary data, (3.40) and (3.41)) for each design parameter in this example are the same. This is not surprising since the independent effect of L_1 and L_2 on the entire bar length is the same. The influence of L_1 and L_2 on the sensitivity solution will be realized in each sub-domain segment. Integrating the CSEs with the boundary data yields the CSE solutions

$${}^{L_1}\sigma_x(x) = \begin{cases} \frac{L_1}{A_1} + \frac{L_2}{A_1} - \frac{x}{A_1} & \text{for } x \in [0, L_1] \\ \frac{L_1}{A_2} + \frac{L_2}{A_2} - \frac{x}{A_2} & \text{for } x \in [L_1, L_1 + L_2] \end{cases} \quad (8.21)$$

$${}^{L_1}u(x) = \begin{cases} \frac{L_1 x}{EA_1} + \frac{L_2 x}{EA_1} - \frac{x^2}{2EA_1} & \text{for } x \in [0, L_1] \\ -\frac{x^2}{2EA_1} + \frac{(L_1 + L_2)x}{EA_1} & \text{for } x \in [L_1, L_1 + L_2] \end{cases} \quad (8.22)$$

Note that in the integration to yield (8.22), the restriction $A_1 = A_2$ has been made explicit¹ when enforcing the integration limit at $x = L_1$. The CSE stress solution (8.21) matches exactly the analytic stress sensitivities in (8.8) and (8.10) obtained from differentiating the analytic solution. If the restriction $A_1 = A_2$ is made in the analytic displacement sensitivity, (8.9) and (8.11), the result is

$$u_{,L_1}(x) = \begin{cases} \frac{L_1 x}{EA_1} + \frac{L_2 x}{EA_1} - \frac{x^2}{2EA_1} & \text{for } x \in [0, L_1] \\ -\frac{x^2}{2EA_2} + \frac{(L_1 + L_2)x}{EA_2} & \text{for } x \in [L_1, L_1 + L_2] \end{cases} \quad (8.23)$$

and

$$u_{,L_2}(x) = \begin{cases} \frac{L_1 x}{EA_1} + \frac{L_2 x}{EA_1} - \frac{x^2}{2EA_1} & \text{for } x \in [0, L_1] \\ -\frac{x^2}{2EA_2} + \frac{(L_1 + L_2)x}{EA_2} & \text{for } x \in [L_1, L_1 + L_2] \end{cases} \quad (8.24)$$

respectively and the agreement with the CSE solution (8.22) is also exact.

This two-parameter example demonstrates how the domain description and boundary parameterization may be more complicated for a multiple design variable CSE problem, but the overall approach does not differ. In this particular example, the CSEs and boundary data were the same for both parameters, so that the CSE solution for each design variable was identical. This is not surprising since the affect of the design parameters from each substructure on the overall structure was the same. There may

¹ The displacement CSE sensitivity determined in closed-form by integrating the strain sensitivity (which comes from the stress sensitivity and the constitutive relation). The force continuity at the interface results in a stress discontinuity at $x = L_1$ if $A_1 \neq A_2$. The simplifying assumption of equal cross-sections at the interface is not necessary, but it does reduce the number of cases for displacement sensitivity solutions and simplifies the comparison with analytic sensitivities below.

exist a general principle or condition for certain types of design parameters and their boundary parameterization that will yield computational savings in multiple design variable problems for built-up structures. This is a good avenue for future research. In general, this should not be expected. However, the challenge in sensitivity analysis for large-scale problems is not unique to the continuous sensitivity approach. One way to deal with problems involving multiple design variables is to solve an adjoint sensitivity system. We explore an adjoint description of the CSEs in Section 8.3. First however, we demonstrate how simple CSE implementation of non-shape design parameters is compared with shape design sensitivity.

8.2 CSE for Material or Sizing Parameters

All of the CSE derivations and examples in this dissertation have focused on shape parameter sensitivity, as that is the more challenging and complicated problem for sensitivity analysis. The challenge is due to the variation of the domain under the influence of the shape parameter and leads to the important distinction, sometimes overlooked, between local and material sensitivities. Much of the difficulty in applying the CSE method to shape sensitivity problems stems from determining the boundary parameterization and the appropriate boundary conditions. The CSE approach, however, easily permits sensitivity analysis for non-shape design parameters, *e.g.* material or sizing parameters, since the boundary does not move and the boundary conditions are often homogeneous.

As an example, consider the sensitivity to the material property E of the two-segment bar problem from the previous section. The associated CSEs for stress and displacement are

$$-\left({}^E\sigma_x A_i\right)_{,x} = {}^E f_x = 0 \quad (8.25)$$

$$E {}^E u_{,x} + u_{,x} - {}^E \sigma_x = 0 \quad (8.26)$$

where the index $i = 1, 2$ for each segment. The sensitivity boundary conditions are

$${}^E u = 0 \quad \text{at } x = 0 \quad (8.27)$$

$${}^E \sigma_x = 0 \quad \text{at } x = L \quad (8.28)$$

and the continuity and equilibrium sensitivity interface conditions hold between each segment as before. Direct integration readily yields the CSE solution

$${}^E \sigma_x(x) = 0 \quad (8.29)$$

$${}^E u(x) = \frac{-1}{E} u(x) \quad (8.30)$$

where $u(x)$ is given by (8.7). Since $u(x)$ has the form

$$u(x) = \frac{1}{E} r(x) \quad (8.31)$$

where r is a polynomial function not containing any factors of E , the analytic material sensitivity is

$$u_{,E}(x) = -\frac{1}{E^2} r(x) = -\frac{1}{E} u(x) = {}^E u(x) \quad (8.32)$$

Thus the CSE and analytic sensitivity to E both yield the same result. As an example of a sizing sensitivity problem, consider the two-segment bar CSEs for cross-sectional area (cross-sectional area is again treated as a constant in each segment)

$$A_j {}^{A_i} \sigma_{x,x} + \delta_{ij} \sigma_{x,x} = -{}^{A_i} f_x = 0 \quad (8.33)$$

$$E {}^{A_i} u_{,x} - {}^{A_i} \sigma_x = 0 \quad (8.34)$$

where δ_{ij} is the Dirac delta function. The index j refers to the bar segment, $j = 1, 2$, and i is the cross-sectional area index. As with the material parameter E CSE system, the displacement sensitivity boundary condition at the base of the bar is homogeneous. However, the tip stress sensitivity boundary condition becomes

$$^{A_i}\sigma_x(L_1 + L_2) = \frac{\partial}{\partial A_i} \frac{P}{A_2} \quad (8.35)$$

Also note that the interface force equilibrium condition is a function of the cross-sectional areas. Differentiating the interface condition, (8.4), provides the sensitivity interface conditions for each segment

$$A_1 ^{A_1}\sigma_x(L_1)_{\Omega_1} + \sigma_x(L_1)_{\Omega_1} = A_2 ^{A_1}\sigma_x(L_1)_{\Omega_2} \quad (8.36)$$

$$A_1 ^{A_2}\sigma_x(L_1)_{\Omega_1} = A_2 ^{A_2}\sigma_x(L_1)_{\Omega_2} + \sigma_x(L_1)_{\Omega_2} \quad (8.37)$$

Note that the $\sigma_x(L_1)_{\Omega_1}$ and $\sigma_x(L_1)_{\Omega_2}$ become nodal loads in the finite element analysis.

The displacement sensitivity interface relation is simply

$$^{A_i}u(L_1)_{\Omega_1} - ^{A_i}u(L_1)_{\Omega_2} = 0 \quad (8.38)$$

We now solve for the CSEs for the sensitivity to cross-sectional area, A_1 . Direct integration again of the A_1 stress CSE yields

$$^{A_1}\sigma_x(x) = \begin{cases} -\frac{1}{A_1} [\sigma_x(x) - \sigma_x(L_1) + \sigma_x(L_1)] & \text{for } x \in [0, L_1] \\ 0 & \text{for } x \in [L_1, L_1 + L_2] \end{cases} \quad (8.39)$$

where the first of last two terms that cancel for $x \in [0, L_1]$ came from the limits of integration and the second stemmed from the interface condition (8.36). Since $\sigma(x)$ has the form

$$\sigma(x) = \begin{cases} \frac{1}{A_1} r_1(x) & \text{for } x \in [0, L_1] \\ r_2(x) & \text{for } x \in [L_1, L_1 + L_2] \end{cases} \quad (8.40)$$

where r_i is a polynomial function not containing any factors of A_1 , the analytic stress sensitivity is

$$\sigma_{,A_1}(x) = \begin{cases} -\frac{1}{A_1^2} r_1(x) = -\frac{1}{A_1} \sigma_x(x) & \text{for } x \in [0, L_1] \\ 0 & \text{for } x \in [L_1, L_1 + L_2] \end{cases} \quad (8.41)$$

which matches the result for ${}^{A_1}\sigma_x(x)$ in (8.39). Thus the CSE and analytic stress sensitivity to A_1 both yield the same result. Direct integration also yields the CSE solution for A_1 displacement sensitivity

$${}^{A_1}u(x) = \frac{1}{E} \int_0^x {}^{A_1}\sigma_x(x) dx = -\frac{1}{A_1 E} \int_0^x \sigma_x(x) dx = -\frac{1}{A_1} u(x) = u_{,A_1}(x) \quad (8.42)$$

which matches the analytic sensitivity in the first segment.

Similarly, in the second bar segment, $x \in [L_1, L_1 + L_2]$,

$${}^{A_1}u(x) = {}^{A_1}u(L_1) + \frac{1}{E} \int_{L_1}^x {}^{A_1}\sigma_x(x) dx = {}^{A_1}u(L_1) + \int_{L_1}^x (0) dx = {}^{A_1}u(L_1) \quad (8.43)$$

where the integration constant comes from the sensitivity interface displacement condition. The analytic sensitivity to A_1 in the second bar segment, $x \in [L_1, L_1 + L_2]$, is

$$u_{,A_1}(x) = -\frac{1}{A_1} \left[\frac{L_1^3}{6EA_1} + \frac{L_1^2 L_2}{2EA_1} + \frac{L_1 L_2^2}{2EA_1} + \frac{PL_1}{EA_1} \right] = -\frac{1}{A_1} u(L_1) = {}^{A_1}u(L_1) \quad (8.44)$$

which is obvious by substituting L_1 into (8.7) and is again the expected result. Thus the CSE and analytic sensitivity to A_1 also yield the same solution.

Because the CSE boundary conditions for non-shape parameter sensitivity problems are typically homogeneous, the CSE solution to material and sizing parameter

problems is generally simple. The straightforward complications in the examples of this section stemmed from the multiple design variables and partitioned domains, and not from the CSE system itself. One approach for dealing with multiple design variables is the adjoint method which is explored in the next section.

8.3 Adjoint CSE

The adjoint method is a common approach to solving design sensitivity problems. For problems with many design variables and load conditions and few active constraints, the adjoint method is generally a more efficient means to obtain the desired sensitivities than direct differentiation. Adjoint methods for discrete sensitivity analysis are well established and documented in structural design texts [34, 59, 60] and several interesting applications have been developed for fluid and aerodynamic optimization problems [66, 67, 90, 109, 110]. See Section 2.3.3 for a more detailed review of the application of adjoint methods to aeroelastic problems.

Although the adjoint approach is typically employed as a discrete sensitivity method, the same rationale and benefits that motivated the development of continuous sensitivity analysis apply equally to direct and adjoint differentiation. Jameson *et al.* have recently developed a continuous adjoint method for unsteady aerodynamic problems [68, 87] which is derived starting from the fluid system residual equations. We now derive a continuous adjoint method that begins from the continuous sensitivity equations instead of the original parent equations.

Returning again to the continuous system

$$\mathbf{A}\mathbf{u}(b) = \mathbf{f}(b) \tag{3.1}$$

Consider an objective or constraint function, $h(\mathbf{u}(b), b)$, of the problem unknowns and the design parameter, b . The sensitivity of h with respect to b is desired. Following the derivation approach of [59], the sensitivity of h to b is

$$\frac{Dh}{Db} = \frac{\partial h}{\partial b} + \left\{ \frac{\partial h}{\partial \mathbf{u}} \right\}^T \cdot \frac{\partial \mathbf{u}}{\partial b} \quad (8.45)$$

where the components of the $\left\{ \frac{\partial h}{\partial \mathbf{u}} \right\}$ vector consist of derivatives of h with respect to each of the u_i components of \mathbf{u} . Adding the product of a Lagrange multiplier and the (linear) continuous sensitivity system (3.14) to (8.45) yields

$$\frac{Dh}{Db} = \frac{\partial h}{\partial b} + \frac{\partial h}{\partial \mathbf{u}} \cdot \frac{\partial \mathbf{u}}{\partial b} + \boldsymbol{\lambda}^T (\mathbf{f}_{,b} - \mathbf{A}\mathbf{u}_{,b} - \mathbf{A}_{,b}\mathbf{u}) \quad (8.46)$$

Note that a linear form for the system (3.1) is assumed in (8.46). In this case, the $\mathbf{A}_{,b}$ term captures explicit dependence of the operator \mathbf{A} on b . Implicit dependence of \mathbf{A} on b due to nonlinearities is not considered in the adjoint derivation (but is considered in the CSE solutions presented in Section 8.4). Regrouping the $\mathbf{u}_{,b}$ CSE unknowns in (8.46) together yields

$$\frac{Dh}{Db} = \frac{\partial h}{\partial b} + \left(\frac{\partial h}{\partial \mathbf{u}} - \boldsymbol{\lambda}^T \mathbf{A} \right) \cdot \mathbf{u}_{,b} + \boldsymbol{\lambda}^T (\mathbf{f}_{,b} - \mathbf{A}_{,b}\mathbf{u}) \quad (8.47)$$

The second term on the right-hand side can be eliminated by solving the adjoint continuous sensitivity problem

$$\mathbf{A}\boldsymbol{\lambda} = \frac{\partial h}{\partial \mathbf{u}} \quad (8.48)$$

where $\boldsymbol{\lambda}$ is the adjoint vector. Note that in the adjoint CSE method delivers the sensitivity

$\frac{Dh}{Db}$, but the sensitivity variables, $\mathbf{u}_{,b}$, are never calculated. Thus, the CSE problem need

not be solved. This is an obvious disadvantage if the \mathbf{u}_b sensitivity is desired or required in addition to the objective/constraint function sensitivity, $\frac{Dh}{Db}$.

8.4 Nonlinear Analysis and “Black-box” implementation of CSE

When the parent problem is a linear problem, the CSE problem is easily solved using the same numerical method used to solve the original problem, since the systems are identical except for their boundary conditions. However, many problems of interest are nonlinear in nature, in which case the sensitivity system takes a different form from the parent system. However, it is still possible in some cases to use the nonlinear solver as a “black-box” (*i.e.*, without access to the source code for modification) to solve the CSE system. Two common iterative approaches are used to solve nonlinear problems via the finite element method: direct substitution (also known as the Picard method of successive substitution) and the Newton-Raphson method. Common variants of the Newton-Raphson method include the modified Newton-Raphson method and the secant or arc-length method.

This section explores using common outputs from nonlinear “black-box” solvers based on the Newton-Raphson and the direct substitution methods to generate the stiffness matrix for the linear CSE problem. This avoids the computational cost of generating and assembling the system for the CSE problem, although the CSE boundary conditions must still be formulated. Both LSFEM and conventional Galerkin weighted residual methods are considered. Restrictions on the nature of the problem and the solution method are stated. This is not an original idea; the literature clearly states that it can be done, but without explanation of how to do so and without any warnings on the

conditions required of the equations or numerical solvers. The recognition and description of the conditions under which numerical solvers can be used in a “black box” manner should allow a more widespread adoption of the CSE method.

8.4.1 Newton-Raphson Nonlinear Iteration for CSE

The Newton-Raphson (N-R) method for FEM is based on Newton’s method for extracting solutions to polynomials. It is generally derived with the implicit assumption of a Galerkin-derived finite element model. We derive it based on Reddy’s [106] approach but for the more general case that includes least-squares finite element models.

The nonlinear finite element model is

$$[\mathbf{K}(\mathbf{U})]\{\mathbf{U}\} = \{\mathbf{F}(\mathbf{U})\} \quad (8.49)$$

where in general both the stiffness matrix, \mathbf{K} , and load vector, \mathbf{F} , may be functions of the finite element solution, \mathbf{U} . The residual vector of (8.49) is

$$\{\mathbf{R}(\mathbf{U})\} \equiv [\mathbf{K}(\mathbf{U})]\{\mathbf{U}\} - \{\mathbf{F}(\mathbf{U})\} \quad (8.50)$$

which equals zero at the exact solution, $\hat{\mathbf{U}}$. Expanding the residual vector in a first-order Taylor series about the finite element solution from the $(r-1)^{\text{th}}$ iteration and evaluating it at the (unknown) exact solution yields

$$\{\mathbf{R}(\hat{\mathbf{U}})\} = \mathbf{R}(\mathbf{U}^{r-1}) + \left(\frac{\partial \{\mathbf{R}\}}{\partial \{\mathbf{U}\}} \right)^{r-1} [\{\hat{\mathbf{U}}\} - \{\mathbf{U}\}^{r-1}] + \dots \approx \mathbf{R}(\mathbf{U}^{r-1}) + \left(\frac{\partial \{\mathbf{R}\}}{\partial \{\mathbf{U}\}} \right)^{r-1} \{\delta \mathbf{U}\} = 0 \quad (8.51)$$

Defining the tangent stiffness matrix

$$\mathbf{K}_T(\mathbf{U}^{r-1}) \equiv \left(\frac{\partial \{\mathbf{R}\}}{\partial \{\mathbf{U}\}} \right)^{r-1} \quad (8.52)$$

yields a means of solving for the increment from \mathbf{U}^{r-1} to achieve the desired solution $\hat{\mathbf{U}}$ by

$$\{\delta \mathbf{U}\} = -[\mathbf{K}_T]^{-1} \{\mathbf{R}(\mathbf{U}^{r-1})\} = -[\mathbf{K}_T]^{-1} \left\{ [\mathbf{K}(\mathbf{U}^{r-1})] \{\mathbf{U}^{r-1}\} - \{\mathbf{F}(\mathbf{U}^{r-1})\} \right\} \quad (8.53)$$

The (improved) approximate solution at the next iteration is then

$$\{\mathbf{U}\}^r = \{\mathbf{U}\}^{r-1} + \{\delta \mathbf{U}\} \quad (8.54)$$

Note that the tangent stiffness matrix, \mathbf{K}_T , is not the same as the system stiffness matrix, \mathbf{K} . In a single degree of freedom case, the tangent stiffness is the slope at a point on the load-displacement curve, whereas the secant matrix is the slope of the line from the origin (or the prior estimate) to the same point. The tangent stiffness matrix can be generated at the element level and assembled in the same manner as the system stiffness matrix. The component form of (8.52) is

$$K_{T_{ij}} \equiv \frac{\partial R_i}{\partial u_j} = \frac{\partial}{\partial u_j} \left(\sum_{m=1}^n K_{im} u_m - F_i \right) = \sum_{m=1}^n \frac{\partial K_{im}}{\partial u_j} u_m + K_{ij} - \frac{\partial F_i}{\partial u_j} \quad (8.55)$$

The distinction between \mathbf{K}_T and \mathbf{K} is obvious from (8.55) where K_{im} are the components of \mathbf{K} . For Galerkin-based finite element models, the $\frac{\partial F_i}{\partial u_j}$ term vanishes if \mathbf{f} is not an

explicit function of \mathbf{u} . This is typically true, since the Galerkin \mathbf{F} is generated by the inner product (ϕ, \mathbf{f}) . Thus, the last term in (8.55) is typically omitted from most definitions of the tangent stiffness matrix. In situations for which $\mathbf{F}(\mathbf{u})$ is an explicit function of \mathbf{u} , it is permissible to redefine $\mathbf{K}(\mathbf{u})$ to absorb the dependence of \mathbf{u} .

Nevertheless, even in this case, the non-zero $\frac{\partial F_i}{\partial u_j}$ term will reappear from $\frac{\partial K_{im}}{\partial u_j}$ so it is

more straightforward to include it in tangent stiffness definition (8.55). In contrast to

Galerkin-based finite element models, for which typically $\frac{\partial F_i}{\partial u_j} = 0$, the finite element

load vector in a least-squares finite element model of the nonlinear system, $\mathbf{A} = \mathbf{A}(\mathbf{u})$, will be a function of \mathbf{u} (even if \mathbf{f} is not an explicit function of \mathbf{u}). This is because the LSFEM load vector is generated by the inner product $(\mathbf{A}\mathbf{v}, \mathbf{f})$ and \mathbf{A} is a nonlinear function of \mathbf{u} . Thus, for LSFEM, $\frac{\partial F_i}{\partial u_j} \neq 0$. Omitting the $\frac{\partial F_i}{\partial u_j}$ term from the definition of the tangent stiffness matrix significantly slows the convergence of the N-R method applied to LSFEM.

Previous researchers [24] have noted that if the Newton-Raphson method is used, then the linear sensitivity system is available in factored form and the final iteration of the tangent stiffness matrix will yield the desired sensitivity matrix. Although they provide no details, this appears to suggest a shortcut to the CSE stiffness matrix without having to generate and assemble the matrix from the CSE system. Though this appears to work for the Galerkin method, it is not generally true for other weighted-residual forms as the two examples that follow demonstrate.

These examples highlight an unanticipated but significant shortcoming of the LSFEM approach to nonlinear analysis. Although the N-R method has a smaller region of convergence, it is generally more efficient than the direct substitution method explored in Section 8.4.2, and thus is one of the most common iterative solution strategies for solving nonlinear systems. There is a computational shortcut for the sensitivity of a nonlinear system from a Galerkin finite element solution, since the final tangent stiffness matrix yields the sensitivity system stiffness matrix without additional computation. The sensitivity system must still be solved for the appropriate sensitivity boundary data, but the computational expense of generating and assembling the stiffness matrix from the

sensitivity system is avoided. A LSFEM solution strategy precludes this computational shortcut, as demonstrated in the following two examples.

8.4.1.1. First-order, univariate example

Consider the nonlinear, first-order, single degree of freedom system

$$u + uu_{,x} = f(x) = 2x \quad (8.56)$$

on the interval $x \in [a, b]$ with boundary data

$$u(b) = 1 \quad (8.57)$$

For $a=0$ and $b=1$, the solution is

$$u(x) = x \quad (8.58)$$

Parameterize the domain as $\mathbf{X}(x) = \left\{ \xi b; \xi = \frac{x}{b} \right\}$ and take b as a domain shape

parameter. The sensitivity system associated with (8.56) is

$$(1 + u_{,x})(^b u) + u ^b u_{,x} = f_{,b}(x) = 0 \quad (8.59)$$

and the sensitivity boundary condition is

$$^b u(b) = D_b u - \nabla u \cdot \mathbf{X}_{,b} = 1 - 1 = 0 \quad (8.60)$$

The solution to the sensitivity system is then

$$^b u(x) = 0 \quad (8.61)$$

A single linear element is sufficient to represent the solution to both the parent and the sensitivity problem. The nonlinear stiffness matrix for the Galerkin finite element model of the parent system is¹

$$\mathbf{K} = \begin{bmatrix} \frac{1}{3} - \frac{1}{3}u_1 - \frac{1}{6}u_2 & \frac{1}{6} + \frac{1}{3}u_1 + \frac{1}{6}u_2 \\ \frac{1}{6} - \frac{1}{6}u_1 - \frac{1}{3}u_2 & \frac{4}{3} + \frac{1}{6}u_1 + \frac{1}{3}u_2 \end{bmatrix} \quad (8.62)$$

and the tangent stiffness matrix is

$$\mathbf{K}_T = \begin{bmatrix} \frac{1}{3} - \frac{2}{3}u_1 + \frac{1}{6}u_2 & \frac{1}{6} + \frac{1}{6}u_1 + \frac{1}{3}u_2 \\ \frac{1}{6} - \frac{1}{3}u_1 - \frac{1}{6}u_2 & \frac{4}{3} - \frac{1}{6}u_1 + \frac{2}{3}u_2 \end{bmatrix} \quad (8.63)$$

The CSE stiffness matrix for the Galerkin FEM is

$${}^b\mathbf{K} = \begin{bmatrix} \frac{1}{3} + \frac{1}{3}(u_2 - u_1) - \frac{1}{3}u_1 - \frac{1}{6}u_2 & \frac{1}{6} + \frac{1}{6}(u_2 - u_1) + \frac{1}{3}u_1 + \frac{1}{6}u_2 \\ \frac{1}{6} + \frac{1}{6}(u_2 - u_1) + \frac{1}{3}u_1 + \frac{1}{6}u_2 & \frac{4}{3} + \frac{1}{3}(u_2 - u_1) + \frac{1}{6}u_1 + \frac{1}{3}u_2 \end{bmatrix} = \mathbf{K}_T \quad (8.64)$$

Thus, the tangent stiffness and CSE stiffness matrices are the same for the Galerkin FEM in this example. The numerical tangent stiffness and CSE stiffness matrices evaluated at the finite element solution $\mathbf{u} = \{0, 1\}^T$ are

$$\mathbf{K}_T = \begin{bmatrix} \frac{1}{2} & \frac{1}{2} \\ 0 & 2 \end{bmatrix} \quad (8.65)$$

and

$${}^b\mathbf{K} = \begin{bmatrix} \frac{1}{2} & \frac{1}{2} \\ 0 & 2 \end{bmatrix} \quad (8.66)$$

which makes the equality more obvious.

¹ The weak enforcement of boundary condition (8.57) is included in the generation of (8.62)-(8.64).

Specifically, $\mathbf{K}_{(\cdot)} = \mathbf{K}_\Omega + \mathbf{K}_\Gamma$ where $\mathbf{K}_\Gamma = \begin{bmatrix} 0 & 0 \\ 0 & 1 \end{bmatrix}$ and $\mathbf{G}_\Gamma = \begin{Bmatrix} 0 \\ 1 \end{Bmatrix}$. Including the weak boundary condition has no effect on the conclusion for either the Galerkin or LSFEM method.

Turning now to the LSFEM model, the LSFEM nonlinear stiffness matrix for the parent system is

$$\mathbf{K} = \begin{bmatrix} \frac{-\frac{1}{3}u_2^3 - \frac{1}{3} + u_1 - u_1^2 + u_1^3}{u_1 - u_2 - 1} & \frac{\frac{1}{6} + \frac{1}{6}u_1 - \frac{1}{6}u_2 - \frac{1}{3}u_1^2 - \frac{1}{3}u_1u_2 - \frac{1}{3}u_2^2}{1} \\ \frac{\frac{1}{6} + \frac{1}{6}u_1 - \frac{1}{6}u_2 - \frac{1}{3}u_1^2 - \frac{1}{3}u_1u_2 - \frac{1}{3}u_2^2}{1} & \frac{\frac{1}{3} + u_2 + u_2^2 + \frac{1}{3}u_2^3 - \frac{1}{3}u_1^3}{1 - u_1 + u_2} + 1 \end{bmatrix} \quad (8.67)$$

and the tangent stiffness matrix is (from (8.55) which includes the $\frac{\partial F_i}{\partial u_j}$ term)

$$\mathbf{K}_T = \begin{bmatrix} u_1^2 - \frac{4}{3}u_1 + \frac{2}{3} - \frac{1}{6}u_2 & -\frac{1}{6}u_1 - u_2^2 + \frac{5}{6} - \frac{1}{3}u_2 \\ -u_1^2 + \frac{1}{3}u_1 - \frac{1}{6} + \frac{1}{6}u_2 & \frac{1}{6}u_1 + u_2^2 + \frac{2}{3} + \frac{4}{3}u_2 \end{bmatrix} \quad (8.68)$$

It is obvious from a comparison of the off diagonal components $K_{T_{12}}$ and $K_{T_{21}}$ that the tangent stiffness matrix based on the LSFEM-generated parent stiffness matrix is not symmetric. Recall that a LSFEM system is always symmetric, so (8.68) cannot equal the LSFEM CSE stiffness matrix as was true for the Galerkin model. The LSFEM CSE stiffness matrix is

$${}^b\mathbf{K} = \begin{bmatrix} \frac{1}{3}u_2^3 + \frac{1}{3}(1 - u_2)^3 & -\frac{1}{6}(1 - 2u_1 + 2u_2) + \frac{1}{2}(1 - 2u_1 + u_2)(1 - 2u_1 + 2u_2) + \frac{1}{2}u_1(-1 + 2u_1 - 2u_2) + u_1(1 - 2u_1 + u_2) \\ sym & 1 + \frac{\frac{1}{3}(1 - u_1 + 2u_2)^3 - \frac{1}{3}u_1^3}{(1 + 2u_1 - 2u_2)} \end{bmatrix} \quad (8.69)$$

Comparison of (8.68) and (8.69) shows that the tangent stiffness cannot yield the LSFEM CSE matrix. The numerical LSFEM tangent stiffness and CSE stiffness matrices evaluated at the finite element solution $\mathbf{u} = \{0, 1\}^T$ are

$$\mathbf{K}_T = \begin{bmatrix} \frac{1}{2} & -\frac{1}{2} \\ 0 & 3 \end{bmatrix} \quad (8.70)$$

and

$${}^b\mathbf{K} = \begin{bmatrix} 1 & 0 \\ 0 & 4 \end{bmatrix} \neq \mathbf{K}_T \quad (8.71)$$

This counterexample is sufficient to show that the computational shortcut of the Galerkin approach is not permitted in a LSFEM approach. This will also be obvious in the proof of the Galerkin equivalence that appears in Section 8.4.1.3.

8.4.1.2. Second-order example

As a higher-order example, consider the second-order nonlinear problem from [106] Example 3.4.1.

$$-\frac{d}{dx}\left(u\frac{du}{dx}\right) = f_0 = -1 \quad (8.72)$$

on the interval $x \in [0, b]$ with boundary data

$$u(0) = 1, \quad u_{,x}(0) = 0 \quad (8.73)$$

The solution is

$$u(x) = \sqrt{1 + x^2} \quad (8.74)$$

The first-order form of (8.72) with $v = u_{,x}$ is

$$v^2 + uv_{,x} = 1 \quad (8.75)$$

which in matrix-operator form is

$$\begin{bmatrix} 0 & 1 \\ 0 & v \end{bmatrix} \begin{Bmatrix} u \\ v \end{Bmatrix} + \begin{bmatrix} -1 & 0 \\ 0 & u \end{bmatrix} \begin{Bmatrix} u_{,x} \\ v_{,x} \end{Bmatrix} = \begin{Bmatrix} 0 \\ 1 \end{Bmatrix} \quad (8.76)$$

Taking b as a domain shape parameter, the sensitivity system associated with (8.72) is

$$u_{,xx} {}^b u + 2u_{,x} {}^b u_{,x} + u {}^b u_{,xx} = 0 \quad (8.77)$$

which has the first-order matrix-operator form

$$\begin{bmatrix} 0 & 1 \\ v_{,x} & 2v \end{bmatrix} \begin{Bmatrix} {}^b u \\ {}^b v \end{Bmatrix} + \begin{bmatrix} -1 & 0 \\ 0 & u \end{bmatrix} \begin{Bmatrix} {}^b u_{,x} \\ {}^b v_{,x} \end{Bmatrix} = \begin{Bmatrix} 0 \\ 0 \end{Bmatrix} \quad (8.78)$$

We again compare the Galerkin tangent stiffness matrix for a single linear element. The nonlinear stiffness matrix for the Galerkin finite element model of the parent system is

$$\mathbf{K} = \begin{bmatrix} \frac{1}{2} & \frac{1}{3} & -\frac{1}{2} & \frac{1}{6} \\ 0 & -\frac{1}{3}u_1 + \frac{1}{4}u_2 - \frac{1}{6}u_3 + \frac{1}{12}u_4 & 0 & \frac{1}{3}u_1 + \frac{1}{12}u_2 + \frac{1}{6}u_3 + \frac{1}{12}u_4 \\ \frac{1}{2} & \frac{1}{6} & -\frac{1}{2} & \frac{1}{3} \\ 0 & -\frac{1}{6}u_1 + \frac{1}{12}u_2 - \frac{1}{3}u_3 + \frac{1}{12}u_4 & 0 & \frac{1}{6}u_1 + \frac{1}{12}u_2 + \frac{1}{3}u_3 + \frac{1}{4}u_4 \end{bmatrix} \quad (8.79)$$

and the tangent stiffness matrix is

$$\mathbf{K}_T = \begin{bmatrix} \frac{1}{2} & \frac{1}{3} & -\frac{1}{2} & \frac{1}{6} \\ -\frac{1}{3}u_2 + \frac{1}{3}u_4 & -\frac{1}{3}u_1 + \frac{1}{2}u_2 - \frac{1}{6}u_3 + \frac{1}{6}u_4 & -\frac{1}{6}u_2 + \frac{1}{6}u_4 & \frac{1}{3}u_1 + \frac{1}{6}u_2 + \frac{1}{6}u_3 + \frac{1}{6}u_4 \\ \frac{1}{2} & \frac{1}{6} & -\frac{1}{2} & \frac{1}{3} \\ -\frac{1}{6}u_2 + \frac{1}{6}u_4 & -\frac{1}{6}u_1 + \frac{1}{6}u_2 - \frac{1}{3}u_3 + \frac{1}{6}u_4 & -\frac{1}{3}u_2 + \frac{1}{3}u_4 & \frac{1}{6}u_1 + \frac{1}{6}u_2 + \frac{1}{3}u_3 + \frac{1}{2}u_4 \end{bmatrix} \quad (8.80)$$

The CSE stiffness matrix for the Galerkin FEM is

$${}^b\mathbf{K} = \begin{bmatrix} \frac{3}{2} & \frac{1}{3} & -\frac{1}{2} & \frac{1}{6} \\ \frac{1}{3}v_{,x} & -\frac{1}{3}u_1 + \frac{1}{2}u_2 - \frac{1}{6}u_3 + \frac{1}{6}u_4 & \frac{1}{6}v_{,x} & \frac{1}{3}u_1 + \frac{1}{6}u_2 + \frac{1}{6}u_3 + \frac{1}{6}u_4 \\ \frac{1}{2} & \frac{1}{6} & -\frac{1}{2} & \frac{1}{3} \\ \frac{1}{6}v_{,x} & -\frac{1}{6}u_1 + \frac{1}{6}u_2 - \frac{1}{3}u_3 + \frac{1}{6}u_4 & \frac{1}{3}v_{,x} & \frac{1}{6}u_1 + \frac{1}{6}u_2 + \frac{1}{3}u_3 + \frac{1}{2}u_4 \end{bmatrix} \quad (8.81)$$

which is identical to the tangent stiffness matrix (8.80) once the finite element approximation $v_{,x} = -u_2 + u_4$ is made for the gradient of the solution of (8.76).

We have demonstrated the equivalence of the Galerkin tangent stiffness and CSE systems in two example problems. We now prove that this equivalence is always exact for Galerkin and is not permitted by LSFEM. Though the equivalence has been employed in several prior works, to the author's knowledge no proof of equivalence has appeared in the literature.

8.4.1.3. Equivalence of Galerkin Tangent Stiffness and CSE Systems

We now prove that the Galerkin-derived tangent stiffness matrix at the final converged solution yields the desired CSE system stiffness matrix. Recall that the first-order sensitivity system may be written as

$$\left(\frac{\partial \mathbf{A}}{\partial \mathbf{u}} \mathbf{u}_\delta + \mathbf{A} \right) \mathbf{u}_{,b} = \mathbf{f}_{,b} - \frac{\partial \mathbf{A}}{\partial b} \mathbf{u} \quad (3.14)$$

where $\frac{\partial \mathbf{A}}{\partial \mathbf{u}} \mathbf{u}_\delta \equiv \frac{\partial \mathbf{A}}{\partial u_i} [u_i \delta_{ji}]$. The Galerkin stiffness matrix for the sensitivity system in operator form is then

$${}^b \mathbf{K} = \int_{\Omega^e} \left(\psi_1, \dots, \psi_{n_{dof}^e} \right)^T \left(\left(\frac{\partial \mathbf{A}}{\partial \mathbf{u}} \mathbf{u}_\delta + \mathbf{A} \right) \psi_1, \dots, \left(\frac{\partial \mathbf{A}}{\partial \mathbf{u}} \mathbf{u}_\delta + \mathbf{A} \right) \psi_{n_{dof}^e} \right) d\Omega \quad (8.82)$$

To avoid confusion between the vector index and the indexed components of the finite element approximation used below, we consider the nonlinear dependence of each component of the vector \mathbf{u} independently. This is permitted by recognizing from (3.12) that the nonlinear effect of each component of \mathbf{u} is the superposition of each component. Denote the nonlinear component of interest by u^* (we intentionally avoid an index since we reserve the index notation for components of the FEM approximation in the next step). This in no way limits the proof since each components of \mathbf{u} may be considered independently which is obvious when the CSE is written in the form of (3.13). We now write the component definition of the Galerkin sensitivity matrix as

$${}^b K_{ij} = \int_{\Omega^e} \psi_i \left(\frac{\partial}{\partial u^*} \mathbf{A} [u_i \delta_{ji}] + \mathbf{A} \right) \psi_j d\Omega \quad (8.83)$$

or

$${}^b K_{ij} = \int_{\Omega^e} \psi_i \mathbf{A} \psi_j d\Omega + \int_{\Omega^e} \psi_i \left(\frac{\partial}{\partial u^*} \mathbf{A} \right) \psi_j [u_i \delta_{ji}] d\Omega \quad (8.84)$$

The first term on the right-hand side is the definition of the Galerkin stiffness matrix for the original system. Introducing the finite element approximation for the continuous function u^*

$$u^* = u_i \psi_i \quad (8.85)$$

where summation on the repeated index is implied. Solving the finite element approximation for the u_j coefficient yields

$$u_j = \frac{u^*}{\psi_j} - \frac{1}{\psi_j} \sum_{i \neq j} u_i \psi_i \quad (8.86)$$

Differentiating (8.86) with respect to the u_j coefficient and noting that the shape functions ψ_i are not functions of the coefficients and that the coefficients are independent are so that $\partial u_i / \partial u_j = 0$ yields

$$1 = \frac{\partial u^*}{\partial u_j} \frac{1}{\psi_j} \quad (8.87)$$

Thus

$$\int \left[\frac{\partial}{\partial u^*}(\cdot) \right] \psi_j d\Omega = \int \left[\frac{\partial}{\partial u^*} \frac{\partial u^*}{\partial u_j} \frac{1}{\psi_j}(\cdot) \right] \psi_j d\Omega = \int \left[\frac{\partial}{\partial u_j}(\cdot) \right] \frac{1}{\psi_j} \psi_j d\Omega \quad (8.88)$$

which yields the identity

$$\int \left[\frac{\partial}{\partial u^*}(\cdot) \right] \psi_j d\Omega = \frac{\partial}{\partial u_j} \int (\cdot) d\Omega \quad (8.89)$$

where $\partial / \partial u_j$ can be pulled out of the integral because it is not a function of the domain.

With (8.89), the Galerkin sensitivity system stiffness matrix (8.84) becomes

$${}^b K_{ij} = K_{ij} + \frac{\partial}{\partial u_j} \int_{\Omega^e} \psi_i(\mathbf{A}) u_m \psi_m d\Omega \quad (8.90)$$

where the finite element approximation has been used for $u_i \delta_{ji}$. Regrouping yields

$${}^b K_{ij} = K_{ij} + \frac{\partial}{\partial u_j} \left[\int_{\Omega^e} \psi_i \mathbf{A} \psi_m d\Omega \right] u_m = K_{ij} + \frac{\partial K_{im}}{\partial u_j} u_m \quad (8.91)$$

which is recognized as the component definition of the tangent stiffness matrix (8.55) for the original system at the converged solution. Thus, for a Galerkin finite element formulation, the nonlinear system tangent stiffness matrix (linearized about the system solution) is identical to the stiffness matrix for the sensitivity system.

A similar analysis for the LSFEM yields

$${}^b K_{ij} = \int \psi_i \mathbf{A}^T \mathbf{A} \psi_j d\Omega + \int \psi_i \mathbf{A}^T \mathbf{A}_{,u} u \psi_j d\Omega + \int u \psi_i \mathbf{A}_{,u}^T \mathbf{A} \psi_j d\Omega + \int u \psi_i \mathbf{A}_{,u}^T \mathbf{A}_{,u} u \psi_j d\Omega \quad (8.92)$$

or

$${}^b K_{ij} = K_{ij} + \frac{\partial}{\partial u_j} K_{im} u_m + \frac{\partial}{\partial u_i} K_{jm} u_m + \frac{\partial}{\partial u_i} \frac{\partial}{\partial u_j} K_{km} u_k u_m \quad (8.93)$$

which is obviously not equal to the N-R tangent stiffness matrix. It is the result of the product rule and the presence of the second set of operators in the integrand which break the parallel with the definition of the tangent stiffness matrix (8.55) enjoyed by the Galerkin form.

The Newton-Raphson method is probably the most widely used iterative method for nonlinear problems, although it is not the simplest. The direct substitution method is simpler than the Newton-Raphson method and often has a wider region of convergence, though it generally does not converge as quickly as the Newton-Raphson method. More importantly for LSFEM, however, is that whereas the Newton-Raphson solution does not permit a computational shortcut for CSE of nonlinear problems, the direct-substitution method does under certain conditions. These conditions apply equally to LSFEM and Galerkin solutions and are the subject of the next section.

8.4.2 Direct Substitution Nonlinear Iteration for CSE

In the direct substitution iterative method (also known as the Picard method of successive substitution), the solution from an initial estimate is used to form the stiffness matrix. With each iteration, the prior solution is used as an estimate for the solution. Thus the n^{th} iterative finite element model is

$$\left[\mathbf{K}(\mathbf{u}^{n-1}) \right] \{ \mathbf{u}^n \} = \{ \mathbf{F}(\mathbf{u}^{n-1}) \} \quad (8.94)$$

Often, the method will separate the stiffness matrix into a stationary component \mathbf{K}_0 and an update component \mathbf{K}_N so that

$$\left[\mathbf{K}(\mathbf{u}^{n-1}) \right] = \left[\mathbf{K}_0 + \mathbf{K}_N(\mathbf{u}^{n-1}) \right] \quad (8.95)$$

Then the n^{th} iterative finite element model can take the form

$$\left[\mathbf{K}_0 \right] \{ \mathbf{u}^n \} = \{ \mathbf{F}(\mathbf{u}^{n-1}) \} - \left[\mathbf{K}_N(\mathbf{u}^{n-1}) \right] \{ \mathbf{u}^{n-1} \} \quad (8.96)$$

For a nonlinear system, $\mathbf{K} \neq {}^b\mathbf{K}$. But if

$$\mathbf{K}_0 = {}^b\mathbf{K}_0 \quad (8.97)$$

and the update takes the form

$${}^b\mathbf{K}_N(\mathbf{u}) = \mathbf{K}_N(r(\mathbf{u})) \quad (8.98)$$

where $r(\cdot)$ is some function, then

$$\left[{}^b\mathbf{K} \right] \{ \mathbf{u} \} = \left[\mathbf{K}_0 + \mathbf{K}_N(r(\mathbf{u})) \right] \{ {}^b\mathbf{u} \} = \{ {}^b\mathbf{F}(\mathbf{u}) \} \quad (8.99)$$

and the direct substitution “black box” solver can be used to solve the CSE system, provided that the solver allows for an initial estimate in the form of a function of the solution, $r(\cdot)$. Before establishing sufficient conditions for the satisfaction of (8.97) and (8.98), we illustrate the process with a series of example problems.

Consider the nonlinear Euler-Bernoulli beam introduced in Chapter 4

$$\rho_y \frac{\partial^2 v}{\partial t^2} + \frac{\partial^2}{\partial x^2} \left(EI \frac{\partial^2 v}{\partial x^2} \right) - \frac{\partial}{\partial x} \left[\frac{EA}{2} \left(\frac{\partial v}{\partial x} \right)^3 \right] = p_y \quad (8.100)$$

The operator matrices for the vector $\mathbf{u} = \{v, \theta, M_z, V_y, \dot{v}\}^T$ are

$$A_t = \begin{bmatrix} 0 & 0 & 0 & 0 & 0 \\ 0 & 0 & 0 & 0 & 0 \\ 0 & 0 & 0 & 0 & 0 \\ 0 & 0 & 0 & 0 & \rho_y \\ 1 & 0 & 0 & 0 & 0 \end{bmatrix} \quad A_0 = \begin{bmatrix} 0 & 1 & 0 & 0 & 0 \\ 0 & 0 & 1/EI & 0 & 0 \\ 0 & a_{32} & 0 & -1 & 0 \\ 0 & 0 & 0 & 0 & 0 \\ 0 & 0 & 0 & 0 & -1 \end{bmatrix} \quad A_1 = \begin{bmatrix} -1 & 0 & 0 & 0 & 0 \\ 0 & -1 & 0 & 0 & 0 \\ 0 & 0 & -1 & 0 & 0 \\ 0 & 0 & 0 & 1 & 0 \\ 0 & 0 & 0 & 0 & 0 \end{bmatrix} \quad \mathbf{f} = \begin{bmatrix} 0 \\ 0 \\ 0 \\ p_y \\ 0 \end{bmatrix} \quad (8.101)$$

The a_{32} component contains the nonlinear term for the system. For the beam problem,

$$a_{32} = \frac{EA}{2} \theta^2 \quad (8.102)$$

For the sensitivity problem

$$a_{32} = \frac{3}{2} EA \theta^2 \quad (8.103)$$

In this example, the update matrix for the parent beam problem and the sensitivity problem are related by

$${}^b\mathbf{K}_N(\theta) = \mathbf{K}_N(\sqrt{3}\theta) \quad (8.104)$$

That is, if $\sqrt{3}\theta$ is substituted into the nonlinear update to the stiffness matrix as an initial guess, then the nonlinear beam solver will solve the sensitivity problem. Of course, the sensitivity boundary conditions must also be specified. Note that only the initial iteration of the direct substitution method is performed in order to solve the sensitivity problem.

As another example, consider the parent system

$$\frac{1}{2} u^2 + u_{,x} = f(x) \quad (8.105)$$

and the associated sensitivity system

$$u({}^b u) + {}^b u_{,x} = f_{,b}(x) \quad (8.106)$$

The parent operator “matrices” are

$$A_0 = \frac{1}{2}u, \quad A_1 = 1 \quad (8.107)$$

and the sensitivity system operator matrices are

$${}^bA_0 = u, \quad A_1 = 1 \quad (8.108)$$

The LSFEM model ($p=1$) for a single element approximation of (8.105) is

$$K_0 = \begin{bmatrix} 1 & -1 \\ -1 & 1 \end{bmatrix}, \quad K_N = \begin{bmatrix} \frac{1}{12}u^2 - \frac{1}{2}u & \frac{1}{24}u^2 \\ \frac{1}{24}u^2 & \frac{1}{12}u^2 + \frac{1}{2}u \end{bmatrix} \quad (8.109)$$

and the LSFEM sensitivity model is

$$K_0 = \begin{bmatrix} 1 & -1 \\ -1 & 1 \end{bmatrix}, \quad {}^bK_N = \begin{bmatrix} \frac{1}{3}u^2 - u & \frac{1}{6}u^2 \\ \frac{1}{6}u^2 & \frac{1}{3}u^2 + u \end{bmatrix} \quad (8.110)$$

Thus, substituting $2u$ into the parent problem update matrix in place of u yields the desired sensitivity system.

Consider now, as a final counterexample, the parent and sensitivity system posed in (8.56) and (8.59) respectively. The parent operator matrices are

$$A_0 = 1, \quad A_1 = u \quad (8.111)$$

and the sensitivity system operator matrices are

$${}^bA_0 = (1 + u_{,x}), \quad A_1 = u \quad (8.112)$$

The LSFEM model ($p=1$) for a single element approximation of (8.56) is

$$K_0 = \begin{bmatrix} \frac{1}{3} & \frac{1}{6} \\ \frac{1}{6} & \frac{1}{3} \end{bmatrix}, \quad K_N = \begin{bmatrix} u^2 - u & -u^2 \\ -u^2 & u^2 + u \end{bmatrix} \quad (8.113)$$

and the LSFEM sensitivity model is

$$K_0 = \begin{bmatrix} \frac{1}{3} & \frac{1}{6} \\ \frac{1}{6} & \frac{1}{3} \end{bmatrix}, \quad {}^bK_N = \begin{bmatrix} \frac{2}{3}u_{,x} + \frac{1}{3}u_{,x}^2 - u - u_{,x}u + u^2 & \frac{1}{3}u_{,x} + \frac{1}{6}u_{,x}^2 - u^2 \\ \frac{1}{3}u_{,x} + \frac{1}{6}u_{,x}^2 - u^2 & \frac{2}{3}u_{,x} + \frac{1}{3}u_{,x}^2 + u + u_{,x}u + u^2 \end{bmatrix} \quad (8.114)$$

$${}^bK_N = K_N + \begin{bmatrix} \frac{2}{3}u_{,x} + \frac{1}{3}u_{,x}^2 - u_{,x}u & \frac{1}{3}u_{,x} + \frac{1}{6}u_{,x}^2 \\ \frac{1}{3}u_{,x} + \frac{1}{6}u_{,x}^2 & \frac{2}{3}u_{,x} + \frac{1}{3}u_{,x}^2 + u_{,x}u \end{bmatrix}$$

In this case, there is no substitution function for the parent update that will yield the sensitivity system, ${}^b K_N(u) \neq K_N(r(u))$.

We are now prepared to state a sufficient condition on the system operators to use the direct substitution solver as a “black box” for the sensitivity system:

Condition 8.1: If the differential operator matrices for the nonlinear parent system are nonlinear only in the operator component upon which they operate, then there exists a substitution function such that ${}^b \mathbf{K}_N(\mathbf{u}) = \mathbf{K}_N(r(\mathbf{u}))$.

In the general case, the parent problem can be nonlinear in a primary variable or the spatial or temporal derivatives of the primary variable. Thus, the general parent operator system has the form

$$\left[\mathbf{A}_0(\mathbf{u}, \nabla \mathbf{u}, \mathbf{u}_{,t}; b) \mathbf{u} + \mathbf{A}_1(\mathbf{u}, \nabla \mathbf{u}, \mathbf{u}_{,t}; b) \mathbf{u}_{,x} + \mathbf{A}_2(\mathbf{u}, \nabla \mathbf{u}, \mathbf{u}_{,t}; b) \mathbf{u}_{,y} + \mathbf{A}_t(\mathbf{u}, \nabla \mathbf{u}, \mathbf{u}_{,t}; b) \mathbf{u}_{,t} \right] = \left[\mathbf{f}(\mathbf{x}, \mathbf{u}; b) \right] \quad (8.115)$$

Equation (8.115) is differentiated with respect to the parameter b to yield the sensitivity system. With respect to the general nonlinear form (8.115), we state three corollaries that follow from Condition 8.1:

Corollary 8.1a: The requirement $\mathbf{A}_0 = \mathbf{A}_0(\mathbf{u}; b)$ only, implies that

$${}^b \mathbf{A}_0(\mathbf{u}; b) = \mathbf{A}_0(r(\mathbf{u}); b) \quad (8.116)$$

Corollary 8.1b: The requirement $\mathbf{A}_i = \mathbf{A}_i(\mathbf{u}_{,i}; b)$ only, implies that

$${}^b \mathbf{A}_i(\mathbf{u}_{,i}; b) = \mathbf{A}_i(r(\mathbf{u}_{,i}); b) \quad (8.117)$$

where $i = 1 \dots \dim$.

Corollary 8.1c: The requirement $\mathbf{A}_t = \mathbf{A}_t(\mathbf{u}_{,t}; b)$ only, implies that

$${}^b \mathbf{A}_t(\mathbf{u}_{,t}; b) = \mathbf{A}_t(r(\mathbf{u}_{,t}); b) \quad (8.118)$$

Note that these sufficient conditions for the existence of the function $r(\cdot)$ apply to both LSFEM and Galerkin finite element models.

8.4.3 Summary of Nonlinear Black-Box Solver Strategies for CSE

As shown in Section 8.4.1, a major limitation of the least-squares finite element method for continuous sensitivity analysis of nonlinear problems is that it usually precludes using the tangent stiffness matrix from the Newton-Raphson method in lieu of generating the stiffness matrix for the CSE system. This is possible in Galerkin-based FEM and may contribute to a significant computational savings. No such restrictions apply to either the LSFEM or Galerkin finite element models when using the direct substitution method, however, the problem must meet the requirements of Condition 8.1. Additionally, the “black box” solver must permit the user to bootstrap a function of the initial approximation variables and to terminate the solver after a single iteration.

In either case, using a “black box” nonlinear solver to execute a single iteration and solve the linear sensitivity system should yield computational savings, since the sensitivity system does not have to be generated and assembled from the sensitivity equations. The sensitivity boundary conditions still must be calculated using the solution to the parent problem.

Finally, we recall that using a nonlinear solver in this manner is not an original idea. Some [59] have claimed, without detail, that it could be done. Other researchers [24] have used the technique, but without warning of the limits to the numerical formulation or equation conditions that must be met. The detail of this section is the only known rigorous treatment of the subject. The recognition and description of the

conditions under which numerical solvers can be used in a “black box” manner should allow a more widespread adoption of the CSE method.

9 Conclusions & Future Work

With the notable exception of the work by a few key progenitors, specifically Borggaard and Burns, and then Pelletier and his students, the continuous sensitivity method has largely been ignored relative to other methods for obtaining design gradient information. This is a shame, particularly with respect to shape variation problems, for the continuous sensitivity analysis approach is a powerful method and is relatively simple to implement within the same numerical mesh and framework of the underlying analysis problem. Some of the lack of widespread adoption of continuous sensitivity analysis is probably due to the early prominence of other methods, *e.g.* discrete sensitivity. Another factor may be that the derivation of the continuous sensitivity equations for the most general cases in many of the textbooks tends to obscure the simplicity of the continuous sensitivity system when posed in local derivative form. This is true of the original formulations for elasticity systems [39] as well as the more recent fluid-structure sensitivity work by Pelletier *et al.* which mixes local and total derivative forms.

The first of two major contributions of the present work is the recognition that the system is simpler to pose in local derivative form. The local sensitivity may then be converted to total (material) sensitivity form as needed. The second contribution is the detailed explanation of how to employ the same code for continuous sensitivity analysis as was used to solve the original analytical problem. Both of these significant contributions, as well as several minor contributions, are explained in further detail in Section 9.3. First, we outline the general conclusions regarding the least-squares continuous sensitivity method in Section 9.1, and then summarize the details from the earlier chapters in Section 9.2. In Section 1), the author recommends areas for future

research. The final word on CSE for FSI applications is discussed in Section 9.5. First, though, we outline the general conclusion of the work.

9.1 General Conclusions

Although continuous sensitivity analysis can be widely applied to both shape and non-shape variation problems, it is particularly suited for shape variation problems since it avoids the computationally expensive mesh sensitivity problems of other sensitivity methods. For the reasons given below (Section 9.3), the continuous sensitivity equations for shape variation applications are best posed in local derivative form. Structural optimization will generally be done with respect to material coordinates for which material gradients are desired, but it is straightforward to transform the local derivative solution from the CSE problem into the desired total (material) sensitivities.

One of the advantages to continuous sensitivity is that it permits the solution of the sensitivity problem using the same numerical mesh and method as was used to solve the original system. The least-squares finite element method was originally pursued for the fluid-structure interaction problem for the reasons summarized in Section 1.2. The LSFEM approach did permit a single numerical framework for both the fluid and structure systems in first-order form. The first-order form was attractive because it permitted direct coupling between the fluid and structure and because the accuracy of all variables was then of the same order. This proved useful in establishing the boundary conditions for the sensitivity system which are based on the solution to the parent FSI problem. However, the LSFEM FSI solution was plagued by dependence of the solution to the residual weights for the domain and interface functionals. More devastating to the

LS-CSE method, however, is that it precludes a significant computational advantage for assembly of the sensitivity system when the Newton-Raphson method is used to solve a nonlinear system. This was explained in Section 8.4.1 and is summarized in Section 9.3.

9.2 Summary of Work

First-order formulations for a range of elasticity and fluid models were derived and posed in a form amenable to solution by the least-squares finite element method. The elasticity and fluid models included both linear and nonlinear, and steady and nonsteady problems and were validated against published or known analytic solutions. The elastic structure and fluid models were then coupled in a series of representative fluid-structure interaction problems. The FSI problems also included linear, nonlinear, steady, and transient problems. All problems were solved using a LSFEM model that was implemented using an original, higher-order p -element method for 1D and 2D-quadrilateral elements in MATLAB[®].

The continuous sensitivity equations for each of the elastic, fluid, and fluid-structure problems explored in Chapters 5-7, were posed and solved using the same computational mesh and solution. A key distinction between the local and total derivative forms of the sensitivity equations was introduced. This distinction, though present in the work of other researchers, is usually obscure at best and at times is ignored or neglected altogether, producing erroneous solutions. The continuous sensitivity system of equations and sensitivity boundary conditions were derived and solved in local derivative form, which was shown to be superior for several applications. The local derivative solution was then transformed to a total derivative solution suitable for

optimization at material points. This process was demonstrated in the optimization of an elasticity problem.

In the present work, the continuous sensitivity systems were solved using the same high-order least-squares finite element method that was used to solve the underlying parent problems. The LSFEM approach is attractive in that it allows a stable mixed element, a better approximation of dual or secondary variable gradients compared to the weak-form Galerkin formulations, an inherent error estimate, and flexibility in norm choice. The improved accuracy of the dual variable gradients inherent in the first-order mixed formulation is particularly important, because the gradients of the underlying solution are used to pose the boundary conditions for the sensitivity system. The higher-order p -element implementation also permitted a straightforward means to achieve a refined solution without needing a refined mesh. Thus, both the parent and sensitivity systems can be solved to any desired level of convergence using a single computational mesh. This is particularly important since, as observed in the literature, the CSE solution often requires finer resolution than the original system.

The fluid-structure models used in the current work were relatively simple models. Despite the simplicity of the models, the coupled fluid-structure system with a structural system incorporating geometric nonlinearity and buckling potential exhibits rather complex transient responses. The real significance of the current work, though, is in the definition of the coupled sensitivity system and the determination of the CSE boundary conditions. The nonlinear effect of the dynamic response for the underlying fluid-structure system was also demonstrated in the solution to the linear sensitivity system.

Overall, the least-squares continuous sensitivity method appears to be a promising option for the optimization of transient, nonlinear, fluid-structure optimization problems. There is no need to determine the proper step size as is required in finite difference methods—a requirement that can become problematic in multivariate optimization problems—and there is no need to compute the mesh sensitivity as is required in discrete sensitivity methods. Additionally, since the CSEs are always linear, there is a potential computational savings in not having to calculate multiple solutions to the underlying nonlinear system. Furthermore, finite difference and traditional discrete methods can yield only the total derivative, whereas the continuous sensitivity method yields both local and total derivatives. The continuous sensitivity approach in local derivative form has an advantage over mixed-derivative form of the CSE FSI approach of Pelletier *et al.* in not having to compute/invert the mesh Jacobian for shape variation problems. This can represent a significant computational savings for the CSE approach in local derivative form.

9.3 Summary of Significant Results and Contributions

This dissertation makes two significant contributions to the state of knowledge for the application of continuous sensitivity methods. Although they were presented in support of the sensitivity analysis for fluid-structure interaction problems, they are more general and more fundamental than the application to FSI.

The first of two major contributions is the explicit distinction between local and total derivatives for shape variation problems. The distinction is present in previous works, but it is obscure and at times overlooked by other researchers. The more

significant aspect of this contribution is the recognition that the sensitivity system was simpler to pose in local derivative form than in total (material) derivative form. This is explained in detail in Chapter 3. The advantage of writing the CSE system in local derivative form is that only the boundary parameterization for shape variation problems need be described, which avoids having to define a parameterization or transformation function for the entire domain. Thus, the CSE problem is generally simpler to pose and solve in term of local sensitivities and to then convert the result to total derivatives for optimization.

The second major contribution is the detailed explanation of how to employ the same numerical method for continuous sensitivity analysis as was used to solve the original analytical problem. This may be done in a “black box” manner without access to the source code and was explained in detail in Chapter 8. Previous researchers have stated, without proof or explanation, that it is possible to use the same code to solve both the analysis and sensitivity problems. However, this is generally not true unless certain conditions to the equation forms are satisfied and is further restricted by the form of the numerical solver. For example, a Galerkin-based finite element model permits use of the final Newton-Raphson tangent stiffness matrix to solve the sensitivity system, but other weighted-residual finite element models, *e.g.* LSFEM, do not. The recognition and description of the conditions under which numerical solvers can be used in a “black box” manner should allow a more widespread adoption of the CSE method. The difficulty in sensitivity analysis for FSI applications lies not in the sensitivity but in the analysis problem, and there are several commercial codes that perform FSI analysis. Being able

to use these commercial codes to also solve the sensitivity system is a potent possibility for continuous sensitivity analysis of fluid-structure interaction problems.

In addition to these two significant contributions, several minor, original contributions have also been advanced. Each of these was explained in more detail in earlier chapters:

- 1) First sensitivity calculation for a nonlinear FSI, transient gust response (Chapter 7)
- 2) Explicit explanation that local sensitivities for shape variation problems are not unique, but that the material derivative is unique (Chapter 3)
- 3) Simpler sensitivity boundary condition for elasticity problems with traction boundary conditions (Chapter 3, Chapter 5)
- 4) Most detailed application of continuous sensitivity to the solution of an elasticity problem to appear in the literature (Chapter 5)
- 5) Demonstration that transient sensitivity problems need not be solved as a transient problem (Chapter 7)
- 6) Demonstration of a condensation and recovery method for improving the condition number of least-squares finite element weakly enforced boundary data (Chapter 4)
- 7) Observations on an apparent relationship between the minimum recommended polynomial order for the least-squares finite element (LSFEM) solution to elasticity problems and the lowest order stable-mixed element for elasticity (Chapter 4)
- 8) First known documented use of an alternative norm solution for a LSFEM elasticity system and comparison with the traditional L^2 norm (Chapter 4)
- 9) Numerical stability analysis for a LSFEM domain with higher-order backward-difference discrete time formulation method for transient LSFEM (Chapter 4)

- 10) Proof of the equivalence of Newton-Raphson tangent stiffness matrix and CSE system matrix for Galerkin FEM (Chapter 8)
- 11) Derivation of an improved Newton-Raphson method for LSFEM (Chapter 8)

9.4 Avenues for Future Research

This research has introduced the local derivative form of the CSEs for fluid-structure interaction problems. Although the method has been successfully demonstrated on a relevant transient, nonlinear aeroelastic gust response problem, the example was relatively simple. Further work is necessary to ensure the theoretical methods developed in this research are a practical option for the aeroelastic optimization of the large-scale applications of interest to the sponsor (Section 1.1). This section describes the next logical steps for scaling the work up as well as other promising avenues for research that appeared during the course of the present effort.

9.4.1 Problem and domain scaling

The examples used to demonstrate the theory developed in this research were limited to 2D by the limits of the numerical finite element solver that was employed. To apply these method to practical design optimization problems, full 3D fluids and 3D structural models are necessary. There are no theoretical limits that preclude the extension of the continuous sensitivity to higher dimension. The boundary parameterization will become more complicated (a line parameter in 2D becomes two surface coordinate parameters in 3D), but the principle of defining the boundary coordinate set in terms of material points still holds. The most successful nonlinear fluid model (in terms of nonlinear, transient examples) was the full compressible potential

model derived and examined in Chapters 4 and 6 respectively. A significant computational savings is possible by solving the linear potential equations, instead of the full compressible potential equations, and correcting the pressure solution for compressibility via one of the well-known compressibility corrections. This is mathematically justifiable in the incompressible limit of the compressible potential equation, and it was also verified in a series of example problems for thin airfoils.

Both *coupled space-time FEM* and *backwards-difference time, FEM space* formulations were developed in this research. The space-time FEM model was the easiest to employ but was limited to 1D space applications because of the 2D limit of the numerical solver. The numerical stability limits of the backwards-difference time method could only be established for the simplest cases. A higher dimension finite element solver would permit higher dimension space-time FEM formulations. For example, brick elements would allow 2D systems to be solved along the 3rd dimension for time. Full 3D space formulations would require a 4th time dimension in the solver.

The use of p -elements permitted an easy method for refining the sensitivity solution without creating a new computational mesh. For higher space-time FEM formulations, the tensor product expansion basis is probably superior to the serendipity expansion. This is primarily due to the uncertainty of how to select the proper serendipity terms. The 3D or 4D “hyper-bubble” modes would be simpler to define by employing the tensor product expansion. A tensor product expansion would also readily permit different p -values in different dimensions (*e.g.* independent p -values for time and space). The cost of the tensor product expansion would be the additional degrees of freedom compared to the serendipity expansion.

9.4.2 Using commercial FSI software to solve the sensitivity system

Fluid-structure interaction problems are not simple to solve. The spectrum of coupling options and the disparate physics in the fluid and structure domains makes the time-accurate solution of nonlinear problems extremely challenging. A large body of research exists for aeroelastic analysis, and some of the fruits of this research is now incorporated in commercial FSI solvers. These are typically “black box” solvers and the user does not generally have access to the source code by which to code the sensitivity equations which, in the nonlinear case, are different from the analysis equations. However, under the conditions and numerical restrictions detailed in Chapter 8, the “black box” solver can be used to solve both the FSI and sensitivity problems. This has been done using our LSFEM research code, but it would be far more convincing using one of the existing commercial solvers. Publication and presentation of results obtained in this manner would also likely encourage further use of the continuous sensitivity method. This is perhaps the quickest path to 3D FSI and sensitivity solutions, but one would have to forego the benefits of p -elements as this is not a current capability in the available commercial codes.

9.4.3 Large-scale CSE (multiple design parameters)

An two-parameter CSE example was demonstrated in Chapter 8, but all other sensitivity problems considered in this dissertation were single parameter designs. Many practical design applications are multivariate in nature, so further study of efficient methods of performing large-scale CSE would be profitable. Each design variable results in a separate CSE system, but there may be formulations and/or parameterizations which result in identical CSE systems for different parameters (the example considered in

Chapter 8 was of this nature). This could permit computational savings in the solution of the sensitivity problem. An CSE adjoint method was derived in Chapter 8, but no examples were considered. The tradeoff between the computational expense of solving multiple CSE systems and an adjoint solution to the continuous sensitivity problem is a worthy topic for further research.

9.5 Final Word on CSE for FSI applications

Fluid-structure interaction problems are not simple to solve. This is obvious from the range of attempts and methods in the literature. In the present work, a significant level of effort was expended in developing the underlying analysis of the transient, nonlinear, fluid-structure interaction methods described in Chapters 4 and 7. By contrast, however, once a valid solution is obtained for the fluid-structure system, the sensitivity analysis is straightforward and avoids many of the numerical complications of the parent fluid-structure problem. This is one of the great advantages of the continuous sensitivity approach: the sensitivity of even a complicated nonlinear, transient, coupled problem is a simple, linear, boundary value problem that need only be solved at a particular point in time. The continuous sensitivity method is particularly well-suited for shape variation problems. For efficient shape parameter gradient calculation, the continuous sensitivity approach is probably best used when a description of the system is still at the continuum level, *i.e.* before discrete sections are defined, which makes the continuous sensitivity approach an ideal choice for preliminary shape optimization. Nevertheless, there are no theoretical reasons that limit further application of the method. Continuous sensitivity

methods are well-suited and deserve more widespread application for aeroelastic design optimization.

Bibliography

- [1] Anderson, J.D., *Fundamentals of aerodynamics*, McGraw-Hill series in aeronautical and aerospace engineering, McGraw-Hill, Boston, 2001.
- [2] Anderson, J.D., *Computational fluid dynamics : the basics with applications*, McGraw-Hill series in mechanical engineering, McGraw-Hill, New York, 1994.
- [3] Arnold, D.N., "Differential complexes and numerical stability," *Plenary address delivered at ICM 2002*, International Congress of Mathematicians, Beijing, China, August 24, 2002.
- [4] Arnold, D.N., "Mixed Finite Element Methods For Elliptic Problems," *Comput. Methods Appl. Mech. Engrg.*, Vol. 82, 1990, pp. 281-300.
- [5] Arnold, D.N., and Awanou, G., "Rectangular Mixed Finite Elements for Elasticity," *Mathematical Models and Methods in Applied Sciences*, Vol. 15, No. 9, 2005, pp. 1417-1429.
- [6] Arnold, D.N., Falk, R.S., and Winther, R., "Finite element differential forms," *Proceedings in Applied Mathematics and Mechanics*, 7:1021901-1021902, 2007.
- [7] Arnold, D.N., and Winther, R., "Mixed finite elements for elasticity in the stress-displacement formulation," *Current Trends in Scientific Computing*, Vol. 329, 2003, pp. 33-42.
- [8] Arnold, D.N., and Winther, R., "Mixed finite elements for elasticity," *Numerical Mathematics*, Vol. 92, No. 3, 2002, pp. 401-419.
- [9] Arora, J.S., Lee, T.H., and Cardoso, J.B., "Structural Shape Sensitivity Analysis: Relationship Between Material Derivative and Control Volume Approaches," *AIAA Journal*, Vol. 30, No. 6, 1992, pp. 1638-1648.
- [10] Arora, J.S., Lee, T.H., and Cardoso, J.B., "Structural Shape Design Sensitivity Analysis: A Unified Viewpoint," *AIAA-91-1214-CP*, 1991, pp. 675-683.
- [11] Barthelemy, B., and Haftka, R.T., "Accuracy Analysis of the Semi-Analytical Method for Shape Sensitivity Calculation," *Mech. Struct. & Mach.*, Vol. 18, No. 3, 1990, pp. 407-432.
- [12] Bathe, K., and Shanhong, H.Z., "Finite element analysis of fluid flows fully coupled with structural interactions," *Computer and Structures*, Vol. 72, 1999, pp. 1-16.

- [13] Bathe, K., and Zhang, h., "Finite element developments for general fluid flows with structural interactions," *International Journal for Numerical Methods in Engineering*, Vol. 60, 2004, pp. 213-232.
- [14] Bathe, K. *Finite element procedures*, Prentice Hall, Englewood Cliffs, N.J., 1996.
- [15] Battin, R.H., *An introduction to the mathematics and methods of astrodynamics*, AIAA education series, American Institute of Aeronautics and Astronautics, Reston, VA, 1999.
- [16] Belgacem, F.B., Chilton, L.K., and Seshaiyer, P., "The hp-mortar finite-element method for the mixed elasticity and stokes problems," *Computers and Mathematics with Applications*, Vol. 46, 2003, pp. 35-55.
- [17] Bendiksen, O.O., "Modern developments in computational aeroelasticity," *Journal of Aerospace Engineering*, Vol. 218, 2004, pp. 157.
- [18] Bhaskaran, R., and Berkooz, G., "Optimization of Fluid-Structure Interaction using the Sensitivity Equation Approach," *Fluid-Structure Interaction, Aeroelasticity, Flow-Induced Vibrations and Noise*, Vol. 1, No. 53-1, 1997, pp. 49-56.
- [19] Bisplinghoff, R.L., and Ashley, H., *Principles of aeroelasticity*, Dover Publications, New York, 1975, pp. 527.
- [20] Blair, M., Canfield, R.A., and Roberts, R., "A Joined-Wing Aeroelastic Design with Geometric Non-Linearity," *Journal of Aircraft*, Vol. 42, No. 4, 2005, pp. 832-848.
- [21] Blazek, J., *Computational fluid dynamics : principles and applications*, Elsevier, Amsterdam ; New York, 2001, pp. 440.
- [22] Bochev, P.B., and Gunzburger, M.D., "Finite Element Methods of Least-Squares Type," *SIAM Review*, Vol. 40, No. 4, 1998, pp. 789-837.
- [23] Borggaard, J., and Burns, J., "A PDE Sensitivity Equation Method for Optimal Aerodynamic Design," *Journal of Computational Physics*, Vol. 136, 1997, pp. 366-384.
- [24] Borggaard, J., and Burns, J., "A Sensitivity Equation Approach to Shape Optimization in Fluid Flows," Langley Research Center, *NASA Contractor Report* 191598 (ICASE Report No. 94-8), 1994.
- [25] Bramble, J.H., Lazarov, R.D., and Pasciak, J.E., "Least-squares methods for linear elasticity based on a discrete minus one inner product." *Comput. Methods Appl. Mech. Engrg.*, Vol. 152, 2001, pp. 520-543.

- [26] Bramble, J.H., Lazarov, R.D., and Pasciak, J.E., "Least-squares for Second-Order Elliptic Problems," *Comput. Methods Appl. Mech. Engrg.*, Vol. 152, 1998, pp. 195-210.
- [27] Brezzi, F., and Bathe, K., "A Discourse on the Stability Conditions for Mixed Finite Element Formulations," *Computer Methods in Applied Mechanics and Engineering*, Vol. 82, 1990, pp. 27-57.
- [28] Bryson, A.E., and Ho, Y., *Applied optimal control; optimization, estimation, and control*, Blaisdell Pub. Co, Waltham, Mass., 1969, pp. 481.
- [29] Cai, Z., Manteuffel, T., McCormick, S., "First-order system least squares for the Stokes equations, with application to linear elasticity," *SIAM Journal of Numerical Analysis*, Vol. 34, No. 5, 1997, pp. 1727-1741.
- [30] Cai, Z., and Starke, G., "First-order system least squares for the stress-displacement formulation: Linear elasticity," *SIAM Journal of Numerical Analysis*, Vol. 41, No. 2, 2003, pp. 715-730.
- [31] Caro, R.D., Hay, A., Etienne, S., "Application of a Shape Sensitivity Equation Method to turbulent flow over obstacles," *18th AIAA Computational Fluid Dynamics Conference*, Miami, Florida, June 25-28, 2007, AIAA-2007-4207.
- [32] Caro, R.D., Hay, A., Etienne, S., "Continuous Shape Sensitivity Equation Method for the k-epsilon Model of Turbulence," *45th AIAA Aerospace Sciences Meeting and Exhibit*, Reno, Nevada, Jan. 8-11, 2007, AIAA-2007-518.
- [33] Chen, P.C., Liu, D.D., and Livne, E., "Unsteady-Aerodynamic Shape Sensitivities for Airplane Aeroservoelastic Configuration Optimization," *Journal of Aircraft*, Vol. 43, No. 2, 2006, pp. 471-481.
- [34] Choi, K.K., and Kim, N.H., *Structural sensitivity analysis and optimization*, Mechanical engineering series, Springer Science, New York, 2005.
- [35] Cook, R.D., Malkus, D.S., and Plesha, M.E., *Concepts and applications of finite element analysis*, Wiley, New York, 1989, pp. 630.
- [36] Cori, J., Etienne, S., Hay, A., "Optimal Design of Airfoils using NURBS and a Continuous Sensitivity Equation method," *45th AIAA Aerospace Sciences Meeting and Exhibit*, Reno, Nevada, Jan. 8-11, 2007, AIAA-2007-1129.
- [37] Demasi, L., and Livne, E., "The Structural Order Reduction Challenge in the Case of Geometrically Nonlinear Joined-Wing Configurations," *48th AIAA/ASME/ASCE/AHS/ASC Structures, Structural Dynamics, and Materials Conference*, Honolulu, Hawaii, Apr. 23-26, 2007, AIAA-2007-2105.

- [38] Demasi, L., and Livne, E., "Exploratory Studies of Joined Wing Aeroelasticity," 46th AIAA/ASME/ASCE/AHS/ASC Structures, Structural Dynamics and Materials Conference , Austin, Texas, Apr. 18-21, 2005, AIAA-2005-2172.
- [39] Dems, K., and Haftka, R.T., "Two Approaches to Sensitivity Analysis for Shape Variation of Structures," *Mech. Struct. & Mach.*, Vol. 16, No. 4, 1988-1989, pp. 501.
- [40] Dems, K., and Mroz, Z., "On shape sensitivity approaches in the numerical analysis of structures," *Structural and Multidisciplinary Optimization*, Vol. 6, No. 2, 1993, pp. 86-93.
- [41] Dems, K., and Mroz, Z., "Variational approach to first- and second-order sensitivity analysis of elastic structures," *International Journal for Numerical Methods in Engineering*, Vol. 21, 1985, pp. 637-661.
- [42] Dems, K., and Mroz, Z., "Variational approach by means of adjoint systems to structural optimization and sensitivity analysis. I - Variation of material parameters within fixed domain," *International Journal of Solids and Structures*, Vol. 19, No. 8, 1983, pp. 677-692.
- [43] Devenport, W., Kapania, R., Rojiani, K., "engApplets," *Java Applets for Engineering Education*, Virginia Tech, <http://www.engapplets.vt.edu/>, 2009.
- [44] Dowell, E.H., and Clark, R., *A modern course in aeroelasticity*, Solid mechanics and its applications, Vol. 116, Kluwer Academic Publishers, Dordrecht ; Boston, 2004.
- [45] Duvigneau, R., and Pelletier, D., "Evaluation of Nearby Flows by a Shape Sensitivity Equation Method," *43rd AIAA Aerospace Sciences Meeting and Exhibit, Reno, Nevada, Jan. 10-13, 2005*, AIAA 2005-127.
- [46] Eason, E.D., "A Review of Least-Squares Methods for Solving Partial Differential Equations," *International Journal for Numerical Methods in Engineering*, Vol. 10, 1976, pp. 1021-1046.
- [47] Etienne, S., Hay, A., Cori, J.-., "An Unsteady Sensitivity Equation Method for Fast Evaluation of FSI Nearby Configurations," *18th AIAA Computational Fluid Dynamics Conference, Miami, Florida, June 25-28, 2007*, AIAA-2007-4306.
- [48] Etienne, S., Hay, A., Garon, A., "Sensitivity Analysis of Unsteady Fluid-Structure Interaction Problems," AIAA-2007-332, 2007.
- [49] Etienne, S., Hay, A., Garon, A., "Shape Sensitivity Analysis of Fluid-Structure Interaction Problems," *36th AIAA Fluid Dynamics Conference and Exhibit, San Francisco, California, June 5-8, 2006*, AIAA 2006-3217.

- [50] Etienne, S. (Ecole Polytechnique de Montreal), "A monolithic formulation for unsteady Fluid-structure Interactions," *44th AIAA Aerospace Sciences Meeting and Exhibit, Reno, Nevada, Jan. 9-12, 2006*, AIAA-2006-694.
- [51] Etienne, S., and Pelletier, D., "A general approach to sensitivity analysis of fluid-structure interactions," *Journal of Fluids and Structures*, Vol. 21, No. 2, 2005, pp. 169-186.
- [52] Farhat, C., Degand, C., Koobus, B., "Torsional springs for two-dimensional dynamic unstructured fluid meshes," *Comput. Methods Appl. Mech. Eng.*, Vol. 163, 1998, pp. 231-245.
- [53] Farhat, C., Lesoinne, M., and Maman, N., "Mixed explicit/implicit time integration of coupled aeroelastic problems," *International Journal for Numerical Methods in Fluids*, Vol. 21, No. 10, 1995, pp. 807-835.
- [54] Fung, Y.C., *An introduction to the theory of aeroelasticity*, Dover Publications, New York, 1993.
- [55] Galligani, I., Magenes, E., Istituto per le applicazioni del calcolo, "Mathematical aspects of finite element methods : proceedings of the conference held in Rome, 10-12 December 1975," *Lecture notes in mathematics ; 606*, Springer-Verlag, Berlin ; New York, 1977, pp. 362.
- [56] Gel'fand, I.M., Fomin, S.V., and Silverman, R.A., *Calculus of variations*, Dover Publications, Mineola, N.Y., 2000.
- [57] Ghattas, O., and Li, X., "Domain Decomposition Methods For Sensitivity Analysis Of A Nonlinear Aeroelasticity Problem " *International Journal of Computational Fluid Dynamics*, Vol. 11, 1998, pp. 113-130.
- [58] Ghattas, O., and Li, X., "A variational finite element method for stationary nonlinear fluid-solid interaction," *Journal of Computational Physics*, Vol. 121, 1995, pp. 347-356.
- [59] Haftka, R.T., and Gürdal, Z., *Elements of structural optimization*, Solid mechanics and its applications, Vol. 11, Kluwer Academic Publishers, Dordrecht ; Boston, 1992.
- [60] Haug, E.J., Choi, K.K., and Komkov, V., *Design sensitivity analysis of structural systems*, Mathematics in science and engineering, Vol. 177, Academic Press, Orlando, 1986.
- [61] Heys, J.J., Manteuffel, T.A., McCormick, S.F., "First-order system least squares (FOSLS) for coupled fluid-elastic problems," *Journal of Computational Physics*, Vol. 195, No. 2, 2004, pp. 560-575.

- [62] Hoblit, F.M., *Gust loads on aircraft : concepts and applications*, AIAA education series, American Institute of Aeronautics and Astronautics, Washington, D.C., 1988.
- [63] Hodges, D.H., and Pierce, G.A., *Introduction to structural dynamics and aeroelasticity*, Cambridge aerospace series, Vol. 15, Cambridge University Press, Cambridge, England ; New York, 2002.
- [64] Hubner, B., Walhorn, E., and Dinkler, D., “A monolithic approach to fluid–structure interaction using space–time finite elements,” *Computer Methods in Applied Mechanics and Engineering*, Volume 193, Issues 23-26, 18 June 2004, Pages 2087-2104.
- [65] Jameson, A., “Aerodynamic Optimization via Control Theory,” *Journal of Scientific Computing*, Vol. 3, No. 3, 1988.
- [66] Jameson, A., Alonso, J.J., Reuther, J., “Aerodynamic Shape Optimization Techniques based on Control Theory,” *29th AIAA Fluid Dynamics Conference, Albuquerque*, June 1998, AIAA 98-2538.
- [67] Jameson, A., and Kim, S., “Reduction of the Adjoint Gradient Formula for Aerodynamic Shape Optimization Problems,” *AIAA Journal*, Vol. 41, No. 11, 2003, pp. 2114-2129.
- [68] Jameson, A., Shankaran, S., and Martinelli, L., “Continuous Adjoint Method for Unstructured Grids,” *AIAA Journal*, Vol. 46, No. 5, 2008, pp. 1226-1239.
- [69] Jiang, B., *The least-squares finite element method: theory and applications in computational fluid dynamics and electromagnetics*, Scientific computation, Springer, Berlin ; New York, 1998.
- [70] Karniadakis, G., and Sherwin, S.J., *Spectral hp element methods for computational fluid dynamics*, Numerical mathematics and scientific computation, Oxford University Press, New York, 2005.
- [71] Kayser-Herold, O., “Least-Squares Methods for the Solution of Fluid-Structure Interaction Problems,” Ph.D. Dissertation, Technische Universität Carolo-Wilhelmina zu Braunschweig, 2006.
- [72] Kayser-Herold, O., and Matthies, H.G., “A Unified Least-Squares Formulation for Fluid-Structure Interaction Problems,” *Computer and Structures*, Vol. 85, 2007, pp. 998-1011.
- [73] Kim, S.D., Manteuffel, T.A., and McCormick, S.F., “First-order system Least-Squares (FOSLS) for Spatial Linear Elasticity: Pure Traction,” *SIAM Journal of Numerical Analysis*, Vol. 38, No. 5, 2000, pp. 1454-1482.

- [74] Kreyszig, E., *Advanced engineering mathematics*, Wiley, New York, 1988.
- [75] Lee, D., and Chen, P., "Nonlinear Aeroelastic Studies on a Joined-Wing with Wing Buckling Effects," *45th AIAA/ASME/ASCE/AHS/ASC Structures, Structural Dynamics and Materials Conference, Palm Springs, California*, Apr. 19-22, 2004 AIAA-2004-1944.
- [76] Lee, S.-., Youn, S.-., Yeon, J.-., "A Study on the Fluid-Structure Interaction using LSFEM," Dep. of Mechanical Engineering, Korea Advanced Institute of Science and Technology, Taejon, Korea, 2000.
- [77] Livne, E., "Future of Airplane Aeroelasticity," *Journal of Aircraft*, Vol. 40, No. 6, 2003, pp. 1066-1092.
- [78] Lucia, D.J., "The SensorCraft Configurations: A Non-Linear AeroServoElastic Challenge for Aviation," *46th AIAA/ASME/ASCE/AHS/ASC Structures, Structural Dynamics and Materials Conference*, Austin, Texas, Apr. 18-21, 2005, AIAA-2005-1943.
- [79] Lund, E., "Shape design optimization of steady fluid-structure interaction problems with large displacements," *42nd AIAA/ASME/ASCE/AHS/ASC Structures, Structural Dynamics, and Materials Conference and Exhibit*, Seattle, WA, Apr. 16-19, 2001, AIAA-2001-1624.
- [80] Mahieu, J., Etienne, S., Pelletier, D., "A Second-order sensitivity equation method for laminar flow," *International Journal of Computational Fluid Dynamics*, Vol. 19, No. 2, 2005, pp. 143-157.
- [81] Matthies, H.G., and Steindor, J., "Partitioned strong coupling algorithms for fluid-structure interaction," *Computer and Structures*, Vol. 81, No. 8-11, 2003, pp. 805-812.
- [82] Maute, K., Nikbay, M., and Farhat, C., "Coupled Analytical Sensitivity Analysis and Optimization of Three-Dimensional Nonlinear Aeroelastic Systems," *AIAA Journal*, Vol. 39, No. 11, 2001, pp. 2051-2061.
- [83] Maute, K., Nikbay, M., and Farhat, C., "Analytically Based Sensitivity Analysis and Optimization of Nonlinear Aeroelastic Systems," AIAA 2000-4825, 2000.
- [84] Michler, C., Hulshoff, S.J., van Brummelen, E.H., "A monolithic approach to fluid-structure interaction," *Computers & Fluids*, Vol. 33, No. 5-6, 2004, pp. 839-848.
- [85] Mor, M., and Livne, E., "Integrated Aeroelastic Shape Optimization of Flight Vehicles," Vol. AIAA 2005-1890, 2005.

- [86] Mor, M., and Livne, E., "Sensitivities and Approximations for Aeroservoelastic Shape Optimization with Gust Response Constraints," *46th AIAA/ASME/ASCE/AHS/ASC Structures, Structural Dynamics and Materials Conference*, Austin, Texas, Apr. 18-21, 2005, AIAA-2005-2077.
- [87] Nadarajah, S.K., and Jameson, A., "Optimum Shape Design for Unsteady Flows with Time-Accurate Continuous and Discrete Adjoint Methods," *AIAA Journal*, Vol. 45, No. 7, 2007, pp. 1478--1491.
- [88] Naylor, A.W., and Sell, G.R., *Linear operator theory in engineering and science*, Applied mathematical sciences, Vol. 40, Springer-Verlag, New York, 1982.
- [89] Newsome, R.W., Berkooz, G., and Bhaskaran, R., "Use of Analytic Flow Sensitivities in Static Aeroelasticity," *AIAA Journal*, Vol. 36, No. 8, 1998, pp. 1537-1540.
- [90] Nielsen, E.J., and Park, M.A., "Using an Adjoint Approach to Eliminate Mesh Sensitivities in Computational Design," *AIAA Journal*, Vol. 44, No. 5, 2006, pp. 948-953.
- [91] Peterson, R.E., *Stress concentration factors; charts and relations useful in making strength calculations for machine parts and structural elements*, Wiley, New York, 1974.
- [92] Phelan, D.G., and Haber, R., B., "Sensitivity analysis of linear elastic systems using domain parameterization and a mixed mutual energy principle," *Computer Methods in Applied Mechanics and Engineering*, Vol. 77, 1989, pp. 31-59.
- [93] Pontaza, J.P., "Least-squares finite element formulation for shear-deformable shells," *Computer Methods in Applied Mechanics and Engineering*, Vol. 194, No. 21-24, 2005, pp. 2464.
- [94] Pontaza, J.P., "Least-Squares Variational Principles And The Finite Element Method: Theory, Formulations, And Models For Solid And Fluid Mechanics," Ph.D. Dissertation, Texas A&M University, 2003.
- [95] Pontaza, J.P., Diao, X., Reddy, J.N., "Least-squares finite element models of two-dimensional compressible flows," *Finite Elements in Analysis and Design*, Vol. 40, No. 5-6, 2004, pp. 629-644.
- [96] Pontaza, J.P., and Reddy, J.N., "Least-squares finite element formulations for viscous incompressible and compressible fluid flows," *Computer Methods in Applied Mechanics and Engineering*, Vol. 195, No. 19-22, 2006, pp. 2454-2494.

- [97] Pontaza, J.P., and Reddy, J.N., "Mixed plate bending elements based on least-squares formulation," *International Journal for Numerical Methods in Engineering*, Vol. 60, No. 5, 2004, pp. 891-922.
- [98] Pontaza, J.P., and Reddy, J.N., "Space-time coupled spectral/*hp* least-squares finite element formulation for the incompressible Navier-Stokes equations," *Journal of Computational Physics*, Vol. 197, No. 2, 2004, pp. 418-459.
- [99] Pontaza, J.P., and Reddy, J.N., "Spectral/*hp* least-squares finite element formulation for the Navier-Stokes equations," *Journal of Computational Physics*, Vol. 190, 2003, pp. 523-549.
- [100] Proot, M.M.J., and Gerritsma, M.I., "Least-squares spectral elements applied to the Stokes problem," *Journal of Scientific Computing*, Vol. 17, No. 1-4, 2002, pp. 285-296.
- [101] Rasmussen, C.C., "Nonlinear Transient Gust Response Using A Fully-Coupled Least-Squares Finite Element Formulation For Fluid-structure Interaction," Ph.D. Dissertation, Air Force Institute of Technology, 2008.
- [102] Rasmussen, C.C., Canfield, R.A., and Reddy, J.N., "Advantages and Disadvantages of a Simultaneously Coupled Least-Squares Finite Element Formulation for Fluid-Structure Interaction," 12th AIAA/ISSMO Multidisciplinary Analysis and Optimization Conference, Victoria, British Columbia, Sep. 10-12, 2008, AIAA-2008-5859.
- [103] Rasmussen, C., Canfield, R., and Reddy, J.N., "Nonlinear Transient Gust Response Using a Fully- Coupled Least- Squares Finite Element Formulation," 49th AIAA/ASME/ASCE/AHS/ASC Structures, Structural Dynamics, and Materials Conference Schaumburg, IL, Apr. 7-10, 2008, AIAA-2008-1821.
- [104] Reddy, J.N., *An introduction to continuum mechanics : with applications*, Cambridge University Press, New York, 2008.
- [105] Reddy, J.N., *An introduction to the finite element method*, McGraw-Hill series in mechanical engineering, McGraw-Hill Higher Education, New York, NY, 2006.
- [106] Reddy, J.N., *An introduction to nonlinear finite element analysis*, Oxford University Press, Oxford ; New York, 2004.
- [107] Reddy, J.N., *Energy principles and variational methods in applied mechanics*, Wiley, New York, 2002.
- [108] Reddy, J.N., *Applied functional analysis and variational methods in engineering*, McGraw-Hill, New York, 1986.

- [109] Reuther, J., Jameson, A., Alonso, J.J., “Constrained Multipoint Aerodynamic Shape Optimization Using an Adjoint Formulation and Parallel Computers, Part I,” *Journal of Aircraft*, Vol. 36, No. 1, 1999, pp. 51--60.
- [110] Reuther, J., Jameson, A., Farmer, J., “Aerodynamic Shape Optimization of Complex Aircraft Configurations via an Adjoint Formulation,” RIACS Technical Report 96.02, 1996.
- [111] Roark, R.J., Young, W.C., and Budynas, R.G., *Roark's formulas for stress and strain*, McGraw-Hill, New York, 2002.
- [112] Sackinger, P.A., Schunk, P.R., and Rao, R.R., “A Newton–Raphson Pseudo-Solid Domain Mapping Technique for Free and Moving Boundary Problems: A Finite Element Implementation,” *Journal of Computational Physics*, Vol. 125, No. 1, 1996, pp. 83-103.
- [113] Schmit, L.A., “Structural Design by Systematic Synthesis,” *Proc. of the Second ASCE Conference on Electronic Computation*, Pittsburgh (1960), pp. 105–122.
- [114] Seshaiyer, P., and Suri, M., “Uniform hp convergence results for the mortar finite element method,” *Mathematics of Computation*, Vol. 69, No. 230, 1999, pp. 521-546.
- [115] Sobieszczanski-Sobieski, J., and Haftka, R.T., “Multidisciplinary aerospace design optimization: survey of recent developments,” *Structural and Multidisciplinary Optimization*, Vol. 14, No. 1, 1997, pp. 1-23.
- [116] Šolin, P., Segeth, K., and Doléžal, I., *Higher-order finite element methods*, Studies in advanced mathematics, Chapman & Hall/CRC, Boca Raton, FL, 2004.
- [117] Sorenson, T.M., and Drela, M., “Aeroelastic Sensitivity Calculations using a Newton-based Full-Potential Equation solver,” AIAA-95-1834-CP, 1995.
- [118] Stanley, L., “Sensitivity analysis for actuator placement on an Euler-Bernoulli beam,” *43rd IEEE Conference on Decision and Control*, 14-17 Dec. 2004, Vol 2, pp 1532- 537, 2004.
- [119] Stanley, L.G., “Computational Methods for Sensitivity Analysis with Applications to Elliptic Boundary Value Problems,” Ph.D. Dissertation, VA Tech, 1999.
- [120] Stanley, L.G.D., and Stewart, D.L., *Design sensitivity analysis : computational issues of sensitivity equation methods*, Frontiers in applied mathematics, Society for Industrial and Applied Mathematics, Philadelphia, 2002.

- [121] Stewart, D.L., “Numerical Methods for Accurate Computation of Design Sensitivities,” Ph.D. Dissertation, VA Tech, 1999.
- [122] Swim, E., and Seshaiyer, P., “A nonconforming finite element method for fluid-structure interaction problems,” *Computer Methods in Applied Mechanics and Engineering*, Vol. 195, 2006, pp. 2088-2099.
- [123] Swim, E., “Nonconforming finite element methods for fluid-structure interaction,” *Computer Methods in Applied Mechanics and Engineering*, Vol 195, Issues 17-18, 15 Mar 2006, pp 2088-2099.
- [124] Szabo, B.A., and Babuška, I., *Finite element analysis*, Wiley, New York, 1991.
- [125] Tannehill, J.C., Anderson, D.A., and Pletcher, R.H., *Computational fluid mechanics and heat transfer*, Series in computational and physical processes in mechanics and thermal sciences, Taylor & Francis, Washington, DC, 1997.
- [126] Thompson, P.A., *Compressible-fluid dynamics*, Advanced engineering series, McGraw-Hill, New York, 1971.
- [127] Timoshenko, S., and Goodier, J.N., *Theory of elasticity*, Engineering societies monographs, McGraw-Hill, New York, 1969.
- [128] Turgeon, E., Pelletier, D., and Borggaard, J., “A Continuous Sensitivity Equation Approach to Optimal Design in Mixed Convection,” AIAA Thermophysics Conference, 33rd, Norfolk, VA, June 28-July 1, 1999, AIAA-1999-3625.
- [129] Walhorn, E., Kölke, A., Hübner, B., “*Fluid-structure coupling within a monolithic model involving free surface flows*,” *Computers and Structures*, Vol. 83, 2005, pp. 2100-2111.
- [130] Wang, X., “Analytical and computational approaches for some fluid-structure interaction analyses,” *Computers and Structures*, Vol. 72, 1999, pp. 423-423-433.
- [131] Wang, Z., Chen, P., Liu, D., “Nonlinear Aeroelastic Analysis for A HALE Wing Including Effects of Gust and Flow Separation,” 48th AIAA/ASME/ASCE/AHS/ASC Structures, Structural Dynamics, and Materials Conference, Honolulu, Hawaii, Apr. 23-26, 2007, AIAA-2007-2106.
- [132] Wang, Z., Chen, P., Liu, D., “Time Domain Nonlinear Aeroelastic Analysis for HALE Wings,” 47th AIAA/ASME/ASCE/AHS/ASC Structures, Structural Dynamics, and Materials Conference, Newport, Rhode Island, May 1-4, 2006, AIAA-2006-1640.

- [133] White, F.M., *Viscous fluid flow*, McGraw-Hill series in mechanical engineering, McGraw-Hill, New York, 1991.
- [134] Wickert, D.P., and Canfield, R.A., "Improving the Matrix Condition Number of Weakly-Enforced Boundary Value Systems," 4th Dayton Engineering Sciences Symposium, 3 Oct 2008.
- [135] Wickert, D.P., and Canfield, R.A., "Least-Squares Continuous Sensitivity Analysis of an Example Fluid-Structure Interaction Problem," 49th AIAA/ASME/ASCE/AHS/ASC Structures, Structural Dynamics, and Materials Conference, Schaumburg, IL, Apr. 7-10, 2008 AIAA-2008-1896.
- [135] Wickert, D.P., Canfield, R.A., and Reddy, J.N., "Continuous Sensitivity Analysis of Fluid-Structure Interaction Problems Using Least-Squares Finite Elements," 12th AIAA/ISSMO Multidisciplinary Analysis and Optimization Conference, Victoria, British Columbia, Sep. 10-12, 2008, AIAA-2008-5931.
- [136] Wickert, D.P., Canfield, R.A., and Reddy, J.N., "Least-Squares Continuous Sensitivity Shape Optimization for Structural Elasticity Applications," *AIAA Journal*, Submitted 2009.
- [137] Wickert, D.P., Canfield, R.A., and Reddy, J.N., "Fluid-Structure Transient Gust Sensitivity Using Least-Squares Continuous Sensitivity Analysis," 50th AIAA/ASME/ASCE/AHS/ASC Structures, Structural Dynamics, and Materials Conference, Palm Springs, California, May 4-7, 2009, AIAA-2009-2535.
- [138] Wickert, D.P., Roberts, R.W., and Canfield, R.A., "Least-Squares Continuous Sensitivity Equations for an Infinite Plate with a Hole," 49th AIAA/ASME/ASCE/AHS/ASC Structures, Structural Dynamics, and Materials Conference, Schaumburg, IL, Apr. 7-10, 2008, AIAA-2008-1797.
- [139] Winston, W.L., *Operations research : applications and algorithms*, Duxbury Press, Belmont, Calif., 1994.
- [140] Yang, S., and Liu, J., "Analysis of Least Squares Finite Element Methods for A Parameter-Dependent First-Order System," *Numerical Functional Analysis and Optimization*, Vol. 19, 1998, pp. 191-213.
- [141] Yang, S., and Liu, J., "Least-squares finite element methods for the elasticity problem," *Journal of Computational and Applied Mathematics*, Vol. 87, No. 1, 1997, pp. 39-60.

VITA

Maj Wickert was the number one academic graduate from the United States Air Force Academy (1995) with degrees in Astronautical Engineering and Mathematics. After commissioning, he earned a Masters of Science degree in Aeronautics and Astronautics from the Massachusetts Institute of Technology (1997). Maj Wickert was the Distinguished Graduate of the Joint Specialized Undergraduate Pilot Training course at Vance AFB, OK, in July of 1998. He received the AETC Commander's Trophy, the Flying Training Award, the Leadership Award, and the Daedalian's Orville Wright Achievement Award. Maj Wickert was also a Distinguished Graduate and Top Gun from F-16 training at Luke AFB, AZ, in July of 1999.

As a fighter pilot with the 4th Fighter Squadron, 388th Fighter Wing, Hill AFB from 1999-2001, Maj Wickert flew combat missions over Iraq during Operation Southern Watch as well as Caribbean drug interdiction and homeland defense missions. He then served as the Wing Electronic Combat Pilot, Asst. Chief of F-16 Weapons and Tactics, and as an F-16 Instructor Pilot in the 51st Fighter Wing, Osan AB, Korea from 2001-2003.

Maj Wickert graduated number one from the United States Naval Test Pilot School at NAS Patuxent River, MD, in June 2004, where he was also the recipient of the Empire Test Pilot School award. He then served as Asst. Director of Operations, Flight Commander, and as the F-16 Chief Experimental Test Pilot for the 40th Flight Test Squadron, Eglin AFB, FL from 2004-2006. Maj Wickert's extensive flight test contributions in loads, flutter, stability and control, certification, and systems development test programs earned him the USAF Air Armament Center's Lt Gen Bobby Bonds Award (2006) and the Air Force Material Command Daedalian Exceptional Pilot Award (2005). Maj Wickert also received the Society of Experimental Test Pilots Ray E. Tehnoff award (2006).

Maj Wickert is a senior pilot with more than 2000 hours in more than 30 aircraft. He is a member of the American Institute of Aeronautics and Astronautics and the Society of Experimental Test Pilots. His awards and decorations include the Aerial Achievement Medal, the Air Force Commendation and Meritorious Service Medals, the AFMC Exceptional Pilot Award, and the Ritchey Leadership Excellence Award. After graduation from the Air Force Institute of Technology his is being reassigned to the faculty of the US Air Force Test Pilot School.

REPORT DOCUMENTATION PAGE				Form Approved OMB No. 074-0188	
<p>The public reporting burden for this collection of information is estimated to average 1 hour per response, including the time for reviewing instructions, searching existing data sources, gathering and maintaining the data needed, and completing and reviewing the collection of information. Send comments regarding this burden estimate or any other aspect of the collection of information, including suggestions for reducing this burden to Department of Defense, Washington Headquarters Services, Directorate for Information Operations and Reports (0704-0188), 1215 Jefferson Davis Highway, Suite 1204, Arlington, VA 22202-4302. Respondents should be aware that notwithstanding any other provision of law, no person shall be subject to a penalty for failing to comply with a collection of information if it does not display a currently valid OMB control number.</p> <p>PLEASE DO NOT RETURN YOUR FORM TO THE ABOVE ADDRESS.</p>					
1. REPORT DATE (DD-MM-YYYY) 10-09-2009		2. REPORT TYPE Doctoral Dissertation		3. DATES COVERED (From – To) Sep 2006 – Sep 2009	
TITLE AND SUBTITLE Least-Squares, Continuous Sensitivity Analysis For Nonlinear Fluid-Structure Interaction				5a. CONTRACT NUMBER	
				5b. GRANT NUMBER	
				5c. PROGRAM ELEMENT NUMBER	
6. AUTHOR(S) Wickert, Douglas P., Maj, USAF				5d. PROJECT NUMBER	
				5e. TASK NUMBER	
				5f. WORK UNIT NUMBER	
7. PERFORMING ORGANIZATION NAMES(S) AND ADDRESS(S) Air Force Institute of Technology Graduate School of Engineering and Management (AFIT/ENY) 2950 Hobson Way, Building 640 WPAFB OH 45433-8865				8. PERFORMING ORGANIZATION REPORT NUMBER AFIT/DS/ENY/09-S04	
9. SPONSORING/MONITORING AGENCY NAME(S) AND ADDRESS(ES) AFOSR, Dr. Fariba Fahroo AFRL/RB, Dr. Raymond Kolonay				10. SPONSOR/MONITOR'S ACRONYM(S)	
				11. SPONSOR/MONITOR'S REPORT NUMBER(S)	
12. DISTRIBUTION/AVAILABILITY STATEMENT APPROVED FOR PUBLIC RELEASE; DISTRIBUTION UNLIMITED.					
13. SUPPLEMENTARY NOTES					
14. ABSTRACT A least-squares, continuous sensitivity analysis method is developed for transient aeroelastic gust response problems to support computationally efficient analysis and optimization of aeroelastic design problems. A key distinction between the local and total derivative forms of the sensitivity system is introduced. The continuous sensitivity equations and sensitivity boundary conditions are derived in local derivative form which is shown to be superior for several applications. The analysis and sensitivity problems are both posed in a first-order form which is amenable to a solution using the least-squares finite element method. Several example and validation problems are presented and solved, including elasticity, fluid, and fluid-structure interaction problems. Significant contributions of the research include the first sensitivity analysis of nonlinear transient gust response, a local derivative formulation for shape variation that requires parameterizing only the boundary, and statement of sufficient conditions for using nonlinear "black box" software to solve the sensitivity equations. Promising paths for future investigation are presented and discussed.					
15. SUBJECT TERMS Continuous Sensitivity Equations, Least-squares Finite Element Method, Fluid-Structure Interaction, Nonlinear Gust Response					
16. SECURITY CLASSIFICATION OF:			17. LIMITATION OF ABSTRACT UU	18. NUMBER OF PAGES 284	19a. NAME OF RESPONSIBLE PERSON Dr Robert A. Canfield
a. REPORT U	b. ABSTRACT U	c. THIS PAGE U			19b. TELEPHONE NUMBER (Include area code) (540) 231-5981 (rac@vt.edu)